(NASA-CR- 157161) THE DEEP SPACE NETWORK Progress Report, No. - Dec. 1977 (Jet Propulsion Lab.) 257 p HC A12/MF A01 CSCL 22A

N78-24187
THRU
N78-24211
Unclas
G3/12 21438

The Deep Space Network Progress Report 42-43

November and December 1977

National Aeronautics and Space Administration

Jet Propulsion Laboratory
California Institute of Technology
Pasadena, California 91103

The Deep Space Network Progress Report 42-43

November and December 1977

February 15, 1978

National Aeronautics and
Space Administration

Jet Propulsion Laboratory
California Institute of Technology
Pasadena, California 91103

Preface

Beginning with Volume XX, the Deep Space Network Progress Report changed from the Technical Report 32- series to the Progress Report 42- series. The volume number continues the sequence of the preceding issues. Thus, Progress Report 42-20 is the twentieth volume of the Deep Space Network series, and is an uninterrupted follow-on to Technical Report 32-1526, Volume XIX.

This report presents DSN progress in flight project support, tracking and data acquisition (TDA) research and technology, network engineering, hardware and software implementation, and operations. Each issue presents material in some, but not all, of the following categories in the order indicated.

Description of the DSN

Mission Support
- Ongoing Planetary/Interplanetary Flight Projects
- Advanced Flight Projects

Radio Astronomy

Special Projects

Supporting Research and Technology
- Tracking and Ground-Based Navigation
- Communications–Spacecraft/Ground
- Station Control and Operations Technology
- Network Control and Data Processing

Network and Facility Engineering and Implementation
- Network
- Network Operations Control Center
- Ground Communications
- Deep Space Stations
- Quality Assurance

Operations
- Network Operations
- Network Operations Control Center
- Ground Communications
- Deep Space Stations

Program Planning
- TDA Planning

In each issue, the part entitled "Description of the DSN" describes the functions and facilities of the DSN and may report the current configuration of one of the five DSN systems (Tracking, Telemetry, Command, Monitor & Control, and Test & Training).

The work described in this report series is either performed or managed by the Tracking and Data Acquisition organization of JPL for NASA.

Contents

DESCRIPTION OF THE DSN

MISSION SUPPORT

Ongoing Planetary/Interplanetary Flight Projects

SUPPORTING RESEARCH AND TECHNOLOGY

Tracking and Ground-Based Navigation

Communications — Spacecraft/Ground

Network Control and Data Processing

NETWORK AND FACILITY ENGINEERING AND IMPLEMENTATION

Network

Ground Communications

Deep Space Stations

OPERATIONS

Network Operations

Deep Space Station

Network Functions and Facilities

N. A. Renzetti
Office of Tracking and Data Acquisition

The objectives, functions, and organization of the Deep Space Network are summarized; deep space station, ground communication, and network operations control capabilities are described.

The Deep Space Network was established by the National Aeronautics and Space Administration (NASA) Office of Space Tracking and Data Systems and is under the system management and technical direction of the Jet Propulsion Laboratory (JPL). The network is designed for two-way communications with unmanned spacecraft traveling approximately 16,000 km (10,000 miles) from Earth to the farthest planets and to the edge of our solar system. It has provided tracking and data acquisition support for the following NASA deep space exploration projects: Ranger, Surveyor, Mariner Venus 1962, Mariner Mars 1964, Mariner Venus 1967, Mariner Mars 1969, Mariner Mars 1971, and Mariner Venus-Mercury 1973, for which JPL has been responsible for the project management, the development of the spacecraft, and the conduct of mission operations; Lunar Orbiter, for which the Langley Research Center carried out the project management, spacecraft development, and conduct of mission operations; Pioneer, for which Ames Research Center carried out the project management, spacecraft development, and conduct of mission operations; and Apollo, for which the Lyndon B. Johnson Space Center was the project center and the Deep Space Network supplemented the Manned Space Flight Network, which was managed by the Goddard Space Flight Center. The network is currently providing tracking and data acquisition support for Helios, a joint U.S./West German project; Viking, for which Langley Research Center provides the project management, the Lander spacecraft, and conducts mission operations, and for which JPL provides the Orbiter spacecraft; Voyager, for which JPL provides project management, spacecraft development, and conduct of mission operations; and Pioneer Venus, for which the Ames Research Center provides project management, spacecraft development, and conduct of mission operations. The network is adding new capability to meet the requirements of the Jupiter Orbiter Probe Mission, for which JPL provides the project management, spacecraft development and conduct of mission operations.

The Deep Space Network (DSN) is one of two NASA networks. The other, the Spaceflight Tracking and Data Network (STDN), is under the system management and technical direction of the Goddard Space Flight Center (GSFC). Its function is to support manned and unmanned Earth-orbiting satellites. The Deep Space Network supports lunar, planetary, and interplanetary flight projects.

From its inception, NASA has had the objective of conducting scientific investigations throughout the solar system. It was recognized that in order to meet this objective, significant supporting research and advanced technology development must be conducted in order to provide deep space telecommunications for science data return in a cost effective manner. Therefore, the Network is continually evolved to keep pace with the state of the art of telecommunications and data

handling. It was also recognized early that close coordination would be needed between the requirements of the flight projects for data return and the capabilities needed in the Network. This close collaboration was effected by the appointment of a Tracking and Data Systems Manager as part of the flight project team from the initiation of the project to the end of the mission. By this process, requirements were identified early enough to provide funding and implementation in time for use by the flight project in its flight phase.

As of July 1972, NASA undertook a change in the interface between the Network and the flight projects. Prior to that time, since 1 January 1964, in addition to consisting of the Deep Space Stations and the Ground Communications Facility, the Network had also included the mission control and computing facilities and provided the equipment in the mission support areas for the conduct of mission operations. The latter facilities were housed in a building at JPL known as the Space Flight Operations Facility (SFOF). The interface change was to accommodate a hardware interface between the support of the network operations control functions and those of the mission control and computing functions. This resulted in the flight projects assuming the cognizance of the large general-purpose digital computers which were used for both network processing and mission data processing. They also assumed cognizance of all of the equipment in the flight operations facility for display and communications necessary for the conduct of mission operations. The Network then undertook the development of hardware and computer software necessary to do its network operations control and monitor functions in separate computers. A characteristic of the new interface is that the Network provides direct data flow to and from the stations; namely, metric data, science and engineering telemetry, and such network monitor data as are useful to the flight project. This is done via appropriate ground communication equipment to mission operations centers, wherever they may be.

The principal deliverables to the users of the Network are carried out by data system configurations as follows:

- The DSN Tracking System generates radio metric data, i.e., angles, one- and two-way doppler and range, and transmits raw data to Mission Control.
- The DSN Telemetry System receives, decodes, records, and retransmits engineering and scientific data generated in the spacecraft to Mission Control.
- The DSN Command System accepts spacecraft commands from Mission Control and transmits the commands via the Ground Communication Facility to a Deep Space Station. The commands are then radiated to the spacecraft in order to initiate spacecraft functions in flight.
- The DSN Radio Science System generates radio science data, i.e., the frequency and amplitude of spacecraft transmitted signals affected by passage through media such as the solar corona, planetary atmospheres, and planetary rings, and transmits this data to Mission Control.

The data system configurations supporting testing, training, and network operations control functions are as follows:

- The DSN Monitor and Control System instruments, transmits, records, and displays those parameters of the DSN necessary to verify configuration and validate the Network. It provides the tools necessary for Network Operations personnel to control and monitor the Network and interface with flight project mission control personnel.
- The DSN Test and Training System generates and controls simulated data to support development, test, training and fault isolation within the DSN. It participates in mission simulation with flight projects.

The capabilities needed to carry out the above functions have evolved in three technical areas:

(1) The Deep Space Stations, which are distributed around Earth and which, prior to 1964, formed part of the Deep Space Instrumentation Facility. The technology involved in equipping these stations is strongly related to the state of the art of telecommunications and flight-ground design considerations, and is almost completely multimission in character.

(2) The Ground Communications Facility provides the capability required for the transmission, reception, and monitoring of Earth-based, point-to-point communications between the stations and the Network Operations Control Center at JPL, Pasadena, and to the JPL Mission Operations Centers. Four communications disciplines are provided: teletype, voice, high-speed, and wideband. The Ground Communications Facility uses the capabilities provided by common carriers throughout the world, engineered into an integrated system by Goddard Space Flight Center, and controlled from the communications Center located in the Space Flight Operations Facility (Building 230) at JPL.

The Network Operations Control Center is the functional entity for centralized operational control of the Network and interfaces with the users. It has two separable functional elements; namely, Network Operations Control and Network

Data Processing. The functions of the Network Operations Control are:

- Control and coordination of Network support to meet commitments to Network users.
- Utilization of the Network data processing computing capability to generate all standards and limits required for Network operations.
- Utilization of Network data processing computing capability to analyze and validate the performance of all Network systems.

The personnel who carry out the above functions are located in the Space Flight Operations Facility, where mission operations functions are carried out by certain flight projects. Network personnel are directed by an Operations Control Chief. The functions of the Network Data Processing are:

- Processing of data used by Network Operations Control for control and analysis of the Network.
- Display in the Network Operations Control Area of data processed in the Network Data Processing Area.
- Interface with communications circuits for input to and output from the Network Data Processing Area.
- Data logging and production of the intermediate data records.

The personnel who carry out these functions are located approximately 200 meters from the Space Flight Operations Facility. The equipment consists of minicomputers for real-time data system monitoring, two XDS Sigma 5s, display, magnetic tape recorders, and appropriate interface equipment with the ground data communications.

DSN Command System Mark III-78

W. G. Stinnett
TDA Engineering Section

The DSN Command System Mark III-78 data processing includes a capability for a data handling method called "store-and-forward." A description of the data processing for command store-and-forward is contained in this article.

I. Introduction

The last DSN Progress Report article discussing the DSN Command System (Volume 42-35) defined the implementation that was in process for the Mark III-77 configuration. The prime implementation was to occur at the Deep Space Stations and at JPL in the Ground Communication Facility (GCF) Central Communications Terminal. At the Deep Space Stations, new minicomputers replaced the existing obsolete computers. Presently, all stations have been upgraded to the Mark III-77 configuration, except DSS 11 at Goldstone, California. In the Central Communication Terminal (CCT), minicomputers were implemented such that automatic data routing (instead of manual line patching) of the high-speed data line traffic could be accomplished. The computers in the CCT have been installed, and the final phases of software testing are in process. As soon as the new minicomputers at DSS 11 are implemented (March 1978) the DSN Command System Mark III-77 configuration will be complete. Due to the fact that this hardware reconfiguration occurred over a 15-month time interval (station-by-station), the command data processing capabilities in the new minicomputers had to be "held" to the level of capabilities that existed in the computers being replaced. That is, the data interfaces with the Mission Operations Control Centers had to be maintained such that those centers could interface with either a Mark III-75 or Mark III-77 configured DSS. Now that all stations (DSS 11 is imminent) have significantly increased command data storage capability, plans are to significantly change the data processing capabilities of the DSN Command System Mark III-78.

The data processing capabilities of the DSN Command System have remained constant since late 1973. The interface with the Mission Control Centers (at JPL and at Ames Research Center) have likewise remained constant. These capabilities have supported Helios, Mariner Venus-Mercury, Pioneers 10 and 11, Viking and Voyager missions. The design of the data processing capabilities was based on the "worst case" mission needs while recognizing the limited command storage capabilities at a DSS.

The types of missions supported, coupled with the constraint of limited command storage at a Deep Space Station dictated a system data processing design in which commands are "held" at the Mission Control Center and "fed" to a Deep Space Station in small quantities. These small quantities of commands are temporarily held at a Deep Space Station prior to radiation to the spacecraft. The data processing capabilities, especially with regard to the data interface with the Mission Control Centers, are complex and highly interactive. This is primarily due to providing the capability for Mission Control to change a command sequence in real-time. The commands temporarily stored at a DSS can be "reshuffled" when a command sequence is changed. This requires numerous software algorithms to ensure the validity of a "new" command sequence.

Due to the nature of recent missions and spacecraft supported by the DSN, the data processing requirements are changing. The natures of the missions are relatively long lasting; thus new data processing capabilities are necessary to minimize operations personnel (costs) that are dedicated to operating and monitoring the Ground Command System. The more recent spacecraft being supported (e.g., Viking, Voyager and the yet to be launched Pioneer Venus) have onboard command storage and sequencing capabilities. Further, the operation of these spacecraft is based on loading this onboard storage well in advance of action to be taken by the spacecraft. That is, very few "direct action" commands are being used now for spacecraft support. Ground Command System data processing capabilities are now being developed which are more compatible with future mission operations and spacecraft concepts. The description of this DSN portion of the Command System data processing is the subject of this article.

II. General Concept – Command Store-and-Forward

The end-to-end command data flow is shown in Fig. 1. Each element of the "system" is responsible to temporarily store, then forward a specific set of spacecraft commands. This method of data delivery has been termed "store-and-forward." At the Mission Operation Center, as part of mission-dependent capabilities, a "set" of commands is generated based upon the particular requirements for a series of mission objectives for a given period of time. These commands are usually computer-generated and are normally generated on the order of days in advance of actual execution by the spacecraft. After generation, the set of commands is then stored for later entry into the real-time ground command system. Entry for temporary storage into the Mission Operation Center real-time command system normally occurs on the order of hours before delivery to the DSN. When a Deep Space Station has been scheduled to track a given spacecraft, it is available for the command function. The station will receive the set of commands from the Mission Control Center via a high-speed data line. This set of commands will normally be received the first few minutes of the stations track. The set of commands is then available for radiation to the spacecraft. At the option of the Mission Operations Team, radiation can begin immediately, or a few hours into the track. Upon receipt by the spacecraft, the commands are stored, normally in an onboard computer, for later execution. As can be seen from the above description, each element in the system receives and stores the complete set of commands prior to forwarding: thus the term store-and-forward. This article discusses the DSN data processing portion of this end-to-end command store-and-forward method of data handling.

III. DSN Data Processing, Command Store-and-Forward

The DSN data processing can best be described by defining three distinct functions that occur to command a spacecraft.

(1) Receiving and storing the command data at a DSS.

(2) Queuing command data to be radiated to the spacecraft.

(3) Radiating the command data to the spacecraft.

Before discussing the above three functions, command files and file elements need to be defined. The data handling design is based upon blocking the command data into files made up of file elements.

A. Command Files

The basic "set" of spacecraft commands that is forwarded from one ground system element to the next is a command file. Generally, multiple files will be generated for forwarding. Every file is composed of two element (1 element = 1 high-speed data block) types. The general structure is:

Header element	0
Command element	1
Command element	2
⋮	
Command element	n

The header element contains file identification information, file processing instruction, and a file checksum for error protection. The file identification information consists of a file time ID, a file text name, and a project reference number. Once generated (normally by project command generation software), the information is unchanged throughout the ground system. The file processing instructions consists of optional file radiation open and close window times, and an optional file bit 1 radiation time. File open and close window times specify the only time interval during which command elements in the file may begin radiation (i.e., a mission sequence may demand that specific commands *not* be sent before or after certain times). The bit 1 radiation time allows the project to specify the exact time at which the file is to begin radiation to the spacecraft. The file checksum is intended to provide error protection for the end-to-end ground command system. It is created at the time of file generation and is passed intact to the DSS. It adds reliability to insure that no data were dropped or altered in the transfer from one facility to another.

The command elements contain the actual command bits to be radiated to the spacecraft, identification information, and

processing-control information. The identification information includes the file time ID and file text name (same as the header element), project reference number, and element number (1-256). The processing-control information consists of an optional delay time. If the project wants to delay radiation of a command element (delay from the previous command), this delay time would be used.

The allocated storage for each file is of fixed length (256 elements). However, a file may not occupy all the storage allocated for it. For a given mission, 8 files can be stored at a DSS. Each command element can contain up to 800 spacecraft command bits. The total storage is thus greater than 1.6 million command bits – far in excess of any currently known spacecraft storage plans.

The data processing of the DSN Command System is based upon the data handling of the above-described command files and file elements.

B. Receiving and Storing Command Data at a DSS

As previously stated, the file(s) or set of commands to be radiated to the spacecraft are sent to a DSS during the first few minutes of a spacecraft track (i.e., just after spacecraft downlink signal acquisition). The first step in receiving and storing command data at a DSS is the process of opening a file area on the Command Processor Assembly (CPA) disk at a DSS. This is accomplished by the Mission Control Center sending a file header element to the DSS CPA. The CPA acknowledges receipt of this "open" instruction. The Mission Control Center immediately sends the command elements (up to 255) at near the high-speed data line maximum rate (maximum rate – 7200 bits/sec). The Mission Control Center then follows with a file "close" instruction. The DSS CPA again acknowledges the "close" instruction indicating file loading successful or unsuccessful. If successful, the Mission Control Center proceeds to send any remaining files (up to 8 total). If unsuccessful, the CPA specifies (in the acknowledge to the Mission Control Center) the reason for the failure and from what point in the file the command elements are to be retransmitted.

There are numerous reasons the CPA rejects the "close" instruction, but the prime one would be an error occurring in the transmission link between the Mission Control Center and the DSS. The Mission Control Center retransmits the data and again attempts to "close" the file. Again, after a successful file close, the Mission Control Center proceeds to send any remaining files. Upon successful "closing" of all files, the loading and storing process is complete. This process will normally take less than 10 minutes to complete. The command data is then available for radiation to the spacecraft.

C. Queuing the Command Data for Radiation

After having loaded the file(s) at the CPA, files may be selected for radiation to the spacecraft. This process is called "attaching." A five-entry queue of file names is provided. The Mission Control Team determines in which order the files are to be attached, normally in the order in which they were sent to a DSS. The order in which they are attached determines the sequence in which they will be radiated: that is, first attached, first to radiate to the spacecraft. Attaching a file to the queue is accomplished by the Mission Control Center sending an "attach" directive to the DSS CPA. Each file, as it is attached, is placed at the bottom of the queue. After attaching the files, the top file in the queue is eligible for radiation to the spacecraft.

D. Command Radiation to the Spacecraft

The first command element in the top (prime) file in the queue begins radiation to the spacecraft immediately after attachment or as soon as all optional file instructions are satisfied. As previously stated, a file can have optional instructions – Bit 1 radiation time and file open and close window times. If used, these instructions control when the first command element in the file begins radiation to the spacecraft. The file is defined to be active when the first command element begins radiation. Upon completion of radiation of the first command element, the CPA radiates the second command element either immediately or when the optional instruction "delay" time has been satisfied. The CPA continues to radiate all command elements in the file until complete. After the first file completes the radiation process, the second file in the queue automatically becomes the prime file and the file radiation process is repeated. After the second file completes radiation, the third file becomes prime, etc. This process is repeated until all files in the queue are exhausted. The Mission Control Center can attach new files to the queue whenever space becomes available (i.e., after the first file radiates).

As the radiation of command elements in a file is in process, periodic reporting via high-speed data line messages to the Mission Control Center is accomplished. Transmission of these messages to the Mission Control Center occurs every three minutes, or after five elements have been radiated, whichever occurs first.

E. Additional Data Processing

The functions of (1) storing the command files at a DSS, (2) attaching the files to the queue and, (3) radiation of the commands to the spacecraft are rather straightforward and the above descriptions assumed nominal-standard operation of the data processing functions. However, the complexity of the

total data processing capabilities is a result of assuming worst case, failure-recovery, or non-nominal operating conditions. Numerous data processing capabilities exist to accommodate these conditions. Below is a list of the optional or non-nominal data processing functions.

1. File erase. The capability exists to delete a file from storage at the DSS CPA. This erase function can be accomplished either locally at a DSS or via high-speed data message from the Mission Control Center. It is expected that files will be stored on disk at the CPA that are not intended to be radiated to the spacecraft. Examples: Test files left from pretrack testing or the Mission Control Center sends wrong files to DSS. The file "erase" function is provided so that unnecessary files stored at the DSS can be deleted to make room for files intended for radiation to the spacecraft.

2. Clearing the queue. Files could be attached to the queue out of order. As previously stated, the order of file radiation to the spacecraft is dependent on the order of files in the queue. The queue can be cleared by a high-speed data message from the Mission Control Center.

3. Suspend radiation. If for some reason, Mission Control desires to stop command radiation, a "suspend" message can be sent from the Mission Control Center. This message stops command radiation to the spacecraft. The file is defined as being in the suspended state.

4. Command abort. As each command bit is radiated to the spacecraft, numerous checks are made to insure validity of the command data. If a failure is detected during radiation, the command element is aborted. Optional methods of treating an abort are provided. Automatic recovery can be attempted (resend the command element) or radiation is terminated until operator intervention occurs. If radiation ceases, again the file is said to be suspended.

5. Resume command radiation. To resume radiation of a suspended file (either suspended intentionally or from an abort) a message can be sent from the Mission Control Center to resume radiation at a specific element in the file.

6. Close window time override. The close window time (previously discussed) can cause an actively radiating file to become suspended. If this occurs, Mission Control can send a message to the DSS CPA to "override" this time. The close window time override directs the CPA to ignore the close window time and proceed as if it were infinity.

IV. Command Store-and-Forward Schedule

The capabilities defined in this article are in the final stages of implementation. Plans are that these capabilities – with corresponding capabilities existing at the Mission Control Center – be available for the Voyager Mission in time to support the encounter with Jupiter. On approximately May 15, 1978, the Voyager Mission will begin test and training with this capability. Plans are that this capability will be operational in September 1978 to command the Voyager spacecrafts.

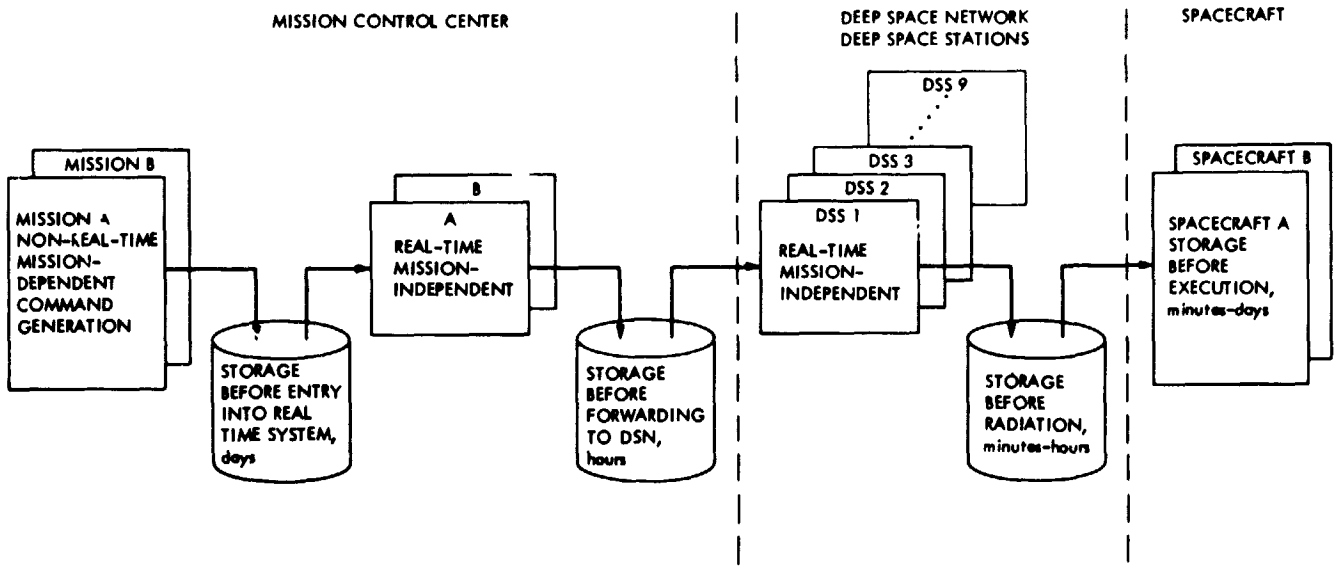

Fig. 1. Command store-and-forward general data flow – typical storage times

DSN Ground Communications Facility

R. H. Evans
TDA Engineering Section

A functional description of the GCF and its relationships with other elements of the DSN and NASCOM is presented together with development objectives and goals and comments on implementation activities in support of Flight Projects.

I. Introduction

The GCF is one of the three elements of the DSN. The GCF provides for transmission, reception, and monitoring of Earth-based point-to-point communications between the Deep Space Stations (DSSs) (one of the DSN elements), and the Network Operations Control Center (NOCC) (the other element) located at JPL Pasadena, and to the Mission Operations Control Center (MOC) at JPL. Voice, teletype, high-speed data, and wideband data channels of the world-wide NASA Communications Network (NASCOM) are utilized for all long-distance circuits, except those between JPL and the Goldstone Deep Space Communications Complex (GCSCC). Goddard Space Flight Center (GSFC) NASCOM Engineering has delegated the responsibilities for planning, budgeting, design, implementation, operation, and maintenance of the communications requirements between Goldstone and JPL to the DSN GCF. Additionally, the GCF provides communications services between the DSSs at each geographic communications complex (Madrid, Australia, and Goldstone, CA.) via intersite microwave system capabilities, and between separated areas of the NOCC at JPL via 230 kbit/s wideband data channels. Also, voice communications are provided within the stations, between the stations, within the complexes, and within the NOCC. The GCF is comprised of five subsystems; Voice, Teletype, High-Speed Data, Wideband Data and Monitor and Control. The DSN Tracking and Data Acquisition Engineering Office of JPL provides the technical direction and systems management of the GCF, and acts as the representative of NASCOM for switching and interconnect functions on the west coast.

II. GCF-NASCOM Interrelationships

The interrelationships at the programmatic level between JPL's DSN GCF and the NASCOM network, managed, engineered, and controlled at GSFC, are characterized as follows:

A. NASCOM

(1) Provides long-haul operational ground communications in support of all NASA projects and mission activities including those supported by the DSN.

(2) Accepts and supports communications requirements established by the DSN and validated through continuing consultation and review.

(3) Establishes in consultation with the users the basic characteristics of the NASCOM systems, such as teletype line rate and block header formats for switching, and the user electrical interfaces.

B. GCF

(1) Provides ground communications for all DSN missions and uses the services of NASCOM.

(2) Establishes additional characteristics of all GCF subsystems on an end to end basis such as block multiplexing, error correction, and monitoring and control.

III. Objectives and Goals

The primary objectives of the GCF are to provide highest quality point-to-point transfer of operational data within the DSN and provide simple user and NASCOM electrical and operational interfaces. These objectives are being met by:

(1) Providing automatic message switching and routing.

(2) Providing data transmission subsystems that are as transparent to the users as possible.

(3) Minimizing project dependent equipment within the GCF.

(4) Providing a centralized common user data records capability.

The goals of the GCF are to provide highly reliable and cost-effective data transmission while continuing an adequate capability balance for multiple mission users, and include:

(1) Equipment and routing redundancy to minimize single-point-of-failure impact.

(2) Error performance which provides essentially block-error-free throughput.

(3) Design coordinated and consistent with the NASCOM Development Program.

IV. Configuration and Functional Subsystem

The current GCF configuration, including the related NASCOM interfaces and functions, is illustrated in Fig. 1. This configuration illustrates the long-haul communication circuit services external to JPL and Deep Space Communications Complexes (except circuits between the Goldstone Complex and JPL) are the responsibility of NASCOM. The voice, teletype, high-speed data, wideband data, and monitor and control subsystems point-to-point communications are serviced by this Fig. 1 configuration.

A. High-Speed Data Subsystem

This subsystem shall consist of GCF assemblies that switch, transmit, record, process, distribute, test, and monitor digital data and is used for transmission of:

(1) All digital data for the DSN command, tracking, and monitor control systems.

(2) All low or medium rate data of the DSN Telemetry System and the DSN Test and Training System.

The High-Speed Data Subsystem provides a capability for transmitting and receiving the serial bit stream formatted data over a single four-wire properly conditioned alternate voice/data channel having a 3.0-kHz bandwidth. This serial bit stream is impressed on communication circuits at a continuous line bit rate divided into message segments referred to as high speed data blocks.

Two types of data blocks are used:

(1) Data blocks containing user data bits to be transmitted.

(2) Filler blocks containing filler data bits provided by GCF when the user data bit/block rate is insufficient to maintain the contiguous bit/block rate required for continuous line monitoring and error control.

The current plans for the GCF Mark III period are to provide the functional capabilities illustrated in Fig. 2. The GCF High-Speed Data Subsystem is standardized on a 1200-bit block size (message segment) and a line bit rate of 7200 bits/s. The other planned changes include conversion from a 33-bit to a 22-bit error detection encoding/decoding polynomial code and increasing the number of bits reserved in the data block ending from 36 to 40 bits. The 40-bit block ending with the 22-bit code provides for numerical serialization and acknowledgement numbers for error correction by retransmission for short outages or errors in GCF end-to-end data transmission.

The error correction capability will significantly reduce the post pass time required for non-real-time replay of blocks received in error to complete the intermediate data record. Figure 3 illustrates the High-Speed Data Subsystem transitional configuration that was planned for the CY 1977 and CY 1978 time period. The transitional configuration (old and new configurations separately or in combinations operational and useable) is required to provide continuous support for ongoing and new projects starting up until the conversion from the old Ground Data System to the new one is completed for support of the Voyager and Pioneer Venus Projects, and to support the continued extended mission of the Viking Project thru early CY 1979. The dual-mode configuration became

operable and useable to support DSN System Testing at the conclusion of acceptance test demonstrations of the Error Detection Correction (EDC) and the High-Speed Switch (HSW) Software in November of CY 1977. The added new computer to computer switched interface to the Mission Control and Computing Center (MCCC), although operable and useable for DSN-MCCC testing, will not be fully operational till June CY 1978.

B. Wideband Data Subsystem

The Wideband Data Subsystem consists of assemblies that switch, transmit, receive, process, distribute, test and monitor data requiring the use of bandwidths greater than those provided by standard high-speed data channels. The GCF Wideband Data Subsystem functionally illustrated in Fig. 4, together with a listing of functional capabilities provided, includes standard wideband circuits as well as all intersite-microwave (area microwave) capabilities. The Wideband Data Subsystem is used for the transmission of:

(1) All DSN Telemetry System high-rate data that exceed High-Speed Data Subsystem capabilities.

(2) Data interchange between the NOCC and GCF Comm Terminal at JPL.

(3) Data interchange between DSSs within a complex via intersite microwave, including critical timing signals.

(4) Simulation System Data from the Mission Control and Computing Center/Mission Operations Center to the DSSs.

(5) DSN Test and Training System data from the Network Operations Control Center to the DSSs.

The wideband data circuits for interchange of data between the DSSs and JPL are impressed with serial bit streams at a continuous line rate typically 27.6, 28.5, 50, 56, 168 or 230.4 kbits/s divided into 2400 or 4800 bit message segments (data blocks). (In CY 1978 the 27.6, 28.5 and 50 kbits/s rates will be deleted). Similar to the high-speed data subsystem the blocks are either data blocks, or filler blocks inserted when the user data load is insufficient to maintain contiguous data blocks on line.

C. Voice Subsystem

The Voice Subsystem consists of GCF assemblies that switch, transmit, receive, distribute, test, and monitor transmissions originally generated in vocal form, and includes internal voice communications within the Deep Space Station Communication Complexes, DSSs, and the NOCC. The subsystem service provides capabilities between those areas and to non-DSN area interfaces as follows:

(1) NOCC and DSS

(2) NOCC and MCCC/MOC (or remote MOC)

(3) MOC and DSS for Command System backup.

The Voice Subsystem functional capabilities and key characteristics include:

(1) Standard voice-data grade circuits for all traffic.

(2) Conferencing capability on one intercontinental circuit during noncritical periods for all deep space stations supporting a single project (individual circuits for each DSS during critical periods, resources permitting).

(3) User controlled intercomm switching.

(4) Circuits used for high-speed data transmission (backup) if required.

(5) Voice traffic recording in the central communications terminal upon request.

D. Teletype Subsystem

This subsystem consists of assemblies that switch, transmit, receive, distribute, test and monitor digital signals originally generated in Baudot format at a teletype (TTY) line rate of 100 words per minute. The operational use of teletype continues to be de-emphasized and is used primarily for emergency-backup operational transmissions and administrative communications. Service functions and key characteristics include:

(1) Handling Air Force Eastern Test Range (AFETR) generated predicts for DSN initial acquisition.

(2) Transmitting non-operational messages between the JPL Message Center and other locations.

(3) Use of standard NASCOM format and the NASCOM communications processor for message switching.

(4) Employment of time division multiplexing techniques to reduce trunk circuit costs.

Conversion to the new eight-level standard will be made when NASCOM resources permit. This conversion is now planned for the CY 1979 to CY 1980 time frame.

V. Typical Configuration

The DSN GCF is designed for multiple mission support. Improvements and additions are integrated to meet new era and project requirements (Voyager and Pioneer-Venus require-

ments being added at present- for example) while continuing to support the Viking, Helios, and Pioneer 6 through 11 Projects. Figure 5, in general, illustrates the GCF configuration for support of these projects. Additionally, remote information centers and other non-DSN NASCOM-serviced installations on the West Coast are serviced through the NASCOM West Coast Switching Center on integral part of the GCF 20/Central Comm Terminal at JPL.

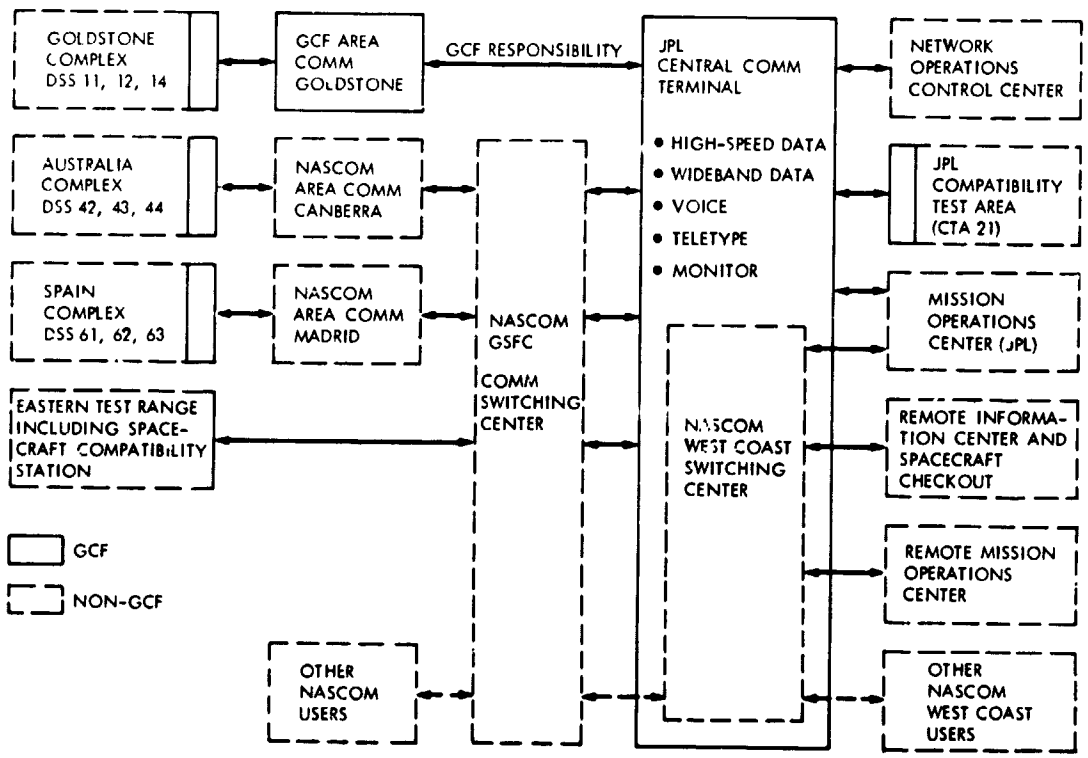

Fig. 1. GCF configuration

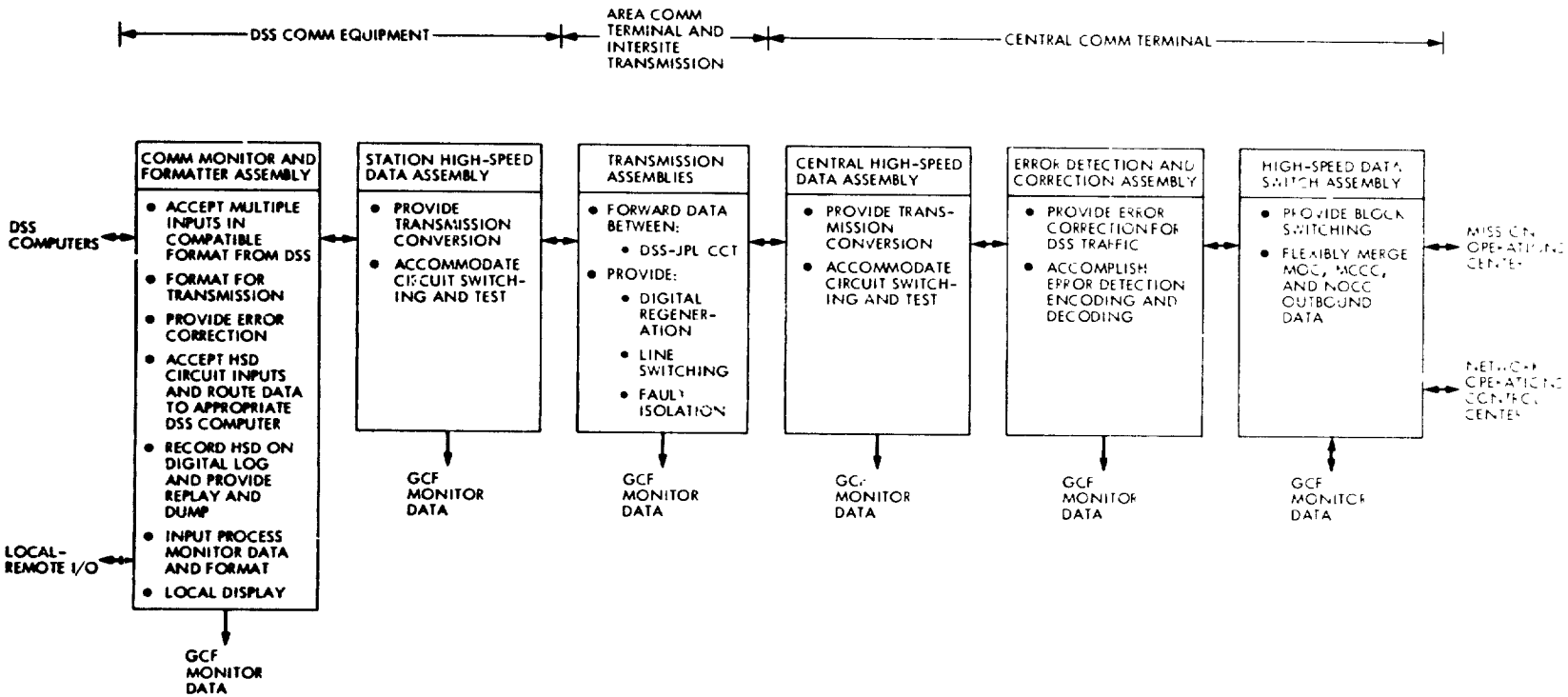

Fig. 2. GCF high-speed data subsystem functional capabilities

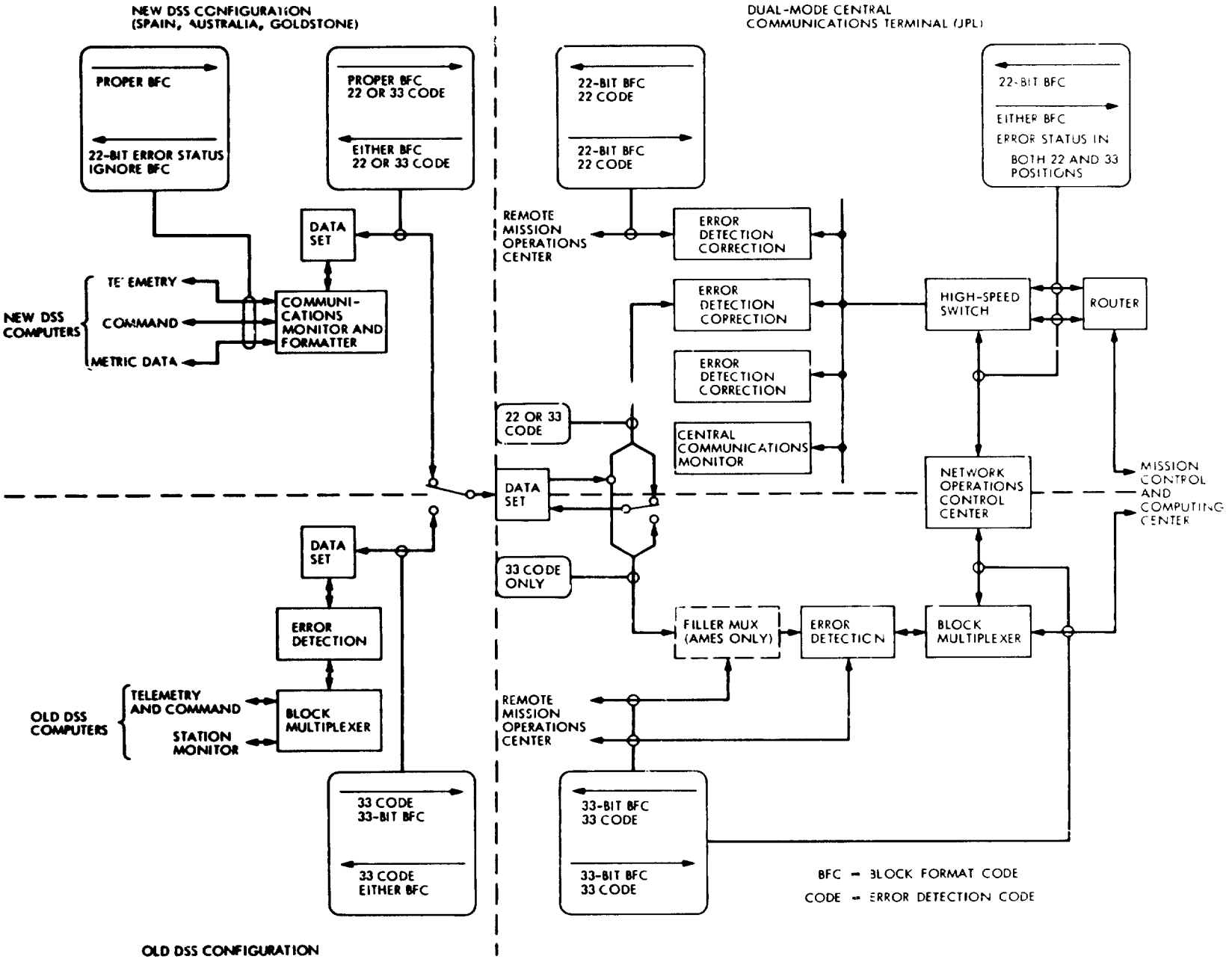

Fig. 3. GCF high-speed subsystem configuration and interfaces, CY 1977 and 1978

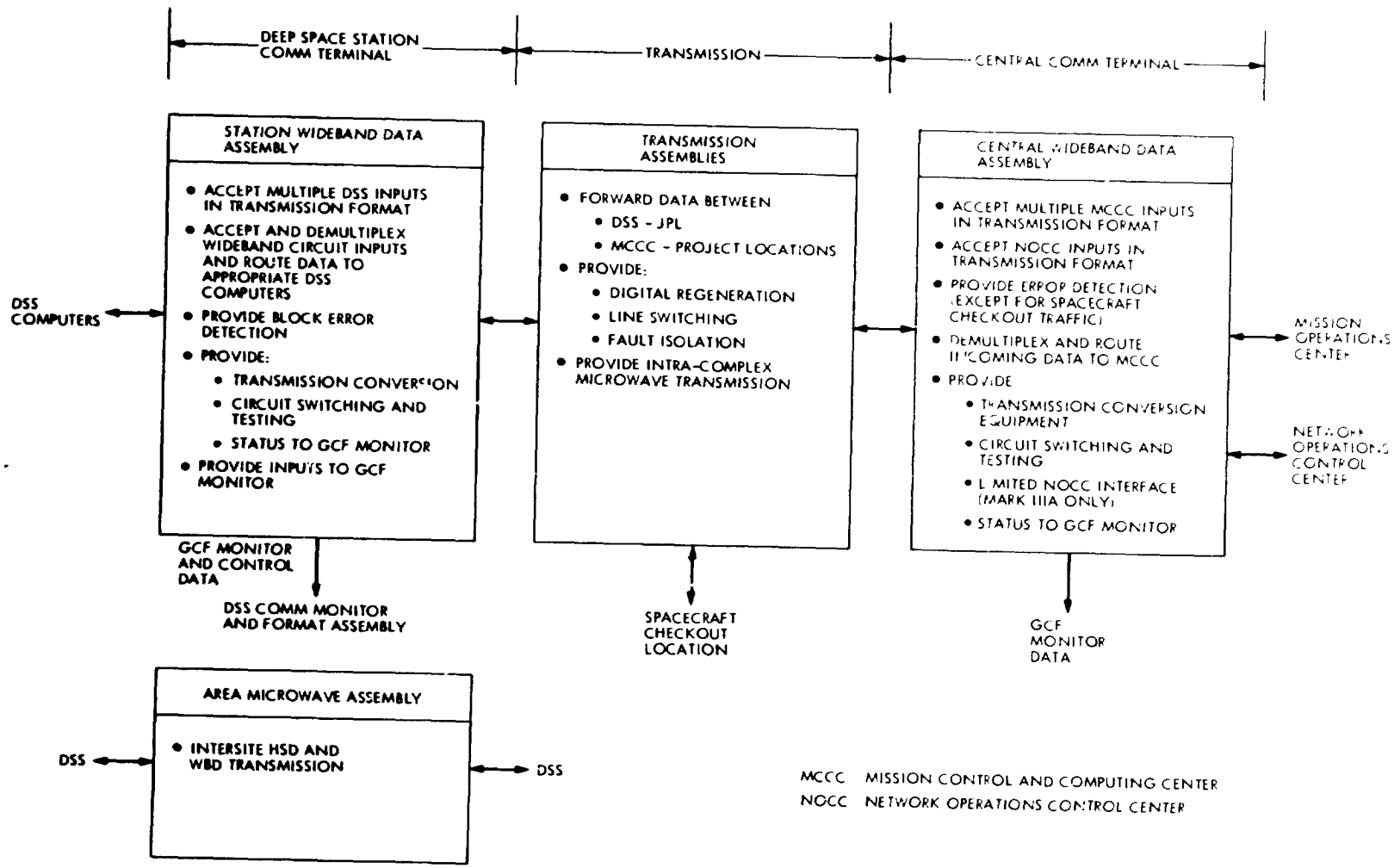

Fig. 4. GCF wideband subsystem

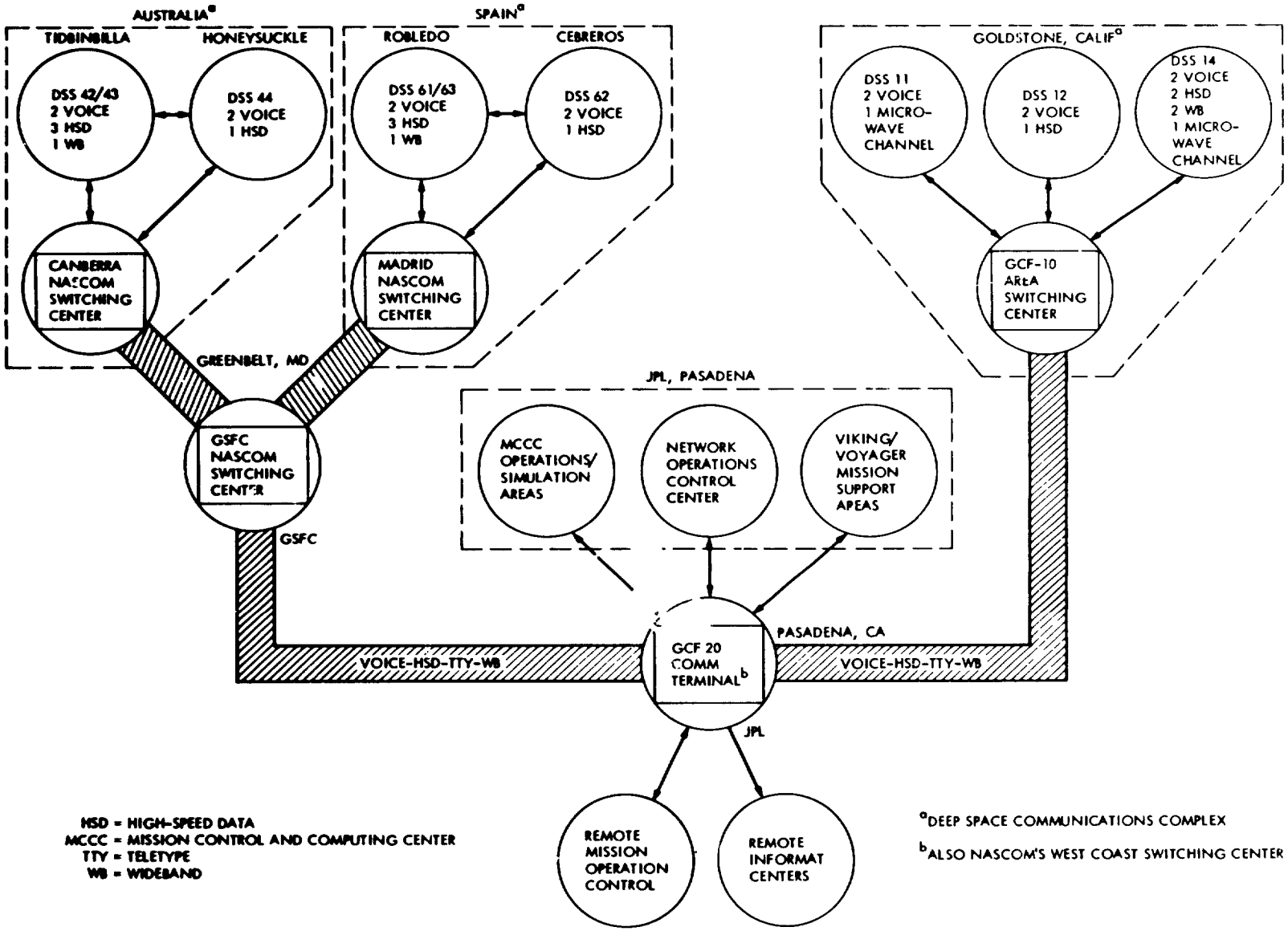

Fig. 5. DSN support locations and GCF-NASCOM circuit requirements

Du

Viking Extended Mission Support

T. W. Howe
Deep Space Network Operations Section

This report covers the period from 1 September through 31 October 1977. It reports on the status of Viking DSN Mark III '77 Data Subsystem Implementation Project (MDS), related testing at DSS 42/43, and also includes reports on the Viking DSN Discrepancy Reporting System, Viking command support, tracking support, and periodic tests conducted with the Viking spacecraft.

I. Viking Operations

A. Status

All four Viking spacecraft continued to return data during this reporting period. The communications link between the spacecraft and the Deep Space Stations (DSSs) continued to improve. This was a result of the combination of decreasing communications range to Earth and a decreasing Earth cone angle for the Orbiter low-gain antennas. The links will continue to improve until mid-January 1978. These improved links made possible the reception of 33-1/3 bps single-subcarrier telemetry data from the Orbiter low-gain antenna by a 64-m station. The 26-m stations processed dual-subcarrier 2-kbps telemetry data routinely during the period. Beginning in October it was possible to receive 8-1/3 bps single-subcarrier telemetry data at 26-m stations.

B. Spacecraft Problems

Two spacecraft problems occurred during this reporting period. The first occurred on September 19 on Viking Orbiter 2 (VO-2) during a planned switch from processor B to processor A. An anomaly caused the Orbiter to go into a safing routine and resulted in a switch to the low-gain antenna and single-subcarrier mode at a data rate of 8-1/3 bps. This was the first attempted processor switch for VO-2, the same switch having been successfully accomplished several times on Viking Orbiter 1 (VO-1).

The first indication of a problem was loss of downlink lock by DSS 44. When lock was reestablished, the downlink was found to be −167 dBm with a low rate engineering signal-to-noise ratio (SNR) near zero.

Following unsuccessful attempts to improve the signal level, a spacecraft emergency was declared by the Viking Project Manager. Since only 26-m stations were scheduled to support Viking from the time of the anomaly until some 10 hours later when DSS 14 would have the spacecraft in view, DSS 43 was contacted and requested to support. The station had not supported any spacecraft tracks since the beginning of the DSN Mark III '77 data Subsystem Implementation Project (MDS) upgrade on 15 July 1977, and was still in the process of conducting system performance tests. The personnel responded to the emergency in remarkable fashion and were able to obtain lock in less than one hour. Following analysis of telemetry downlink indications, it was confirmed that a safing sequence had occurred. Commands were transmitted to reestablish normal links. DSS 63 was brought up at the end of DSS 43's view period and received a spacecraft memory readout. DSS 63 was released from Viking support approximately 7 hours after the emergency.

The cause of the anomaly was determined to be a timing offset between Processor A and Processor B on the Viking Orbiter.

The second problem occurred over DSS 4 on 6 October 1977 during a VL-2 direct link. Downlink lock was lost approximately 14 minutes prior to the scheduled time of end of link. Attempts by DSS 14 and DSS 43, which was supporting a demonstration pass, to lock to the downlink were unsuccessful. An attempt to obtain lock the following day was also unsuccessful.

The apparent cause of the anomaly is a fault in the low-voltage power supply for the traveling wave tube amplifier (TWTA). About one year ago the other TWTA failed to come on during a scheduled direct link, and no attempt has been made to use it since that time. Lander 2 will continue to operate with an uplink capability and Lander-to-Orbiter relay links. The present VL-2 sequences provide a good science mission with most of the data being returned via the relay link.

C. Maneuvers

Three Mars Orbit Trim (MOT) maneuvers with VO-2 occurred during this reporting period.

MOT-11 occurred on 26 September 1977 during the DSS 63 view period. The purpose of this maneuver was to prepare for Deimos encounters on 10, 15, and 20 October. The trim maneuver was successful. DSS 63 was unable to obtain downlink telemetry lock during the 9-sec motor burn, even though the spacecraft was on the high-gain antenna and the downlink telemetry signal level was predicted to be -143 dBm. As a result, two-way tracking data was lost, and telemetry data was not available until played back from the Orbiter.

MOT-12 was supported by DSS 14 on 9 October 1977. Motor burn lasted 6 seconds and finalized the orbit for Deimos encounter. All uplink and downlink activities for this maneuver were accomplished properly and on time.

MOT-13 occurred on 23 October 1977 and accomplished three goals: (1) it changed the periapsis altitude from 591 to 300 km, (2) it changed the orbital period from 21 hours 13 minutes to 23 hours 59 minutes, and (3) it provided an orbit that will overfly the Viking Lander 1 (VL-1) site on 13 November. The maneuver was supported by DSSs 14 and 43 during an overlapping view period. Imaging Science data will be taken during the overflight of the VL-1 site on 13 November and a comparison will be made in terrain as seen from the Orbiter and as seen from the Lander to help pinpoint the exact VL-1 landing site.

D. Radio Science

Radio Science activities and data taking continued during September and October.

Experiments included Near Simultaneous Lander/Orbiter Ranging, Periapsis Gravity Field, and Occultation. Plans are now being made for a Bistatic Radar Experiment which will begin in November 1977. Details of this experiment will be covered in the next article of this series.

E. Spacecraft Tests

Routine spacecraft testing continued during this reporting period. An average of two Command Detector Unit (CDU) signal-to-noise ratio estimator (SNORE) tests were conducted each week for both Viking Orbiters. High-gain antenna calibrations were also supported.

II. Network Support

Table 1 shows the Viking Extended Mission (VEM) Tracking Support for 1977. The month of October produced the fewest number of tracking hours in support of Viking for 1977, with September showing the fewest number of Viking tracks for 1977. This may be due in part to the fact that Lander 2 direct telemetry link passes ended on 6 October due to the TWTA failure.

Table 2 gives the total number of commands transmitted during 1977. The month of September was a record month for commanding with 11,617 commands transmitted, more than half of which were sent from 26-m stations.

Table 3 identifies the DSN VEM Discrepancy Reports generated during the period and 1977.

A. Viking Uplink Spectrum Analysis

On September 2, during a lander direct link over DSS 63, the Viking Lander-1 uplink signal level was noted to be 37 dBm lower than predicted and the spacecraft receiver static phase error was in error by 13 Khz. Investigation by DSS 63 during subsequent Viking passes revealed sideband signal "spurs" on the station uplink carrier, both above and below the carrier at about 13 to 15 Khz from the carrier and a -30 dB below the actual carrier signal level. DSS 63 engineering tests revealed that the sidebands were caused by the data synthesizer or the 50 Mhz reference signal from the Frequency and Timing Subsystem (FTS). The remainder of the stations supporting Viking were requested to monitor their uplink carrier for sideband spurs which could result in a degraded uplink signal. However, no significant spurs were found on any of the other transmitters in the network.

III. DSN Mark III '77 Data Subsystem Implementation (MDS) Testing and Status

As indicated in the last report on this series, MDS test and training had been completed at DSSs 12, 44, 62 and 14. DSSs 42/43 had been released from tracking support and had started their MDS upgrade on July 15.

A. DSS 42/43 Test Status

The DSS 42/43 test and training began and was completed during this reporting period The scheduled completion date for the MDS implementation phase at DSS 42/43 was 30 September 1977, with testing scheduled to begin on 1 October 1977. These stations completed their implementation phase ahead of schedule, and at the suggestion of station management Viking Operational Verification Tests (OVTs) were conducted during these extra days. It was the opinion of DSS 42/43 and DSN Operations personnel that Viking OVT's would provide the stations with the best training possible, since a Viking OVT would exercise more equipment and configurations than any other type of test. OVT testing began on the 26th of September.

The plan was to conduct 10 OVTs and to insure at least 2 OVTs with each of the 4 operational shifts. Of the OVTs conducted, 2 were unsuccessful, while the other 8 were successful. The tests exercised the MDS configurations to be used for Viking support. All telemetry data rates were processed, manual and automatic commanding demonstrated and data replay was exercised. Due to equipment problems, replay of analog telemetry data from the FR-1400 recorders could not be exercised. The last OVT was completed on 30 September 1977.

Viking Extended Mission DSN/MCCC System Interface Testing (SIT) was conducted on the 4th of October 1977. The test was successful and a scheduled retest was cancelled.

Viking Extended Mission Ground Data System (GDS) testing was conducted on the 8th of October 1977. Due to problems with MCCC computer support, simulation, and the Ground Communications Facility (GCF), the test could not be completed. A retest was conducted on 11 October 1977 to complete a 2-hour portion of the timeline and to test the replay capability of Digital Original Data Records (DODR). This retest was successful.

Demonstration passes began on 7 October 1977 and involved both DSS 42 and 43. Passes also occurred on the 9th, 10th, 12th, 15th, and 16th of October. The third demonstration pass demonstrated the ability of DSS 43 to support the Viking project while DSS 42 was supporting another flight project (PN-11). The pass was successful in that no interference was detected.

The testing phase at DSS 42/43 was completed on 16 October 1977 and these stations were placed under Viking configuration control on 18 October 1977.

Table 1. VEM tracking support 1977

DSS	Jan.	Feb.	Mar.	Apr.	May	Jun.	Jul.	Aug.	Sept.	Oct.	Nov.	Dec.
	Track / hr											
11	23 135	22 142	10 100	17 118	38 228	40 289	44 322	42 343	26 210	40 408		
12	4 11	1 6	–	24 176	17 119	1 4	1 1	1 7	–	–		
14	52 341	59 392	50 368	20 176	–	–	10 46	16 126	28 363	43 329		
42	21 247	25 226	58 453	17 138	17 162	14 112	10 69	–	–	14 100		
43	68 721	62 627	–	63 603	60 521	57 486	31 238	–	1 01	24 141		
44	–	–	7 7	1 4	–	–	16 99	26 166	6 22	12 51		
61	35 261	29 227	12 72	40 317	54 461	51 475	37 337	35 322	38 345	22 203		
62	–	2 7	4 22	9 55	3 14	2 7	–	–	–	3 23		
63	38 327	28 202	66 525	15 78	23 186	15 136	40 399	64 590	57 590	15 136		
Total	241 2043	228 1830	207 1547	206 1665	212 1691	180 1509	189 1511	184 1554	156 1531	173 1391		

Number of tracks represent the summation of all Viking spacecrafts tracked. Track time, in hours, represent scheduled station support.

Table 2. Number of commands transmitted in Viking Extended Mission during 1977

DSS	Jan.	Feb.	Mar.	Apr.	May	Jun.	Jul.	Aug.	Sept.	Oct.	Nov.	Dec.
11	1521	1394	1027	117	811	0	1	795	2028	3687		
12	0	0	0	1314	721	0	0	0	–	–		
14	769	1404	1206	274	-	-	74	108	2704	2108		
42	2072	953	1778	8	1886	1619	-	-	–	18		
43	919	2523	0	2094	1447	972	1190	-	–	456		
44	0	0	2	1	–	–	-	5	19	2		
61	605	1116	1328	1925	1922	3838	4257	5589	5256	1371		
62	0	0	1	1991	-	496	–	-	–	–		
63	795	472	2039	381	675	383	2579	2318	1610	847		
Total	6681	7862	7381	6180	7465	7308	8101	8815	11,617	8489		

Table 3. DSN VEM discrepancy reports

DSS	Jan.	Feb.	Mar.	Apr.	May	Jun.	Jul.	Aug.	Sept.	Oct.	Nov.	Dec.
	0[a] / C[b]											
11	4 / 0	3 / 4	4 / 6	1 / 3	2 / 3	2 / 6	2 / 7	1 / 7	1 / 1	1 / 3		
12	4 / 0	0 / 0	0 / 0	5 / 2	7 / 5	0 / 7	0 / 0	0 / 0	0 / 0	0 / 0		
14	14 / 2	11 / 19	4 / 33	3 / 9	2 / 2	0 / 2	6 / 2	4 / 18	5 / 14	10 / 24		
42	0 / 1	2 / 3	0 / 7	0 / 2	0 / 0	0 / 0	0 / 0	0 / 0	0 / 0	1 / 0		
43	10 / 13	11 / 10	0 / 12	9 / 11	8 / 17	1 / 14	1 / 6	0 / 1	0 / 0	0 / 5		
44	0 / 0	0 / 0	0 / 2	0 / 1	0 / 0	0 / 0	1 / 0	1 / 4	0 / 1	0 / 0		
61	1 / 9	1 / 6	0 / 3	0 / 1	1 / 2	0 / 6	1 / 4	0 / 7	0 / 4	0 / 4		
62	0 / 0	0 / 8	1 / 2	2 / 1	0 / 2	0 / 1	0 / 0	0 / 0	0 / 0	2 / 0		
63	1 / 4	7 / 3	1 / 18	0 / 6	4 / 4	3 / 12	4 / 4	9 / 17	8 / 17	4 / 7		
Others[c]	4 / 3	3 / 9	2 / 10	4 / 7	7 / 12	10 / 13	8 / 16	5 / 9	7 / 8	10 / 15		
Total	38 / 32	38 / 62	12 / 93	24 / 43	31 / 47	17 / 61	23 / 39	20 / 63	21 / 45	28 / 58		

[a] 0 = Number remaining open at end of month.

[b] C = Number closed during month.

[c] Other = DSN, NDPA, NOCA, GCF

Helios Mission Support

P. S. Goodwin
TDA Mission Support Section

G. M. Rockwell
Deep Space Network Operations Section

This article reports on activities of the Network Operations organization in support of the Helios Project from 15 October 1977 through 15 December 1977.

I. Introduction

This article is the nineteenth in a continuing series of reports that discuss Deep Space Network support of Helios Mission Operations. Included in this article is information on Mark III Data Subsystem (MDS) testing at the conjoint Deep Space Stations (DSS) 42/43 (Canberra, Australia); MDS implementation at DSS 61/63 (Madrid, Spain), Radio Science update, and other mission-related activities.

II. Mission Operations and Status

The Helios 1 spacecraft sixth perihelion occurred on 21 October 1977 at 02:20 UTC over DSS 43 (Australia). This was 1045 days, 19 hours, 09 minutes and 30 seconds after launch. The spacecraft telemetry data rate was 1024 bits per second, and the round-trip light time was 20 minutes, 14 seconds. The spacecraft was configured with TWTA 2, at medium power using high-gain antenna, with all science experiments operating. All systems and experiments performed nominally.

The Helios 2 spacecraft fourth perihelion occurred on 26 October 1977 at 08:34 UTC, also over DSS 43. This was 650 days and 3 hours after launch. The spacecraft round-trip light time was 17 minutes, 56.2 seconds, and the telemetry data rate was 2048 bits per second. The spacecraft configuration was TWTA 1 at medium power using high-gain antenna, and all science experiments operating. All spacecraft subsystems and experiments performed nominally.

One anomaly did occur right at perihelion for Helios 2. The temperature of the spin thruster assembly increased very rapidly, culminating on 27 October 1977 at 1200 GMT at a temperature of 205.0 deg Celsius. The calculated temperature measurement stub "X" (D-111) also increased in the same way, reaching 181.6 deg Celsius at the same time. During the earlier testing phase of the thruster units, a leakage occurred on a model that was cooled down from about 200 deg Celsius. It was suspected that this might recur during the coming aphelion phase; therefore, a decision was made to dump excess gas before possible uncontrolled spin-rate changes could take place.

The gas-dumping maneuver was performed 12 December 1977. The maneuver was performed in ten single steps.

Step 1	16 pulse precession maneuver to verify technical capability and exclude unsymmetrical forces.
Step 2	256 pulse precession maneuver.
Step 3	512 pulse precession maneuver. Spacecraft shows a slight nutation of 3 data numbers

(DN) between 0.4612 and 0.5151-deg sun sensor angle.

Step 4 to 7 — 512 pulse precession maneuvers. No change in nutation. Increased spacecraft spin-rate by one DN from 60.952 to 61.012 rpm.

Step 8 — 328 pulse precession maneuvers, leaving a gas mass of approximately 0.25 kg.

Step 9 — 16 pulse spin-down maneuver, spin-rate to 60.591 rpm.

Step 10 — 4 pulse spin-down maneuver; spin-rate is now 60.472 rpm.

All steps using the precession nozzle were carried out as combined roll positive/roll negative maneuvers to eliminate the resulting forces and to avoid attitude changes

The maneuver occurred over DSS 11 and DSS 12 with a round-trip light time ranging from 3 minutes, 0.43 seconds to 2 minutes, 59 seconds. The spacecraft was programmed to telemetry format 4 (engineering data only) to allow closest control. Following the maneuver, the condition of the attitude system was:

Gas pressure high	7.108 bar
Gas pressure low	3.449 bar
Gas tank temperature	- 10.00 deg Celsius
Sun sensor angle	0.4912 deg
Spin rate	60.472 rpm
Gas mass approx.	0.25 kg

The gas saved for later correction (if necessary) allows for a spin-rate change of 3 rpm in either direction. Yet uncontrolled leakage will not jeopardize the mission. Throughout the maneuver, the spacecraft performance was excellent, as was the support from all participants.

Overall coverage of both Helios 1 and Helios 2 for this period is listed in Table 1.

III. Special Activities

A. DSN Mark III Data Subsystem (MDS) Support of Helios:

As reported earlier (Ref. 1) DSS 42/43 began its MDS test and training period on 26 September 1977. During this period, 8 Helios demonstration tracks were conducted with overall success prior to placing the complex in configuration control. DSS 42/43 was placed under configuration control on 18 October 1977.

DSS 61/63 (Madrid, Spain) began MDS implementation on 16 October 1977. The complex is scheduled to begin test and training on the 1st of January 1978. As with other MDS stations, the Helios training will consist of scheduled demonstration tracks to verify proper MDS support of Helios flight operations. The results of this training will be reported in a future article.

B. Support of On-Board and Ground Experiments

In the last article coverage of the Special Traveling Interplanetary Phenomena (STIP), period IV was briefly discussed. This activity involved primarily the alignment of Helios 2 with Voyagers 1 and 2. Figure 1 shows the Voyager and Helios trajectories during this period. The coverage of this alignment is scheduled to end on 31 December 1977. At this writing, no results have been released, but hopefully some data will be available in the near future.

On 7 December 1977 a pitch maneuver was performed on Helios 2 to provide data for Experiment 9. Experiment 9 is the Zodiacal Light Photometer. From these observations, information is obtained about spatial distribution of interplanetary dust and the size and nature of the dust particles. This experiment provides a completely new and very promising type of scientific information about interplanetary dust and its variation with distance from the Sun. The maneuver was needed for optical alignment and proper data collection.

During the last perihelion periods of Helios 1 and Helios 2 (Ref. 1), a large amount of data was collected in regard to Experiment 12 (Faraday Rotation). It was hoped that by the time of this article some results could be available for this report, but due to the amount of data collected processing is taking longer than originally thought.

It is hoped some substantial results will be available for publication during the next period. However, those readers desiring a comprehensive report on Helios science results will find that the entire issue of Ref. 2 is devoted to that purpose. That issue's editor is H. Porsche, Helios Project Scientist.

References

1. Goodwin, P. S., Burke, E. S., Rockwell, G. M., "Helios Mission Support", in *The Deep Space Network Progress Report 42-42*, Jet Propulsion Laboratory, Pasadena, California, October 15, 1977.

2. *Journal of Geophysics* (Springer International), Vol. 42, No. 6, 1977, pp. 551-742. Edited by H. Porsche.

Table 1. Helios tracking coverage

Month	Spacecraft	Station type	Number of tracks	Tracking time (h, min)
October	Helios 1	26 meter	51	251:11
		64 meter	13	57:05
	Helios 2	26 meter	17	115:54
		64 meter	33	176:41
November	Helios 1	26 meter	46	288:12
		64 meter	10	60:12
	Helios 2	26 meter	40	368:32
		64 meter	18	119:25

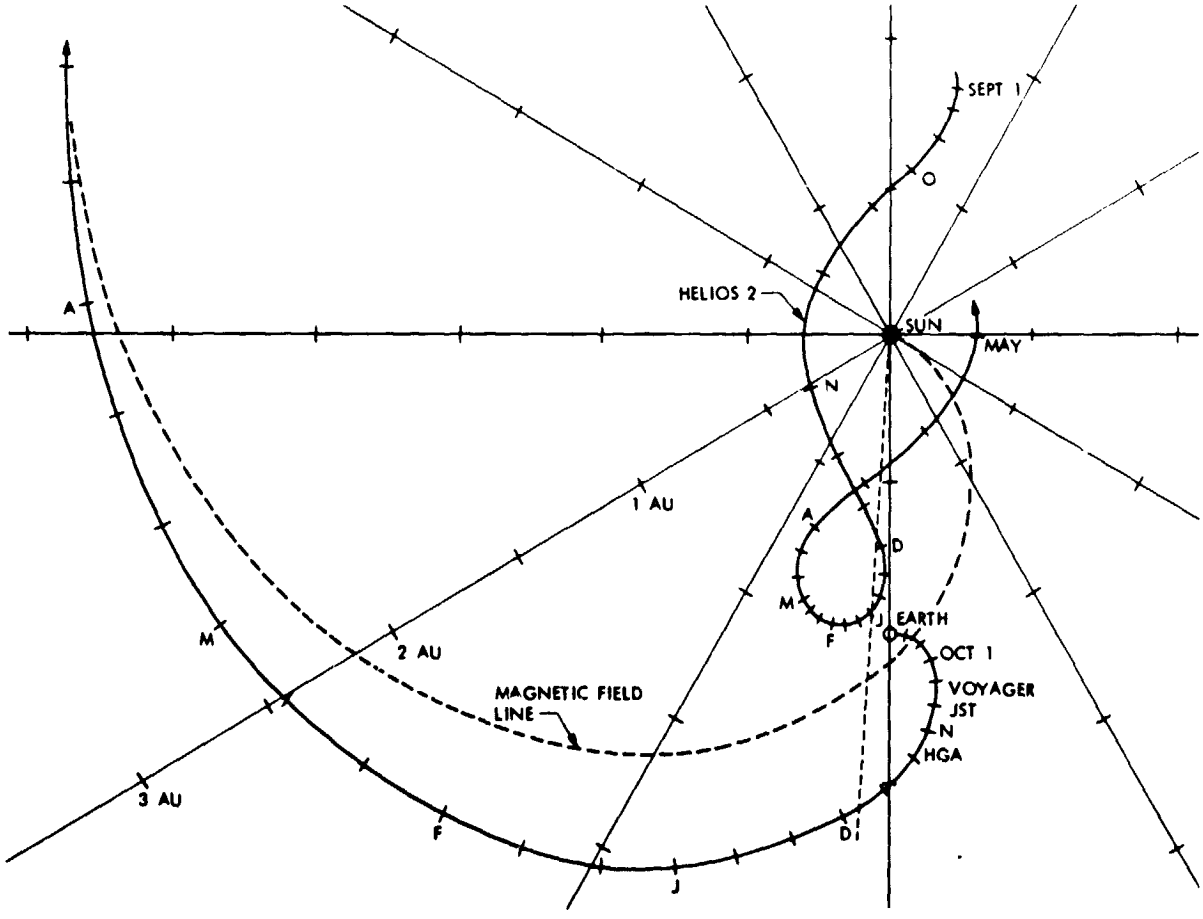

Fig. 1. Voyager and Helios trajectories (fixed Earth-Sun line plot)

Estimates of Precession and Polar Motion Errors from Planetary Encounter Station Location Solutions

G. E. Pease
Navigation Systems Section

Jet Propulsion Laboratory Deep Space Station (DSS) location solutions based on two JPL planetary ephemerides, DE 84 and DE 96, at eight planetary encounters have been used to obtain weighted least squares estimates of precession and polar motion errors. The solution for precession error in right ascension yields a value of 0.3×10^{-5} $\pm 0.8 \times 10^{-6}$ deg/year. This maps to a right ascension error of 1.3×10^{-5} $\pm 0.4 \times 10^{-5}$ deg at the first Voyager 1979 Jupiter encounter if the current JPL DSS location set is used. Solutions for precession and polar motion using station locations based on DE 84 agree well with the solution using station locations referenced to DE 96. The precession solution removes the apparent drift in station longitude and spin axis distance estimates, while the encounter polar motion solutions consistently decrease the scatter in station spin axis distance estimates.

I. Introduction

In the course of JPL DSS location determination, many sources of systematic error have been identified and modeled in order to improve the accuracy of the estimates. The largest errors were traced to the planetary ephemerides, polar motion and timing, tropospheric refraction, and charged particle effects. Dramatic improvements have been made in these areas through the use of more refined radar ephemerides, BIH polar motion and timing corrections, interstation and seasonal tropospheric corrections, and Faraday rotation, differenced range versus integrated doppler (DRVID), and S-X dual frequency calibrations. The addition of recent planetary encounter data (Mariner 10 at Venus and Mercury, Vikings 1 and 2 at Mars) has greatly increased the quantity and time span of planetary encounter tracking data from which station locations may be determined.

Current location sets (Ref. 1) utilize tracking data from Mariners 4, 5, 6, 9, and 10 planetary encounters of Mars, Venus, and Mercury to obtain combined estimates referenced to JPL ephemerides, DE 84 and DE 96. In addition, Campbell and Rinker (Ref. 2) have estimated station location corrections relative to Location Set (LS) 44 from Viking 1 and 2 Mars encounter tracking data. Planetary encounter station location solutions are thus now available over an 11-year span, from Mariner 4 in 1965 to Viking in 1976.

The station longitude solutions (Figs. 1 and 3) reveal an apparent secular drift of about -0.3×10^{-5} deg/year over the 11-year span. Lieske (Ref. 3) has predicted an apparent station longitude drift of this size due to the known error in Newcomb's constant of general precession.

Fliegel and Wimberly (Ref. 4) have shown that BIH polar motion errors could be greater than 1 meter, if systematic errors are considered in addition to observational scatter. Such an error at a planetary encounter would affect the spin axis distance and longitude estimates of all DSN tracking stations.

For this report, DSS longitude and spin axis distance solutions (Figs. 1-4) from eight planetary encounters were used to estimate the precession error and individual encounter polar motion errors. The DE 84 and DE 96 solutions agree very closely. The solution for precession yields a correction of $0.31 \times 10^{-5} \pm 0.8 \times 10^{-6}$ deg/year in right ascension, which is essentially Lieske's predicted correction. The consequent predicted right ascension error at the first Voyager 1979 Jupiter encounter is $1.3 \times 10^{-5} \pm 0.4 \times 10^{-5}$ deg. The values obtained from DE 84 and DE 96 locations differ by only 0.1×10^{-6} deg/year. It appears likely, therefore, that the principal source of error is in the transformation from the equinox and equator of 1950.0 to the equinox and equator of date at the planetary encounter times for the computed doppler and range observables. This includes errors from rigid-body approximations in the nutation. These may be significant in the large-amplitude term having an 18.6-year period. As seen in Fig. 5, the nutation in celestial longitude is almost linear from Mariner 4 encounter where it is -15".2 on July 15, 1965, to Mariner 10 Venus encounter, Feb. 5, 1974, where it is +18".8. For this 8½-year span, a 0.1% error in the long-period nutation terms would contribute 0".034 error, or about 0.1×10^{-5} deg/year. The contribution, if any, of "equinoctial drift" is unknown.

II. Data Equations and Partial Derivatives

Polar motion corrections X and Y, in radians, are approximated in Ref. 5 as follows:

$$\lambda = \lambda_0 + \frac{Z_0}{r_{s_0}}(X \sin \lambda_0 + Y \cos \lambda_0), \tag{1}$$

$$r_s = r_{s_0} - Z_0 (X \cos \lambda_0 - Y \sin \lambda_0), \tag{2}$$

where

λ_0 = uncorrected Greenwich east longitude of tracking station, in radians

r_{s_0} = uncorrected distance of tracking station from Earth's spin axis

Z_0 = distance of tracking station from Earth's equator

The correction X is measured south along the 1903.0 meridian of zero longitude; Y is measured south along the 90°W meridian of 1903.0. For the purposes of this paper, these corrections are in the form of corrections to the BIH Circular D smoothed values (see Ref. 4).

The partial derivatives of interest are, therefore,

$$\partial r_s / \partial X = -Z_0 \cos \lambda_0 , \tag{3}$$

$$\partial r_s / \partial Y = Z_0 \sin \lambda_0 . \tag{4}$$

$$\partial \lambda / \partial X = \frac{Z_0}{r_{s_0}} \sin \lambda_0 , \tag{5}$$

$$\partial \lambda / \partial Y = \frac{Z_0}{r_{s_0}} \cos \lambda_0 , \tag{6}$$

It is seen that the above partial derivatives are functions only of 1903.0 station cylindrical coordinates Z_0, λ_0, and r_{s_0}.

Precession corrections (Ref. 6) are

$$P_\alpha = m + n \sin \alpha \tan \delta, \tag{7}$$

$$P_\delta = n \cos \alpha, \tag{8}$$

where

m = the precession in right ascension

n = the precession in declination

α = the right ascension of the spacecraft at planetary encounter

δ = the spacecraft declination at planetary encounter

The appropriate station location corrections (see Ref. 7) are, to first order,

$$\lambda = \lambda_0 + \dot{\alpha}_\gamma (t - t_0)(1 + \tan \epsilon \sin \alpha \tan \delta), \tag{9}$$

$$r_s = r_{s_0} + \dot{\delta}_\gamma (t - t_0) r_{s_0} \cos \alpha \tan \delta, \tag{10}$$

where (see Fig. 6)

ϵ = the obliquity of the ecliptic

t = planetary encounter time

t_0 = reference time at which a station location set is free of precession error

$\dot{\alpha}_\gamma$ = observed error in m, from station longitude estimates

$\dot{\delta}_\gamma$ = observed error in n, from station spin axis distance estimates

The partial derivatives are then,

$$\frac{\partial \lambda}{\partial \dot{\alpha}_\gamma} = (t - t_0)(1 + \tan \epsilon \sin \alpha \tan \delta), \tag{11}$$

$$\frac{\partial r_s}{\partial \dot{\delta}_\gamma} = (t - t_0) r_{s_0} \cos \alpha \tan \delta, \tag{12}$$

$$\frac{\partial \lambda}{\partial t_0} = -\dot{\alpha}_\gamma (1 + \tan \epsilon \sin \alpha \tan \delta), \tag{13}$$

$$\frac{\partial r_s}{\partial t_0} = -\dot{\delta}_\gamma r_{s_0} \cos \alpha \tan \delta. \tag{14}$$

III. Least Squares Formulation

The data equation is

$$z = Ax + \eta = \begin{bmatrix} r_s(i) \\ \lambda(i) \end{bmatrix}, \quad i = \text{DSS index} \tag{15}$$

$$x = [X, Y, \dot{\alpha}_\gamma, \dot{\delta}_\gamma, t_0]^T, \tag{16}$$

$$A = \left[\frac{\partial z_i}{\partial x}\right], \tag{17}$$

where x is the 5 X 1 vector of estimated parameters and A is the $2i$ X 5 mapping matrix, with i equal to the number of tracking stations for which r_s and λ estimates are input. The normalized data equation,

$$\bar{z} = \bar{A}x + \bar{\eta}, \tag{18}$$

is used where

$$[\bar{A}, \bar{z}] = w^{-1/2} [A, z], \tag{19}$$

and

w = the covariance weighting matrix of observables.

Introducing a priori information

$$\tilde{R}\tilde{x} = \tilde{z}, \tag{20}$$

where R is the a priori square root information matrix,

$$\begin{bmatrix} \tilde{R} & \tilde{z} \\ \bar{Z} & z \end{bmatrix} \text{ orthogonal } = [R\hat{z}], \tag{21}$$

$$[R\hat{z}]^{-1} = [R^{-1}, \hat{x}] = [P^{1/2}, \hat{x}], \tag{22}$$

where $\hat{x}$ is the estimate of the polar motion and precession parameters and P is the covariance on the estimate.

Bierman and Nead's Estimation Subroutine Package (ESP) was used for the upper triangular matrix computations (Refs. 8, 9). The program incorporating these routines was written by F. H. Brady for the specific problem of using encounter station location estimates to obtain estimates of precession and polar motion parameters and to plot the residuals.

IV. Computational Procedure

The computations were organized to process station location λ and r_s residuals (Figs. 1-4), adding one encounter set at a time. The upper rows correspond to the polar motion parameters, X and Y. By zeroing and initializing the upper two rows with $\tilde{R}(X,Y)$ before each encounter, an independent estimate of X and Y is obtained at each encounter while the precession parameters $\dot{\alpha}_\gamma$, $\dot{\delta}_\gamma$, and t_0 are sequentially estimated. The final values of $\dot{\alpha}_\gamma$, $\dot{\delta}_\gamma$, and t_0 are then used to obtain smoothed estimates of X and Y for each encounter. New λ and r_s residuals from the smoothed estimates are then plotted.

V. Data Weighting

Diagonal weighting matrices were used to obtain the results of this paper. These weights are the "consider" variances of the location estimates associated with LS 44 (Ref. 1) and the Viking solutions (Ref. 2). They are tabulated in Table 1. Special weights were adopted for DSS 41 at Mariner 5 Venus encounter and DSS 42 at Mariner 10 Mercury I encounter as a result of weak λ and r_s solutions for these passes. These weights more realistically represent the actual scatter in the station location solutions compared with the "consider" variances.

VI. A Priori Uncertainties

A priori uncertainties for the estimated parameters were input, based on information in Refs. 3 and 4. For the results

of this paper the following a priori standard deviations were assumed

$$\sigma_X, \sigma_Y = 0.2 \text{ rad} = 1.27 \text{ meters}$$

$$\sigma_{\dot{\alpha}_\gamma} = 2 \times 10^{-13} \text{ deg/sec} = 0.63 \times 10^{-5} \text{ deg/year}$$

$$\sigma_{\dot{\delta}_\gamma} = 1 \times 10^{-13} \text{ deg/sec} = 0.32 \times 10^{-5} \text{ deg/year}$$

$$\sigma_{t_0} = 0.1 \times 10^{9} \text{ sec} = 1157.4 \text{ days}$$

VII. Polar Motion Solutions

Three solutions for polar motion were performed. Two of these used station location estimates based on DE 84 (Figs. 1 and 2). The first DE 84 solution was for polar motion only and did not include precession parameters. The other DE 84 solution estimated polar motion and precession parameters and used the final precession solution to obtain smoothed polar motion estimates. The third solution obtained smoothed polar motion estimates in the same fashion, but used station location estimates based on DE 96 (Figs. 3 and 4). These solutions are summarized in Table 2.

It is seen that the solutions are in good agreement, with the exception of the Mariner 4 and Mariner 6 solutions for X, in which the polar-motion-only solution yields substantially smaller values than the smoothed solution. The good agreement between DE 84 and DE 96 solutions for X and Y is especially interesting, the implication being that if ephemeris errors are contributing heavily to the polar motion solutions, then both DE 84 and DE 96 have very similar errors.

The uncertainties on these X and Y estimates range from 0.4 to 1.1 meters, running about 0.7 meter for the most part. No seasonal trends are evident in the solutions, other than a noticeable peak in the Y solutions in the months of July and August.

Figures 7 and 8 are the λ and r_s residual plots after the solution for polar motion only. Comparing Figures 1 and 7, no improvement is evident in the longitude residuals, with the exception of the Mariner 6 and Viking 1 residuals. They display slightly less scatter, but other encounters show slightly increased scatter, if anything. The r_s residuals, however, are significantly improved by the solution for polar motion only. This is quite evident, comparing Figures 2 and 8. The square root of the weighted sum of squares (SRWSOS) of all λ and r_s residuals dropped from 8.37 before the fit to 7.73 after the fit for polar motion only.

VIII. Precession Solutions

The precession solutions are summarized in Table 3. For the [illegible]s which included polar motion in the solutions, essentially the value predicted by Reference 4 was obtained. The agreement between DE 84 and DE 96 $\dot{\alpha}_\gamma$ solutions is excellent. The most significant difference is in the t_0 solutions, which differ by 6 months, or about 0.6σ. This is equivalent to a small system rotation of inner planet right ascensions between DE 84 and DE 96 of about 0.16×10^{-5} deg, or 0".006. This once again represents remarkable agreement between DE 84 and DE 96.

The solution for just precession error yields a slightly smaller correction in $\dot{\alpha}_\gamma$ than the solutions which include polar motion (see Table 3). In the precession-only solution, the square root of the weighted sum of squares of λ and r_s residuals was reduced from 8.37 before the fit to 7.35 after the fit.

The sequential solutions for precession parameters $\dot{\alpha}_\gamma$, $\dot{\delta}_\gamma$ and t_0 are respectively plotted in Figs. 9, 10, and 11. The excellent agreement between DE 84 and DE 96 solutions is once again apparent. The precession-only solution displays a less systematic nature in $\dot{\delta}_\gamma$ and t_0 (Figs. 10 and 11). The plotted points for all three sets of solutions represent the results of adding encounter station location solutions cumulatively, one encounter at a time.

Referring to Fig. 5, it is tempting to speculate that some of the systematic nature of Figs. 9, 10, and 11 may be due to an error in the 18.6-year period nutation term.

The results obtained from precession and smoothed polar motion estimates are plotted in Figs. 12-15. The square root of the weighted sum of squares of the DE 84 λ and r_s residuals dropped from 8.37 before the fit to 5.92 after the smoothed fit. The SRWSOS of the DE 96 residuals dropped from 8.33 before the fit to 5.84 after the smoothed fit.

IX. Conclusions

DSS location solutions at eight planetary encounters have been used to obtain weighted least squares estimates of precession and polar motion errors. The indicated precession correction in right ascension is 0.31×10^{-5} deg/year $\pm 0.8 \times 10^{-6}$ deg/year, essentially the value predicted by Lieske in Ref. 3. This corresponds to a predicted right ascension error of $1.3 \times 10^{-5} \pm 0.4 \times 10^{-5}$ deg at the first Voyager 1979 Jupiter encounter. The solutions for precession and polar motion errors

using station locations based on DE 84 agree well with the solution using station locations referenced to DE 96.

The degree to which ephemeris error contributes to these solutions is unknown. However, the consistency between DE 84 and DE 96 solutions suggests that contributing ephemeris errors are largely common to both DE 84 and DE 96. The degree to which nutation error contributes to the precession solution is also unknown, but it is likely that nutation error is a principal cause of the systematic nature of the sequential solutions for precession error, possibly contributing as much as 0.1×10^{-5} deg/year in $\dot{\alpha}_\gamma$.

Acknowledgments

I wish to thank F. H. Brady, who wrote the computer program used to obtain these results, and G. J. Bierman and H. M. Koble, who gave invaluable assistance in organizing the filter algorithms appropriate to this problem.

References

1. Koble, H. M., Pease, G. E., and Yip, K. W., "LS 44 – An Improved Deep Space Network Station Location Set for Viking Navigation," in *The Deep Space Network Progress Report 42-35*, Jet Propulsion Laboratory, Pasadena, Calif., Oct. 15, 1976.

2. Campbell, J. K., and Rinker, G. C., "An Evaluation of Deep Space Network Station Locations from the Viking Encounters," Engineering Memorandum 314-107, Jet Propulsion Laboratory, Pasadena, Calif., Jan. 11, 1977 (an internal document).

3. Lieske, J., "Effect of Precession and Nutation Errors on Radar Observations," in *Space Program Summary 37-54, Vol. III*, Jet Propulsion Laboratory, Pasadena, Calif., Nov. 30, 1968.

4. Fliegel, H. F., and Wimberly, R. N., *Time and Polar Motion*, Technical Report 32-1587, Jet Propulsion Laboratory, Pasadena, Calif., Mar. 1, 1974.

5. Moyer, T. D., *Mathematical Formulation of the Double-Precision Orbit Determination Program (DPODP)*, Technical Report 32-1527, Jet Propulsion Laboratory, Pasadena, Calif., May 15, 1971.

6. *The American Ephemeris and Nautical Almanac for the Year 1974*, U. S. Government Printing Office, Washington, D. C., 1972, p. 9.

7. Hamilton, T. W., and Melbourne, W. G., "Information Content of a Single Pass of Doppler Data from a Distant Spacecraft," in *Space Program Summary 37-39, Vol. III*, Jet Propulsion Laboratory, Pasadena, Calif., May 31, 1966.

8. Bierman, G. J., and Nead, M. W., "An Estimation Subroutine Package: Part 1 – Parameter Estimation," Engineering Memorandum 314-4, Jet Propulsion Laboratory, Pasadena, Calif., Sept. 20, 1976 (an internal document).

9. Bierman, G. J., *Factorization Methods for Discrete Sequential Estimation*, Academic Press, 1977.

Table 1. Diagonal elements of $w(\sigma^2_{r_s}, \sigma^2_\lambda)$

DSS	Encounter							
	M4	M5	M6	M9	M10 Venus	M10 Merc I	Vik 1	Vik 2
$\sigma^2_{r_s}$ (meters)^2								
11	.4476						.7225	1.0201
12		18.6710	5.8709	1.2499	.8263	4.4100		
14		1.9321	6.7133	16.717	.5155	.2510	2.4964	.7396
41		16.[a]	4.2271	.7604				
42	.4160				1.337	16.[a]		.6400
43					.3318	.1190	.7744	.7396
51	.4942		6.9116					
61							1.0000	.4096
62		1.7716	3.4559	.8742	1.2860	1.0962		
63					.3919	.1340	.5776	
$\sigma^2_\lambda (10^{-5}$ deg$)^2$								
11	2.1993						1.9044	1.0816
12		27.6781	1.6053	4.5156	7.7562	2.5824		
14		74.4251	1.8117	8.6318	7.5900	1.1342	2.8900	1.4884
41		64.[a]	1.3948	3.1791				
42	1.9155				8.5031	64.[a]		1.0000
43					7.5735	1.1172	1.6384	1.5129
51	1.6384		3.0241					
61							2.1316	1.0816
62		19.5100	1.8279	4.5924	9.6100	1.7082		
63					7.6452	1.1236	1.8496	

[a] An a priori weight

Table 2. Planetary encounter polar motion solutions

Encounter	Date	X (JPL – BIH) meters			Y (JPL – BIH) meters		
		DE 84 PM only	DE 84 Smoothed	DE 96 Smoothed	DE 84 PM only	DE 84 Smoothed	DE 96 Smoothed
Mariner 4	07/15/65	.46	1.83	1.73	.57	.85	.99
Mariner 5	10/19/67	.36	.74	.82	.39	.40	.52
Mariner 6	07/31/69	-.71	.13	.42	.99	1.02	.73
Mariner 9	11/14/71	-1.39	-1.64	-1.93	-.40	-.55	-.54
Mar 10 Ven	02/05/74	-.29	-.34	-.56	-.10	-.08	-.44
Mar 10 Mer	03/29/74	.09	.11	.38	-.30	-.33	-.24
Viking 1	06/19/76	.41	.38	.30	-.46	-.08	.01
Viking 2	08/07/76	-.90	-1.44	-1.11	.25	.75	.66

Table 3. Planetary encounter secular right ascension and declination drifts, Mariner 4 through Viking 2

Solution	$\dot{\alpha}_\gamma$ (10^{-5} deg/yr)	$\dot{\delta}_\gamma$ (10^{-5} deg/yr)	t_0
DE 84, polar motion not in solution	-.268 ±.072	.297 ±.218	10/14/74 ±281 days
DE 84, polar motion in solution	-.321 ±.079	.286 ±.237	06/08/74 ±319 days
DE 96, polar motion in solution	-.310 ±.079	.377 ±.237	12/05/74 ±319 days

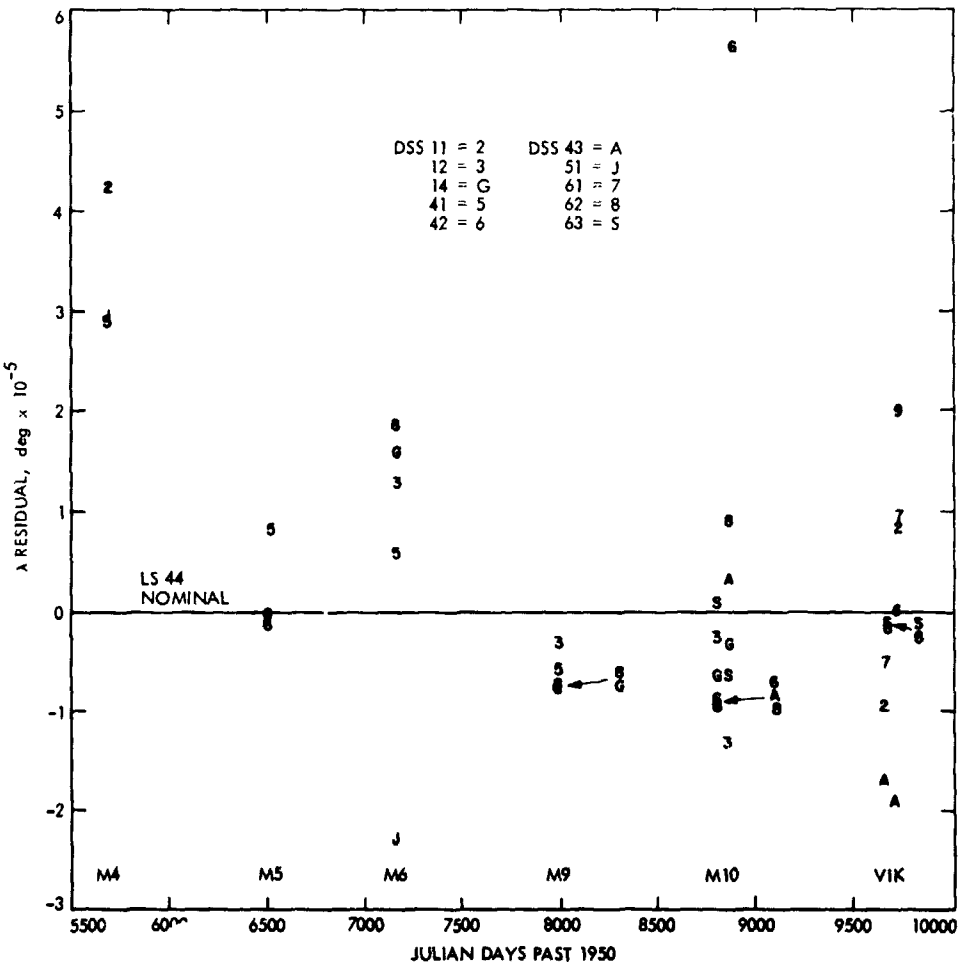

Fig. 1. DE 84 input λ residuals

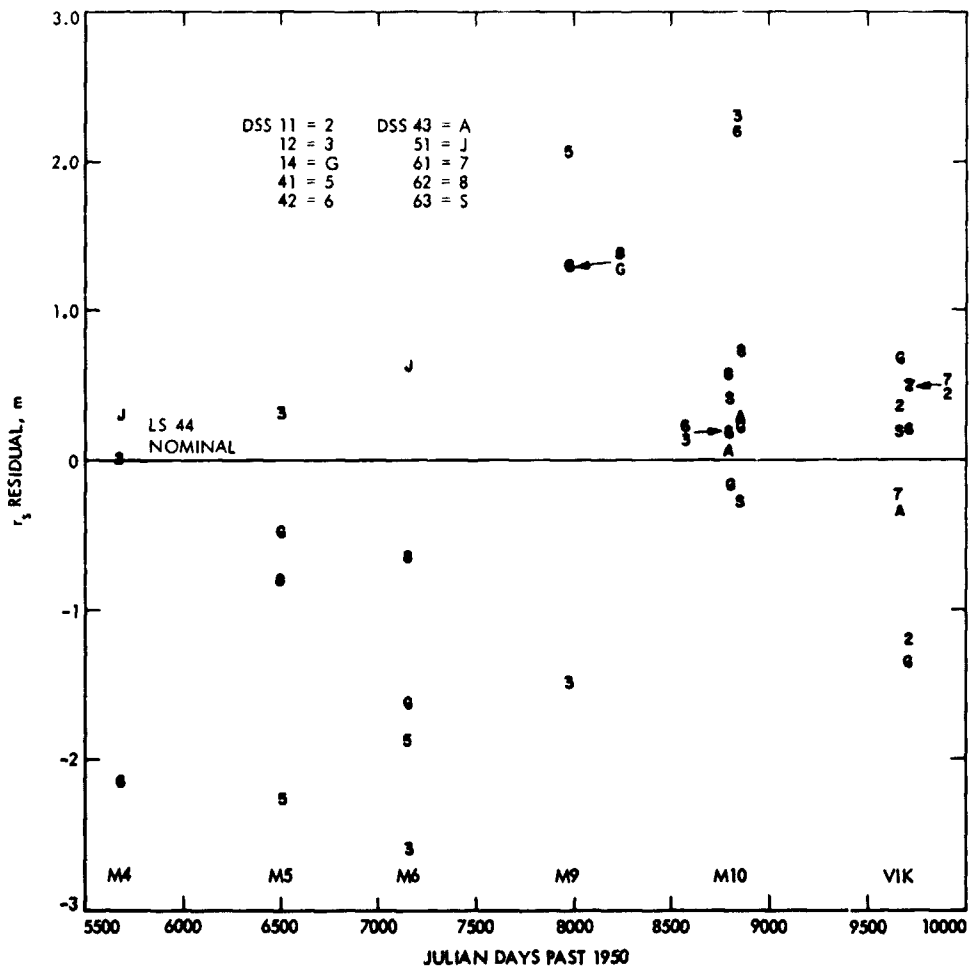

Fig. 2. DE 84 input r_s residuals

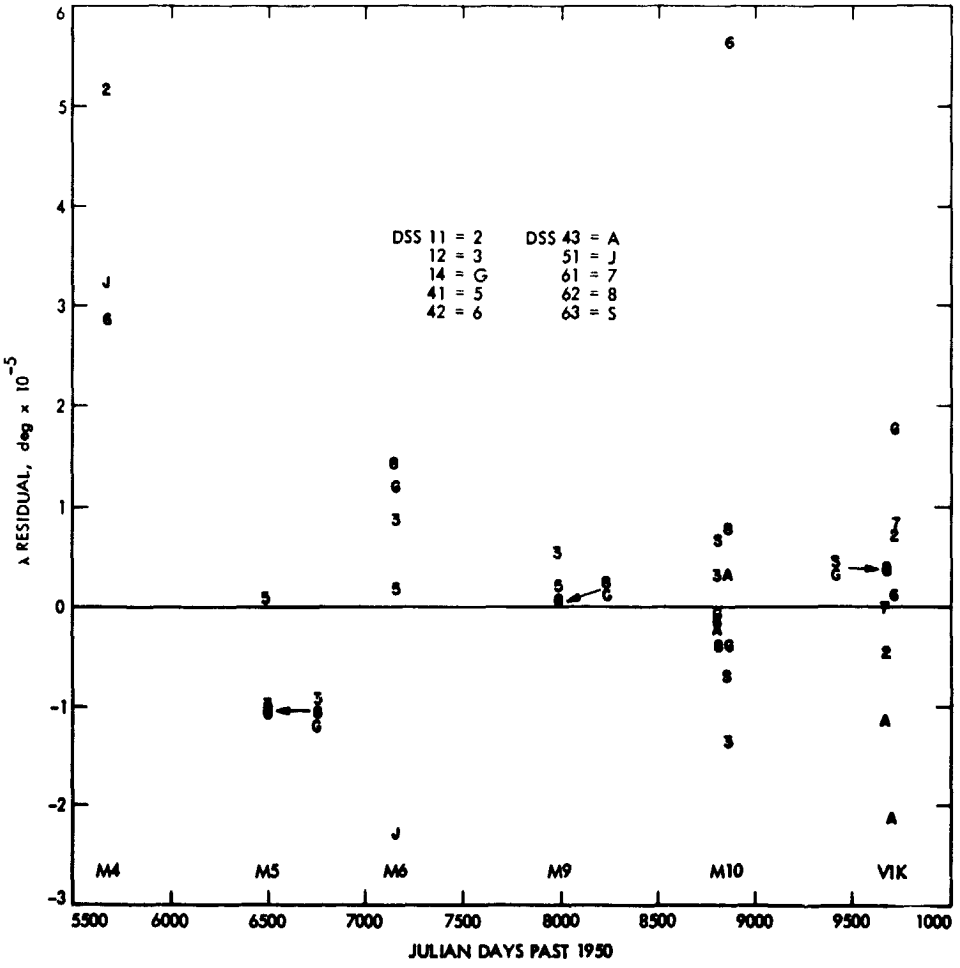

Fig. 3. DE 86 input λ residuals

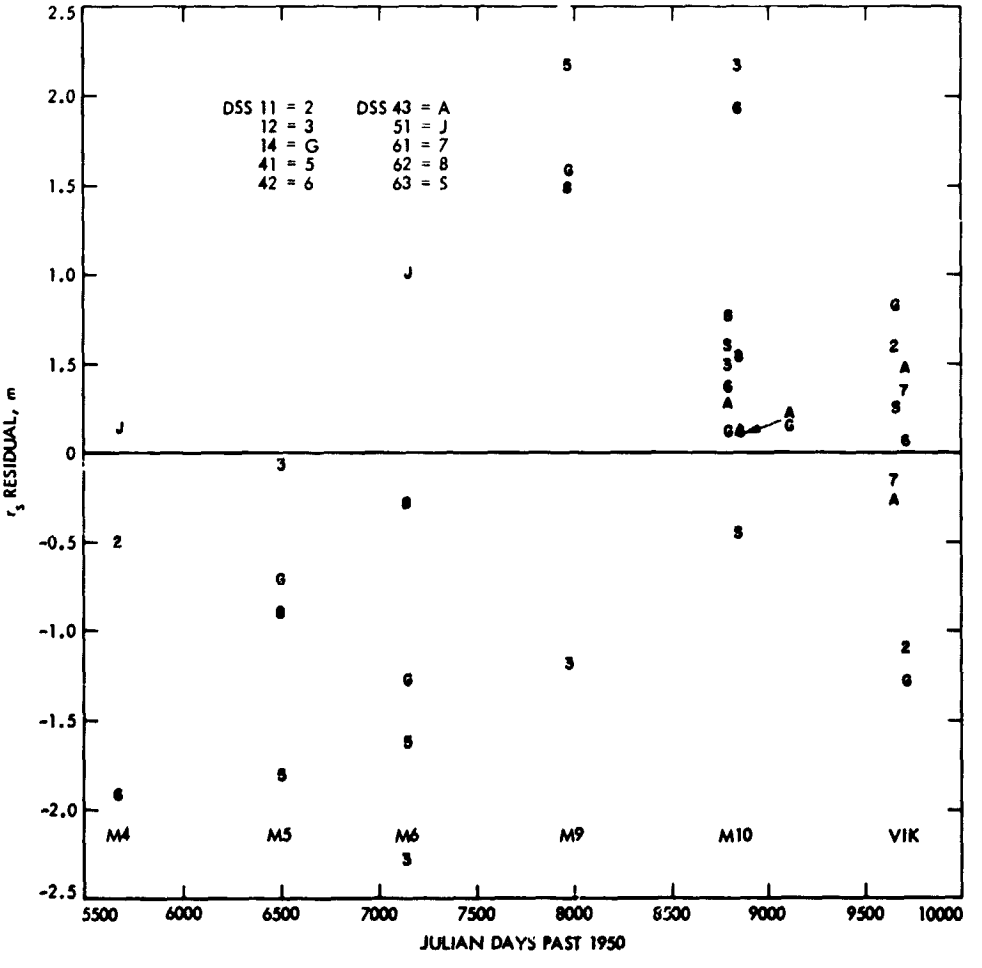

Fig. 4. DE 96 input r_s residuals

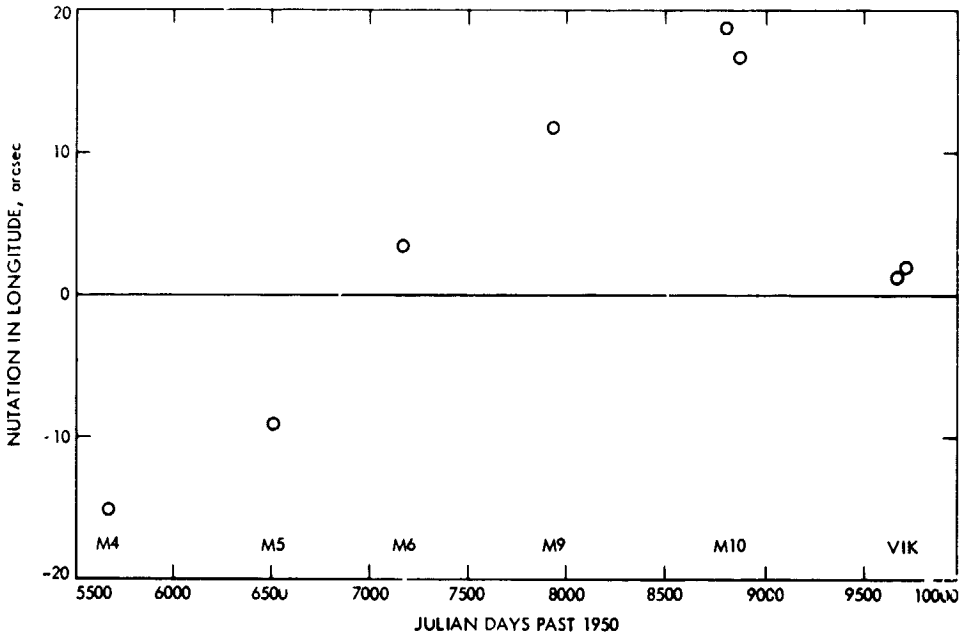

Fig. 5. Nutation in celestial longitude at planetary encounters

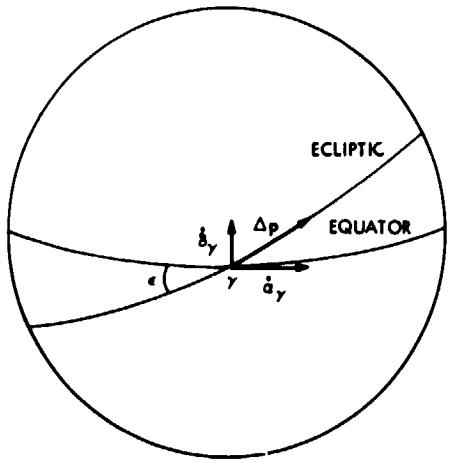

Fig. 6. Celestial sphere showing precession errors, $\dot{\alpha}_\gamma$, $\dot{\delta}_\gamma$

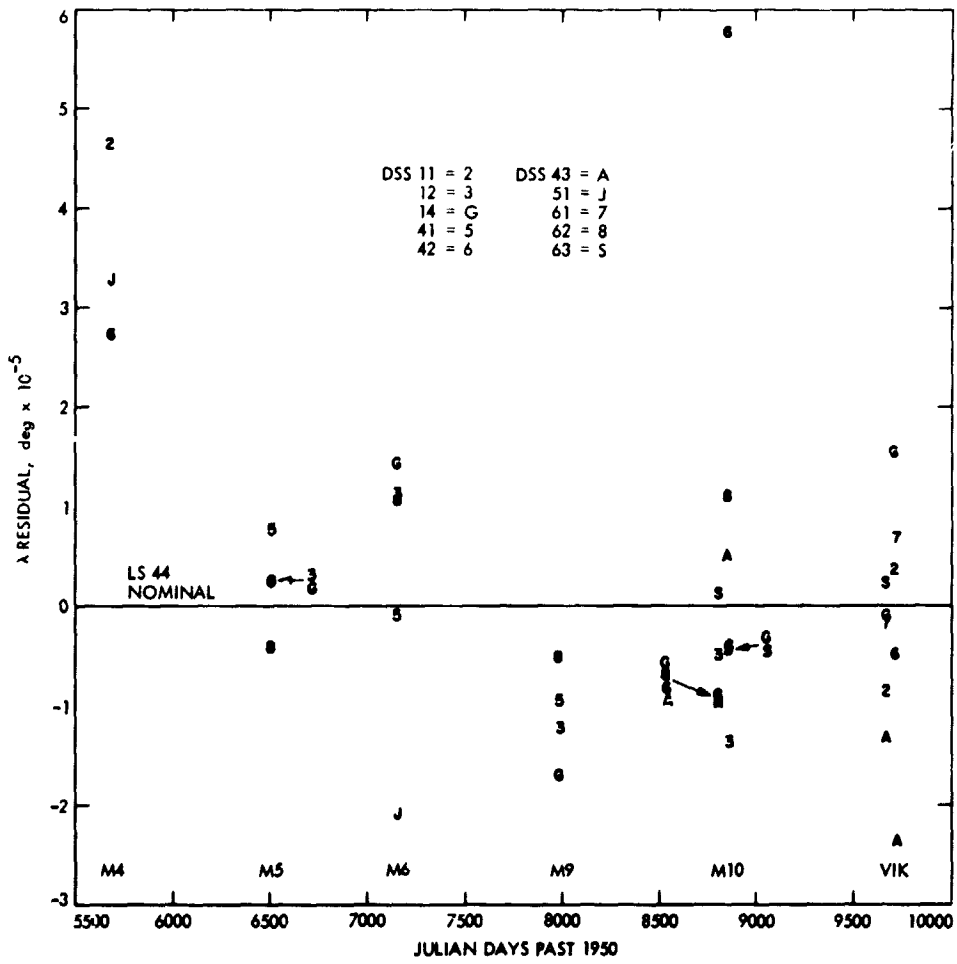

Fig. 7. DE 84 λ residuals after estimating polar motion only

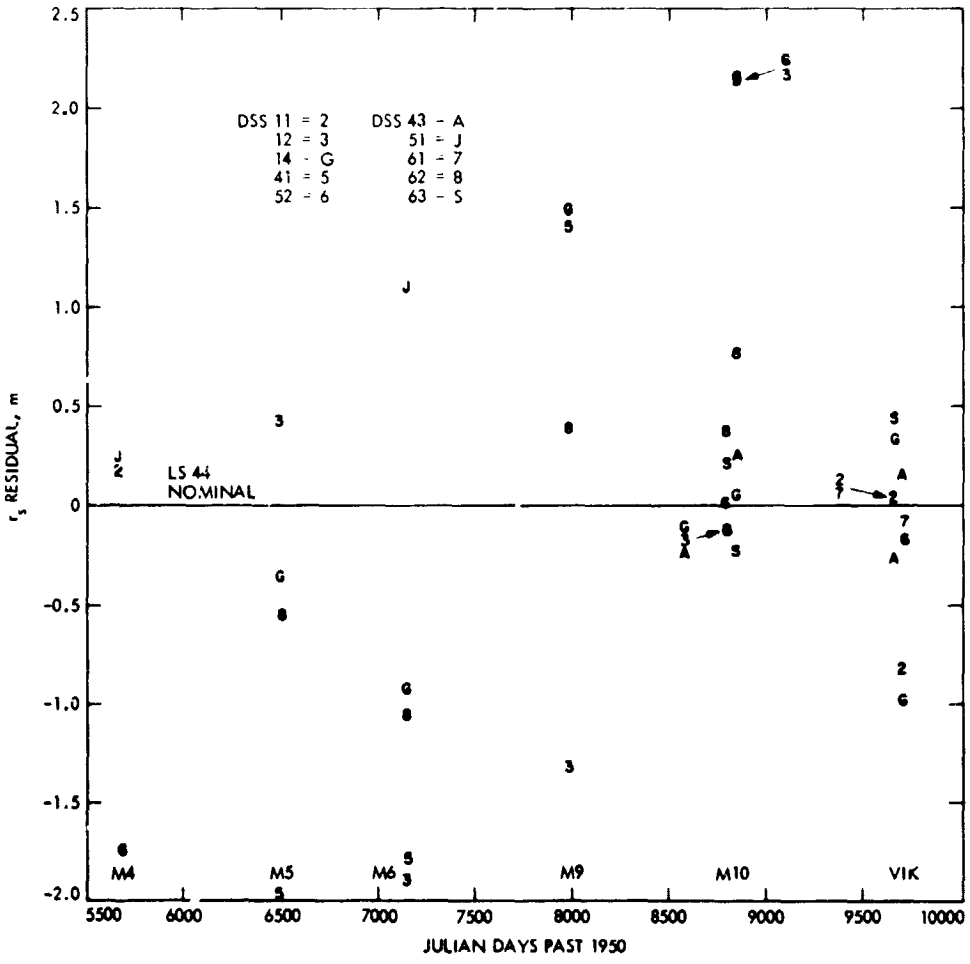

Fig. 8. DE 84 r_s residuals after estimating polar motion only

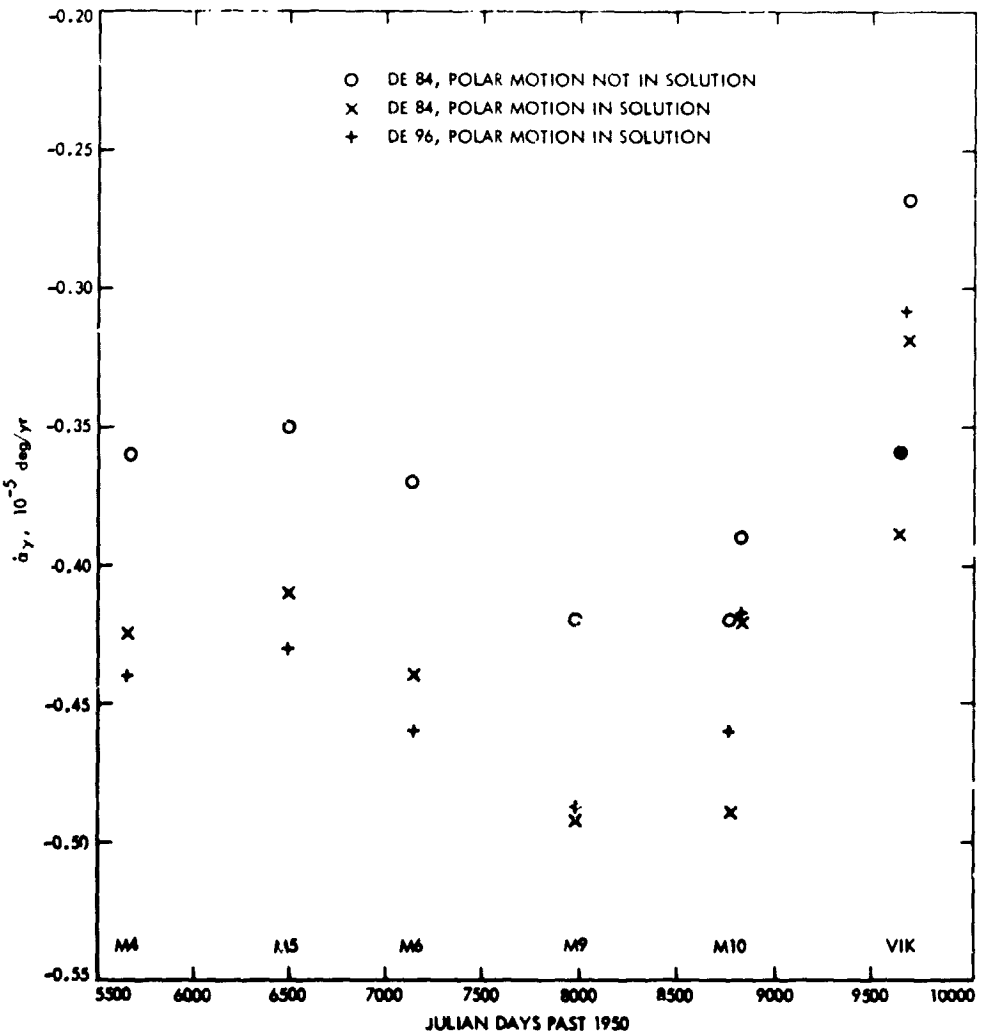

Fig. 9. Sequential solutions for right ascension drift, $\dot{\alpha}_y$

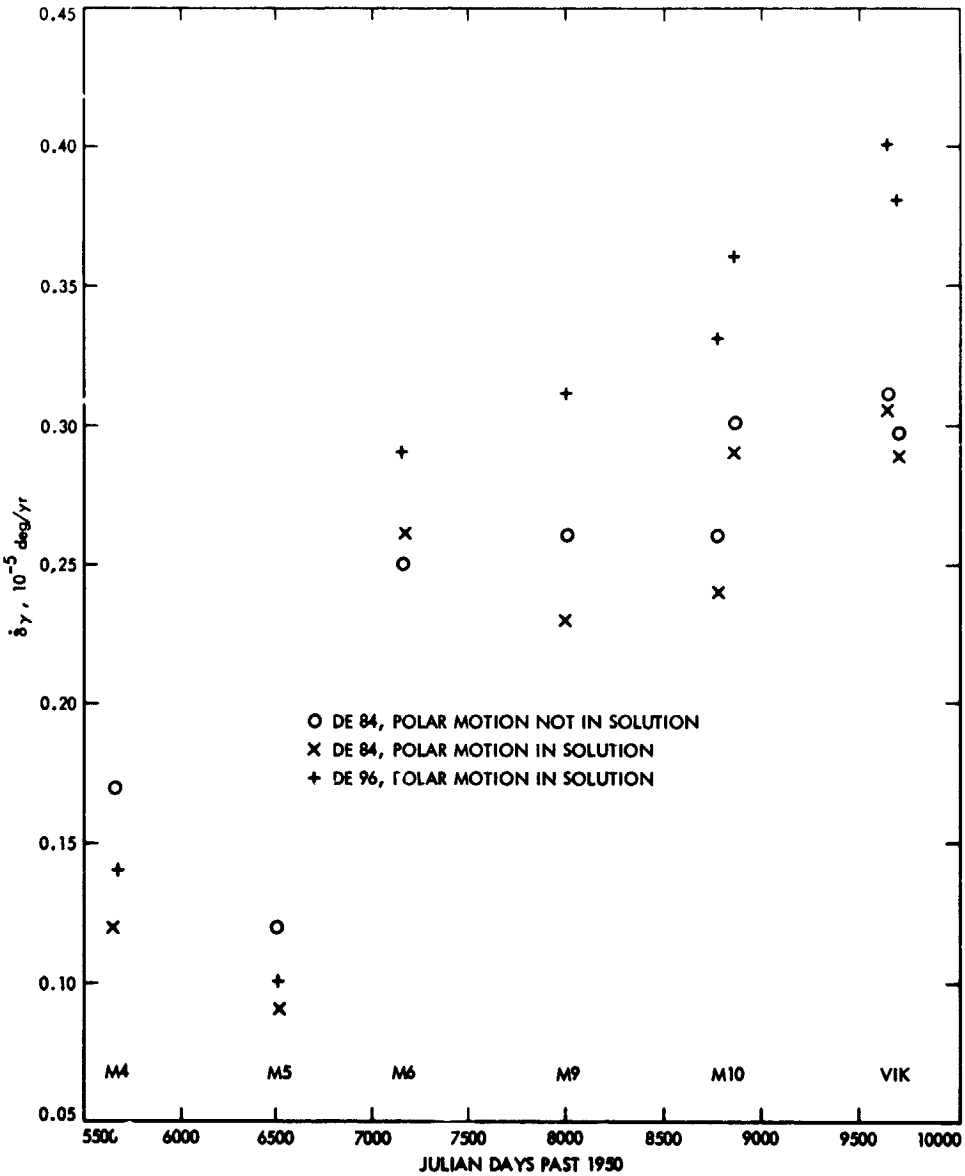

Fig. 10. Sequential solutions for declination drift, $\dot{\delta}_\gamma$

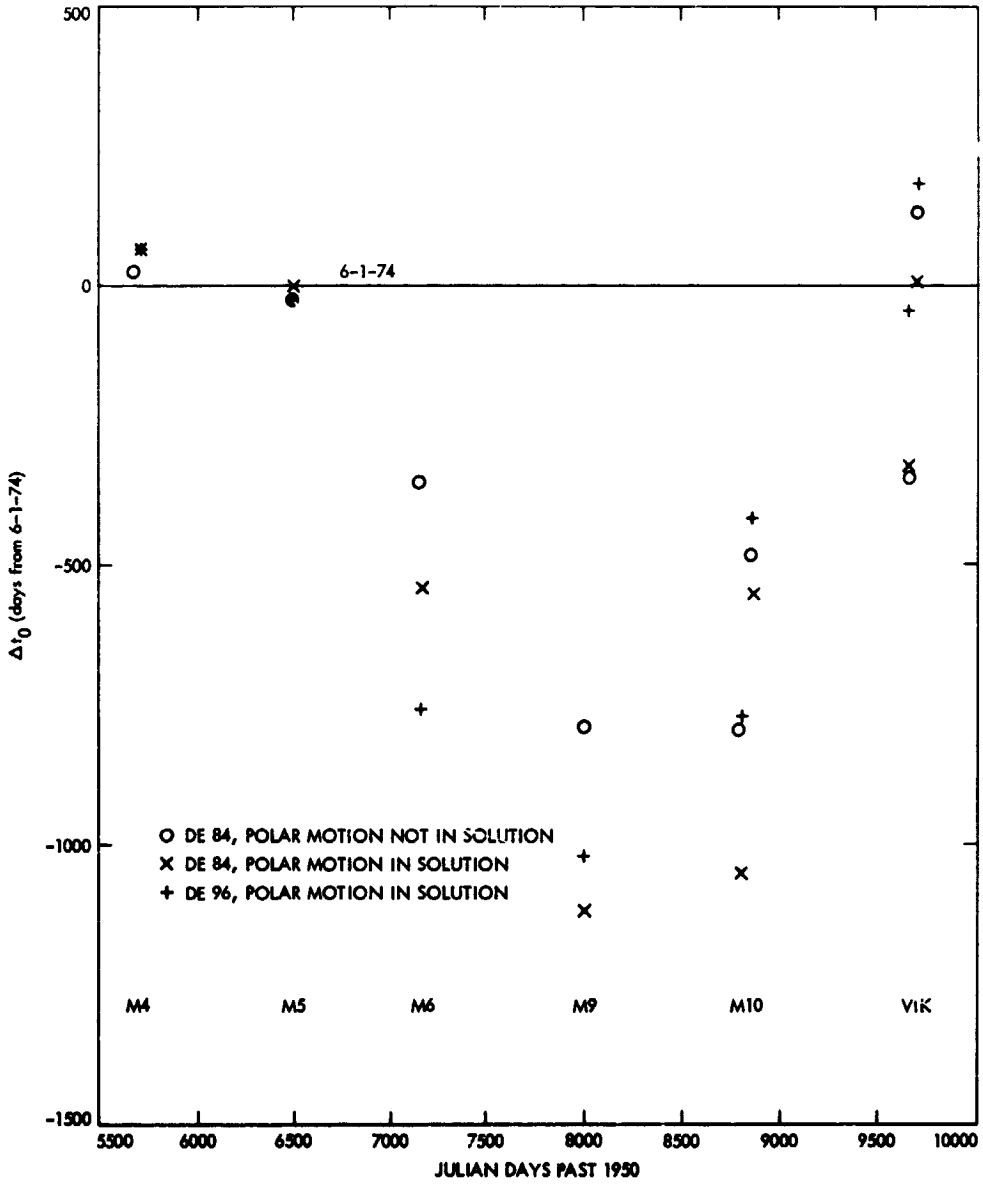

Fig. 11. Sequential solutions for equinox drift epoch, t_0

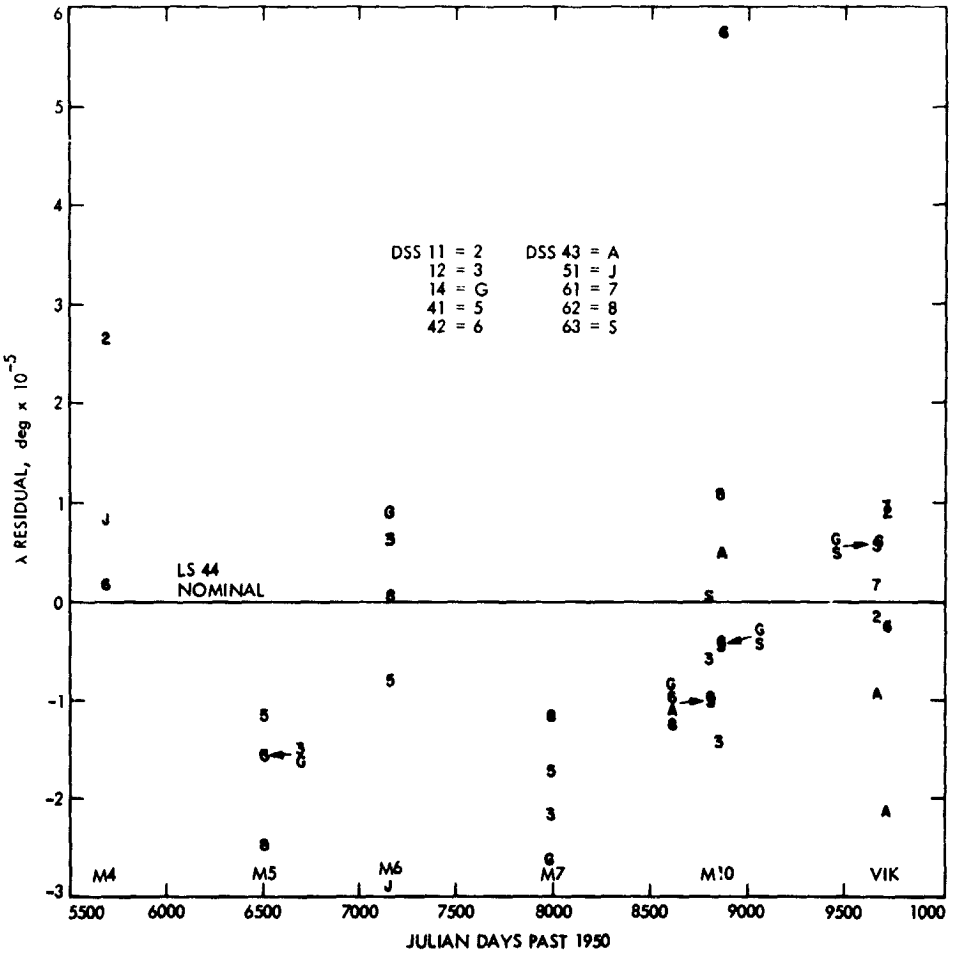

Fig. 12. DE 84 λ residuals after estimating precession and smoothed polar motion

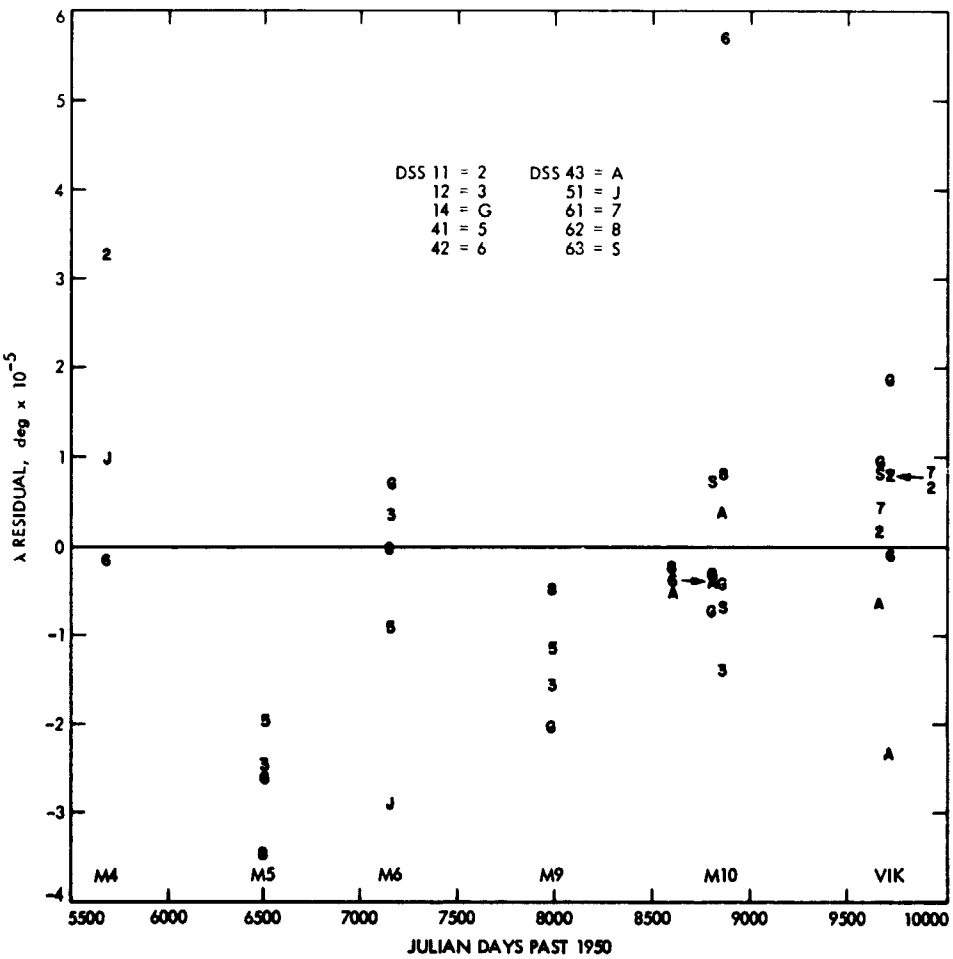

Fig. 13. DE 96 λ residuals after estimating precession and smoothed polar motion

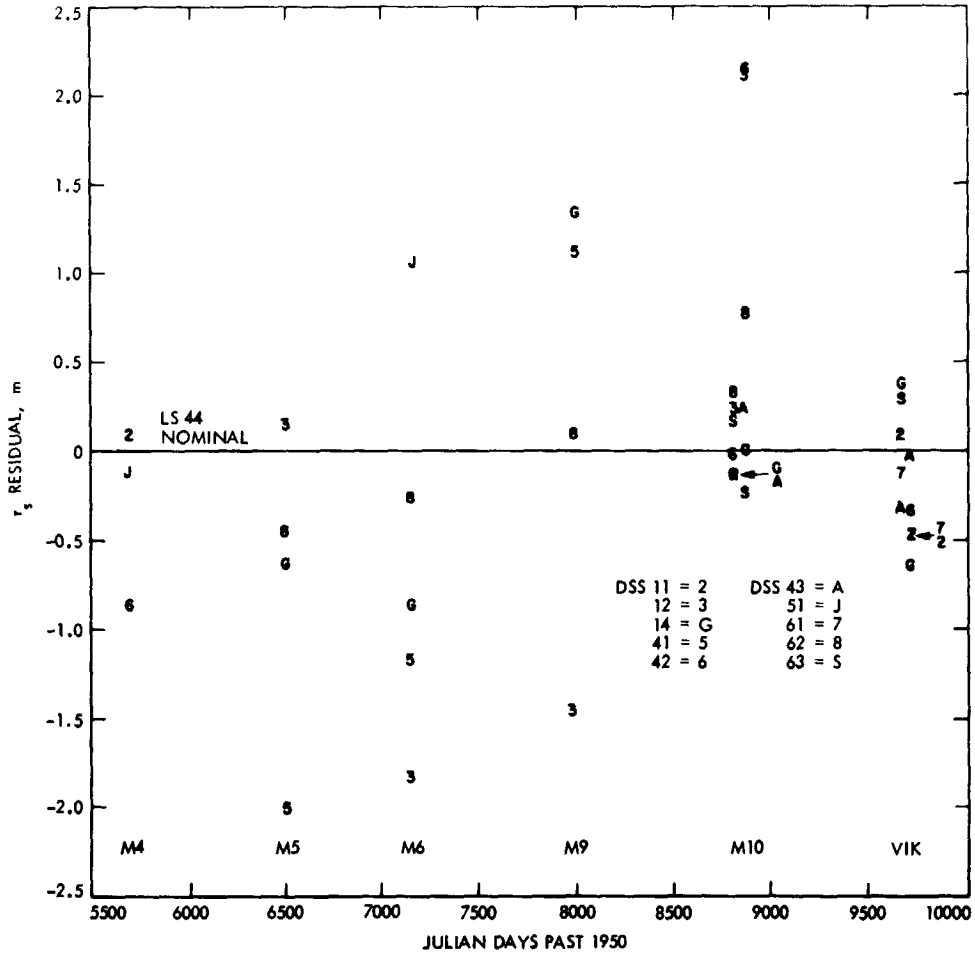

Fig. 14. DE 84 r_s residuals after estimating precession and polar motion

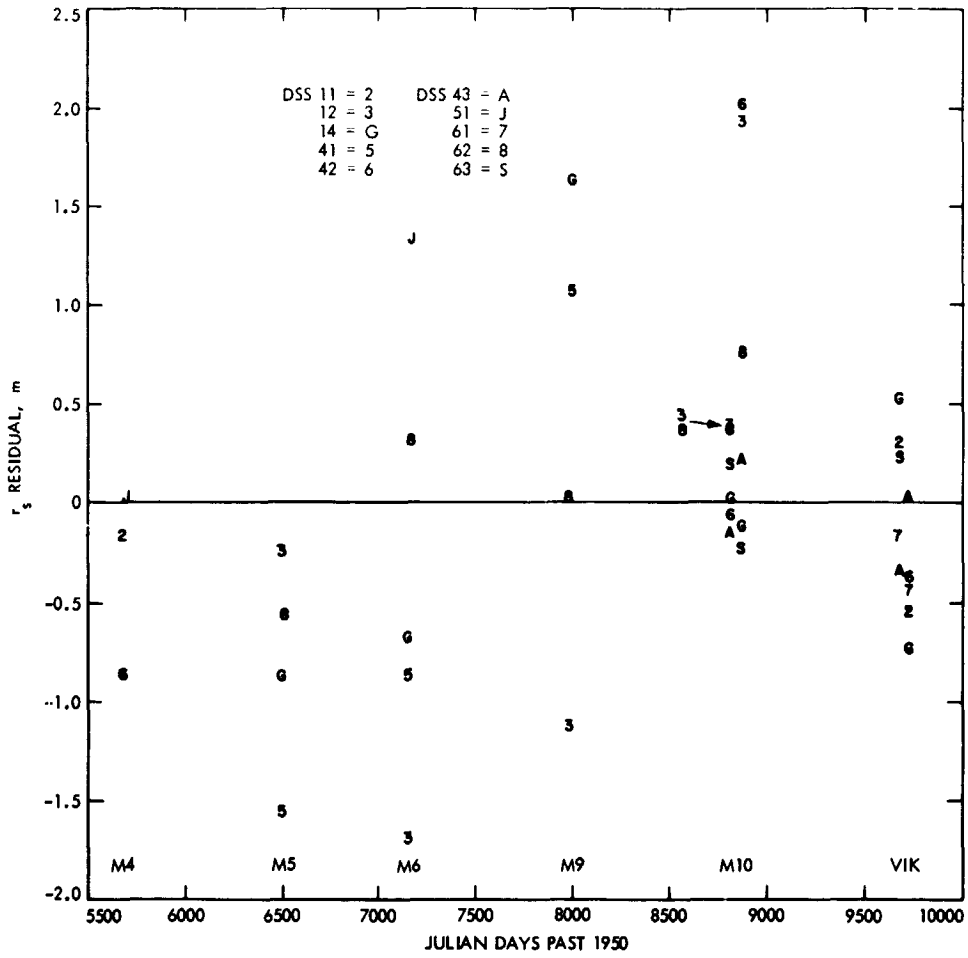

Fig. 15. DE 96 r_s residuals after estimating precession and polar motion

A Demonstration of Dual Spacecraft Tracking Conducted With the Viking Spacecraft During the Approacn Phase

C. C. Chao
Navigation Systems Section

The potential improvements in navigation capability of dual spacecraft tracking have been demonstrated using Viking approach data. Under unfavorable conditions of large plasma noise, low spacecraft declination and large Earth-spacecraft distance, the dual spacecraft tracking technique improved the Viking B approach accuracy based on short-arc radio metric data, by a factor of 7, to less than 200 km at Mars Orbit Insertion (MOI) minus 3 days. From the results of an analytical expansion and the Viking demonstration with a large intentional error in Mars ephemeris, we are able to conclude that dual spacecraft data types are insensitive to ephemeris error. Results also reveal the potential reduction of tracking time requirements during planet approach.

I. Introduction

For interplanetary space missions involving two spacecraft, such as Viking or Voyager, significant navigation advantages may sometimes be achieved (at least for the trailing vehicle) by determining the orbit of one relative to the other, or otherwise combining the data from the two spacecraft, rather than treating them independently as has been done in the past. Analysis of the dual spacecraft navigation concept and results of a demonstration using data from the early cruise phase of the Viking mission were reported in Refs. 1 and 2. Results from the analysis in Ref. 2 show that:

(1) Dual spacecraft data types, which are relatively insensitive to platform parameter errors, transmission media effects, low declination problems, and ephemeris errors, may improve navigational capabilities by a factor of 5 to 10, under the conditions of small angular separation ($\leq$3 deg) of the two spacecraft and well determined trajectory of the reference spacecraft.

(2) Dual spacecraft tracking has the potential of significantly reducing DSN tracking time requirements.

This paper presents new analytical models for the dual spacecraft data types and reports new results from a more recent demonstration conducted during the approach phase of the Viking mission. The demonstration was based on data taken two weeks before MOI of the second Viking spacecraft, when the first spacecraft had been in orbit for several weeks and its orbit relative to Mars was well determined. The demonstration was designed to show that the approaching probe could be tied accurately to the planet through the orbiter.

II. Analytic Expansion of Dual Spacecraft Data

The information content of dual spacecraft data has been analyzed in Refs. 1 and 2, and the reduction in sensitivity to platform parameter errors, low declination problems and transmission media effects are clearly understood. However, the cancellation of ephemeris error during a dual spacecraft flyby has not been investigated. Furthermore, the previous analysis using a Hamilton-Melbourne (Ref. 3) type of approximation

ignores higher order terms, some of which become important after differencing.

During the approach phase, the planetocentric distances of the two spacecraft are much smaller then the geocentric distances, as shown in Fig. 1. The range and range-rate observables (ρ and $\dot{\rho}$) from one spacecraft may be expressed in terms of planetocentric coordinates $\vec{r}$, the geocentric position of the planet $\vec{R}$, and the position vector of the tracking station $\vec{s}$ as follows:

$$\rho = [(\vec{R} + \vec{r} - \vec{s}) \cdot (\vec{R} + \vec{r} - \vec{s})]^{1/2}$$

$$\dot{\rho} = \frac{\vec{\rho} \cdot \dot{\vec{\rho}}}{\rho} = \frac{1}{\rho}(\vec{R} + \vec{r} - \vec{s}) \cdot (\dot{\vec{R}} + \dot{\vec{r}} - \dot{\vec{s}})$$

The above equation for the range observables may be rewritten as

$$\rho = [R^2 + r^2 + s^2 + 2(\vec{R} \cdot \vec{r} - \vec{R} \cdot \vec{s} - \vec{r} \cdot \vec{s})]^{1/2}$$

$$= R(1 + \epsilon)^{1/2}$$

where

$$\epsilon = 2\left(\frac{\vec{R} \cdot \vec{r} - \vec{R} \cdot \vec{s} - \vec{r} \cdot \vec{s}}{R^2}\right) + \left(\frac{r}{R}\right)^2 + \left(\frac{s}{R}\right)^2$$

When a spacecraft is encountering a planet, ϵ is small because

$$1 \gg \frac{r}{R} \gg \frac{s}{R}$$

After expansion we have

$$\rho = R\left(1 + \frac{1}{2}\epsilon - \frac{1}{8}\epsilon^2 + \ldots\right)$$

Then to the first order in s/R and second order in r/R we have

$$\rho = R + (x - s_x)\cos\delta'\cos\alpha' + (y - s_y)\cos\delta'\sin\alpha'$$

$$+ (z - s_z)\sin\delta' + \frac{1}{2}r\left(\frac{r}{R}\right)\sin^2\psi$$

$$- \left(s_x\frac{x}{R} + s_y\frac{y}{R} + s_z\frac{z}{R}\right) \qquad (1)$$

where ψ is the angle between vectors $\vec{R}$ and $\vec{r}$.

Similarly the range rate observable may be expanded as

$$\dot{\rho} = \frac{1}{R}\left(1 - \frac{1}{2}\epsilon + \frac{3}{8}\epsilon^2 + \ldots\right)(\vec{R} \cdot \dot{\vec{R}} + \vec{R} \cdot \dot{\vec{r}} - \vec{R} \cdot \dot{\vec{s}}$$

$$+ \vec{r} \cdot \dot{\vec{R}} + \vec{r} \cdot \dot{\vec{r}} - \vec{r} \cdot \dot{\vec{s}}$$

$$- \vec{s} \cdot \dot{\vec{R}} - \vec{s} \cdot \dot{\vec{r}} + \vec{s} \cdot \dot{\vec{s}})$$

or

$$\dot{\rho} = C + \left(\cos\delta'\cos\alpha' + \frac{x}{R} - \frac{s_x}{R}\right)\dot{x}$$

$$+ \left(\cos\delta'\sin\alpha' + \frac{y}{R} - \frac{s_y}{R}\right)\dot{y}$$

$$+ \left(\sin\delta' + \frac{z}{R} - \frac{s_z}{R}\right)\dot{z} + E_x\frac{x}{R}$$

$$+ E_y\frac{y}{R} + E_z\frac{x}{R} \qquad (2)$$

where C and E_x, E_y, E_z are functions of planet and station location coordinates

$$C = (\dot{R}_x - \dot{s}_x)\left(\cos\delta'\cos\alpha' - \frac{s_x}{R}\right)$$

$$+ (\dot{R}_y - \dot{s}_y)\left(\cos\delta'\sin\alpha' - \frac{s_y}{R}\right)$$

$$+ \dot{R}_z\left(\sin\delta' - \frac{s_z}{R}\right)$$

$$E_x = (\dot{R}_x - \dot{s}_x)(1 - \cos^2\delta'\cos^2\alpha')$$

$$- \frac{1}{2}(\dot{R}_y - \dot{s}_y)\cos^2\delta'\sin 2\alpha'$$

$$- \frac{1}{2}\dot{R}_z\sin 2\delta'\cos\alpha'$$

$$E_y = -\frac{1}{2}(\dot{R}_x - \dot{s}_x)\cos^2\delta'\sin 2\alpha'$$

$$+ (\dot{R}_y - \dot{s}_y)(1 - \cos^2\delta'\sin^2\alpha')$$

$$-\frac{1}{2}\dot{R}_z \sin 2\delta' \sin\alpha'$$

$$E_z = -\frac{1}{2}(\dot{R}_x - \dot{s}_x)\sin 2\delta'\cos\alpha'$$

$$-\frac{1}{2}(\dot{R}_y - \dot{s}_y)\sin 2\delta'\sin\alpha' + \dot{R}_z\cos^2\delta'$$

If the two spacecraft are being tracked simultaneously from the same site, a new data type may be formed by differencing the corresponding observables from the two spacecraft.

$$\Delta\rho = \rho - \rho_1 = \cos\delta'\cos\alpha'(x - x_1) + \cos\delta'\sin\alpha'(y - y_1)$$

$$+ \sin\delta'(z - z_1) + \frac{1}{2}r\left(\frac{r}{R}\right)\sin^2\psi - \frac{1}{2}r_1\left(\frac{r_1}{R}\right)\sin^2\psi_1$$

$$+ s_x\frac{(x - x_1)}{R} + s_y\frac{(y - y_1)}{R} + s_z\frac{(z - z_1)}{R} \qquad (3)$$

$$\Delta\dot{\rho} = \dot{\rho} - \dot{\rho}_1 = \left(\cos\delta'\cos\alpha' - \frac{s_x}{R}\right)(\dot{x} - \dot{x}_1)$$

$$+ \left(\cos\delta'\sin\alpha' - \frac{s_y}{R}\right)(\dot{y} - \dot{y}_1)$$

$$+ \left(\sin\delta' - \frac{s_z}{R}\right)(\dot{z} - \dot{z}_1) + \frac{1}{R}(x\dot{x} + y\dot{y} + z\dot{z} - x_1\dot{x}_1 - y_1\dot{y}_1$$

$$- z_1\dot{z}_1) + E_x\frac{(x - x_1)}{R} + E_y\frac{(y - y_1)}{R}$$

$$+ E_z\frac{(z - z_1)}{R} \qquad (4)$$

The above data types are called two spacecraft 2-station range and range rate (doppler). It is clear that the terms, R and C in Eqs. (1) and (2), which are sensitive to planet ephemeris and station location errors, are removed. The ephemeris and station location coordinates in the above equations are multiplied by the small factors of $(x - x_1)/R$ or $1/R$ etc., thus these errors could be reduced accordingly. Furthermore, the quality of the above differenced data is improved due to the cancellation of transmission media effects. However, they are still sensitive to unmodeled spacecraft accelerations, i.e., attitude-control gas leaks and solar pressure anomalies. These noises may be removed by differencing the data simultaneously obtained from two widely separated stations. Consistent with Ref. 2, the single spacecraft 2-station data type and two spacecraft 4-station data types are to be derived next.

When simultaneous 2-station tracking from one spacecraft is assumed, the differenced range and range rate may be obtained from Eqs. (1) and (2) and expressed in terms of baseline coordinates r_B, α_B and z_B.

$$D\rho = r_B\cos\delta'\sin(\alpha_B - \alpha') + z_B\sin\delta'$$

$$+ r_B\left(\frac{x}{R}\sin\alpha_B + \frac{y}{R}\cos\alpha_B\right) + Z_B\frac{z}{R} \qquad (5)$$

$$D\dot{\rho} = \omega r_B\cos\delta'\cos(\alpha_B - \alpha') + \frac{\omega r_B}{R}[G_x x + G_y y + G_z z]$$

$$+ \frac{r_B}{R}[\sin\alpha_B\dot{x} + \cos\alpha_B\dot{y}] + \frac{z_B}{R}\dot{z} \qquad (6)$$

where

$$G_x = \sin\alpha_B(1 - \cos^2\delta'\cos^2\alpha') - \frac{1}{2}\cos\alpha_B\cos^2\delta'\sin 2\alpha'$$

$$G_y = -\frac{1}{2}\sin\alpha_B\cos^2\delta'\sin 2\alpha' + \cos\alpha_B(1 - \cos^2\alpha'\cos^2\alpha')$$

$$G_z = -\frac{1}{2}\sin\alpha_B\sin 2\delta'\cos\alpha' - \frac{1}{2}\cos\alpha_B\sin 2\delta'\sin\alpha'$$

The above data types are the one spacecraft 2-station range and range rate.

The first two terms in Eq. (5) and the first term in Eq. (6) contain the angular position of the planet (α', δ') and therefore, the data are sensitive to planet ephemeris errors. In addition, the baseline parameters r_B, z_B and α_B are another

major error source. After the second differencing, the 2 spacecraft 4-station range and rate are

$$D\rho - D\rho_1 = r_B\left[\sin\alpha_B\left(\frac{x - x_1}{R}\right) + \cos\alpha_B\left(\frac{y - y_1}{R}\right)\right] + z_B\frac{z - z_1}{R} \tag{7}$$

$$D\dot{\rho} - D\dot{\rho}_1 = r_B\left\{\omega\left[G_x\frac{(x - x_1)}{R} + G_y\frac{(y - y_1)}{R} + G_z\frac{(z - z_1)}{R}\right] + \sin\alpha_B\frac{(\dot{x} - \dot{x}_1)}{R} + \cos\alpha_B\frac{(\dot{y} - \dot{y}_1)}{R}\right\} + z_B\frac{(\dot{z} - \dot{z}_1)}{R} \tag{8}$$

With those common terms removed, the dual spacecraft 4-station data types are not only insensitive to planet ephemeris and station location errors, but also free from noises resulting from transmission media and unmodeled spacecraft accelerations. This clean data type thus can accurately tie one spacecraft to the other.

The above expansions provide some insight into various observables and are helpful in examining the information content of the dual spacecraft data types. Due to the fact that the planet relative state of the two encountering spacecraft change appreciably over a short time (one day), the information content from a single pass of data cannot be extracted in the same manner as in Ref. 2. However, the sensitivities to planet ephemeris error and station location uncertainties may be seen from the partial derivatives which may be easily derived from the above equations. These approximate equations of observables and partial derivatives may be useful for performing certain types of preliminary analysis of dual spacecraft tracking during a planet approach.

Although the potential reduction in sensitivities to planet ephemeris and station location errors has been shown through the analytical expansion, a simplified example based on those equations may be helpful. If $\vec{r}$ and $\vec{r}_1$ are assumed fixed, one may compute using Eqs. (1) to (8) the equivalent error in each observable which corresponds to (or would be induced by) a given ephemeris error. If the computed bias is large compared with the inherent accuracy of the observable, then the ephemeris error will corrupt the estimate of $\vec{r}$. A simplified example of this type of analysis for the Saturn approach of the Voyager mission is shown by the upper charts of Fig. 2. The two Voyager spacecraft will be separated by 9 deg when the second probe approaches Saturn in 1981. Most of the 2000 km (conservative estimate) ephemeris error cancels as the dual spacecraft data types are differenced (Fig. 2). For the dual spacecraft 2-station data type, the bias left in the differenced data is still quite large (see upper left chart of Fig. 2). This is due to the fact that the cancellation of the ephemeris error in right ascension and declination is not as effective as that along the line-of-sight direction that may be seen from Eq. (4). Because of the asymmetry of the two sets of state parameters, $x, y, \ldots, x_1, y_1, \ldots$, in Eq. (4), this sensitivity may be removed by estimating both spacecraft. After regression analysis one may lead to the following relations:

$$\frac{\partial x}{\partial\delta'} = f, \qquad \frac{\partial x_1}{\partial\delta'} = -f_1, \qquad \begin{matrix} x \to y, z \\ \delta' \to \alpha' \end{matrix}$$

For spacecraft not far away from each other, the values of f and f_1 should be fairly close. Thus, errors in α' and δ' will cancel implicitly. Results of the Viking demonstration that are to be discussed later show that most of the simulated Mars ephemeris error (2000 km) was removed only when both spacecraft were estimated.

The comparison in the lower chart of Fig. 2 reveals the same conclusion as in Ref. (2) that dual spacecraft data types are not sensitive to platform parameters. The degree of error cancellation depends on the angular separation between the two spacecraft.

The information content and major error sensitivities of the four kinds of data types discussed earlier may be summarized in the table in Fig. 3. It clearly shows that the dual spacecraft 4-station data type is the best as far as the data quality is concerned. However, the information content is also decreased as a result of the double differencing process when the differential range and range rate ($\Delta\rho$, $\Delta\dot{\rho}$) information, which are highly sensitive to the planet gravitation acceleration, are removed. How to select and combine the proper data types to maximize the navigation capability depends on various conditions such as the geometry of the trajectories of the two spacecraft, Sun-Earth-probe angle and the magnitude of unmodeled spacecraft accelerations, etc.

III. A Demonstration Conducted with Viking Spacecraft

A. Geometry of the Viking 2 Approach Trajectory

The two Viking spacecraft were launched in late August 1975 and arrived at Mars in the summer of 1976. When the

Viking 1 spacecraft went into orbit about Mars on June 19, 1976, Viking 2 was about 40 days away from the planet. Thus during this last month of the approach phase of Viking 2, the technique of dual spacecraft tracking could be used to tie Viking 2 spacecraft to the planet through Orbiter 1. Figure 4 shows the approximate geometry of the two spacecraft. It reveals two of those navigation difficulties mentioned previously. First, the relatively small Sun-Earth-probe (SEP) angle increases the data noise caused by active solar plasma effects. Secondly, the long geocentric distance makes the errors in station locations significant. In addition, the low declination ($\delta \approx 5$ deg), which cannot be seen from the figure, gives another difficulty in orbit determination. Consequently, these error sources caused the navigation uncertainty using conventional data to be as large as 1100 km, as will be discussed later. During the last two weeks of the approach phase of the second spacecraft, the angular separation between the two spacecraft was very small being 0.15 deg. Thus good cancellation of both transmission media noise and station location errors was expected. This provided a good opportunity for the dual spacecraft technique to demonstrate its potential capability in navigation.

B. Strategy

The success of the interplanetary orbit determination effort is best measured by the accuracy of its delivered estimates for midcourse maneuvers. These estimates generally come from three independent orbit determination solutions: the long arc, the short-arc, and the optical. The optical data, although proved to be most accurate during planet approach, are not as reliable as the radiometric data. The long-arc through-maneuver solutions, according to Ref. 4, are stable, yet are not particularly accurate. The Viking 1 long-arc solutions, in fact, were in error beyond that predicted by covariance analysis. Furthermore, the long-arc solutions are computationally expensive. The short-arc solutions which contain the most up-to-date information of the spacecraft state are usually corrupted by such error sources as platform parameter uncertainties and transmission media effects, etc. The goal of this demonstration was to improve the orbit determination accuracy of the short-arc solutions with dual spacecraft data, which are relatively free of those error sources.

The data span selected for this study covers a short-arc of 8 days immediately after the last midcourse maneuver of Viking 2. The data arc stops 3 days before the MOI of Viking 2 occurred on August 7, 1976. During this period, Viking 1 was in orbit around Mars for many revolutions and its orbits were well determined relative to the planet. Thus the dual spacecraft tracking data from this eight-day arc may accurately tie the second spacecraft to Mars and consequently improve the estimate for the final MOI delivery one day before the event. The improvement in orbit determination accuracy of this short-arc may be of great benefit to navigation if it is done in real time.

A carefully designed demonstration plan had been made and presented to the Viking Flight Path Analysis Group for support before the two spacecraft were launched in 1975. The request for dual spacecraft tracking data including 2-station and 4-station data types was not successful due to the strong resistance to any non-mission activities. As a result, the data base used for this demonstration is whatever the Viking mission requested and was available during this period. The data distribution for the dual spacecraft 2-station data is relatively poor, particularly for dual spacecraft 2-station range, compared to that of convention data (Fig. 5). Unfortunately the dual spacecraft 4-station Doppler was not scheduled during the entire Viking mission.

C. Algorithm of Data Processing

An algorithm for processing dual spacecraft data was briefly explained in Ref. 2. This algorithm generates new data types by differencing conventional data files (ACCUME FILES) obtained from orbit determination runs made for each spacecraft separately. The new file contains the differenced data types and the conventional data from the second spacecraft. The partial derivatives for the state and other parameters of the referenced spacecraft are included. For dual spacecraft 2-station range and doppler, they may be expressed by the following form of differential correction.

$$\Delta\rho_{2\ S/C} = \Delta\rho - \Delta\rho_o = \frac{\partial\rho}{\partial q_i}\Delta q_i - \frac{\partial\rho_o}{\partial q_{oi}}\Delta q_{oi}$$

$$\Delta\dot{\rho}_{2\ S/C} = \Delta\dot{\rho} - \Delta\dot{\rho}_c = \frac{\partial\dot{\rho}}{\partial q_i}\Delta q_i - \frac{\partial\dot{\rho}_o}{\partial q_{oi}}\Delta q_{oi} \qquad (9)$$

where

$\Delta\rho_{2\ S/C}$, $\Delta\dot{\rho}_{2\ S/C}$ are two spacecraft range and doppler residuals,

$\Delta\rho$, $\Delta\dot{\rho}$ are range and doppler residuals of the trailing spacecraft,

$\Delta\rho_o$, $\Delta\dot{\rho}_o$ are range and doppler residuals of the leading or reference spacecraft.

q_t and q_{o_t} are parameters that affect the trajectory of the trailing and reference spacecraft respectively, and they may be expressed as:

$$q_t = \begin{bmatrix} X \\ Y \\ P \end{bmatrix} \qquad q_{o_t} = \begin{bmatrix} X_o \\ Y_o \\ P_o \end{bmatrix}$$

where

X = state of the trailing spacecraft

X_o = state of the leading (reference) spacecraft

Y = dynamical parameters (such as unmodeled spacecraft accelerations, etc.) of the trailing spacecraft

Y_o = dynamical parameters of the leading spacecraft

P = nondynamical parameters (such as station locations, etc.) of the trailing spacecraft

P_o = nondynamical parameter of the leading spacecraft.

The procedure for data processing and differencing may be seen from Fig. 6. The computer program "DIFFER" differences the two data files (ACCUME) and creates new data types as defined by Eq. (9). The names of state and other dynamical parameters of the reference spacecraft (X_o, Y_o) in the new data file (REGRES) are changed to 'X1', 'Y1' ... 'ATAR1' ... etc. that are different from the corresponding parameters of the second spacecraft. Calibrations for transmission media effects and other types of adjustments are applied to the "computed" observables during the differencing. Thus they should not be applied to the new data file later during differential corrections using dual spacecraft data.

In the previous analysis (Ref. 2), the six state parameters of the reference spacecraft were not estimated, but their errors were considered. Results of the analytical expansions suggest that both spacecraft should be estimated in the presence of large ephemeris error. In this study the referenced spacecraft was first considered and then estimated.

When the state of the referenced spacecraft X_o is considered, the covariance (considered) from the solution of the best estimate using flyby or long arc conventional data should be used as the *a priori* covariance for X_o. The cancellation of station location errors in dual spacecraft tracking depends on the knowledge of the relative locations at each complex. According to the results of geodetic survey and short baseline VLBI[1] determinations, the current station location coordinates used in the orbit determination program are accurate to better than 15 cm in relative locations within a site. This information may be incorporated into the *a priori* covariance for the desired cancellation of station location errors. The correlations between near-by stations used in this analysis may be shown by the following matrix

	$r_{s_{11}}$	$r_{s_{14}}$	λ_{11}	λ_{14}	$\dot{r}_{11}$	$\dot{r}_{14}$
	2.25D-6	2.448875D-6	0	0	0	0
	0.99944	2.25D-6	0	0	0	0
	0	0	9.D-10	8.995D-10	0	0
A priori values	0	0	0.99944	9.D-10	0	0
	0	0	0	0	2.25D-4	2.24995D-4
	0	0	0	0	0.999978	2.25D-4

Correlations are shown in the lower left triangle, and

$r_{s_{11}}, r_{s_{14}}$ = distance off spin axis of DSS 11 and DSS 14 in km

$\lambda_{11}, \lambda_{14}$ = longitude of DSS 11 and DSS 14 in degrees

IV. Results and Discussion

The orbit period of the Viking 1 spacecraft is about one day and 37 minutes. The current gravity model for Mars has difficulty in fitting the Doppler data longer than one revolution. Even for a two revolution continuous fit, the linearized residuals are considerably larger than that of the single revolution fit. The large residuals due to gravity anomalies will eventually corrupt the estimate of the second spacecraft through the two spacecraft data. This effect may be minimized by data processing strategies or stochastic models, etc. Two different attempts were tried in processing these 8-day dual spacecraft data.

A. Reference Spacecraft is Considered

In the first attempt, the reference trajectory which consists of 8 revolutions of the orbiter was obtained from the Viking Flight Path Analysis Group (Ref. 5). Each revolution was fitted individually with 1-1/2 hours of data before and after the periapsis passage deleted. These 8 orbits of data were combined by allowing small discontinuities ($\Delta r \approx 1$ km, $\Delta \dot{r} \approx 1$ m/sec) between revolutions. This pseudo continuous best fit orbit was used as the reference orbit. Then the two-spacecraft data were generated by differencing the data from the orbiter and the data from the second spacecraft. The B-plane predictions based on the two-spacecraft data and the conventional

[1] Very long baseline interferometry

data of the same data arc were plotted in Fig. 7. Compared with the current best estimate (CBE), the predictions using two-spacecraft data had no improvement over the conventional data. According to the charged particle calibration studies (Ref. 6), most of the 1100 km error was caused by the relatively high solar plasma noise present in the 8 days of conventional data. It seems to imply that the plasma effect was not removed by differencing. A careful investigation of the Doppler residuals of both trajectories helped to discover that significant noise due to solar plasma exists in the data of the second spacecraft, but does not exist in the after-fit residuals of the orbiter. This is true particularly on August 2 when the solar noise caused a range change of about 10 m in less than 6 hours (Fig. 8). The resulting effect in doppler is as large as 16 mHz with a 8.5-mHz bias in that pass of data from the second spacecraft. While in the same pass of data of the reference spacecraft the bias is −2.2 mHz. It strongly suggests that the single revolution fit of the orbiter data absorbed the plasma noise, thus there is little or no cancellation during the differencing. When this particular pass of data was deleted, the B-plane prediction using two spacecraft data moved closer to the CBE by 600 km. This seems to confirm the above speculation. Therefore, we may conclude that for this particular case this is not the proper procedure to process 2-spacecraft data. The large plasma effects, which occurred during the last few days of the approach phase, have made this demonstration very rewarding.

The experience gained in the first attempt suggests that differencing of the two data types should take place before the orbit-by-orbit differential corrections of the reference spacecraft. In other words, the two spacecraft should be estimated simultaneously using differenced dual spacecraft data to prevent the absorption of plasma signature by the single orbit fit.

B. Both Spacecraft are Estimated

In the second attempt, the 12 state parameters of the two spacecraft were estimated by treating the state of the reference spacecraft, the orbiter, as nondynamic stochastic parameters. The batch size is equal to the orbit period with zero correlation time. This procedure removes unmodeled gravity errors in the same manner as the single revolution fit. The orbiter data were first processed with a continuous 8-day or 8-revolution nominal trajectory with reasonably good initial conditions. Then the two-spacecraft data were differenced, and the common plasma noise was expected to cancel. The residuals of the differenced data were still considerably large (10th to 100th of a hertz) due to the inadequacy of the gravity model for a longer time span. This would be refined by the sequential estimation of the state of the first spacecraft as mentioned earlier. It was found that this method of data processing had not only successfully removed the plasma noise but had also effectively taken care of the unmodeled accelerations caused by the Mars gravity field.

As mentioned earlier, the Viking 2 target plane (B-plane) prediction based on 8 days conventional doppler and range was badly corrupted by solar plasma effects and the error was as large as 1100 km. After the second attempt of processing the two-spacecraft data, as described in the above paragraph, the plasma noise was largely removed and the new data type which covers the same 8-day arc gave a B-plane prediction only 170 km away from the post MOI best estimate (Fig. 9). This nearly seven-times improvement in accuracy using actual two spacecraft tracking data is consistent with the results from earlier simulation analysis (Ref. 2), and it clearly reveals the potential capability of this new data type.

A series of B-plane predictions based on various combinations of data weights and data types were tried. The three predictions based on two spacecraft data shown by triangles in Fig. 9 represent three different data combinations. The one that has best agreement with the CBE is from the solution weighting the two spacecraft doppler at 0.015 Hz (1 mm/s) and two-spacecraft range at 20 m. When loosely weighted conventional data (doppler at 0.15 Hz and range at 1 km) are included, the change in the B-plane prediction is small. However, as the data weight of the conventional doppler is increased, the solution moves away from the CBE and agrees better with the solution using conventional data alone. This is because the plasma noise which is present in conventional data will start to show its effect when such data are relied on more heavily. When the two spacecraft range is deweighted by a factor of 10 (to 200 m), the prediction using two spacecraft doppler and range moved slightly away from the CBE. The agreement is still better than 300 km. The linearized residuals of the differenced two spacecraft doppler with 10-min count time are reasonably small with pass-by-pass noise of about 0.003 to 0.004 Hz.

It is also important to examine the time history of B-plane improvements of using the new data type. Figure 10 shows the comparison of B-plane prediction between long and short arc solutions of conventional data and the short arc solutions of dual spacecraft data. This comparison clearly demonstrates the following facts:

(1) The short-arc dual spacecraft solutions are linearly converging to the current CBE. This shows the stability of the new data type.

(2) At one day before the final MOI delivery, dual spacecraft data give more accurate prediction than conventional data.

(3) Dual spacecraft tracking has the potential of significantly reducing DSN tracking time requirements.

Therefore, one may conclude that with limited data the two spacecraft tracking technique is able to improve the navigation accuracy by nearly a factor of 7 in the presence of significant space plasma noise and under the unfavorable geometry of low declination. The insensitivity to ephemeris errors cannot be demonstrated by comparing with the standard Viking solutions because of the accurate knowledge of Mars ephemeris ($\lesssim$ 30 km). To enhance our understanding of this capability, a large error was introduced to the Mars ephemeris and the results will be discussed next.

C. Improvements Under Simulated Mars Ephemeris Error

An actual error of about 2000 km in Mars position (1000 km in range, 1000 km downtrack and 1500 km out of plane), which is about the current uncertainty of the planet Saturn, was introduced in the ephemeris (DE84) by Newhall (Ref. 5). Then the data from the Viking approach phase (same 8 day arc) were processed in the same way as the second attempt; i.e. both spacecraft were estimated. Large residuals were induced both in doppler data (100th to 10th of a hertz) and in range data (70 km in Viking B spacecraft and 1000 km in Viking A spacecraft) as a result of the 2000 km ephemeris error. The resulting B-plane error after fitting the 8 days of conventional data (state only) is as large as 11,000 km using doppler only and 20,000 km with range included. When Mars ephemeris parameters are estimated, the errors become even larger. This is believed to be due to the fact that this 8-day arc which ends 3 days away from Mars encounter does not have enough information to estimate the 12 extra ephemeris parameters. The differenced two-spacecraft data together with loosely weighted conventional doppler helped to bring the B-plane prediction to within 400 km of the CBE as seen in Fig 11. Two other solutions using two spacecraft data are all less than 800 km away from the best estimate. The linearized residuals of the two spacecraft data are as small as that of the previous case without the large ephemeris error. This more than 10 times improvement both in B-plane predictions as well as in data noise clearly shows the insensitivity of the two-spacecraft data to large ephemeris error. This particular advantage of two-spacecraft navigation will be very useful for future missions to the outer planets with large ephemeris errors such as Saturn, Uranus, etc.

V. Conclusions

The potential improvements in navigation capability of dual spacecraft tracking have been successfully demonstrated using Viking approach data. Under unfavorable conditions of low SEP, low declination and large Earth-spacecraft distance, the dual spacecraft tracking technique improved the Viking 2 approach accuracy, by a factor of 7, to less than 200 km at MOI-2 days. Results also reveal the potential reduction of tracking time requirements during planet approach. The 8-day solution of dual spacecraft tracking yields slightly better B-plane prediction than the 40-day solution of conventional data. From the results of the analytical expansion and the Viking demonstration with a large intentional Mars ephemeris error, we are able to conclude that dual spacecraft data types are insensitive to ephemeris error.

VI. Recommendations for Further Study

As a result of this analysis, the following recommendations are proposed:

(1) Examine the potential benefits of dual spacecraft tracking for future missions involving two spacecraft.

(2) Conduct demonstrations of dual spacecraft tracking when the leading spacecraft is a flyby rather than an orbiter.

(3) The dual spacecraft 4-station doppler data type should be included in the demonstration.

(4) Modify and standardize the prototype software for operational use.

Acknowledgements

The author would like to give sincere thanks to J. Campbell, E. Christensen, J. Ellis, C. Hildebrand, X. Newhall, J. Ondrasik, G. Rinker, and H. Siegel for their help in the processing and analyzing of the Viking data.

Thanks are also due to R. Rudd and R. Hastrup for their effort in extending tracking coverage for dual spacecraft study, and to S. Finley for programming support.

Special thanks to J. McDanell for many helpful discussions and suggestions.

References

1. Preston, R. A., "Dual Spacecraft Radio Metric Tracking," *DSN Progress Report*, 42-22, May/June, pp. 51-65.

2. Chao, C. C., V. J. Ondrasik, and H. L. Siegel, "Improvements in Navigation Resulting from the Use of Dual Spacecraft Radiometric Data," AIAA Paper 76-834 presented at the AIAA/AAS Astrodynamics conference held at San Diego, California, August 18-20, 1976.

3. Hamilton, T. W., and W. G. Melbourne, "Information Content of a Single Pass of Doppler Data from a Distant Spacecraft," in *The Deep Space Network*, Space Programs Summary 37-39, Vol. 3, pp. 18-23, JPL, May 31, 1966.

4. Rourke, K. H., et al., "The Determination of the Interplanetary Orbits of Viking 1 and 2," AIAA Paper 77-71 presented at the AIAA 15th Aerospace Science meeting held at Los Angeles, California, January 24-26, 1977.

5. Hildebrand, C. E., et al., "Viking Satellite Orbit Determination," AIAA Paper 77-70, presented at the AIAA 15th Aerospace Science meeting held at Los Angeles, California, January 24-26, 1977.

6. Yip, K. W., F. B. Wim, and S. C. Wu, "Viking 1 S/X Dual Doppler Demonstration," EM 391-53, July 28, 1976 (JPL internal document).

7. Newhall, X. X., private communication.

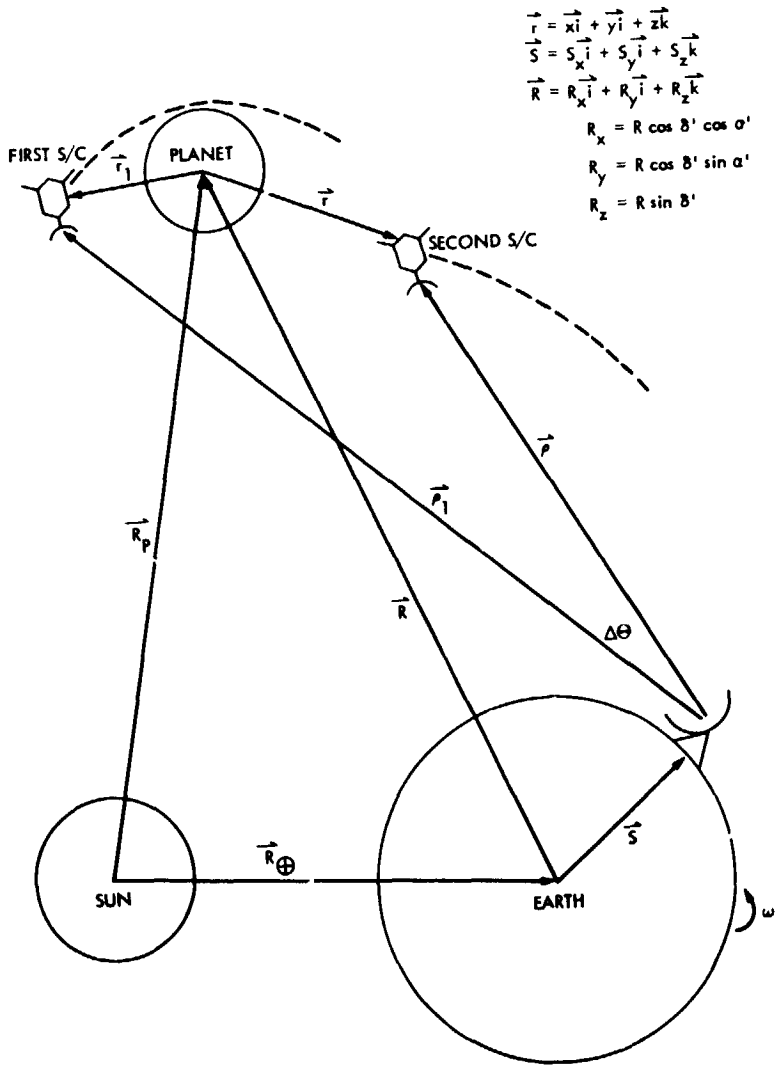

Fig. 1. Geometry of dual spacecraft fly-by of a planet

(a) ASSUMED SATURN EPHEMERIS ERRORS: Δr = 800 km, $\Delta\alpha = \Delta\delta$ = 1500 km at $\delta = 0^\circ$ and $\Delta\theta = 9^\circ$

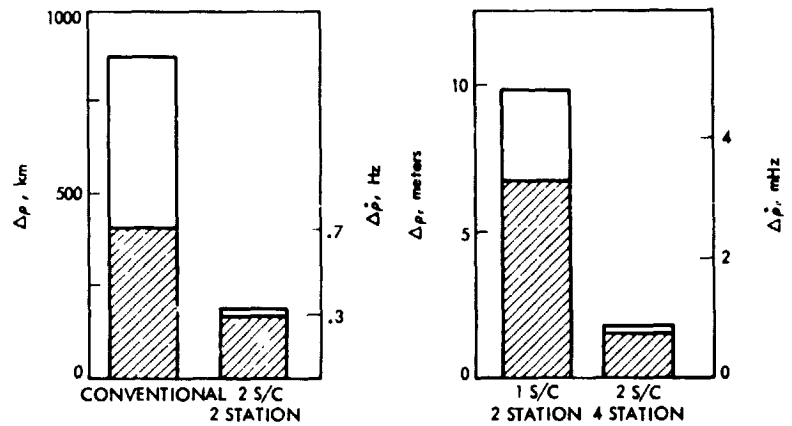

(b) ASSUMED STATION LOCATION ERRORS: Δr_s = 3 m, $\Delta\lambda$ = 5 m, Δz = 15 m, and ($\Delta\theta = 9^\circ$)

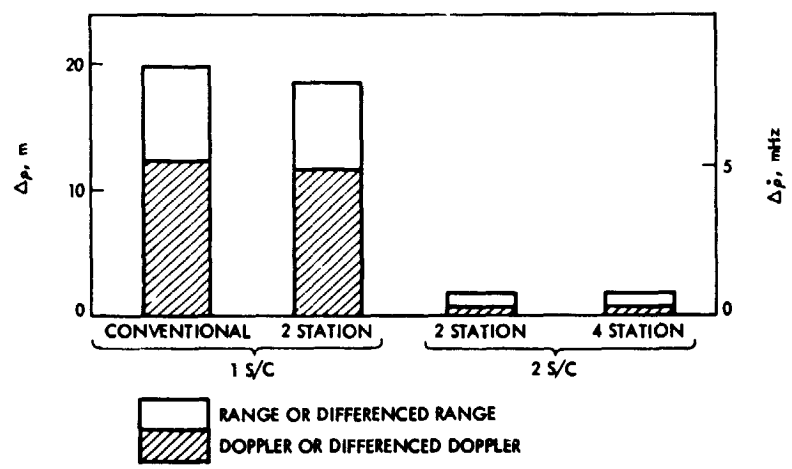

Fig. 2. Bias induced in observables due to assumed errors in ephemeris and station location

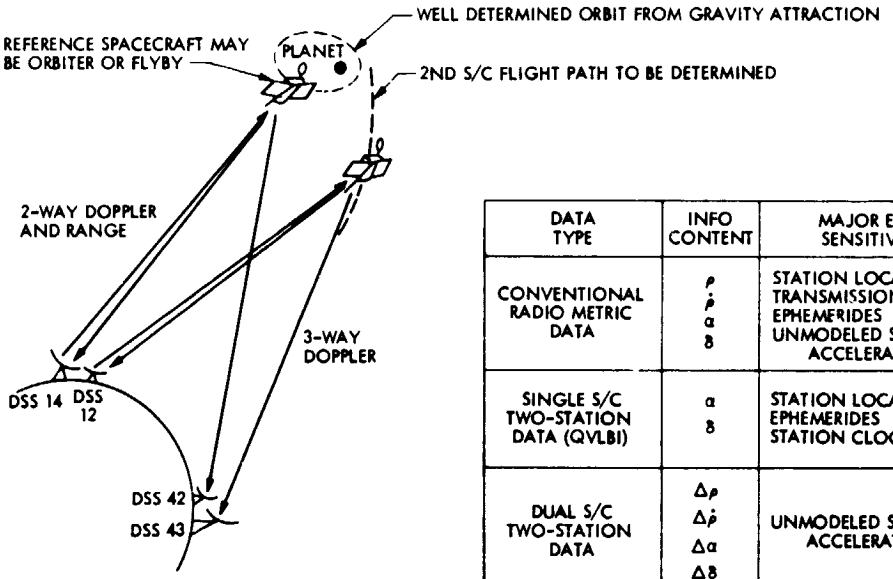

DATA TYPE	INFO CONTENT	MAJOR ERROR SENSITIVITIES
CONVENTIONAL RADIO METRIC DATA	ρ $\dot{\rho}$ α δ	STATION LOCATIONS TRANSMISSION MEDIA EPHEMERIDES UNMODELED SPACECRAFT ACCELERATIONS
SINGLE S/C TWO-STATION DATA (QVLBI)	α δ	STATION LOCATIONS EPHEMERIDES STATION CLOCKS
DUAL S/C TWO-STATION DATA	$\Delta\rho$ $\Delta\dot{\rho}$ $\Delta\alpha$ $\Delta\delta$	UNMODELED SPACECRAFT ACCELERATIONS
DUAL S/C FOUR-STATION DATA	$\Delta\alpha$ $\Delta\delta$	NONE

Fig. 3. Dual spacecraft tracking concept and data types

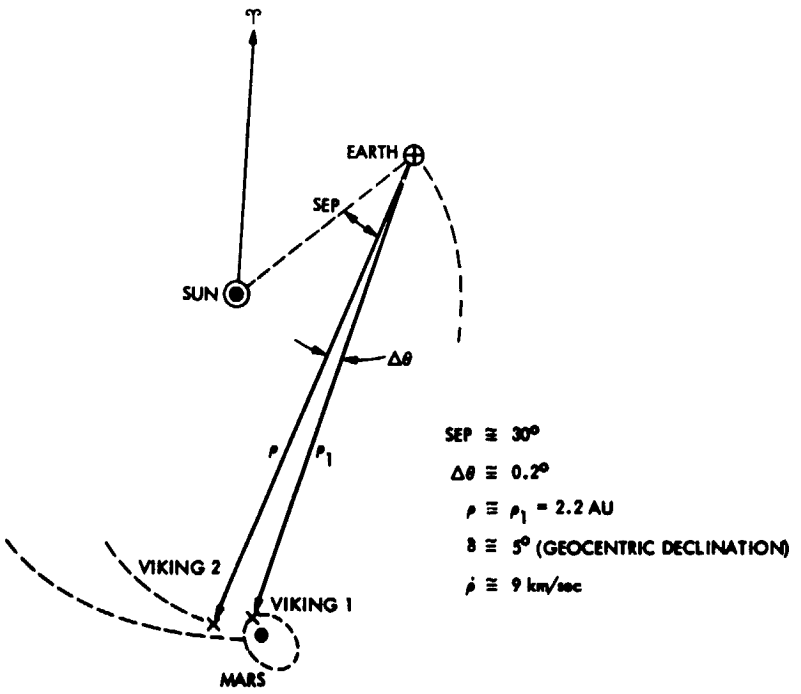

Fig. 4. Projection of approximate heliocentric trajectories in ecliptic plane during the approach of Viking B spacecraft

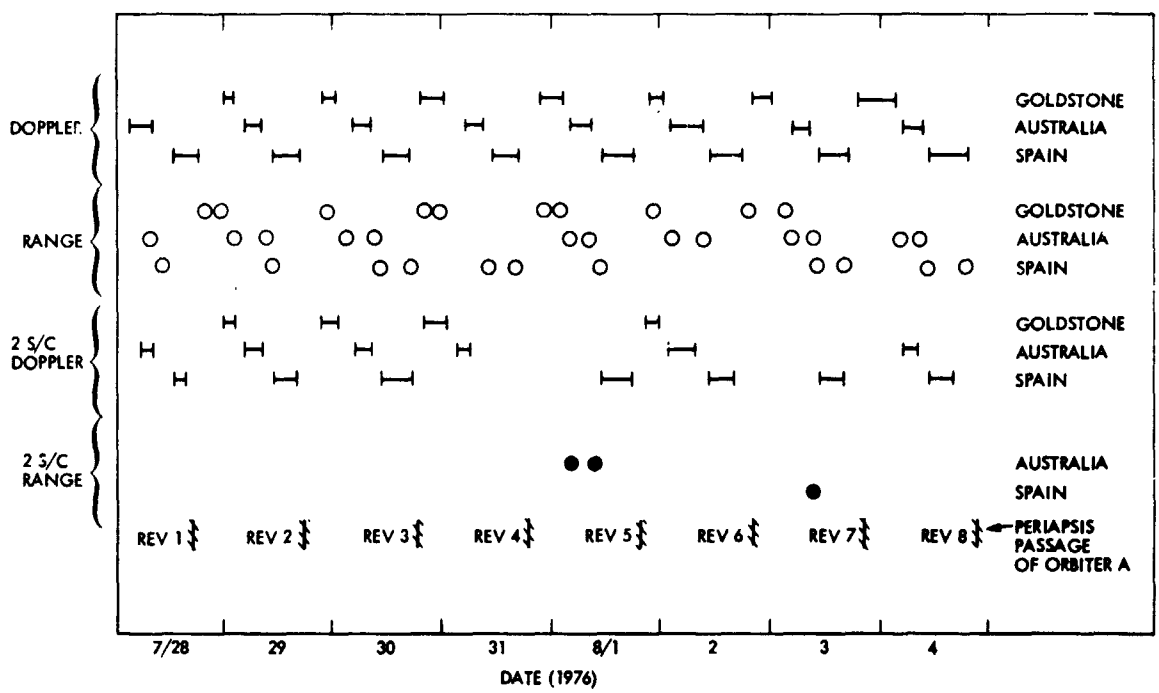

Fig. 5. Data distribution of dual spacecraft and conventional data types

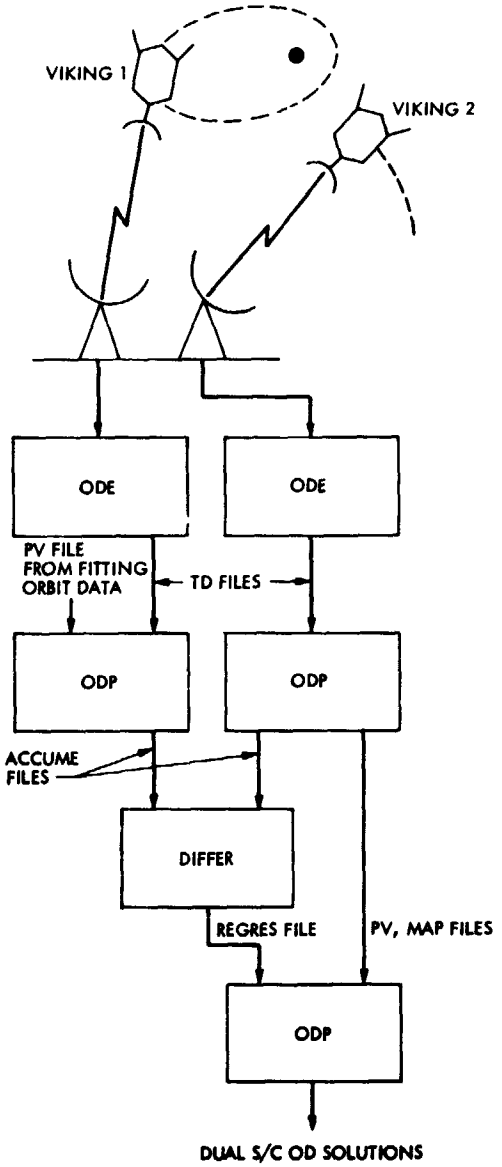

A MODIFIED VERSION OF ODE MAINTAINS DOPPLER SIMULTANEITY AFTER DATA EDITING AND COMPRESSION

STANDARD ODP COMPUTES OBSERVABLES PV FILE, PARTIAL DERIVATIVES AND ATMOSPHERE CALIBRATIONS

DIFFERENCE 2 S/C DATA AND USE 'X1', 'Y1' . . . AND 'ATAR1' . . . FOR PARAMETERS OF THE REFERENCE S/C

ATMOSPHERE CALIBRATIONS SHOULD NOT BE APPLIED HERE

Fig. 6. Dual spacecraft orbit determination software interfaces

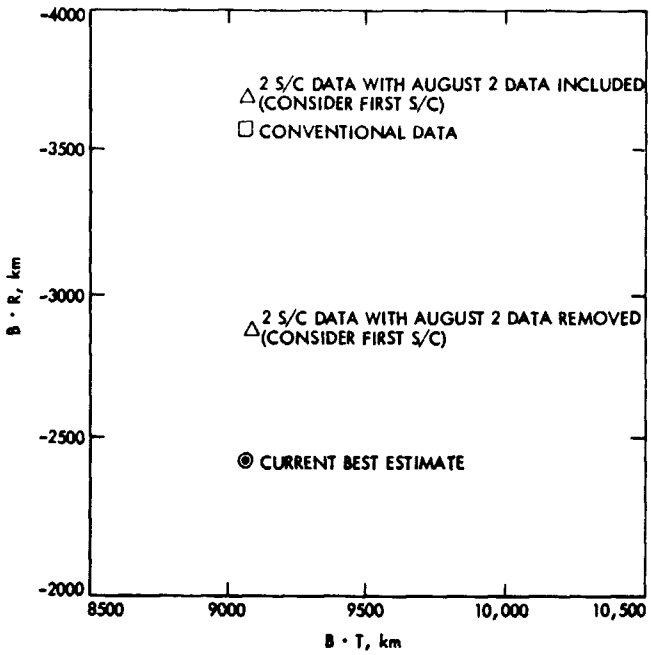

Fig. 7. Viking 2 B-plane predictions at MOI-3 day with 8 days of data

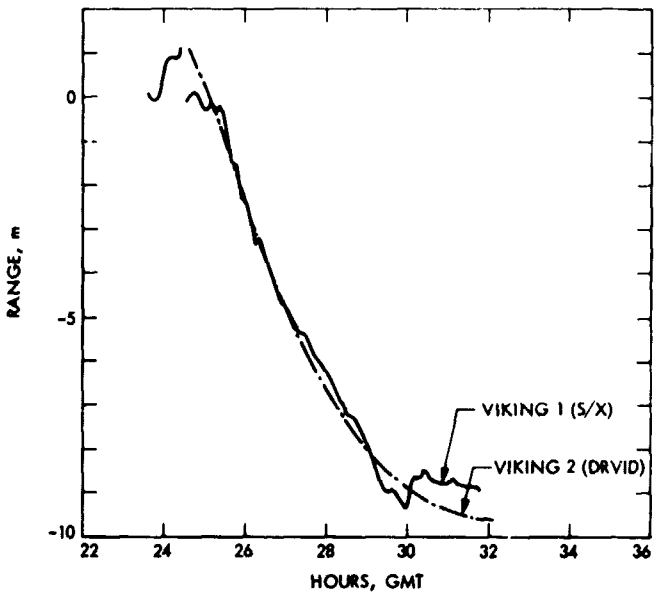

Fig. 8. One-way range change due to charged particle effect on August 2, 1976

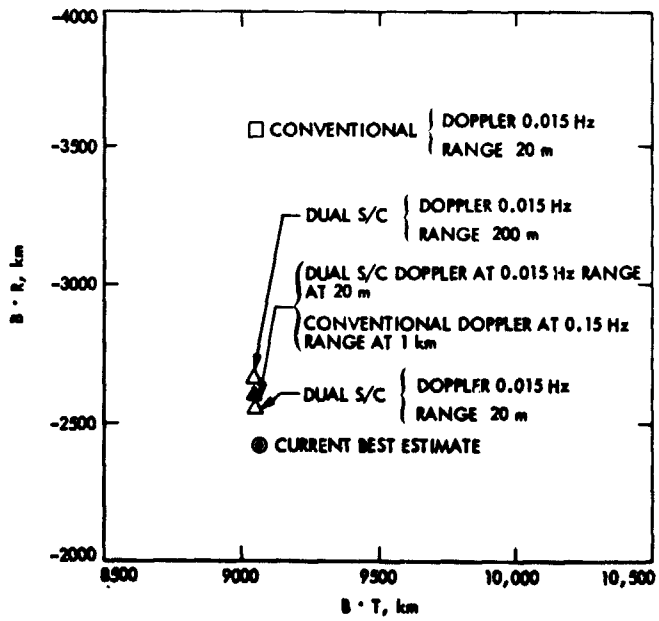

Fig. 9. Viking 2 B-plane predictions at MOI-3 day with 8 days of data

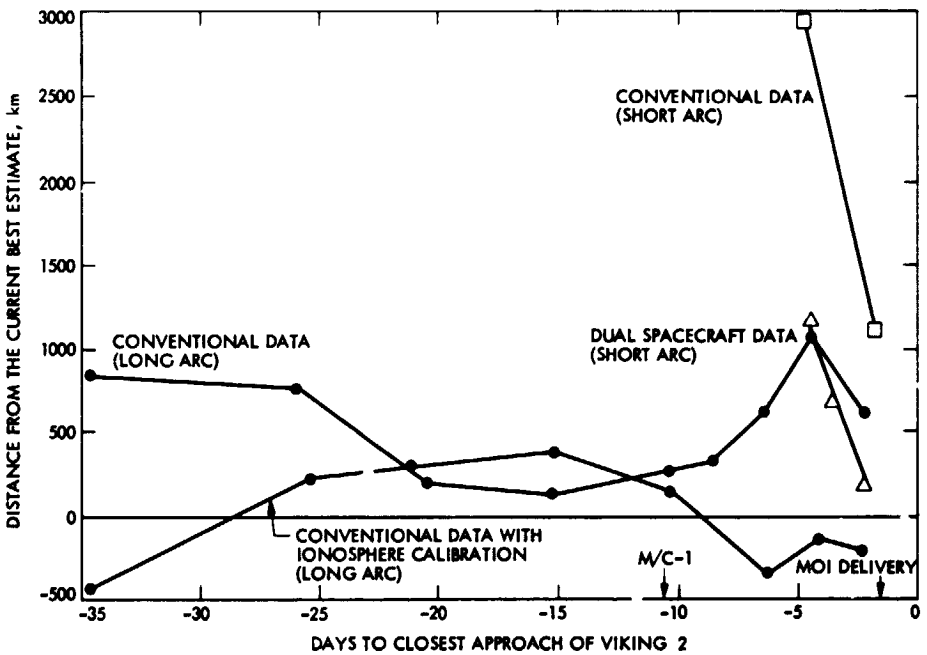

Fig. 10. History of navigation improvement from dual spacecraft tracking

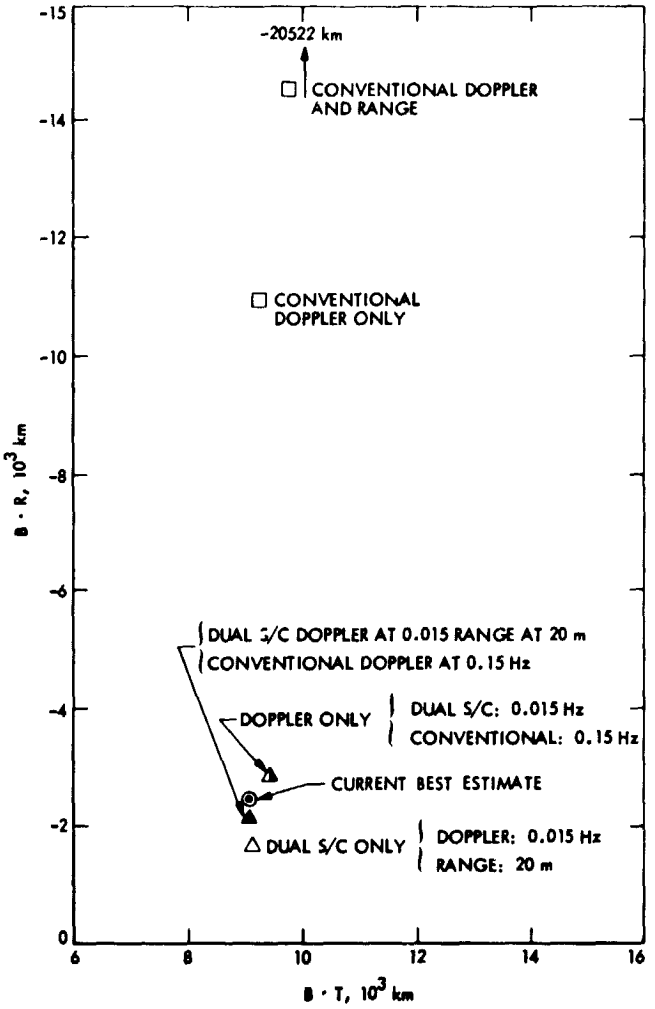

Fig. 11. Viking 2 B-plane predictions at MOI-3 day with 8 days of data in the presence of large ephemeris error (2000 km)

Frequency Selection and Calibration of a Water Vapor Radiometer

S. C. Wu
Tracking Systems and Applications Section

The calibration coefficients of existing water vapor radiometers are dependent upon meteorology profiles. This is shown to be due mainly to incorrect frequency pairs. By properly selecting an optimum frequency pair, the dependency can be reduced to a relatively small amount which can be handily adjusted by surface measurement alone. Hence, a universal calibration equation is applicable to all environmental conditions – site, seasonal and diurnal variations. Optimum frequency pairs are systematically searched. Error analysis indicates that calibration for the water vapor phase delay accuracy to <2 cm is possible at all elevation angles >15 degrees.

I. Introduction

Tropospheric water-vapor phase delay calibration by means of a ground based water-vapor radiometer (WVR) has long been desired. During the last several years, investigations of dual-frequency WVRs (Refs. 1,2) have been carried out. It has been demonstrated that under "ideal" weather conditions SMILE[1] (Ref. 1) provides a calibration to better than 2 cm for elevation angles down to 10 deg; under "adverse" weather conditions the error is 3 to 5 times worse. It was felt that probably no single set of calibration coefficients can be applied to all weather types.

The frequency pairs for the two radiometers are such that one channel is centered right at the water-vapor resonance frequency of 22.235 GHz, with the other channel centered at a frequency outside of the resonance band. For SMILE in Reference 1, the second frequency is 31.4 GHz, while for the Deep Space Network (DSN) prototype in Reference 2 it is 18.5 GHz. The frequency pairs so selected have the advantage of high sensitivity to the variation of water-vapor content. However, it will be seen in the following analysis that such frequency pairs have an undesirable high degree of dependence on meteorology profiles. This is due to the unequal contribution of the differential water-vapor phase delay along the ray path and to the lack of means to correct for different weather types.

Menius et al. (Ref. 4) found that there exists a frequency on each side of the water-vapor resonance line at which the profile dependence is minimal. Gaut (Ref. 5) improved the dependence by linear combination of two or more frequencies. This approach is ideal when there is no cloud (liquid water droplets). The existence of cloud in the atmosphere may result in significant error in the inferred phase delay. In this paper, a *constrained* dual-frequency approach is adopted. The constraint is such that the radiations due to liquid water at the two frequencies cancel one another when linearly combined.

Minimizing the profile dependence is no more than equalizing the weight on each differential water vapor phase delay

[1] Scanning Microwave Inversion Layer Experiment Radiometer, a unit similar to SCAMS (Ref. 3) but only two of the five channels are used.

along the ray path. With such constant weight, the residual dependence of the calibration coefficients on the environmental conditions can be handily corrected for by surface measurement alone: the weight at the surface is factored out as an additional observable so that a set of universal calibration coefficients is applicable under all circumstances independent of site, season, profiles, and diurnal variation.

II. Weighting Function

The phase delay due to water vapor is

$$\Delta\rho = k \int_0^\infty \frac{\sigma}{T} dS, \quad k = 1.723 \times 10^{-3}\ \mathrm{K/(g/m^3)} \quad (1)$$

where σ and T are the density and temperature of water vapor along the ray path S. On the other hand, the brightness temperature of a ground-based radiometer at a frequency f due to the same water vapor, to oxygen and to cloud is

$$T_B = T_c e^{-\tau_\infty} + \int_0^\infty T \alpha e^{-\tau} dS \quad (2)$$

where

$$\tau_\infty = \int_0^\infty \alpha\, dS$$

is the opacity of the atmosphere,

$$\tau = \int_0^S \alpha\, dS$$

T_c is the cosmic noise of ~ 2.9K and α is the total absorption coefficient of the constituents along the ray path, $\alpha = \alpha_v + \alpha_0 + \alpha_l$, with v, o and l denoting the water vapor, the oxygen and the liquid water respectively.

For a dual-frequency radiometer, the two brightness temperatures are

$$T_{B,1} = T_{c,1} + \int_0^\infty T\alpha_1 e^{-\tau_1} dS$$
$$T_{B,2} = T_{c,2} + \int_0^\infty T\alpha_2 e^{-\tau_2} dS \quad (3)$$

where the attenuated cosmic-noise terms have been replaced by two constants $T_{c,1}$ and $T_{c,2}$. This is valid since $T_c \ll T_B$ and the opacity $\tau_\infty \ll 1$ for frequencies $f < 40$ GHz. In this frequency range, the absorption coefficient of cloud α_c is proportional to f^2 (Ref. 6). Hence, from Eq. (3), we have

$$\frac{T_{B,1} - T_{c,1}}{f_1^2} - \frac{T_{B,2} - T_{c,2}}{f_2^2} = \int_0^\infty W(S) \frac{\sigma}{T} dS + T_0 \quad (4)$$

where

$$W(S) = \frac{T^2}{\sigma}\left[\frac{\alpha_{v,1}}{f_1^2} e^{-\tau_1} - \frac{\alpha_{v,2}}{f_2^2} e^{-\tau_2}\right] \quad (5)$$

and

$$T_0 = \int_0^\infty T\left[\frac{\alpha_{0,1}}{f_1^2} e^{-\tau_1} - \frac{\alpha_{0,2}}{f_2^2} e^{-\tau_2}\right] dS \quad (6)$$

By comparing Eqs. (1) and (4) it is obvious that $W(S)$ is a weighting function with which the incremental water-vapor phase delays are summed to a quantity proportional to the linear combination of the two brightness temperatures $T_{B,1}$ and $T_{B,2}$. A nonconstant $W(S)$ implies nonuniqueness of phase delay inferred by the linear combination of $T_{B,1}$ and $T_{B,2}$:

$$\Delta\rho = a_0 + a_1 T_{B,1} + a_2 T_{B,2} \quad (7)$$

In other words, the coefficients a_0, a_1 and a_2 are functions of the profile of σ/T. If $W(S) = W_m$, a constant, then Eq. (4) reduces to Eq. (7) with constant coefficients:

$$a_0 = \left[T_{c,2}/f_2^2 - T_{c,1}/f_1^2 - T_0\right] k/W_m$$
$$a_1 = k/f_1^2 W_m \quad (8)$$
$$a_2 = -k/f_2^2 W_m$$

III. Modified Weighting Function and Linearized Brightness Temperature

The weighting function defined in Eq. (5) may be constant at low air masses for which τ_1 and τ_2 are small. For high air masses, these quantities increase rapidly and the two terms in the bracket of Eq. (5) will decrease with S and hence $W(S)$ will

be lower at larger S. To maintain constant $W(S)$ it is desirable not to have such exponential terms in Eq. (5). This is possible if the brightness temperatures are "linearized"

The "linearized" brightness temperature is *defined* as

$$T'_B \equiv T_c \left(1 - \int_0^\infty \alpha\, dS\right) + \int_0^\infty T\alpha\, dS \qquad (9)$$

$$= T_c + \int_0^\infty (T - T_c)\,\alpha\, dS \qquad (10)$$

Following the procedures of the previous section, we arrive at the difference of the brightness temperatures in Eq. (10) for frequencies f_1 and f_2 respectively:

$$\frac{T'_{B,1} - T_c}{f_1^2} - \frac{T'_{B,2} - T_c}{f_2^2} = \int_0^\infty W'(S)\,\frac{\sigma}{T}\,dS + T'_0 \qquad (11)$$

where the weighting function is now modified to be

$$W'(S) = \frac{T(T - T_c)}{\sigma}\left[\frac{\alpha_{v,1}}{f_1^2} - \frac{\alpha_{v,2}}{f_2^2}\right] \qquad (12)$$

and where

$$T'_0 = \int_0^\infty (T - T_c)\left[\frac{\alpha_{0,1}}{f_1^2} - \frac{\alpha_{0,2}}{f_2^2}\right] dS \qquad (13)$$

This weighting function does not have the exponential terms as in Eq. (5). This implies that $W'(S)$ as defined in Eq. (12) is identical for all air masses; a constant $W'(S)$ for a zenith ray path will also be constant for lower elevation angles as long as homogeneity exists.

For a constant $W'(S) = W'_m$, Eq. (11) reduces to

$$\Delta\rho = a_0 + a_1 T'_{B,1} + a_2 T'_{B,2} \qquad (14)$$

with

$$a_0 = [T_c (f_2^{-2} - f_1^{-2}) - T'_0]\; k/W'_m$$

$$a_1 = k/W'_m f_1^2, \qquad (15)$$

$$a_2 = -k/W'_m f_2^2.$$

The T'_0 included in a_0 is a quantity proportional to the number of air masses. It is practically constant for small air masses the absorption coefficient of oxygen is proportional to $P^2 T^{2.85}$ (Ref 6), tropospheric P and T profiles can be represented by standard models with ±3% variation in P and ±10% variation in T. Hence the error in $T\alpha_0$ is within 27%. The proportionality of α_0 with frequency squared is better than 60%. Therefore, the quantity $T(\alpha_{0,1}/f_1^2 - \alpha_{0,2}/f_2^2)$, and hence T'_0, is constant to within 11%. This corresponds to <1 mm error in $\Delta\rho$ for a zenith ray path. For ray paths at low elevation angles adjustment is needed as will be described later.

In Eq. (14) it is the "linearized" brightness temperatures $T'_{B,1}$ and $T'_{B,2}$ that are used to infer the phase delay $\Delta\rho$ due to atmospheric water vapor. On the other hand, the quantities that are measured are the "saturated" brightness temperatures $T_{B,1}$ and $T_{B,2}$. Fortunately, T'_B can be calculated from T_B to high accuracy. Equations (2) and (9) can be rewritten as

$$T_B = T_c e^{-\tau_\infty} + T_{eff}(1 - e^{-\tau_\infty}) \qquad (16)$$

and

$$T'_B = T_c (1 - \tau_\infty) + T'_{eff}\,\tau_\infty \qquad (17)$$

where T_{eff} and T'_{eff} are effective temperatures in Eqs. (2) and (9) respectively, defined as

$$T_{eff} = \frac{\displaystyle\int_0^\infty T\alpha e^{-\tau}\, dS}{\displaystyle\int_0^\infty \alpha e^{-\tau}\, dS} \qquad (18)$$

and

$$T'_{eff} = \frac{\displaystyle\int_0^\infty T\alpha\, dS}{\displaystyle\int_0^\infty \alpha\, dS} \qquad (19)$$

T_{eff} and T'_{eff} are highly correlated and can be connected by $T_{eff} \doteq (1 + Q)\,T'_{eff}$, as will be seen later.

Eliminating τ_∞ between (16) and (17) yields

$$T'_B = T_c - (T'_{eff} - T_c)\ln\left(1 - \frac{T_B - T_c}{T_{eff} - T_c}\right) \qquad (20)$$

It is easy to show, for the case $Q = 0$ (i.e., $T'_{eff} = T_{eff}$), that a 10 K error in T_{eff} will result in only ~ 1 K error in T_B. This is also true for $Q \ll 1$. Hence T'_B can be calculated from T_B even with a T_{eff} not well estimated. Study indicates that T_{eff} can be estimated to better than 5 K from the surface temperature alone, as will be seen later.

IV. Optimum Frequency Search

In this section, frequency pairs for which $W'(S)$ remains nearly constant along the ray path are to be sought. Since water vapor concentrates almost exclusively at altitudes below 5 km, a nearly constant $W'(S)$ over only this altitude range is of concern. The searching labor can be reduced by first examining the two components of the weighting function in Eq. (12) separately. The pairs having similar variations with ray path can be picked out as possible candidates. The weighting functions $W'(S)$ for these candidates are then calculated for further comparison.

Another factor to be considered is the sensitivity of the inferred phase delay to the error in measured brightness temperatures. This can be shown to be inversely proportional to the magnitude W'_m: Let $\delta_{T'_B}$ be the error in $T'_{B,1}$ and $T'_{B,2}$. Then the error in $\Delta\rho$ from Eq. (14), assuming uncorrelated errors in $T'_{B,1}$ and $T'_{B,2}$, is

$$\epsilon_{T'_B} = (a_1^2 + a_2^2)^{1/2}\ \delta_{T'_B}$$

$$= \frac{k}{W'_m}\left(\frac{1}{f_1^4} + \frac{1}{f_2^4}\right)^{1/2} \delta_{T'_B} \equiv \beta\delta_{T'_B} \qquad (21)$$

Therefore, in selecting the optimum frequency pair, a compromise between constant $W'(S)$ and a minimum error factor $\beta \equiv kW'^{-1}_m (f_1^{-4} + f_2^{-4})^{1/2}$ has to be made. In other words, an optimum frequency pair will have constant as well as large $W'(S)$.

For the calculation, radiosonde measurement of the meteorology profiles at Point Mugu, California, on February 24, 1976, is selected arbitrarily. These profiles are shown in Fig. 1. It will be demonstrated later that for a specific frequency pair, the shape of weighting function is similar for different profile shapes. Hence it is sufficient to examine the profiles of only one radiosonde launch. The weighting function components $T(T - T_c)\alpha_v/\sigma f^2$ are calculated and plotted in Fig. 2 for frequencies within the range of 18.5 to 31.4 GHz. Any pair having equal vertical distance in Fig. 2 will have a constant $W'(S)$. It is obvious that the resonance frequency 22.235 GHz can only be paired with frequencies very close to itself, which would result in singularity (large $\epsilon_{T'_B}$ as indicated by Eq. 21). The pair having the largest and most constant vertical separation turns out to be 20.3 and 31.4 GHz. The higher frequency can be varied by ±2 GHz without appreciably affecting the results. Other possible pairs are 20.0/26.5 GHz, 24.5/31.4 GHz, etc.

The variations of the normalized weighting functions $[W'(S) - W'(0)]/W'(0)$ are plotted in Fig. 3 for these three candidates. The DSN prototype (22.235/18.5 GHz) and the SMILE (22.235/31.4 GHz) are also included for comparison. It is seen that the existing radiometers have large variation in $W'(S)$ and hence their calibration coefficients are profile-dependent.

The three frequency pairs selected have very similar shapes in $W'(S)$ which are constant to within 5% for all altitudes <5 km where most water vapor resides. The pair 20.3 31.4 GHz has a slightly better error factor β (as defined in Eq. 21) than the other two pairs, and the choices are heavily dependent upon hardware availability and simplicity. For instance, the pair 20.0/26.5 GHz is convenient since a common waveguide may be shared by the two channels.

To further demonstrate the above features, data from two more radiosonde launches are selected. These launches are carefully selected to represent two completely different weather conditions from the preceding analysis, a dry day (3/12/76) and a day with high-altitude water vapor concentration (3/16/76), again at Point Mugu. The profiles are shown in Figs. 4 and 5. The resulting weighting functions are plotted in Fig. 6. It is seen that the constancy of these weighting functions does not show any degradation under such extreme weather conditions. It is believed that with these frequency pairs the weighting functions will remain within a range ±10% of their surface values for all weather conditions.

V. Adjustments of Calibration Coefficients

It has been desired to have a simple means to adjust the calibration coefficients a_0, a_1 and a_2 in Eq. (15) to cover different ground altitudes as well as diurnal and seasonal variations of temperature. Having a constant $W'(S)$ along a ray path S implies that the adjustment factor, in this case the mean weighting function W'_m, is simply $W'(0)$, a quantity which can be calculated by surface measurement alone (cf Eq. 12). In practice, the adjustment can be avoided by factoring out the weighting function W'_m in Eqs. (14):

$$\Delta\rho = (b_0 + b_1 T'_{B,1} + b_2 T'_{B,2})/W'_m \qquad (22)$$

A set of nominal calibration coefficients b_0, b_1 and b_2 is determined by a constrain[2] linear least-squares fit[2] of Eq. (22) with actual measurement of $\Delta\rho$, $T'_{B,1}$, $T'_{B,2}$ and $W'_m = W'(0)$, the surface value of the weighting function. These coefficients are independent of W'_m and hence will remain constant under all conditions. When inferring $\Delta\rho$ from $T'_{B,1}$ and $T'_{B,2}$ of a dual-frequency radiometer, Eq. (22) is used with W'_m being the weighting function calculated from surface measurement only.

When the radiometer is making brightness temperatures measurement at more than one air mass, at extreme temperature and/or at an altitude different appreciably from where it was calibrated, the oxygen radiation term T'_0 included in b_0 (cf Eqs. 14, 15 and 22), will have to be corrected. A simple means to do this is to separate T'_0 from the cosmic-noise term $T_c(f_2^{-2} - f_1^{-2})$ and adjust T'_0 by the number of air masses m, the surface pressure P_S and the surface temperature T_S. The absorption coefficient of oxygen is proportional to $P^2T^{-2.85}$ (Ref. 6) and T'_0 in Eq. (13) is nearly proportional to $P^2T^{-1.85}$. Hence

$$b_{0,\,\text{corrected}} = [b_0 - kT_c(f_2^{-2} - f_1^{-2})]\, m(P_S/\bar{P})^2(\bar{T}/T_S)^{1.85} + kT_c(f_2^{-2} - f_1^{-2})$$

$$= G\,b_0 + T_c(G-1)(b_1 + b_2) \qquad (23)$$

where

$$G = m(P_S/\bar{P})^2(\bar{T}/T_S)^{1.85} \qquad (24)$$

with m being the air masses and $\bar{P}$ and $\bar{T}$ being the mean surface pressure and temperature of the radiosonde launches, which are used in the determination of b_0, b_1 and b_2 by the least-squares fit. b_1 and b_2 will remain fixed under all circumstances.

VI. Estimation of Effective Temperatures

An accurate calculation of "linearized" brightness temperature requires a sufficiently accurate (< 5 K) estimate of the effective temperatures defined in Eqs. (18) and (19). T'_{eff} in Eq. (19) is independent of the number of air masses while T_{eff} in Eq. (18) is larger for large m, due to lower weight (as compared to that for T'_{eff}) at higher altitudes where T is smaller. Study of 25 soundings from Point Mugu indicates that $T_{eff} \doteq (1 + 0.0009m)\,T'_{eff}$ with a standard deviation of ~0.06 K. Also found in analyzing these 25 soundings is the correlation between T'_{eff} and the surface temperature T_S: $T'_{eff} \doteq 0.950T_S$ for 20.0, 20.3 and 24.5 GHz, $T'_{eff} = 0.946T_S$ for 26.5 GHz and $T'_{eff} \doteq 0.940T_S$ for 31.4 GHz with standard deviations of < 3.5K. Another correlation found is that the errors in calculated T'_{eff} and T_{eff} are always in the same direction and nearly equal for the two frequencies used in a radiometer. This reduces the impact on the accuracy of the calculated range change through Eq. (22) since b_1 and b_2 have opposite signs. With the error in T'_{eff} and T_{eff} specified above, the error in $\Delta\rho$ will be ~ 0.2 cm for both frequency pairs at elevation angles down to $\gamma = 10°$. At higher elevation angles the error will reduce according to $1/\sin\gamma$.

VII. Demonstration of Phase Delay Determination

The same 25 soundings are used to determine the calibration coefficients b_0, b_1 and b_2 by least squares fitting Eq. (22) at $\gamma = 90°$. These are listed in Table 1 for the three optimum frequency pairs and for the pair 22.235/18.5 GHz of one of the existing WVR. In the least-squares fits the constraint $b_1/b_2 = -(f_2/f_1)^2$ has been enforced to explicitly remove the effect of cloud. This will not be needed if actual brightness temperatures (containing cloud effect) measured by a radiometer are used in place of calculated brightness temperatures (not containing cloud effect) from radiosonde profiles.

The calibration coefficients are used to calculate $\Delta\rho$ at zenith as well as at 10 deg elevation angle and then subtracted by the measured $\Delta\rho$ to indicate the error in the calculated $\Delta\rho$. These are summarized in Table 2. The same sets of calibration coefficients, which have been determined from Point Mugu data, are applied to 21 radiosonde launches at Edwards AFB, taken randomly over the whole year. The results are also shown in Table 2. The three optimum frequency pairs result in very similar solutions, which are all better than the 22.235/18.5 GHz pair by a factor of 4 to 6. The results at Point Mugu are somewhat overoptimistic since they are the result of forced fitting between the two sets of "measurements." On the other hand, the results at Edwards AFB are free from forced-fitting effect and are more objective. Hence, in the following error analysis, results at Edwards AFB only will be used.

The above errors are mostly due to nonconstant weighting functions, with a slight contribution from the imperfect effective temperature estimation. Other error sources which have to be considered in the WVR design include brightness temperature measurement error, elevation angle (antenna

[2] With the constraint $b_1/b_2 = -(f_2/f_1)^2$ to remove the effect of cloud.

pointing) error, and radiosonde measurement[3] error. The calculations of these error components are outlined in the Appendix. Figure 7 shows the $\Delta\rho$ error components for the four frequency pairs. The dominant error source for the existing WVR (22.235/18.5 GHz) is that due to nonconstant weighting function. With optimum frequency pairs this error source is reduced to an amount smaller than that due to radiosonde measurement. The total RSS errors in $\Delta\rho$ are compared in Fig. 8. The optimum systems have an RSS error of <2 cm for all elevation angles >15 deg. The existing system has an error >2 cm for elevation angles <42 deg.

The error source from radiosonde measurement can be reduced by using more launches in the determination of calibration coefficients. Currently the use of "two-color" (optical-radio) ranging system is under consideration as a perfect calibration standard in place of radiosonde. With such calibration standard, the error source marked RADIOSONDE in Fig. 7 is essentially zero. This improves the current system only slightly (being not a major error source), while it improves the optimum systems considerably (being a major error source).

[3]Radiosonde measurement is needed in the determination of calibration coefficients through least-squares fit, since accurate measurement of atmospheric absorption coefficients is not available.

VIII. Conclusion

Three frequency pairs have been found to have nearly constant weighting functions along a ray path. These are: 20.3/31.4 GHz, 20.0/26.5 GHz and 24.5/31.4 GHz. The 31.4 GHz can be varied by ±2 GHz and the 26.5 GHz by ±1 GHz without appreciably affecting the results. The constancy of the weighting functions reduces WVR error in two respects: (1) it reduces the profile dependence of the calibration coefficients and (2) it makes possible accurate adjustment of coefficients by surface measurement alone to account for different environmental conditions (site, season, diurnal variation, etc.). With such weighting function constancy, a single set of universal calibration coefficients is applicable throughout.

With any of these optimum frequency pairs, a WVR is capable of inferring the tropospheric water-vapor phase delay to <2 cm accuracy for all elevation angles >15 deg. The accuracy can be further improved by using better calibration standard in place of radiosonde launches, e.g., an optical-radio ranging system.

References

1. Winn, F. B., et al., "Atmospheric Water Vapor Calibrations: Radiometer Techniques," *DSN Progress Report 42-32*, Jet Propulsion Laboratory, Pasadena, Calif., Apr. 15, 1976, pp. 38-49.

2. Slobin, S. D., and Batelaan, P. D., "DSN Water Vapor Radiometer Development – A Summary of Recent Work, 1976-1977," *DSN Progress Report 42-40*, Jet Propulsion Laboratory, Pasadena, Calif., Aug. 14, 1977, pp. 71-75.

3. Staelin, D. H., et al., "The Scanning Microwave Spectrometer (SCAMS) Experiment," *Nimbus 6 User's Guide*, Goddard Space Flight Center, 1975.

4. Menius, A. C., et al., "Tropospheric Refraction Corrections Using a Microwave Radiometer," Technical Staff Technical Memo, No. 19, ETV-TM-64-12, Pan American Airways. Nov. 16, 1964.

5. Gaut, N. E., "Study of Atmospheric Water Vapor by Means of Passive Microwave Techniques". Technical Report 467, MIT Research Laboratory of Electronics, Dec. 20, 1968.

6. Van Vleck, J. H., et al., "Atmospheric Attenuation," *Propagation of Short Radio Waves*, D. E. Kerr, ed., McGraw-Hill, 1951, Chapter 8.

Table 1. Calibration coefficients determined from 25 radiosonde launches at Point Magu, California

Frequency pair	b_0	b_1	b_2	β
22.235/18.5 GHz	0.814	0.184	−0.265	0.98
20.3/31.4 GHz	−1.13	0.419	−0.175	0.82
20.0/26.5 GHz	−0.945	0.432	−0.246	1.35
24.5/31.4 GHz	−0.455	0.289	−0.176	0.97

b_0 is in $(10^{-5})K^2/(g/m^3)/(GHz)^2$

b_1 and b_2 are in $(10^{-5})K/(g/m^3)/(GHz)^2$

$\beta = (b_1^2 + b_2^2)^{1/2}/\overline{W}'_m$ is in cm/K

Table 2. Error in calculated $\Delta\rho$, assuming perfect radiosonde and T_B Measurement; calibration coefficients determined from Point Mugu Data

Frequency pair	Point Mugu (25 launches)		Edwards AFB (21 launches)	
	γ=90°	γ=10°	γ=90°	γ=10°
22.235/18.5 GHz	0.79 cm	4.39 cm	1.27 cm	6.90 cm
20.3/31.4 GHz	0.13	0.84	0.28	1.65
20.0/26.5 GHz	0.14	0.83	0.28	1.38
24.5/31.4 GHz	0.14	0.88	0.30	1.76

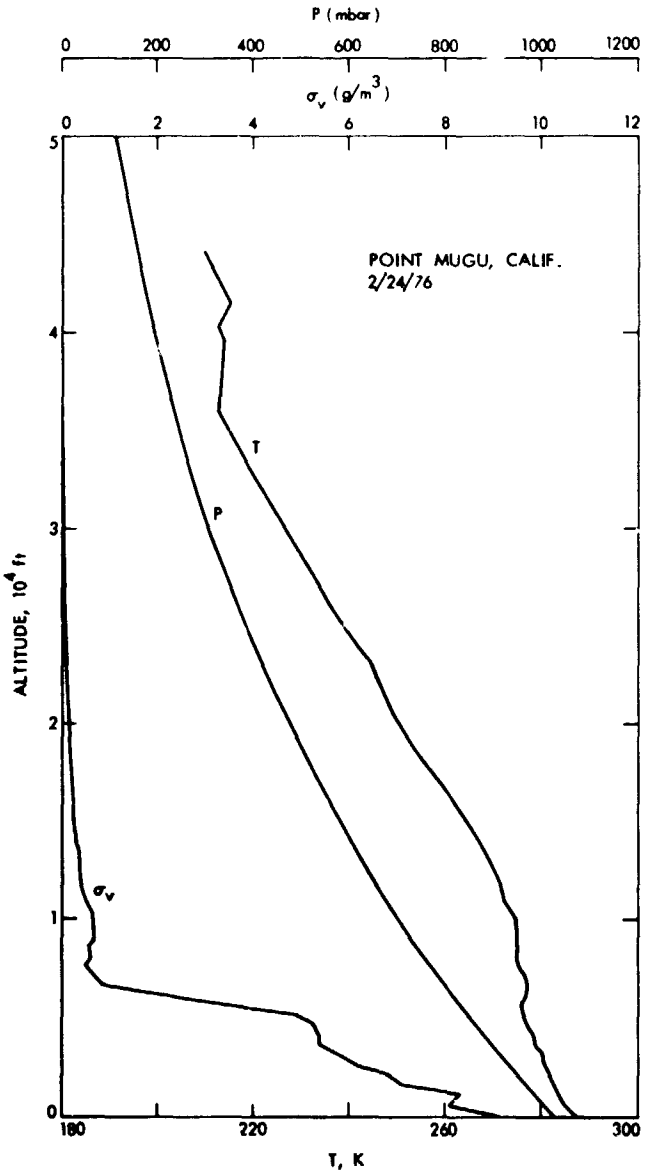

Fig. 1. Typical profiles of atmospheric temperature, pressure and water-vapor density

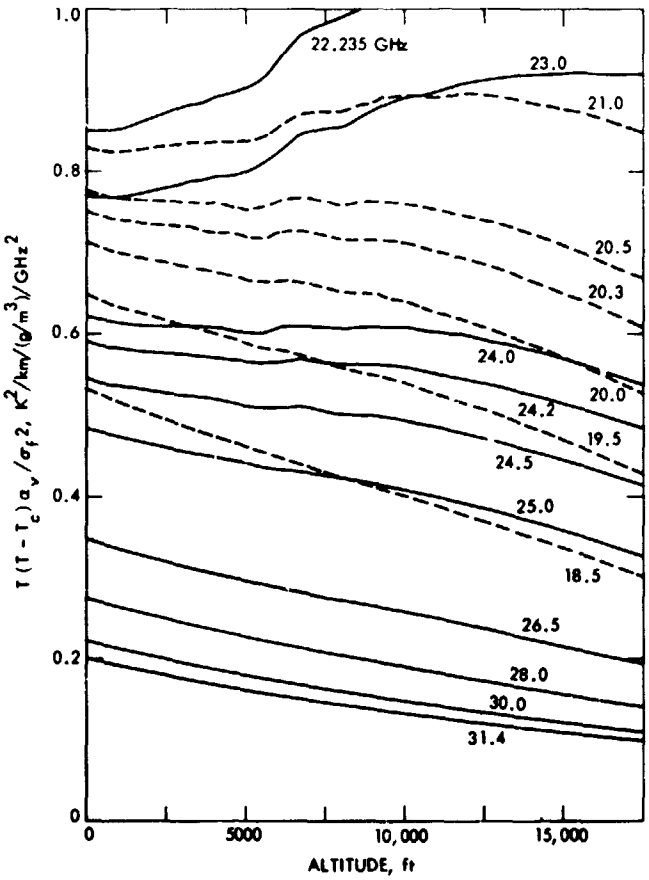

Fig. 2. Components of weighting functions for various frequencies

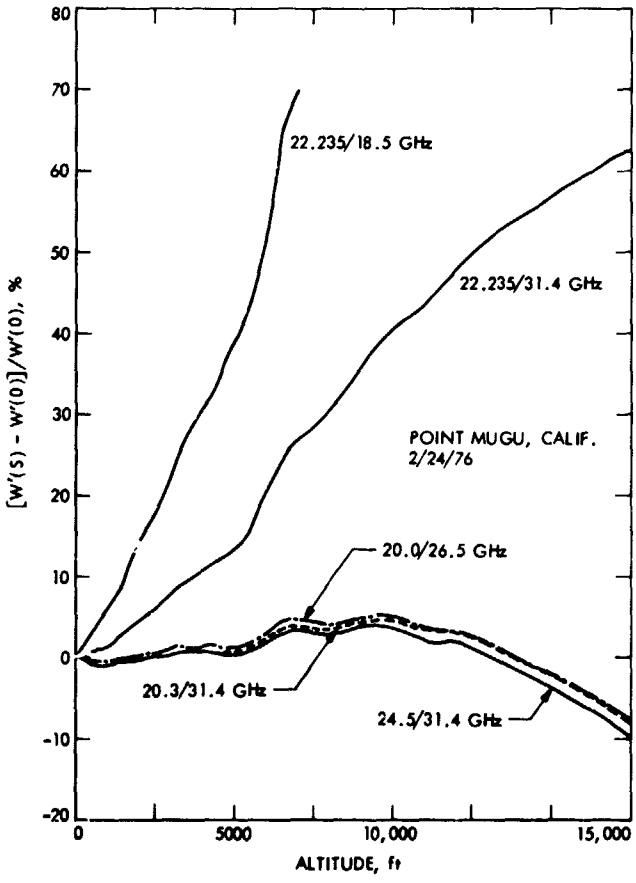

Fig. 3. Normalized weighting functions for various frequency pairs

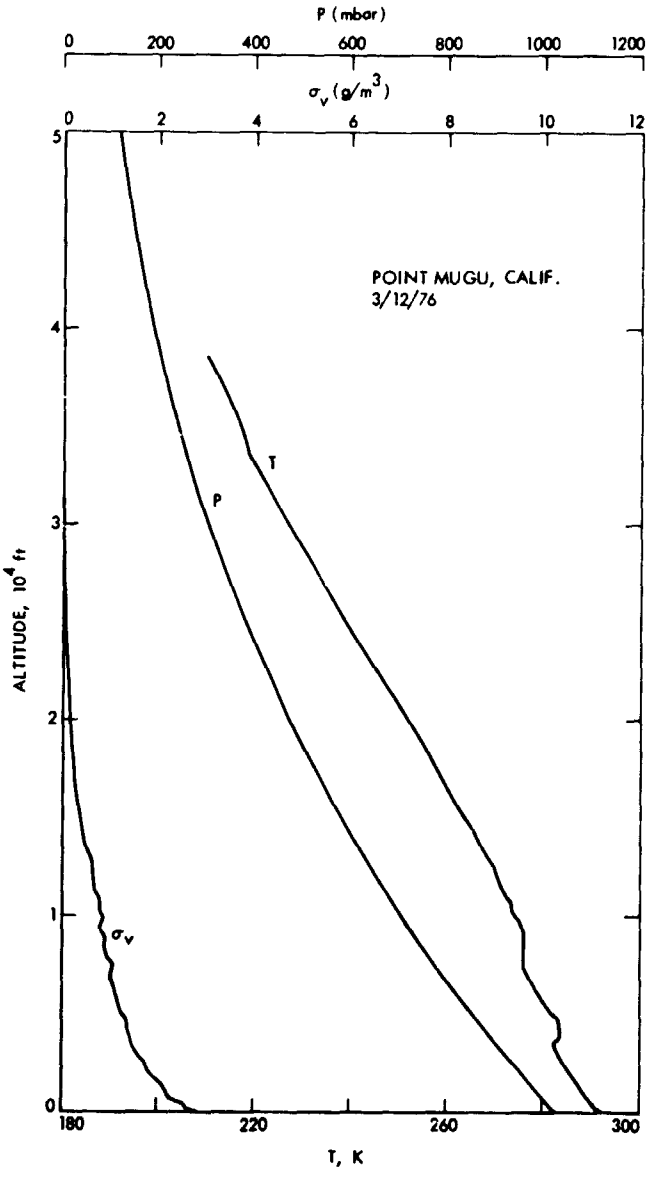

Fig. 4. Profiles of atmospheric temperature, pressure and water-vapor density for a dry day

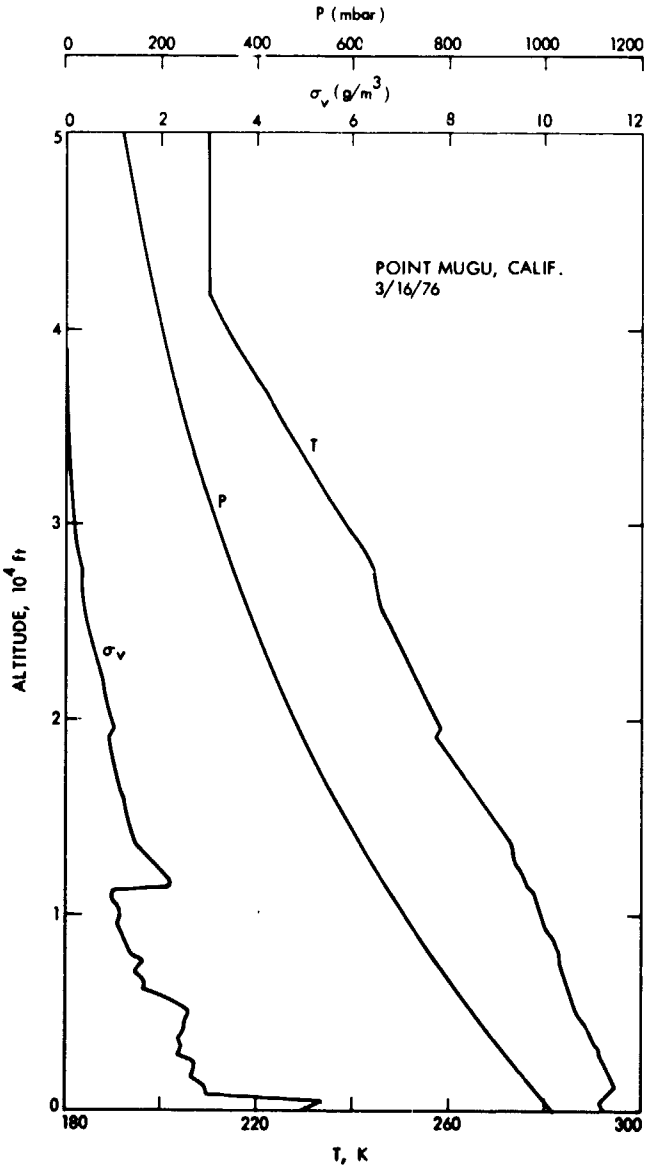

Fig. 5. Profiles of atmospheric temperature, pressure and water-vapor density for a day having high-altitude concentration of water vapor

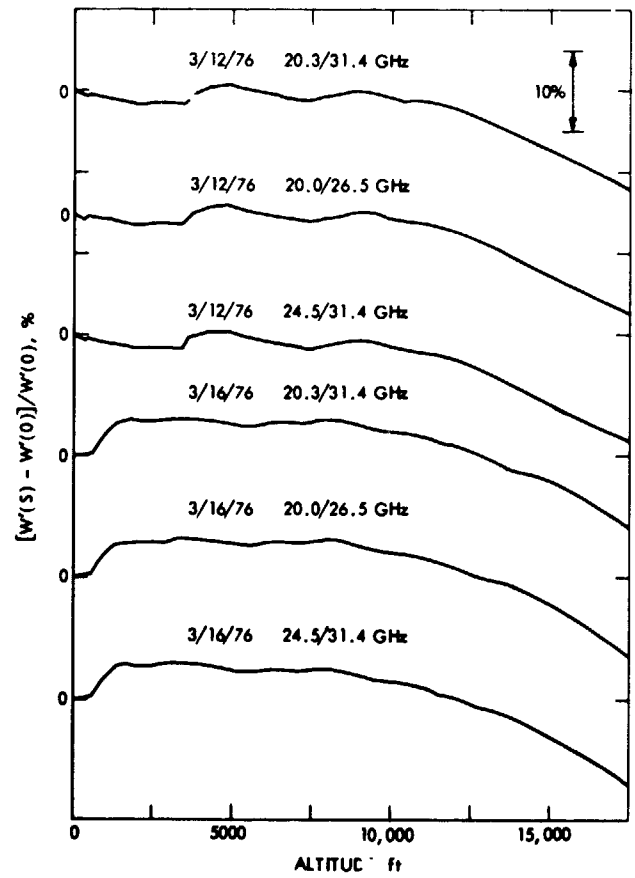

Fig. 6. Normalized weighting functions under extreme weather conditions

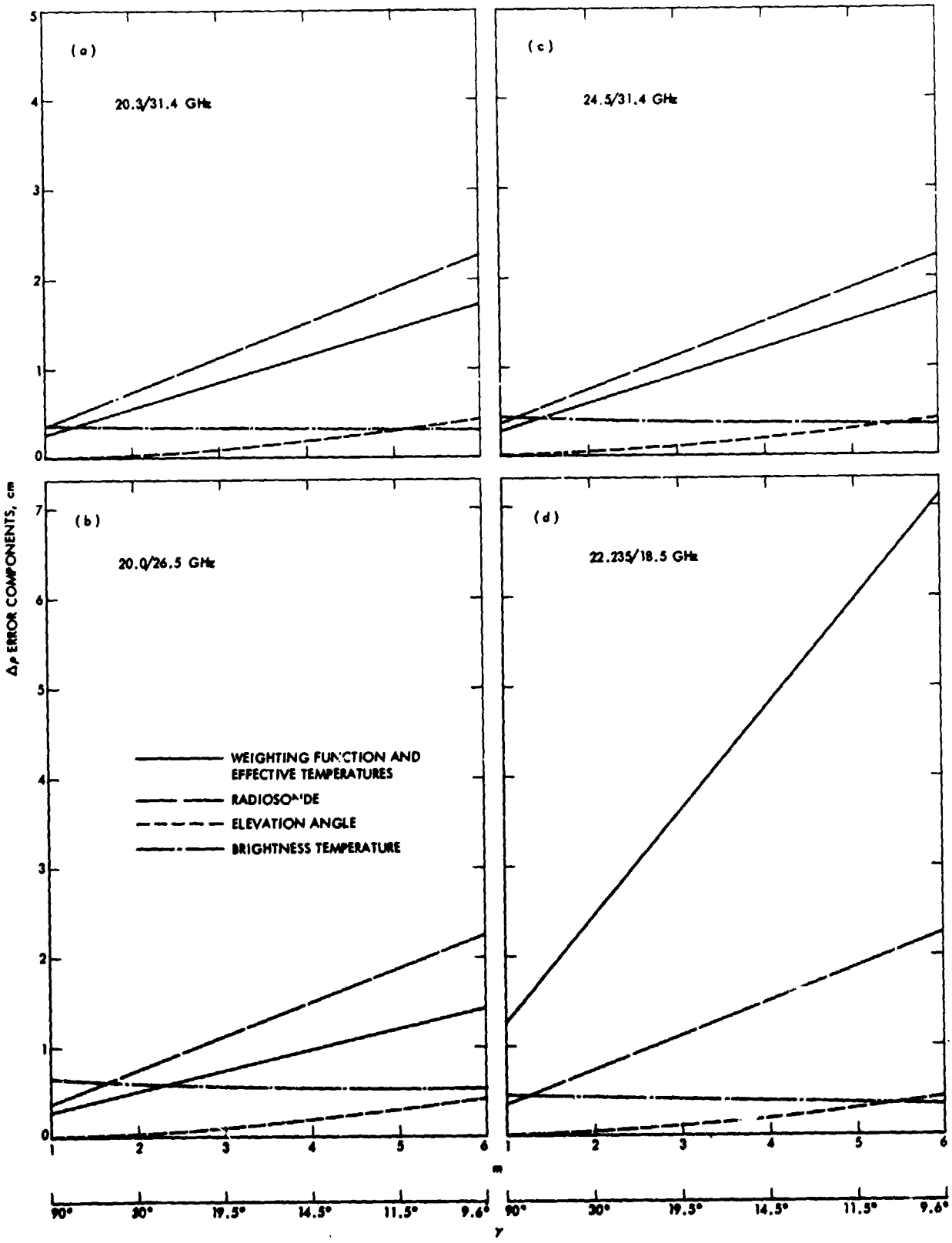

Fig. 7. Components of error in water-vapor phase delay inferred by a dual-frequency WVR

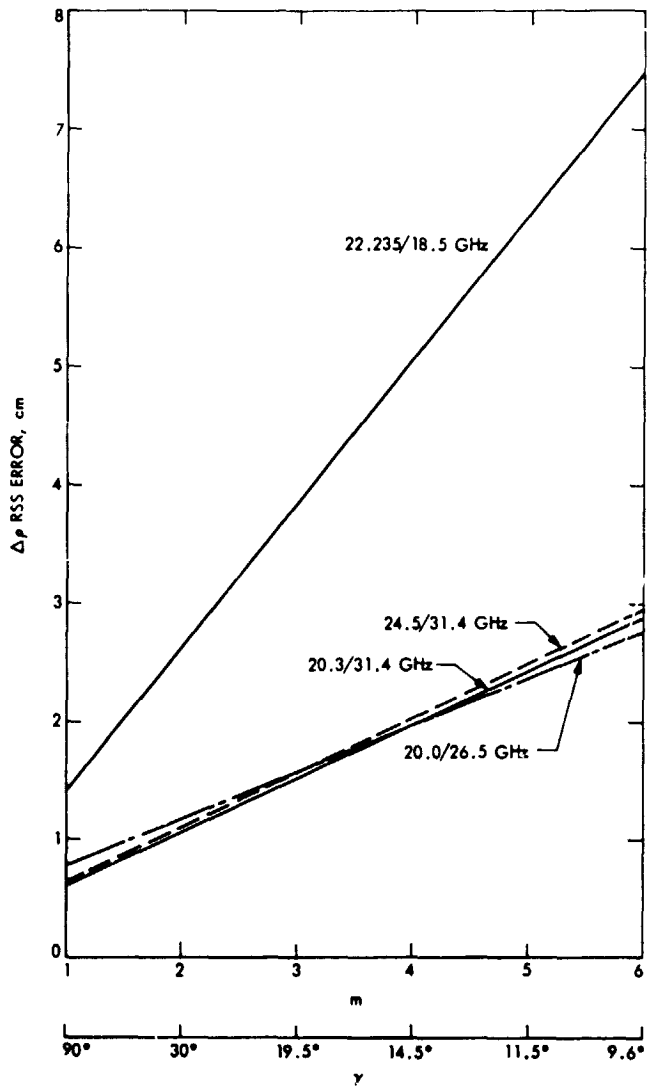

Fig. 8. Total RSS error in water-vapor phase delay inferred by a dual-frequency WVR

Appendix

Error Component Calculations

A. Nonconstant Weighting Functions and Imperfect Effective Temperatures:

The errors calculated in the last two columns of Table 2 (at Edwards AFB) using coefficients derived at Pt. Mugu are adopted with the assumption that they increase linearly with air masses between 1 and 6.

B. Radiosonde:

Assume: 1 cm random error in each launch (along zenith), increases with air masses (m).

$$\text{Number of launches} = n_l = 21$$

$$\text{Number of coefficients} = n_c = 3$$

$$\epsilon_{\text{radiosonde}} = 1.0\, m/(n_l/n_c)^{1/2}$$

$$= 0.378\, m \quad \text{(cm)}$$

C. Elevation Angle (Antenna Pointing):

Assume: Error in elevation angle $\epsilon_\gamma = 0.1°$. Zenith phase delay $\Delta\rho_z = 7$ cm (mean value of 46 soundings in Table 2).

$$\epsilon_{\text{elevation}} = \left| \frac{\partial}{\partial\gamma}\left(\frac{\Delta\rho_z}{\sin\gamma}\right) \right| \epsilon_\gamma$$

$$= (7\cos\gamma/\sin^2\gamma)\,(0.1\,\pi/180)$$

$$= 0.0122\, m(m^2 - 1)^{1/2}\,, m = 1/\sin\gamma$$

D. Brightness Temperature Measurement (T_B'):

Assume: Hot load has a nominal temperature $T_H = 450$ K with a long-term absolute uncertainty of ±1 K and a short term jitter of ±0.2 K. Ambient load has a nominal temperature $T_M = 300$ K with a long-term absolute uncertainty of ±0.5 K and a short-term jitter of ±0.1 K.

Calibration line equation:

$$T_B' = T_M + \frac{T_H - T_M}{N_H - N_M}(N_M - N_B)$$

where N's are the radiometer digital "counts."

$$\frac{\partial T_B'}{\partial T_H} = -\left(\frac{T_M - T_B'}{T_H - T_M}\right) = -\left(\frac{300 - T_B'}{150}\right)$$

$$\frac{\partial T_B'}{\partial T_M} = 1 + \left(\frac{T_M - T_B'}{T_H - T_M}\right) = \frac{450 \quad T_B'}{150}$$

The hot load long-term uncertainty is correlated to ambient load long-term uncertainty by using tipping curve so that (cf. Fig. A-1).

$$\sigma_H/\sigma_M = \frac{T_H - 2.9}{T_B - 2.9} = 1.5$$

$$\sigma_H = 1.5\,\sigma_M = 0.75 \text{ K}$$

The error in T_B' due to these correlated uncertainties is

$$\epsilon_c = \left| \frac{\partial T_B'}{\partial T_H}\sigma_H + \frac{\partial T_B'}{\partial T_M}\sigma_M \right|$$

$$= \left| \frac{-(300 - T_B')}{150}(0.75) + \frac{450 - T_B'}{150}(0.5) \right|$$

$$= 0.25\, T_B'/150$$

The error in T_B' due to the uncorrelated jitter[4] in T_H and in T_M is

$$\epsilon_u = \left[\left(\frac{\partial T_B'}{\partial T_H}\,0.2\right)^2 + \left(\frac{\partial T_B'}{\partial T_M}\,0.1\right)^2\right]^{1/2}$$

[4] To reduce the effect of receiver gain drift it is necessary to repeat the "internal calibration" by looking at T_H and T_M once in a while.

$$= \left[\frac{(300 - T'_B)^2}{150^2}(0.2)^2 + \frac{(450 - T'_B)^2}{150^2}(0.1)^2\right]^{1/2}$$

$$= (0.05\,T'^2_B - 33\,T'_B + 5625)^{1/2}/150$$

The total error in T'_B is the RSS of ϵ_c and ϵ_u:

$$\epsilon_{c+u} = (\epsilon_c^2 + \epsilon_u^2)^{1/2}$$

$$= (0.1125\,T'^2_B - 33T'_B + 5625)^{1/2}/150$$

The calibration equation is (Eq. 22):

$$\Delta\rho = (b_0 + b_1\,T'_{B,1} + T'_{B,2})/W'_m$$

The typical values for b_1/W'_m, b_2/W'_m, and $T'_{B,1}$, $T'_{B,2}$ for the four systems are

f_1/f_2	b_1/W'_m	b_2/W'_m	$T'_{B,1}$	$T'_{B,2}$
22.235/18.5	0.559	-0.805	30 m	15 m
20.3/31.4	0.754	-0.315	20	19
20.0/26.5	1.174	-0.668	20	19
24.5/31.4	0.826	-0.503	23	19

where m is the number of air masses.

The error in $\Delta\rho$ due to error in T'_B is:

$$\epsilon_{T'_B} = \left[\left(\frac{b_1}{W'_m}\epsilon_{c+u}|_{T'_{B,1}}\right)^2 + \left(\frac{b_2}{W'_m}\epsilon_{c+u}|_{T'_{B,2}}\right)^2\right]^{1/2}$$

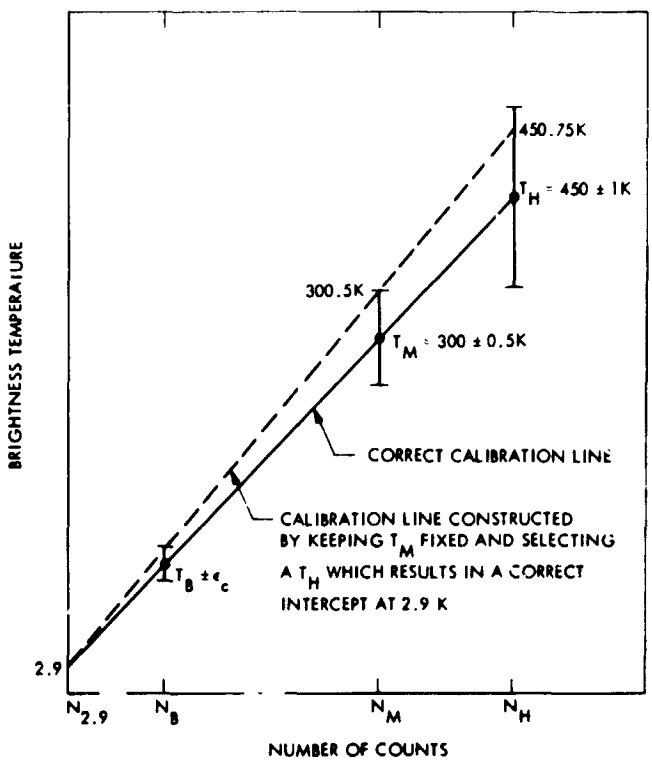

Fig. A-1. Error in linearized brightness temperature due to correlated long-term absolute uncertainties in hot-load and ambient-load temperatures

Mission Applications of the Dual Spacecraft Tracking Technique

C. C. Chao and J. P. McDanell
Navigation Systems Section

This article discusses the potential application of the dual spacecraft tracking technique to the Voyager mission. First, the concept and technology status is reviewed briefly. Then results pertaining to the JSX-Uranus option Saturn encounter, where potential navigation benefits are greatest, are presented. Results for a Jupiter encounter demonstration also are given and, finally, software modifications and tracking requirements are discussed.

I. The Concept

When two interplanetary spacecraft lie along similar geocentric lines-of-sight, significant navigation advantages may sometimes be achieved by differencing data acquired simultaneously from the two spacecraft and, in effect, determining the orbit of the second encountering spacecraft relative to the first rather than treating them independently. The potential benefits result from reduced sensitivity to at least three of the major error sources affecting orbit determination with radiometric data. First, and probably most important, is reduced sensitivity to target ephemeris errors. After encounter, the trajectory of the first spacecraft is known precisely relative to the planet. Thus, the second spacecraft may be accurately tied to the planet through the first. Second, the effect of platform parameter errors is reduced. When the two spacecraft are tracked simultaneously from nearby ground stations, errors common to both stations cancel when the data are differenced. The reduced sensitivity to station location errors that results should also make the low declination problem of orbit determination somewhat less severe. Finally, when the angular separation between the two lines-of-sight is very small, most of the transmission media effects should also cancel. The geocentric information that is lost by differencing the data may be easily restored by including a suitable amount of conventional range and/or doppler, deweighted to avoid reintroducing the error sensitivities.

II. Technology Status

Extensive studies of dual spacecraft tracking have been performed (Refs. 1-3) including analytic investigation of the information content of dual spacecraft data types and two flight demonstrations with the Viking spacecraft, one during early cruise and the other during the approach phase of Viking 2. Results indicate that dual spacecraft data types may improve navigation accuracy by a factor of 2 to 10 under the conditions of small angular separation of the two spacecraft and well determined trajectory of the reference spacecraft.

The most recent demonstration conducted with the two Viking spacecraft during the approach phase is worth special attention. With only 8 days of dual spacecraft tracking, the actual B-plane error of the trailing spacecraft was determined to better than 200 km compared with 1000 km for the same data arc using conventional radiometric data. The 1000 km error using conventional data is believed to be due to large

plasma noise (SEP ≅ 17 deg), low declination ($\delta < 5$ deg) and station location errors. Reduced sensitivity to planet ephemeris errors was also verified in this demonstration by introducing an intentional 2000 km error in the Mars ephemeris. Dual spacecraft tracking gave a factor of 10 improvement over conventional data in the presence of this large ephemeris error. Although the Viking orbiter/approach configuration differs substantially from the Voyager dual flyby, the Viking demo has verified feasibility of the concept and gives confidence that the potential benefits for Voyager can, in fact, be realized.

III. Application to the Uranus Option Saturn Encounter

The Uranus option in Saturn is well suited for a dual spacecraft strategy for the following reasons:

(1) The Uranus option for the second spacecraft will not be exercised unless a successful Saturn encounter is achieved by the lead spacecraft. Thus, the assumption that the first spacecraft will be available as a reference for the Uranus-targeted spacecraft is valid.

(2) The Uranus option trajectory design on certain launch days stretches propellant reserves nearly to the limit (Ref. 4). A precise Saturn encounter by the second spacecraft will reduce the magnitude of the post-Saturn maneuver and increase the probability of having sufficient propellant for a successful Uranus encounter. In fact, if a large injection error or other propellant-wasting event should occur, the dual spacecraft strategy might be a means of preserving the Uranus option without relying entirely upon optical navigation.

A series of simulated analyses of dual spacecraft tracking for the JSX-Uranus option at Saturn have been carefully performed. The data distribution and arc length of the conventional data types for the second spacecraft are the same as used for the baseline analysis reported in Section 2 of Ref. 5. (Note that "conventional" data in this context include dual station doppler and near-simultaneous range.) For the dual spacecraft tracking simulation, the approach tracking pattern for the second spacecraft was duplicated during the same time interval for the first spacecraft, which at this point has already flown by Saturn and is nine months ahead of the second. The encounter analysis was done using both two-station and four-station dual spacecraft data types. The data types will be described as the results for each are presented.

A. Results Using Dual Spacecraft Two-Station Data

Dual spacecraft two-station differenced doppler is formed by differencing conventional two-way doppler received simultaneously from the two spacecraft by two stations within the same station complex. Dual spacecraft two-station differenced range is constructed in the same manner, but can be obtained only at the Goldstone complex where two range machines are available. In this analysis two-station differenced doppler is weighted at 15 mHz (1 mm/s) at 60-s integration time, and the conventional doppler, if included, is loosely weighted at 150 mHz to retain the geocentric range rate information without degrading the planet relative information. The two-station differenced range is weighted at 20 m, and the conventional range (near-simultaneous) is loosely weighted at 1 km. Based on various combinations of these data types and different strategies of estimation, a series of B-plane solutions were obtained. These solutions may be grouped into two kinds: (1) estimating the state of the second spacecraft and considering the state of the first one, (2) estimating the state of both spacecraft. Both (1) and (2) are considering station locations and range biases as error sources that are not estimated. The results are given in Fig. 1.

The improvements in navigation accuracy of the second spacecraft using two spacecraft tracking depend heavily on how well the first spacecraft is tied to the planet during the approach of the second one. A post flyby long arc solution (radio only) of the first spacecraft was tried, and it yielded a position error of about 250 km relative to Saturn at the epoch of the trajectory of the trailing spacecraft. Later this is used as the a priori covariance for the state of the first spacecraft whether it is considered or estimated.

B-plane solutions of the first kind, where the first spacecraft state is considered, show significant improvements from the results of conventional radiometric data types beginning about 11 days before encounter. These solutions, which give a time history of Saturn B-plane statistics as shown by the uppermost broken line in Fig. 1, are based on dual spacecraft two-station doppler combined with loosely weighted conventional range (no conventional doppler) with nongravitational accelerations of both spacecraft estimated stochastically. The rapid increase in B-plane accuracy during the last 10 days of Saturn approach would offer substantial benefit to the mission if the final approach maneuver could be delayed to, say, E-7 days. Delivery and knowledge accuracy would be improved by 35% and 60%, respectively, in this case. The local maximum at E-18 days is believed to be due to the fact that the sensitivity to the reference spacecraft is magnified by the zero declination of the second spacecraft which occurs at E-22 days. This sensitivity becomes even greater when the dual spacecraft two-station range is included. These large sensitivities suggest that the state of the first spacecraft should be estimated as well

When the states of both spacecraft are estimated, improvements in B-plane accuracy occur much earlier as may be seen

from the appropriate curves in Fig. 1. The data set used in generating these orbit determination (OD) solutions is the same as for the first cases except that dual spacecraft two-station range is also included. The upper curve of the two where both spacecraft states are estimated represents the case where stochastic nongravitational accelerations from both spacecraft are estimated sequentially with a two-day batch size and a one-day correlation time. The B-plane accuracy improvement after E-8 days is fairly consistent with the first case, where the state of the first spacecraft is not estimated, but the performance prior to E-8 days is dramatically improved. Because the improvement occurs earlier in this case, it would not be necessary to delay the final approach maneuver from its nominal time at E-10 days in order to realize the potential benefits of this strategy.

If the stochastic unmodelled accelerations from both spacecraft are assumed to be negligible during the Saturn approach, sequential estimation of these parameters becomes unnecessary, and further improvement in B-plane accuracy may be expected as shown by the lower curve in Fig. 1. A factor of 4 improvement in both delivery and knowledge may be possible provided that the above optimistic assumption is valid.

B. Results Using Dual Spacecraft Four-Station Doppler

The sensitivity to nongravitational accelerations indicated by the difference between the two lower curves in Fig. 1 and the sensitivity to the state of the reference spacecraft indicated by the upper curve provide the motivation for considering the use of dual spacecraft four-station doppler data. If the same spacecraft is simultaneously tracked from two widely separated tracking stations such as Goldstone and Australia, differencing of the corresponding doppler data from the two stations provides differenced doppler that is unaffected by geocentric range rate changes and hence relatively uncorrupted by unmodelled spacecraft accelerations. With dual spacecraft tracking the differenced doppler data from both spacecraft will again be differenced. This twice differenced new data type requires simultaneous tracking by four stations, and thus is called dual spacecraft four-station doppler.

This new data type is insensitive to nearly all the error sources usually associated with radiometric data, and therefore the OD capabilities depend heavily on the quality and quantity of such data within a given arc of the trajectory. In this analysis, during the three station overlaps of each tracking cycle (as defined in Section 2.1.2 of Ref. 5) a total of 8 to 10 hours of dual spacecraft four-station doppler was generated. Four different OD solutions were tried using this data, and the resulting B-plane histories are shown in Fig. 2. The two curves shown with nonuniform dashed lines are the results of the same estimation strategy (estimating the state of the second spacecraft and the constant part of nongravitational accelerations and considering the state of the first spacecraft and station locations) with different data weights. The upper curve has the four-station doppler weighted at the standard 1 mm/s with conventional range loosely weighted; the lower one has the weight of the four-station doppler reduced to 0.5 mm/s to account for the expected improvement in data quality after double differencing. It is clear that the improvement in navigation depends strongly on the quality of this new data type which has not yet been demonstrated.

Although a 40% improvement in delivery may be possible with the four-station doppler and conventional range, the improvement at the knowledge point is not as good as that of dual spacecraft two-station data. This is because the information contained in the four-station doppler observables consists only of the differential angles between the two spacecraft, which are less effective in determining the bending of the trajectory caused by the planet than the differential range and range rate information in the two-station data types. The range rate information may be provided by including loosely weighted conventional doppler. The results for this case are given by the remaining two dashed curves in Fig. 2, which show substantial improvement after E-5 days, where planetary bending begins to occur.

The two-station and four-station dual spacecraft data types were analyzed separately to determine the characteristics and accuracy potential of each. The four-station doppler is "cleaner" and less vulnerable to unmodelled accelerations, but its information content is less, and it can only be obtained during view period overlaps between stations. It may be possible to gain the advantages of both by combining them in a single solution. However, the strategy for doing this (relative data weights, choice of estimated parameters, etc.) must be carefully investigated as new error sensitivities may be introduced by the combined data set which will offset the potential advantages.

IV. Demonstration Opportunity at Jupiter

Although the Viking demonstrations were successful, further verification of dual spacecraft tracking for the Voyager application is needed for the following reasons:

(1) Four-station dual spacecraft data was not available during the Viking demonstrations; therefore, its quality is uncertain and its utility has not been verified.

(2) Angular separation of the Viking spacecraft at encounter was extremely small (0.15 deg). Voyager separation will be 5 to 6 deg at Jupiter, 9 deg at Saturn.

(3) In the Viking encounter demonstration the reference spacecraft was an orbiter. Voyager is a dual flyby with relatively large time separation between encounters.

(4) The information content of the differenced data is a function of local accelerations, which will be quite different for the massive outer planets than for Mars.

The Voyager dual flyby at Jupiter provides a good opportunity to demonstrate this technique for application at Saturn. Furthermore, if the test can be conducted in near-real time, the results may be of direct benefit for navigation of the trailing spacecraft at Jupiter. To determine the potential navigation enhancement at Jupiter, analysis was performed using the JSX-CB10 encounter. This trajectory was selected because it is the more difficult of the two JSX Jupiter encounters considered in the baseline analysis. The Jupiter relative and Callisto relative B-plane time histories for dual spacecraft tracking are compared with the corresponding baseline results in Figs. 3 and 4, respectively.

Figure 4 shows that dual spacecraft two-station data are capable of reducing Callisto relative errors to the level of the satellite ephemeris error (300 km) at the delivery epoch (E-13.5 days) and gives a factor of 3 improvement over conventional data at the knowledge epoch (E-3.5 days). The Jupiter relative improvement shown in Fig. 3 is more dramatic, since it results from the combination of a direct effect (reducing Jupiter relative errors which exist prior to the Callisto flyby) and an indirect effect (reducing the magnitude of the Callisto perturbation uncertainty by reducing Callisto relative errors).

The relative performance of the two-station and four-station dual spacecraft data types at Jupiter is similar to that observed in the Saturn encounter analysis. However, since the conventional data performance is better at Jupiter, the four-station doppler (with its limited information content) does not show substantial improvement over the baseline results until fairly close to encounter, near the knowledge epoch. This is true even though the four-station doppler was assumed to be of high quality in this analysis (0.5 mm/s).

V. Tracking and Data Processing Requirements

Dual spacecraft tracking, by definition, requires the acquisition of radiometric data simultaneously from two spacecraft. This means, of course, that the first spacecraft must be given relatively dense tracking coverage during the approach phase of the second, which would normally be a quiescent period for the first. However, the Viking demonstrations and covariance analyses have shown that relatively short arcs of dual spacecraft data are effective (a characteristic that is shared with differential VLBI, which is very similar to dual spacecraft tracking in principle). Therefore, tracking requirements are not excessive. In fact, one of the potential benefits of dual spacecraft tracking is an overall reduction of tracking time.

Dual spacecraft tracking requires no hardware changes and only minor modifications to navigation software. For the Viking demonstrations a special version of the program ODE was created to maintain simultaneity of dual spacecraft doppler after editing and compression. Another special program was developed to difference the two-station and four-station data types. The differenced data can be processed by the Voyager ODP with no additional modifications. The demonstration software is available and can serve as a prototype software.

References

1. Preston, R. A., "Dual Spacecraft Radio Metric Tracking," *The Deep Space Network Progress Report 42-22*, JPL May to June 1974.

2. Chao, C. C., Siegel, H. L., and Ondrasik, V. J., "Improvements in Navigation Resulting from the Use of Dual Spacecraft Radiometric Data," *The Deep Space Network Progress Report 42-38*, April 15, 1977.

3. Chao, C. C., "A Demonstration of Dual Spacecraft Tracking Conducted with the Viking Spacecraft During the Approach Phase," Paper presented at the AAS/AIAA Astrodynamics Conference, Jackson, Wyoming, Sept. 7-9, 1977, and published in this issue of DSN Progress Report pp.

4. PD 618-115, Rev. A, Voyager Navigation Plan, 20 April 1977 (JPL internal document).

5. McDanell, J. P., et al., "Voyager Orbit Determination Strategy and Accuracy," PD 618-118, 1 August 1977.

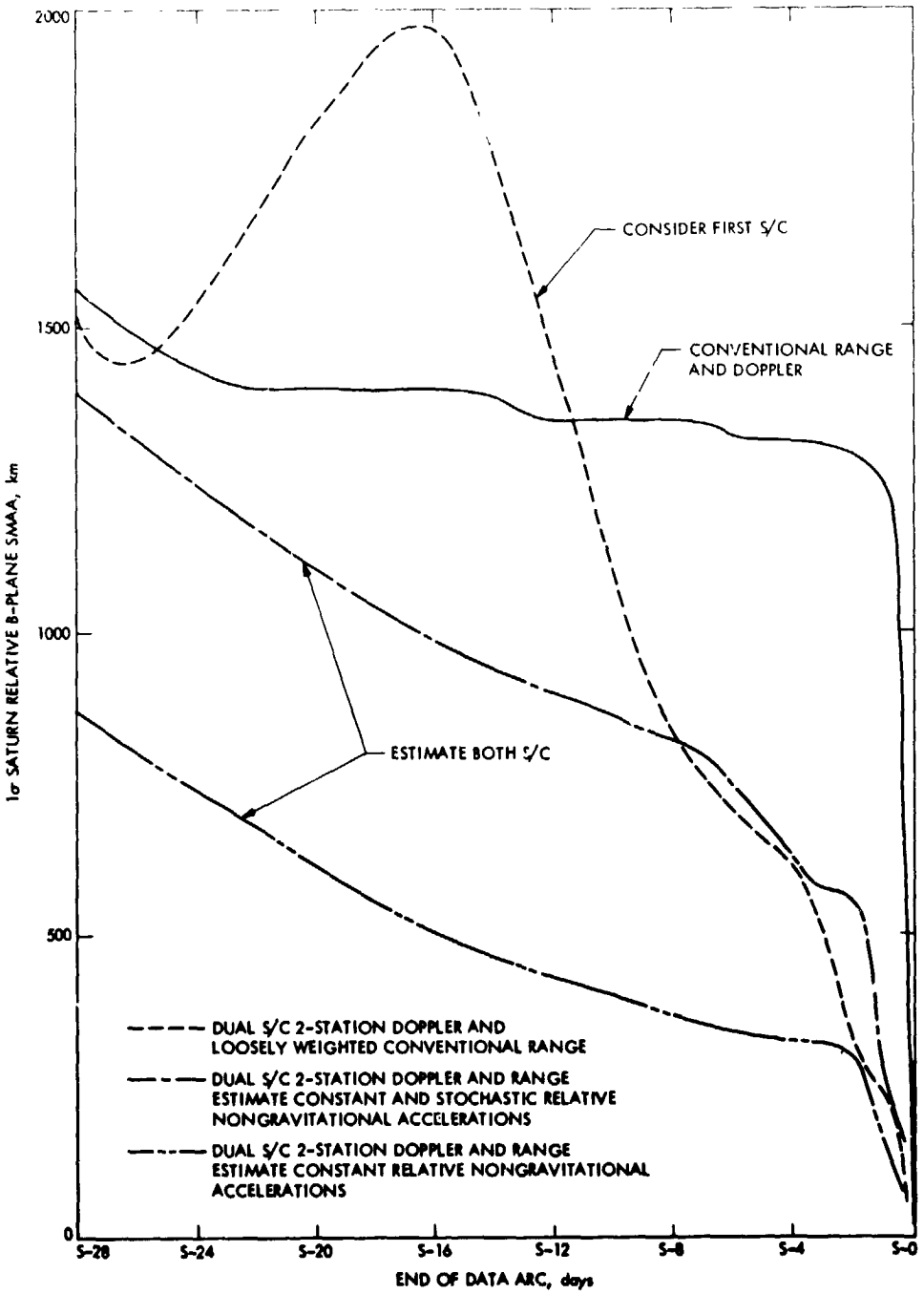

Fig. 1. JSX-Uranus option Saturn relative B-plane errors using dual spacecraft two-station data

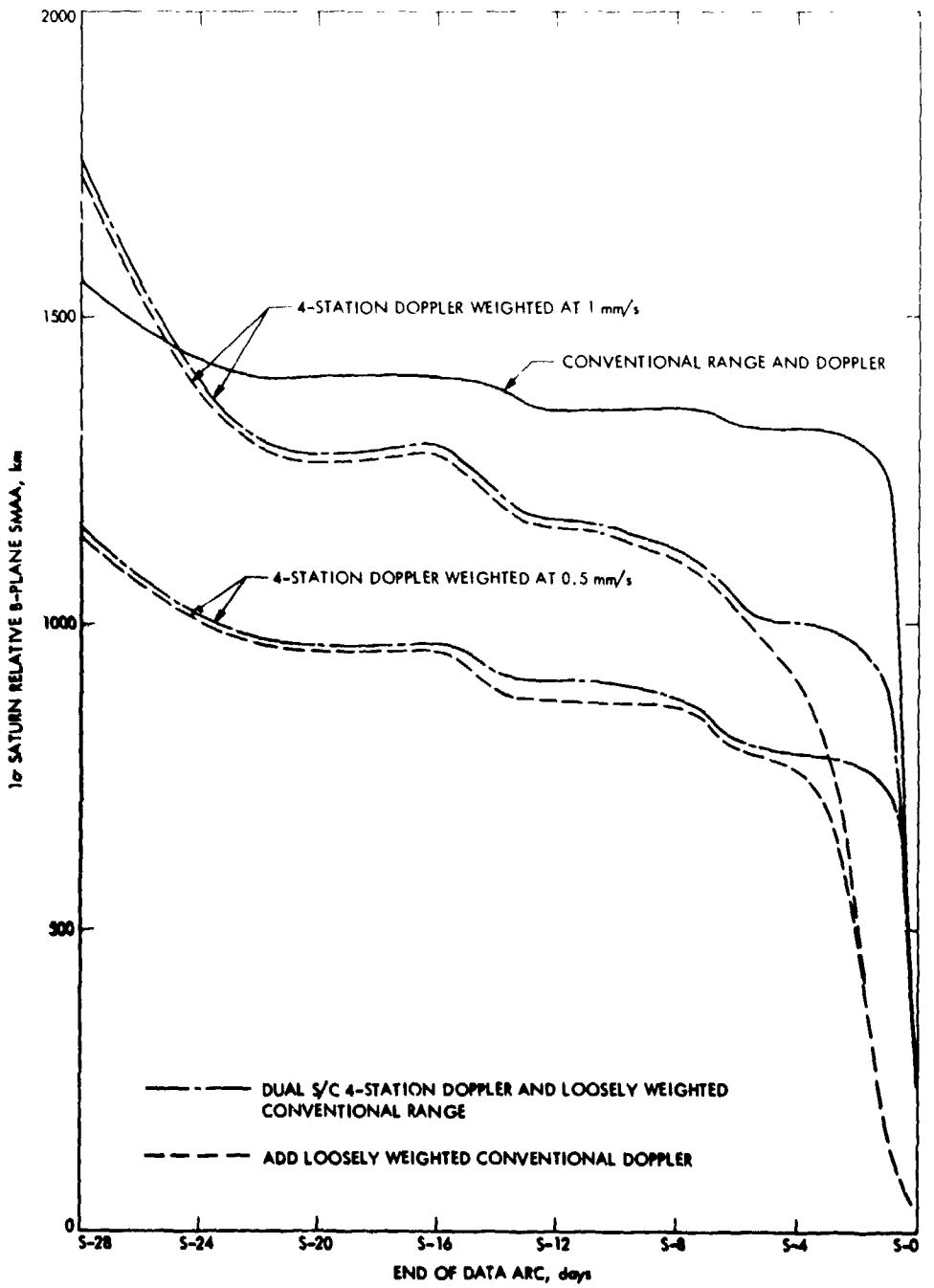

Fig. 2. JSX-Uranus option Saturn relative B-plane error using dual spacecraft four-station doppler

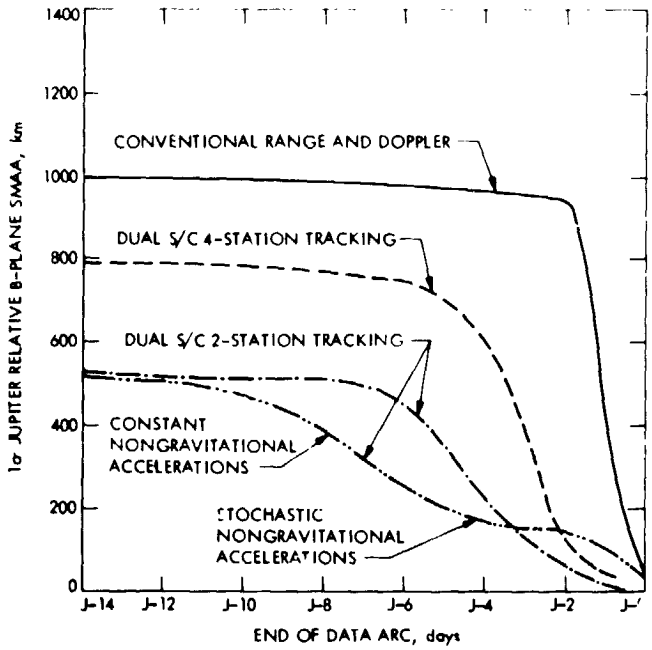

Fig. 3. JSX-CB10 Jupiter relative B-plane errors with dual spacecraft tracking

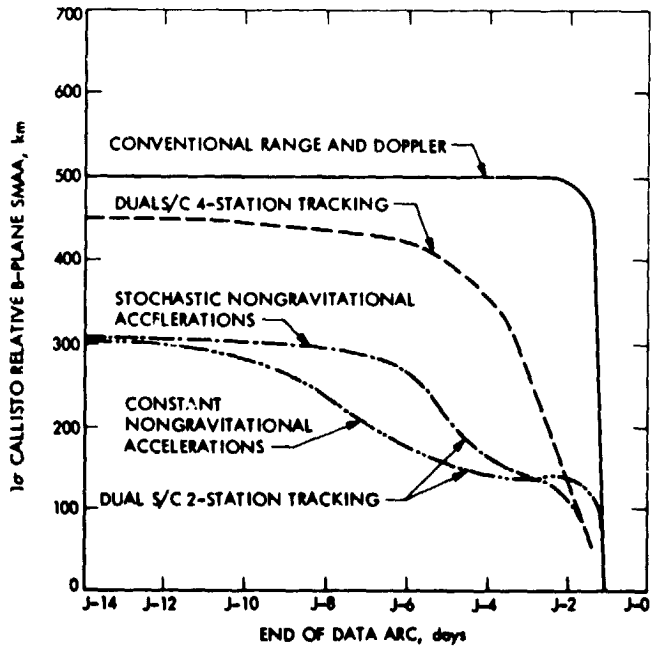

Fig. 4. JSX-CB10 Callisto relative B-plane errors with dual spacecraft tracking

Preliminary Design Work on a DSN VLBI Correlator

W. A. Lushbaugh and J. W. Layland
Communications Systems Research Section

The DSN is in the process of fielding high-density digital instrumentation recorders for support of the Pioneer Venus 1978 Entry Experiment and other related tasks. It has long been obvious that these recorders would also serve well as the recording medium for VLBI experiments with relatively weak radio sources, provided that a suitable correlation processor for these tape recordings could be established. This article describes the overall design and current status of a VLBI correlator designed to mate with these tape recorders.

I. Introduction

The DSN is in the process of fielding high-density digital instrumentation recorders for support of the Pioneer Venus Entry Experiment (Ref. 1) and other related tasks. It has long been obvious that these recorders would also serve well as the recording medium for VLBI experiments with relatively weak radio sources, provided only that a suitable correlation processor for these tape recordings could be established. This article describes the overall design and current status of a VLBI correlator which we had planned to mate with these tape recorders. This design work began in mid 1976 and is terminating as of EO FY'77 with the transfer of Design Responsibility for the VLBI Correlator to DSN Implementation.

II. Overview of a VLBI Correlation Processor

The role of the VLBI correlation processor can best be understood by reference to Fig. 1, which shows the entirety of the VLBI instrumentation, exclusive of calibration tools. Acquisition of the VLBI data, a broadband noise signal from a natural radio source, occurs in the Tracking Stations shown at the left of Fig. 1. Data from the two widely separated data acquisition sites are brought together at the correlation processor by shipment of the tape recordings, which can contain in excess of 10^{10} bits each.

There is a relative delay d between the arrival of the noise signal at the two tracking stations that depends upon the observing geometry: the relative position of the two stations on the Earth, the position of the radio source, and the position of the Earth at the instant of arrival. At each tracking station, the signal is filtered, translated in frequency by a local oscillator, sampled and quantized to one-bit (sign only) for recording. The principal function of the correlation processor is to perform cross-correlation detection of these sampled signals to estimate as precisely as possible the delay d, and the amplitude of the radio-source noise signal. The delay d must be known well enough a priori to be compensated for in the alignment of the recorded bit streams and in the doppler reference signal shown in Fig. 1. This can be accomplished either by providing precise polynomial predicts for each observation, or by allowing the correlation processor to compute from the observing geometry. In either case, the

predicted delay must be computed to an accuracy which is compatible with the intended final system precision, and much more accurately than is needed to simply perform the correlation detection. Inaccuracies in the models used to predict d can be mostly eliminated by computing for the output interface the total estimated delay, instead of the offset from the model. Inaccuracies in computing the modeled delays directly become inaccuracies in results.

The summed bit-wise cross-products of the sampled data streams are an intermediate output from the correlation processor as shown. They are also a feasible interface that is comparable in complexity to the use of polynomials to predict the a priori delay. The signal detection operation is completed by estimating cross-correlation amplitude, delay, delay rate, phase and phase rate from the summed cross-products.

In designing any high precision, wide bandwidth VLBI System, it is often tacitly assumed that the wide bandwidth is achieved through the bandwidth synthesis technique (Ref. 2). Thus, a significant consideration in our correlator design was that it be capable of bandwidth synthesis operation with the 4 Mb sample rate of the Mark II recorders (Ref. 3). The DSN Instrumentation recorders could be easily partitioned into six such channels. If additional tracks are implemented, then eight 4-Mb channels can be extracted through relatively simple stream-partitioning electronics. We believe that the incremental cost of these additional tracks is low enough that they should be implemented when the tape recorders are configured for VLBI use. Our basic correlator design includes eight 8-Mb correlator channels, which would typically be run at the 4-Mb rates in bandwidth synthesis operation. Each correlator channel computes bit-wise cross products for an adjacent eight complex "lags." The channels can be concatenated to form a single 64-lag correlator for searching through a range of delays when the delay is only poorly known a priori. The channels can also be connected in tandem to provide a wideband single channel correlator.

III. Overview of Correlator Hardware

Figure 2 is a functional block diagram of the correlation processor hardware. Fundamental structure and parameter values in this design are based largely upon the recently completed Mark-II correlator at C.I.T. Some changes from the CIT design, such as including delay rate and phase acceleration terms, and extending the length of the accumulator and phase-reference registers, have been made to eliminate minor deficiencies seen in the earlier design (Ref. 4). We have also provided the capability to read the contents of the phase-reference generator registers into the computer to verify its operation, and enhance the accountability of its phase.

The tape recorders shown in Fig. 2 are the high density instrumentation recorders described by Kimball (Ref. 1). The tape control unit must adjust the relative position of the tapes during playback so that the data streams are approximately in time correspondence. The final alignment of data streams is done in the variable delay buffer between the tape recorders and the correlator proper. This buffer must be large enough to adapt the changes in delay needed to retain the proper alignment of data streams at the correlator to the dynamical capabilities of the tape recorders. The design-wise simplest system has the tapes completely aligned in time with all adjustments for observing geometry made in the variable delay buffers. In this case, however, the buffers are large, containing enough data to shift the delay by an Earth-radius or about 1.6×10^6 bits if tapes are played at 64 Mb.

The stream partitioning is a parallel-to-serial conversion into the 4-Mb channel bit streams from the parallel word of the tape recorder. It appears after the variable delay to allow the delay buffer to be a single entity. The variable delay could follow the stream partitioning, resulting in a more modular structure to the correlation processor, but at the cost of having eight identical variable delay buffers responding in concert to the delay adjustment commands.

The actual cross-correlation of the two data streams takes place in the correlation pre-scaler module. There, the bit stream from one channel on one tape is multiplied by quadrature "sine waves" from the phase reference generator, and by eight adjacent delayed copies of the bit stream from the corresponding channel on the other tape. The phase reference generator provides doppler compensation. The correlation prescaler also multiplies each of the data streams individually by quadrature "sine waves" to coherently detect the tones of the phase calibrator, which is necessary for accurate bandwidth synthesis VLBI. The low-order counter bits for the summation of cross-products are the "pre-scaler" part of correlation prescaler. Overflows from these short counters are transferred to the master accumulator. One correlation prescaler, and one phase reference generator share a physical module associated with one data channel.

The master accumulator is one physical module, which adds the overflows from up to eight prescaler units into a random access memory. Correlations are summed into only one half of this memory at a time, while completed sums can be transferred at leisure into the controlling computer.

The master timer contains a microprocessor which computes the phase and phase-rate data values for each of the phase reference generators from the phase, phase rate, and phase acceleration data provided by the controlling computer. It computes the delay, as a function of time, for the variable

delay buffer from the delay and delay rate data provided by the controlling computer. It contains the logical timing chains needed to relate "data time," as counted from the clock pulses from the tape recorders, to the event timing within the phase reference generators, and master accumulator.

The computer interface unit provides the controlling computer the capability to control the master timer and read the accumulated correlations. We also intend it to provide the capability to read the phase reference generator registers for diagnostic purposes. In addition, pathways would be provided to supply a data stream from the controlling computer into each of the correlation prescalers. This would provide a tool for test and diagnosis of the system operation. In addition, this path would allow real data recorded on computer-compatible tapes to be processed by this correlation processor, or perhaps on a subset machine that contained only one phase reference/correlation prescaler module.

The following sections present details of the VLBI correlator hardware.

IV. Lobe Rotator

The phase-reference generator, or the lobe rotator, is a device that supplies doppler sine and cosine information to the correlator. The sine-cosine outputs are two bit approximations to a sine wave. One of these two bits is used to control whether the signal from Station A is to be compared to the signal from Station B or to its complement. The second bit controls whether the correlated waveforms are to be counted or not. Figure 3 shows the composite waveforms of the sine and cosine.

The lobe rotator consists of four 32 bit registers, a 32 bit adder, a 32 X 8 ROM for converting the sine and cosine, and control circuitry. A block diagram is shown in Fig. 4. The four registers are called the A, B, $\Delta\emptyset$, and $\emptyset$ registers, with the adder connecting the $\Delta\emptyset$ and $\emptyset$ registers.

The $\emptyset$ register holds the value of the present phase, and is updated each clock pulse by the amount in the $\Delta\emptyset$ register via a 32 bit adder to be described in detail below. The 5 most significant bits of the $\emptyset$ register are used as the address of a 32 word ROM which contains the two-bit approximations to the sine and cosine.

The A and B registers are hold registers for the $\Delta\emptyset$ register. Two hold registers were needed to handle the two different modes of controlling the $\emptyset$ register. The first of these modes simply changes $\Delta\emptyset$, which will result in a new rate of change for the contents of the $\emptyset$ register. The second mode introduces a phase shift into the output phase and then changes $\Delta\emptyset$ one clock pulse later to produce a new slope for the phase information. This second mode requires the second hold register. When the B register is loaded with the phase shift value and the A register has the new $\Delta\emptyset$, a command can be given to clock the B register into the $\Delta\emptyset$ register and the A register into the B. One clock pulse later, the B register is again transferred into the $\Delta\emptyset$ register to establish the new phase rate.

The A register is divided into 4 eight-bit byte sections. The first of these four sections is connected to a data bus that will be driven by the output of a microprocessor. When an A register clock is supplied from signals delivered by the microprocessor, the 8 bits from the data bus are clocked in the first section of the A register and each of the other three sections receives the 8 bits from the section to its left in shift register fashion. After 4 bytes have been loaded into the A register, a command may be sent to the lobe rotator by the microprocessor, to parallel transfer all 32 bits into the B register, in preparation for the transfer into the $\emptyset$ register as described above.

The adder used in the lobe rotator is of an unusual design necessitated by the requirement that the 32-bit sum be accomplished in 120 ns. Figure 5 shows a block diagram of the adder. For clarity, the inputs from the two registers are not shown. The technique used in the adder is to break the sum into four groups of 8 bits each. The carry into the least significant group of bits is known to be zero, and so a regular adder can be used. Each of the groups containing more significant bits are added *twice*, once with the carry set to zero and once with it set to one. The actual carry is computed in parallel and used to select the correct sum via a multiplexer. Adding each group of four bits twice does not increase the hardware chip count; since the carry output of an adder with a zero carry input is a term usually called Generate (G) in carry look-ahead schemes, while the output of an adder with the carry input set to one is a term usually called Propagate (P). Generate means that the group being added will generate a carry by itself, while Propagate means that the group being added will propagate an input carry to the next group above. The carry look-ahead equation is

$$C_n = G_{n-1} + P_{n-1} G_{n-2} + P_{n-2} P_{n-1} G_{n-3} + \cdots$$

where the subscripts n would refer to a group of eight bits. Figure 5 shows two SN74S64 used to compute the actual (inverted) carries $\overline{C}_{15}$ and $\overline{C}_{23}$, which, in turn, are used to select the correct sum via the SN74LS157 multiplexer. The 32-bit sum through the adder, the carry computation and select takes 66-ns worst case, which allows ample time for register output delays and input setup times in the 120 ns time allotted.

V. Correlation Prescaler

The basic correlator design includes eight 8-Mb correlator channels each of which computes bit-wise cross products for eight adjacent complex "lags." In addition, each channel computes 7 other sums that are used to calibrate the system and in the computation of the final results. These signals are

(1) Total clock pulses minus tape bad signals

(2) Total clock pulses minus tape bad or sine = 0

(3) Total clock pulses minus tape bad or cos = 0

(4) Sin Ref ⊕ A(n) but not tape bad

(5) Sin Ref ⊕ B(n) but not tape bad

(6) Cos Ref ⊕ A(n) but not tape bad

(7) Cos Ref ⊕ B(n) but not tape bad

Each channel was built with these 23 correlation counters and one spare to make 24 per channel and 196 total in the system. The correlation prescaler counts the agreements between signal $A(n)$, (the nth channel from tape recorder A and the signal $B(n)$. It is assumed that each "channel" of the tape recorder also supplies a bad tape signal which is used to inhibit the correlation counter when the signal is known to be bad. Each counter in the prescaler consists of 8 bits, out of a total of 31 bits in the correlation accumulator.

The most significant bit from each of the 24 counter forms the output of the prescaler. These most significant bits from each counter are sampled every 15 μs and stored in a shift register. Between the 15 μs sampling times, this 24-bit shift register shifts the most significant bit of each counter to the master accumulator to be further processed.

The correlation prescaler also provides the gating for rearranging the available storage registers (lag-registers) in various ways. Figure 6 shows a block diagram of the eight bits of storage on two adjacent channels, channel n and channel n+1 where n is assumed to be even. Each of the four boxes shown in Fig. 6 is an SN74LS163 (a four bit shift register) which also can be parallel loaded depending upon the status of the S/$\overline{L}$ signal. The chip is wired so that the lower three bits act as a shift register for either state of S/$\overline{L}$. This means that S/$\overline{L}$ actually only controls which of two inputs to the shift register shall enter. The shifting input is shown vertically while the loading input is shown horizontally.

Under regular correlation conditions, all four shift registers are given the shift command and the input signal $B(n)$ is delayed eight units of time necessary for the correlation.

Another desired configuration is to concatenate all the lags together. This mode is useful in initialization when the position of the correct lag is more uncertain than 8 positions. If the upper shift register in each channel (except the first) is signaled to load, the input to each register will be $L(n-1)$, i.e. the output of the preceding channel. If the lower shift register is still in the shift mode, this accomplishes the desired arrangement.

One other mode of the S/$\overline{L}$ signals is very useful. When the top two units shift (i.e., input $B(n)$ and $B(n+1)$) and the bottom two load, (input $B(n+1)$ and $B(n)$ respectively), correlation can be a double sideband operation, i.e., where adjacent tracks on the tape are real and imaginary components of the signal. In this case, only 4 lags per channel are obtained. This same mode of operation is also useful when the adjacent tracks on the tape are even and odd samples of the same data, i.e., the data is coming in twice as fast as usual. In the mode described, it will be noticed that $L(n)$ (the even bits of the sample) will be copied twice, once into the top register on the left and once into the lower 4-bit register on the right. A similar situation exists for the odd numbered signal bits. The A(N) signals, not shown on the diagram for clarity, are also assumed to be even and odd numbered bit stream from the other recorder. Thus, the even bits of B are correlated with the even bits of A on the top 4 bits at the left, the even bits of B correlated with the odd bits of A on the lower left, etc. The net result is to have 8 lags for *half* as many the original channels. Also, the correlation sum is broken into two parts and will have to be added together by the master computer.

VI. Master Accumulator

The master accumulator takes the eight streams of most significant bits from each correlator prescaler and uses this information to form the 23 most significant bits of the correlation sum.

The master accumulator is divided into three sections, an input section, an intermediate summing section and the final output accumulator stage. Each section has a major timing cycle of 15-5/8 μs during which the 24 parallel computations are made. The 15-5/8 μs major cycle time is divided from the 8-MHz clock rate at which the data enters the correlator prescaler. At this rate, the most significant bit of any prescaler counter can change only every 16 μs. The 15-5/8 μs cycle time contains 24 minor timing cycles of 5/8 μs each for processing the information from the 24 prescaler counters and one extra cycle to allow one memory access for output.

The input section to the master accumulator contains a 24 word by 8 bit memory. Each word of this memory holds a copy of the MSB from the prescaler counter for each of the channels. One word of the memory is used for each of the 24

counters on the prescaler. The input for the master accumulator is the present value of this MSB which together with the previous value can be used to determine if an overflow of one of the counters occurred in the last major cycle. The output of this first section of the master accumulator is 8 bits each minor cycle, with a logic 1 for an overflow in each of the 8 positions. These overflow bits feed the intermediate summing section, which consists of eight 48 word by 4 bit memories, one for each of the eight channels. On each minor cycle of 5/8 μs, a word is accessed from each memory, loaded into a 4 bit counter, and incremented if the overflow bit from the input section is set, and returned to memory. Only half of the 48 words are used during any major cycle, the other half holding the results from the previous correlation interval. This intermediate summation is done to further reduce the overflow rate from any counter. The prescaler had to be sampled every 16 μs but an overflow from one of those counters could only occur every 32 μs. The overflows from this intermediate counter can occur at a maximum rate of 1 every 512 μs and so the most significant bit of this stage must be sampled more frequently than once every 256 μs. Actually, these bits are sampled every 125-130 μs depending upon how many cycles are stolen for output. The eight most significant bits of each counter on the intermediate stage are sampled every eight or nine microseconds, and stored in an 8 bit shift register to be shifted to the output accumulator. The sampling is done in an 8-8-9 μs pattern to get all 24 positions of the 8 channels from the intermediate stage sampled in 125 μs. This time will be increased by 5/8 μs for each cycle stolen to output data from the previous correlation interval. Since one of these output cycles is constrained to occur only once every major cycle (15 μs) only 8 minor cycles or 5 μs at most will be added to the 125 μs figure above, to transfer all the overflows from the intermediate stage to the output accumulator.

The output accumulator stage of the master accumulator consists of two 196 word by 20 bit memories. The two memories have their outputs on a common buss and as before, one section holds the data from the previous correlation interval, while the other half of the memory is used for the present accumulation. During each minor cycle, the 20 bits are loaded into an up counter and incremented if the overflow bit from the intermediate stage is a one. An all-ones detector is included in the counter that inhibits further counting if the value is at a maximum. The 20 bits from the output stage and 3 bits from the intermediate stage are supplied as inputs to a 23-bit register that holds these bits for output. This output register is sent through a multiplexer to the host computer as three consecutive bytes.

Although the design of the master accumulator may seem overly complex, the hardware savings due to this design, as compared to straight binary counters, makes it worth while. The master accumulator replaces 196 counters of 23 bits each, which if built with 4 bit binary counters would use 1,176 chips, not including any chips for output. The present master accumulator uses 95 chips including timing and output plus 3 extra chips on each prescaler for a total of 119 chips in an 8 channel system.

VII. Master Timer

The master timer is the unit that controls the overall signal flow in the correlator. This unit is responsible for supplying the Δf information to all eight lobe rotators as well as calculating these values from the $\Delta\Delta\phi$ information determined by the geometry of the VLBI observation and supplied by the controlling computer. At least part of the master timer will utilize a flexible high-speed microprocessor, such as the Z80. The master timer will also have timing chains running at 8 MHz. These timers will be controlled by the microprocessor and are necessary to control transfers to the lobe rotators with an 8 MHz precision. The microprocessor in the master timer would do the 48-bit additions necessary to calculate the new $\Delta\phi$ from the $\Delta\Delta\phi$'s. The processor would also be responsible for controlling the time at which all 8 lobe rotators simultaneously receive the updated $\Delta\phi$s as directed by the control computer. The microprocessor would also be responsible for clearing the ϕ and $\Delta\phi$ registers of all lobe rotators at the start of a correlation interval. Starting the correlation after this would then be similar to changing $\Delta\phi$.

As the correlation process continues, one data stream slips with respect to the other due to the rotation of the Earth. If no correction were made, the best lag at the highest correlation counter would drift out of the range of the 8 lags provided. For this reason, one data stream is moved periodically by one bit with respect to the other. With a sampling rate of 8 MHz, lags are separated in time by 120 ns, which corresponds roughly to a distance of 40 m at the speed of light. When the two stations move differentively, so that one is about 40 m further from the star, a signal is given to the hardware to change the lag by one. A rough calculation of the minimum time for two stations on earth to move apart from a star by 40 m gives about 100 ms. The master timer would handle the details of the timing shift. If single side band sampling is used, there is an approximate 90 deg shift in the ϕ accompanying such a change of lag. In this case, the microprocessor would load both registers of the lobe rotator and give a command to change the phase followed by a change in $\Delta\phi$. In double side band sampling there is no 90 deg phase shift when the lags are changed.

VIII. Tape Recorder Interface

The tape recorder interface has two main sections the tape control unit and the buffer memory and its controls. The tape control unit supplies signals to the tape recorder to act as a vernier on its speed. This correction is needed to establish time correspondence between data samples on the two tape recorders.

The tape control unit also must read and interpret the time information on the tapes so as to be able to approximately align the tapes before the run starts.

The buffer memory is needed to provide a variable delay between the tape recorders and the correlator accumulators. The buffer must be large enough to accommodate the doppler shift of the data streams over, for example, a 20-min run, which is 12,000 bits per channel at a doppler slippage rate of 10 bits/s.

The conceptually simplest interface between the tape recorder and the correlator is to have a buffer large enough to accommodate 25 ms worth of data, which corresponds to the maximum signal path delay between any two stations. This buffer would be about 1.6×10^6 bits if the tapes are played at 64 Mb. This may turn out to be the best solution, however, since only 100 of the recently introduced 16K bit memory integrated circuits would be needed. If such a large memory were used, it would be necessary to switch its input between the two tape recorders as either recorder may lead or lag the other as various signal sources are scanned.

IX. Summary and Status

This article describes the initial design work on a high-speed digital VLBI correlator that could mate with the high-density digital instrumentation recorders. This correlator has 8 complex channels with 8 lags in each.

These channels are capable of being rearranged into either 4, 2 or 1 channels with a corresponding number of lags equal to 16, 32, or 64, respectively. Each of the 8 channels has a lobe rotator or phase reference generator to control the sine and cosine correlations. These lobe rotators have 32-bit arithmetic units to compute the phase from the phase rate information. The most significant 5 bits of the phase are used to compute the 3 level sine and cosine approximations from a ROM. Each accumulator on each of the 196 lags in the correlator has 31 bits. The most significant 23 bits of these registers are double buffered to allow their transfer to the controlling computer.

At this time, the lobe rotator and correlation prescaler units have been designed, built, and debugged. It has been confirmed that the 32-bit arithmetic unit works at its 8-Mhz design limit. The master accumulator has been designed and is under construction. Both of these units have been configured on a DSN standard integrated circuit packaging panel. The lobe rotator-prescaler module occupies one panel while the master accumulator is slightly less.

Acknowledgement

The authors wish to acknowledge the assistance of a number of JPL personnel, particularly J. L. Fanselow, W. J. Hurd, and D. J. Rogstad, during the formative stages of this work.

References

1. Kimball, K. R., "Implementation of Wideband Digital Recording Equipment in the DSN," *The DSN Progress Report 42-31*, Feb. 15, 1976, pp. 96-104.

2. Rogers, Alan E. E., "Very Long Baseline Interferometry With Large Effective Bandwidth for Phase Delay Measurements," *Radio Science*, 5:10, pp. 1239-1247, Oct. 1970.

3. Clark, B. G., "The NRAO Tape Recorder Interferometer System," *Proc. IEEE*, Vol. 61, No. 9, p. 1242, 1973.

4. Fanselow, J. H., Rogstad, D. H., private communication.

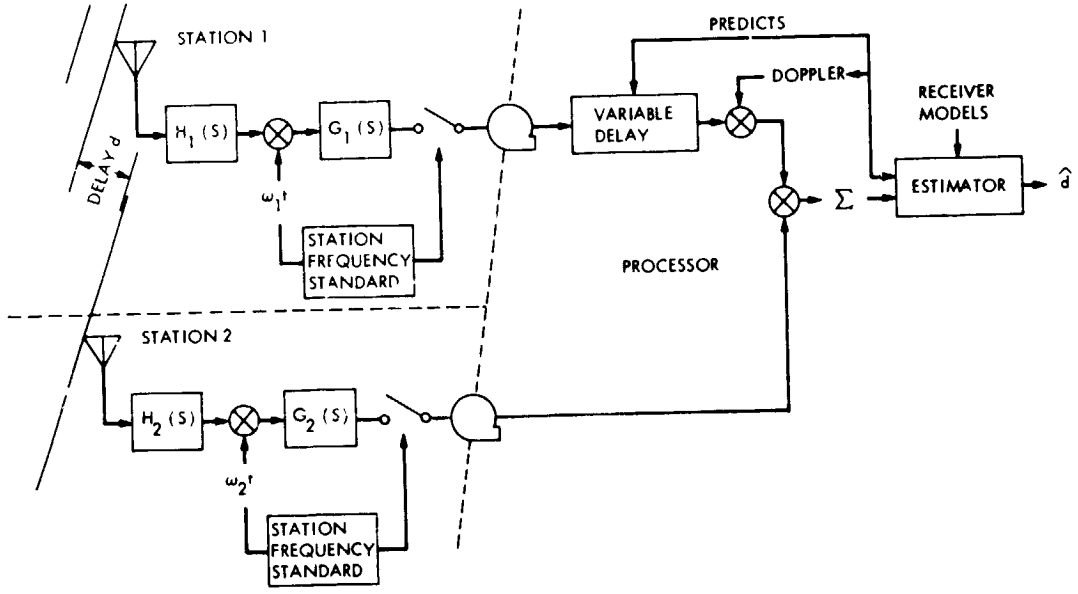

Fig. 1. VLBI instrument (simplified)

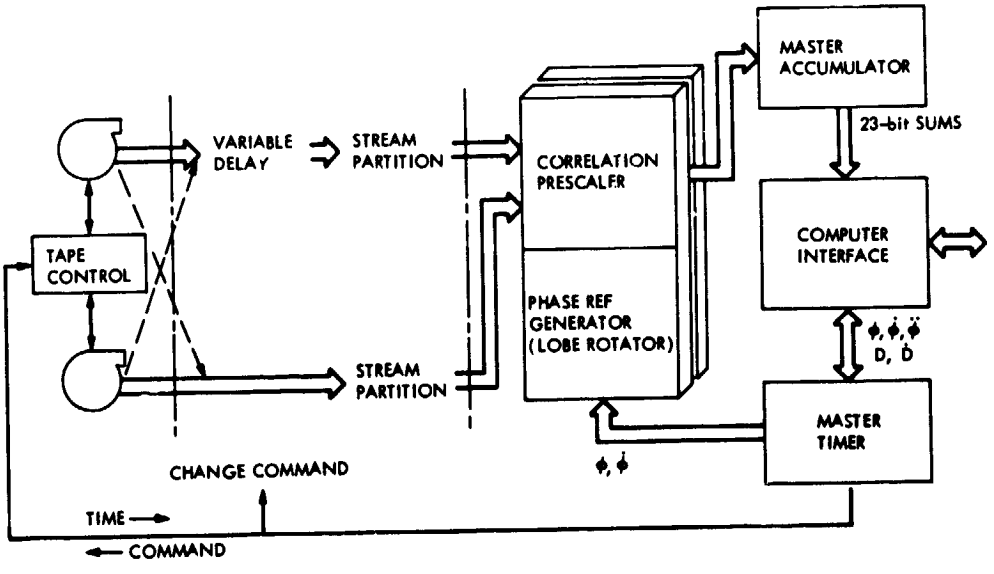

Fig. 2. VLBI correlation processor

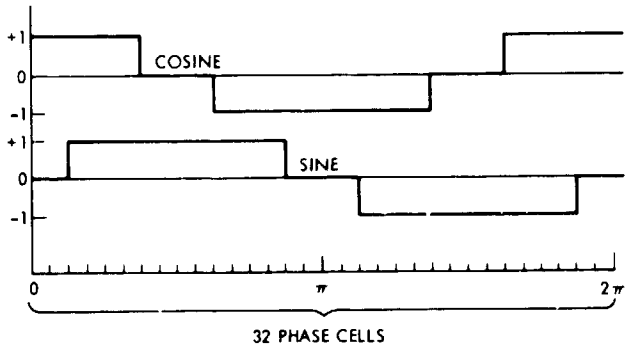

Fig. 3. Sine and cosine approximations

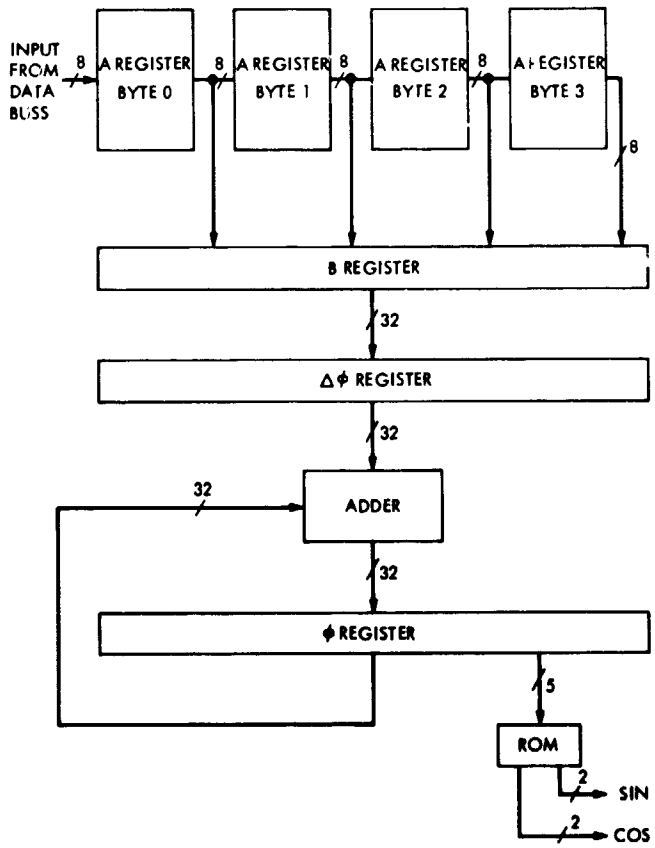

Fig. 4. Lobe rotator block diagram

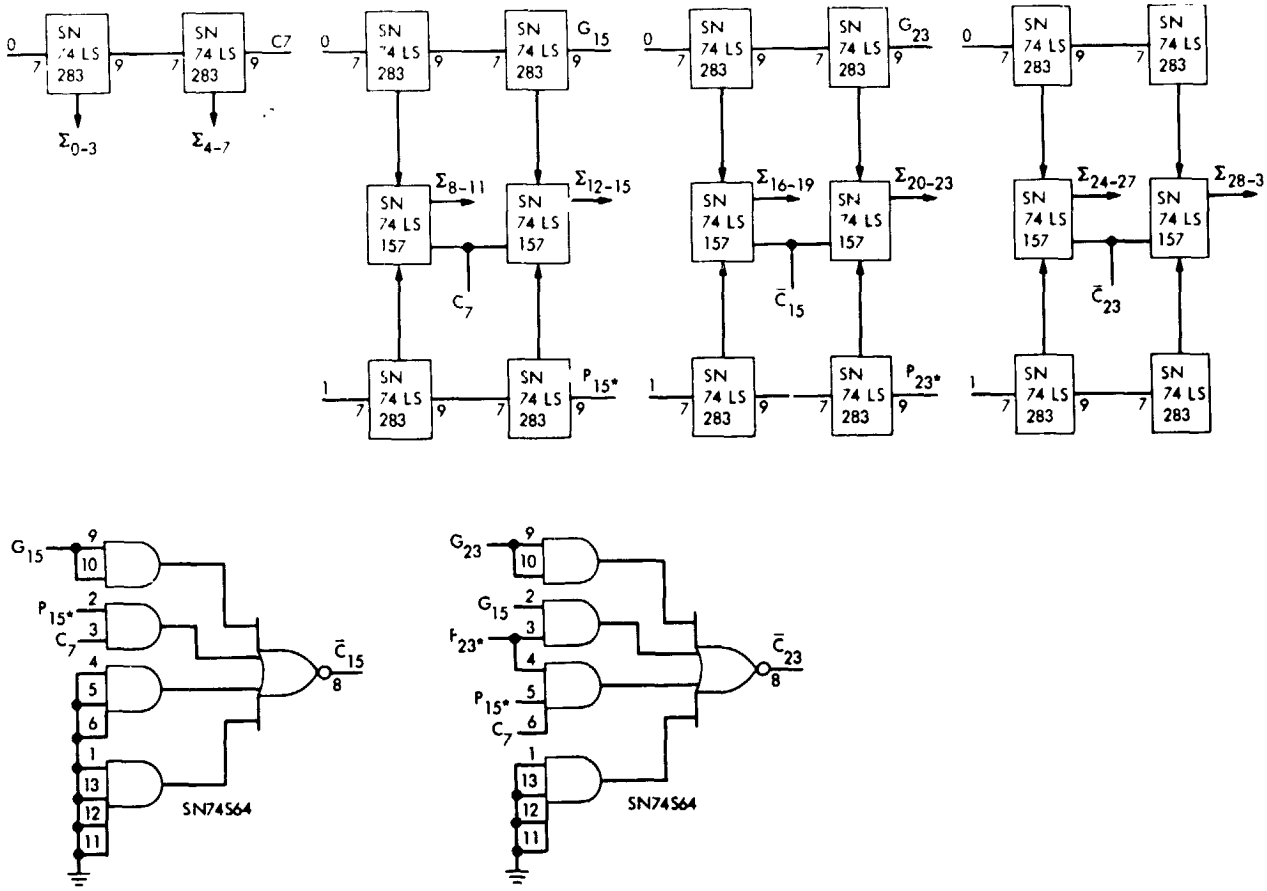

Fig. 5. Adder block diagram

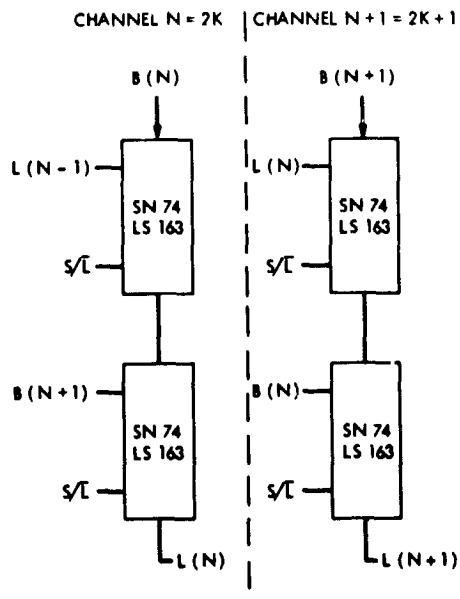

Fig. 6. Lag rearrangement

Three-Channel Integrating Analog-to-Digital Converter

G. L. Stevens
Communications Systems Research Section

A three-channel integrating analog-to-digital converter has been added to the complex mixer system. It accepts the baseband, complex signals generated by the complex mixers and outputs binary data to the digital demodulator for further processing and recording. It was first used for processing multistation data in radar experiments in the spring of 1977.

I. Introduction

A three-channel integrating analog-to-digital converter (IADC) has been added to the Complex Mixer System (Ref. 1) in the pedestal room at DSS 14. The IADC performs the integrate and dump function, accepting the real and imaginary baseband signals generated by the complex mixers, and supplying six-bit binary integral values to the digital demodulator (DDM) for further processing and recording.

This unit was designed to be operated with the modified complex mixer modules (Ref. 2). Signals from one, two, or three complex mixer modules can be processed simultaneously by the IADC, with each channel receiving its own timing reference signal from the DDM. Integration times of 1.3, 5, 15, or 45 μs can be accommodated by the unit.

II. Equipment Description

A block diagram showing one channel of the three channel IADC is shown in Fig. 1. Three identical but independent complex channels exist within the unit. Each channel is comprised of two identical signal paths whose sampling, conversion, and digital functions are synchronously controlled by a shared timing generator.

The analog signals processed by the IADC are generated by the complex mixers. Real and imaginary baseband signals are produced in each complex mixer module by splitting the IF signal into two paths and mixing with local oscillator signals that are in phase quadrature. The resulting real and imaginary baseband signals are then bandlimited to 2 MHz by low-pass filters and amplified to a nominal output level of 2 V_{p-p}.

Each of the three complex channels within the IADC receives a separate clock signal generated within the DDM. The positive-going transition of each clock pulse initiates a timing sequence within each channel. Timing signals are generated to operate the sampling and conversion processes as well as controlling the digital dump, front panel indicators and output data registers.

Each signal path within this equipment employs a digital dump which calculates an approximation to the desired integral values. This technique is described in detail in Ref. 3. Each analog input signal is first passed through a simple RC low-pass filter which acts as an imperfect integrator. The filtered signal is then amplified, sampled, and A-D converted. The digital sample values are then fed to data registers contained within the digital dump logic. One register holds the current sample value, while a second register holds the previous sample value.

From these two values, the digital dump calculates an approximation to the required integral ΔE from

$$\Delta E = E_n - \frac{3}{4} E_{n-1}$$

where E_n is the present voltage sample, and E_{n-1} is the previous voltage sample.

The low-pass filter time constant τ is determined by the word size in the dump logic and the integration time T. The ratio T/τ is chosen to minimize errors introduced by this technique. For this equipment

$$\frac{T}{\tau} = 0.288$$

with a corresponding degradation of less than 0.1 dB when compared to a perfect integrate and dump. This unit has been operated at various sampling rates from 1.3 to 45 μs by selecting appropriate filter time constants and associated gain control elements.

The internal sample values and the computed integral values are bipolar 8-bit numbers. The word size of the output data is 6-bits, with negative values represented in two's complement. Front panel data/ $\overline{\text{data}}$ switches allow the selection of positive-true or one's-complemented output data. A front panel gain control switch associated with each complex channel allows the user to select the desired binary scaling of the 6-bit data word.

Three positions are available:

X1: In this mode, the sign bit (bit 1) and the five adjacent bits (2 through 6) of the 8-bit integral value are selected as the output data word. No overflows can occur in this mode. Rounding is provided in this gain position.

X2: In this mode, the sign bit plus the five intermediate bits (3 through 7) of the 8-bit integral value are selected. In this mode, the full-scale integral values that can be represented in the 6-bit data word is reduced to one-half of that that could be represented in the X1 gain mode. Simultaneously, the resolution is increased by a factor of two by using these lower order bits. Should a rollover occur into the unused bit 2, the condition is detected, and the appropriate positive or negative full-scale code is forced onto the output data lines. A front panel light-emitting diode (LED) indicator is simultaneously pulsed on, indicating that the saturation has occurred. Rounding is provided in this gain position.

X4: In this mode, the sign bit and the five least significant bits (4 through 8) of the computed integral value are selected. Rollovers are detected, corrected and displayed.

When operating in the X2 or X4 gain modes, internal overflows can occur. These overflows are detected, and the output data lines are forced to the appropriate saturation code. In addition, the occurrence of an overflow in one of the channels triggers a one-shot multivibrator and driver which momentarily turns on a front panel LED indicator, yielding a visual indication that the data saturation has occurred. Each of the six signal channels has two associated LEDs, one for positive and one for negative data saturations. Occasional flashing of these indicators indicates that the full dynamic range of the IADC is being exercised. Continuous illumination of any LED indicates improper signal level adjustment or hardware failure.

The analog signals supplied to the IADC should have a level of approximately 0.33 V_{rms}. At this level, 3 σ noise peaks of 2 V_{p-p} will be passed without clipping. Six input signal level monitors continuously check the input signal levels and drive front panel meters. These monitors are not intended for use in making precise measurements, as these simple uncalibrated meters are used only to confirm proper input signal levels. A red line on each meter face indicates the nominal reading.

III. Performance

The IADC is designed to process the baseband output signals generated by the complex mixers and supply output data to the DDM. Input and output characteristics were therefore determined by these systems. Table 1 summarizes the IADC's specifications.

IV. Packaging

The three-channel IADC is a self-contained rack-mounted unit that occupies 17.8 cm (7 in.) of rack space. Four wire wrap boards hold the digital logic and A-D converter modules. These four logic boards plus power supplies are mounted within the logic cage pictured in Fig. 2. Figure 3 shows the component side of one of the logic boards.

V. Summary

A three-channel IADC has been added to the complex mixer system. Installed in the pedestal room at DSS 14 in March of 1977, this unit was used to process planetary radar signals received at DSS 12, DSS 13 and DSS 14 in March and April.

References

1. Constenla, L. C., *Complex Mixer System*, Technical Report 32-1526, Jet Propulsion Laboratory, Pasadena, California, Dec. 15, 1972.

2. Stevens, G. L., "Complex Mixer System Modifications," in *The Deep Space Network Progress Report 42-42*, Jet Propulsion Laboratory, Pasadena, California, Dec. 1977.

3. Winkelstein, R. A., "High Rate Telemetry Project, Digital Equipment," in *The Deep Space Network*, Space Programs Summary 37-48, Vol. II, pp. 111-112, Jet Propulsion Laboratory Pasadena, California, Nov. 30, 1967.

Table 1. Three-channel IADC specifications

Parameter	Value	Comment
Sampling period	1,3,5,15 or 45μs	
Input impedance	50 Ω	Each of 6 analog inputs
Input signal level	0.33 V_{rms}	Nominal output level of complex mixers
Input signal bandwidth	DC to 2 MHZ	Nominal bandwidth of complex mixers
Output word size	6 bits	
Output coding	2's complement	Negative values are represented in 2's complement
Output polarity	Positive-true or one's complemented	Controlled by front panel DATA/$\overline{\text{DATA}}$ switches

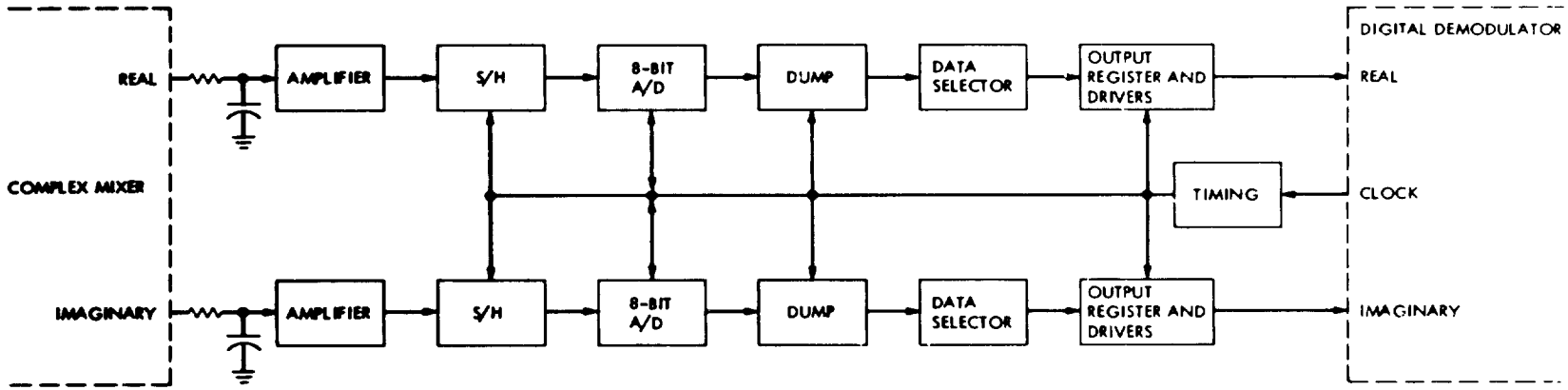

Fig. 1. Block diagram showing one channel of the three-channel IADC

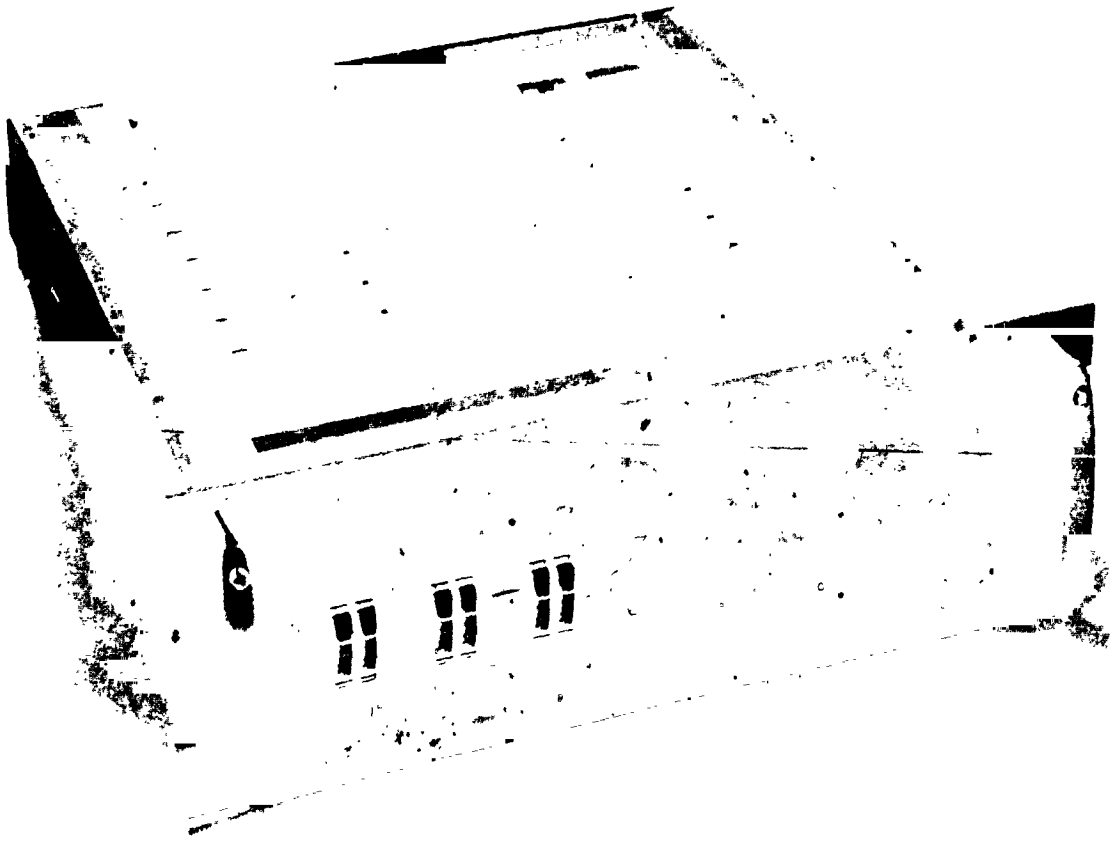

Fig. 2. Three-channel integrating analog-to-digital converter

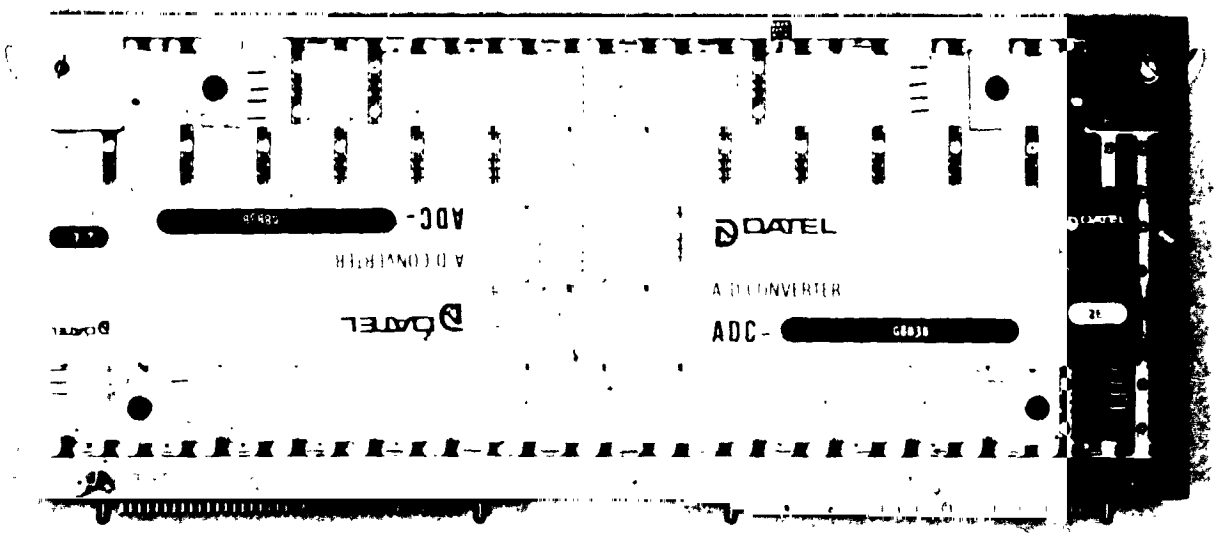

Fig. 3. Component side of analog-to-digital converter card

N78-24199

The Role of Interest and Inflation Rates In Life-Cycle Cost Analysis

I. Eisenberger and D. S. Remer
Communications Systems Research Section

G. Lorden
California Institute of Technology

The effect of projected interest and inflation rates on life cycle cost calculations is discussed and a method is proposed for making such calculations which replaces these rates by a single parameter. Besides simplifying the actual method clarifies the roles of these rates. An analysis of historical interest and inflation rates from 1950 to 1976 shows that the proposed method can be expected to yield very good projections of life-cycle cost even if the rates themselves fluctuate considerably.

I. Introduction

In life-cycle cost (LCC) studies it is common practice to estimate future costs in constant dollars and to use an assumed inflation rate to transform these estimates to actual dollars. The choice of an inflation rate for such projections can strongly affect the computed LCC. Table 1 shows the effect of the inflation rate on the 10-year LCC of a project whose yearly cost is $1 in constant dollars (reflecting prices and wages at the start of the project).

Frequently LCC studies take into account the "time value of money" by discounting future expenditures using an assumed discount rate (interest rate). The effect of discounting on LCC (assuming no inflation) is illustrated by Table 2.

These tables show how strongly LCC computations reflect the choice of rates. Even when both inflation and discounting are considered, if a wide range of possible choices for the rates is permitted, then the comparison of a project with high initial cost and, say, another project with low initial cost but comparatively high recurring costs can vary drastically.

This report proposes a simplified method of LCC calculation using a single parameter V that combines the effects of inflation and discounting, taking advantage of the fact that, to a large extent, they cancel each other out. Historical data on interest rates and inflation rates from 1950 to 1976 are analyzed to determine how stable the parameter V is and to indicate a reasonable value for this parameter and the accuracy one can expect from its use in LCC projections.

II. Combining Discount and Inflation Rates

Whenever the "time value of money" is considered, the life-cycle cost is the sum of all costs in the life-cycle *discounted* at an interest rate i to some time point t_0. One might choose t_0 to be the beginning of the operational phase or, perhaps, the time of first expenditure not yet committed. Furthermore, it is common practice to pick a time point t_1 at

which wages and prices are known and then to estimate all costs in "t_1 dollars." *Actual dollar* expenditures are estimated by transforming from t_1 dollars, using an assumed inflation rate j. (For simplicity, we ignore the straightforward refinement where different j's are applied to different types of costs such as labor costs or material costs.)

There is good reason to choose t_0 and t_1 to coincide. The LCC then depends only on

$$V = \frac{1+j}{1+i}$$

This is because an expenditure at time t of an amount C in t_1 - dollars implies a cost in actual dollars of

$$C(1+j)^{t-t_1},$$

and the discounted value of this at time t_0 is

$$C(1+j)^{t-t_1}(1+i)^{-(t-t_0)},$$

which, if $t_0 = t_1$, is equal to CV^{t-t_0}. Thus, one can compute the LCC by specifying only the assumed V rather than both i and j. Specifically, if $C_1, \ldots, C_n$ are the estimated yearly costs in current dollars, then the LCC (evaluated at the present) is given by

$$LCC = \sum_{k=1}^{n} C_k V^k$$

There are obvious advantages to dealing with only one "arbitrary" parameter. For example, one can bracket the LCC by computing it using "high" and "low" choices of V. A more important benefit from considering V is to reduce substantially the seeming unpredictability of future interest and inflation rates. Historically, interest rates tend to exceed inflation rates by about 2-3%. Figure 1 shows this tendency over the years 1950 to 1976, using for illustration the long-term Treasury bond yield (Refs. 1 and 2) and the index of consumer prices by the Bureau of Labor Statistics (Ref. 3). Furthermore, V is essentially a function of the difference of rates, $i - j$, as Fig. 2 reveals. (In fact, the approximation $V = 1 - (i-j)/(1+i) \approx 1 - (i-j)$ is good enough for most purposes). It is natural, then, to ask how stable is V historically or, more important, how much do LCC's vary when computed using the *actual* interest and inflation rates over different historical periods?

A study was made using the inflation and interest rate data for 1950 - 1976 to determine what actual LCCs would have been for projects spanning all 5, 10, 15, or 20-year subintervals of that period, assuming costs of one dollar per year expressed in current dollars at the start of the project. The LCC for, say, a 10-year project starting in year m is then obtained from the formulas

i_k = interest rate in year k

j_k = inflation rate in year k

$$V_k = \frac{1+j_k}{1+i_k}$$

$$LCC = V_m + (V_m V_{m+1}) + \cdots + (V_m V_{m+1} \cdots V_{m+9})$$

The results of these computations are displayed in Fig. 3. The conclusion indicated by these results is clearly that LCCs based on actual rates are quite stable historically. Over this 27-year period the variations of LCCs are a relatively small percentage of the LCCs themselves. If this stability continues (and recall that the actual yearly rate fluctuations in Fig. 1 are considerable), it should be possible to choose a value of V that will project future experience with a reasonable degree of accuracy and confidence. Standardizing the to be used in LCC calculations for the DSN has the advantages of simplicity and uniformity.

What is a good choice of V for the DSN? The value of V that yields a 10-year LCC matching the average of the 10-year LCCs in Fig. 3 is 0.983, and choosing $V = 0.98$ (for simplicity) seems reasonable to us.

This choice agrees very well with the data for 5, 10, 15, and 20 years. A good case can be made for setting $V = 1$, thereby letting interest and inflation cancel completely and simplifying LCC calculations. How much difference does it make in the LCC when one makes small changes in V? Routine computation shows that for V between 0.9 and 1 each decrease of 0.01 in V yields about the same percentage decrease in LCC, the amount of this decrease depending on the length of the life cycle. Table 3 illustrates the outcomes for $n = 5$, 10, 15, and 20 years with $V = 0.97$ and 0.98. Note that for a 10-year project the LCC with $V = 1$ is 10 and drops to about 9.5, 9.0, 8.5 as V goes through 0.99, 0.98, 0.97.

Whatever value of V is settled upon, this approach to inflation and discounting seems to us a valid and simple alternative to the conventional numbers game of trying to predict future interest and inflation rates.

III. Conclusion

As pointed out in the introduction, the choice of inflation and discount rates can have a powerful effect on the results of

LCC calculations. Inflating costs without discounting (or the reverse) can easily lead to making the wrong choice between competing projects. Even when both rates are used, arbitrary choices can lead to a wide range of possible results.

Our analysis shows that inflation and discounting largely cancel each other and it is essentially only the difference between them that affects LCC. This difference is relatively small, discount rates generally being slightly higher than inflation rates. Furthermore, fluctuations in the rates tend to cancel out over project lifetimes. As a consequence, a single parameter V can be chosen to estimate the net effect of future discount and inflation rates with a reasonable degree of confidence. The value $V = 0.98$, reflecting discount rates about 2% higher than inflation rates, is recommended for DSN use, based on a good fit to actual rates over the period 1950–1976.

References

1. "Business Conditions Digest," U.S. Department of Commerce, Bureau of Economic Analysis, p. 108, Feb. 1976.
2. Federal Reserve Bulletin, p. A27, June 1977.
3. "Business Conditions Digest," U.S. Department of Commerce, Bureau of Economic Analysis, p. 97, Mar. 1977.

Table 1. Effect of inflation rate on LCC

Inflation rate, %/yr	LCC	% increase over zero inflation
0	10.0	–
2	11.17	11.7
4	12.49	24.9
6	13.97	39.7
8	15.65	56.5
10	17.53	75.3
15	23.35	133.5

Table 2. Effect of discount rate on LCC

Discount rate, %/yr	LCC	% decrease over zero discounting
0	10.00	–
2	8.98	10.2
4	8.11	18.9
6	7.36	26.4
8	6.71	32.9
10	6.14	38.6
15	5.02	49.8

Table 3. LCC of a project costing $1 per year

No. years	$V = 0.97$	$V = 0.98$	% increase
5	4.57	4.71	3.1
10	8.49	8.96	5.6
15	11.86	12.81	8.0
20	14.75	16.29	10.4

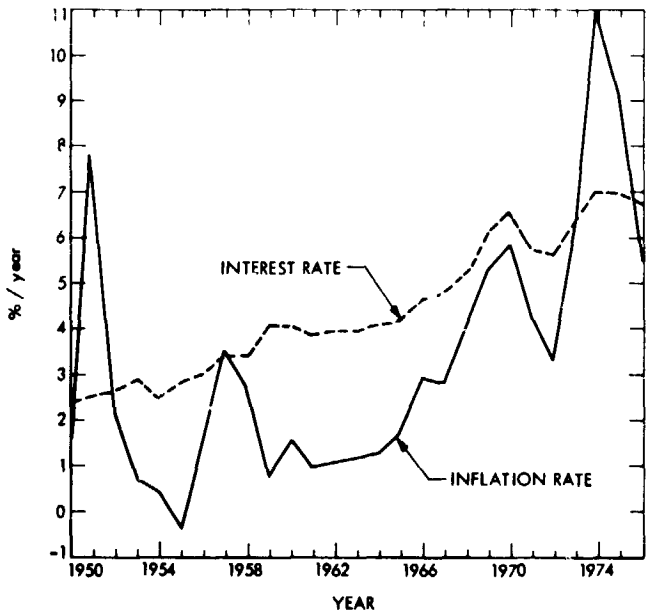

Fig. 1. Interest and inflation rates (1950–1976)

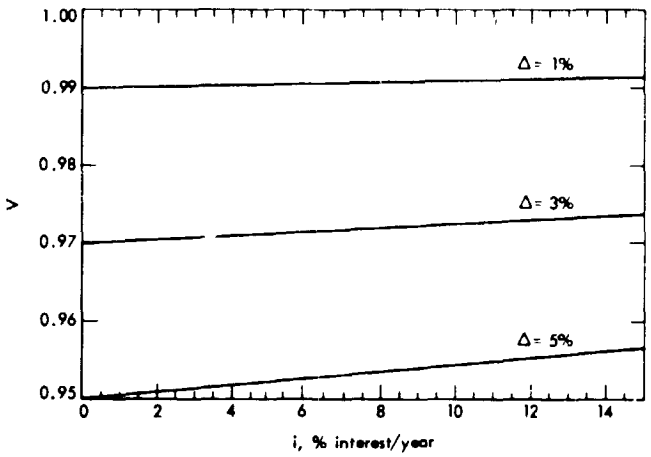

Fig. 2. *V* as a function of *i* for fixed $\Delta = i - j$

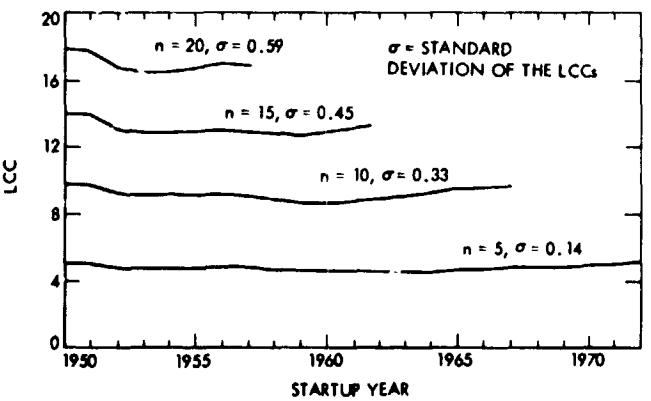

Fig. 3. LCC for *n*-year lifetimes, with startup years from 1950–1972

Deep Space Telecommunications and the Solar Cycle: A Reappraisal

A. L. Berman
TDA Engineering Office

Observations of density enhancement in the near corona ($r \leqslant 5r_\odot$) at solar cycle (sunspot) maximum have rather uncritically been interpreted to apply equally well to the extended corona ($r \geqslant 5r_\odot$), thus generating concern about the quality of outer planet navigational data at solar cycle maximum. Spacecraft have been deployed almost continuously during the recently completed solar cycle 20, providing two powerful new coronal investigatory data sources: (1) in-situ spacecraft plasma measurements at approximately 1 AU, and (2) plasma effects on monochromatic spacecraft signals at all signal closest approach points.

A comprehensive review of these (solar cycle 20) data leads to the somewhat surprising conclusion that for the region of interest of navigational data ($r \geqslant 30r_\odot$), the highest levels of charged-particle corruption of navigational data can be expected to occur at solar cycle minimum, rather than solar cycle maximum, as previously believed.

I. Introduction

A modern view of electron density in the near corona (here to be defined as $r \leqslant 5r_\odot$, where r is the solar radial distance and $r_\odot$ is the solar radius) begins with the careful eclipse white light photometry analysis of van de Hulst in the late 1940s (Refs. 1 and 2). The white light corona is composed of two primary components, the K corona, resulting from Thompson scattering by free electrons, and the F corona (zodiacal light), resulting from scattering by interplanetary dust. Van de Hulst made various assumptions which allowed him to separate out the F corona, and hence obtain the K corona, or the desired near corona electron density. As part of this exercise, van de Hulst adopted a value of 1.8 for the ratio of solar (sunspot) cycle maximum equatorial electron density to solar (sunspot) cycle minimum equatorial electron density, based on coronal brightness comparisons (eclipse photometry) between solar cycle maximum and minimum. At about the same time, Saito (see Billings, Ref. 3), also working to obtain coronal electron density, deduced a similar value of approximately 2.0 for the solar cycle ratio (subsequently in this report, the term "solar cycle ratio" will be defined for a given parameter as the parameter (average) value at solar cycle maximum divided by the parameter (average) value at solar cycle minimum).

Since that time, a number of coronal investigators, performing eclipse photometry analysis, have obtained similar near corona equatorial electron density solar cycle ratios. For instance, the composite eclipse photometry analysis by Blackwell, et al. (Ref. 4) produced a solar cycle ratio of 1.9 ($2_\odot$). A consensus of eclipse photometry, radio interferometry, and radio scattering experiments into the mid-1960s (Newkirk,

Ref. 5) produced a solar cycle ratio for near corona electron density of approximately 2.0. More recently, Hansen et al. (Ref. 6), using a K coronameter to investigate the near corona region under $2r_\odot$ on a daily basis during the ascendant portion of solar cycle 20 (1964 to 1967), convincingly confirmed the near corona solar cycle ratio of approximately 2.0.

The observed density enhancement of the near corona at solar cycle maximum has (not surprisingly!) come to be applied to the extended corona (here defined as $r \gtrsim 5r_\odot$) as well, to the point where it is now considered axiomatic that the highest electron densities (and density fluctuations) in the extended corona occur at solar cycle maximum. This assumption has resulted in an elevated level of anxiety about navigational data (doppler and range) quality[1] during the upcoming (1979-1981) solar cycle 21 maximum. There exists particular concern about radiometric data quality during the pre-Saturn encounter periods for both Pioneer 11 and Voyager.

Prior to the start of solar cycle 20 (1964), the main tools available for coronal electron density investigation were white light eclipse photometry, K coronameter, and natural radio source scattering (principally of the Crab Nebula). However, the advent of solar cycle 20 marked the near continuous deployment of deep space probes (both Earth orbiters beyond the magnetosphere and planetary probes), offering two new incredibly powerful coronal investigatory tools:

(1) In-situ plasma measurements at approximately 1 AU

(2) Columnar measurements over all signal closest approach points of the plasma effects on a monochromatic spacecraft signal

A comprehensive review of both types of spacecraft measurements made during the full extent of solar cycle 20 reveals startling results which strongly contradict the "conventional wisdom" concerning enhanced density in the extended corona during solar cycle maximum, these results being:[2]

Density region (equatorial)	Solar cycle ratio
Near corona ($r \lesssim 5r_\odot$)	~2.0
Extended corona ($r \gtrsim 5r_\odot$)	
$r = 10r_\odot$	~1.0
$r = 1$ AU	~0.65

[1] A detailed derivation and description of the effect of free electrons on doppler and range can be found in MacDoran, Ref. 7.

[2] Note that these results are in no way contradictory. For instance, if the particle flux were assumed constant with solar cycle, all that is required is a change in the radial solar wind velocity signature with solar cycle, as is sketched in Fig. 1.

For radio metric (navigational) data quality, the $10r_\odot$ to 1 AU results are the most important, and indicate (if solar cycle 21 proves similar to solar cycle 20):

(1) Electron density (and density fluctuations) between $10r_\odot$ and 1 AU can be expected to stay roughly the same ($10r_\odot$) or decrease (1 AU) between now and approximately 1981.

(2) The extensive doppler phase fluctuation work done during the 1975 to 1976 solar cycle 20 minimum (Refs. 8–18), should provide an *upper bound* for the expected radio metric data plasma corruption over the next solar cycle.

The following sections will describe the solar cycle variations (in both mean value and fluctuation) of electron density (at $10r_\odot$ and 1 AU), solar wind velocity at 1 AU, particle flux at 1 AU, and the columnar density fluctuation spectral index.

II. Solar Wind Variations With Solar Cycle at 1 AU

As mentioned in Section I, many deep space probes have been deployed since the beginning of solar cycle 20 (1964), particularly Earth orbiters (beyond the magnetosphere) at approximately 1 AU. The major obstacle in utilizing the resultant in-situ plasma measurements is that each spacecraft has separate systematic errors (bias and linear) in each of the parameters measured (density, wind velocity, etc.), hence it would be of dubious value to compare the "unnormalized" plasma measurements from the 10 plus spacecraft needed to span the solar cycle 20 time frame. Fortunately, the problem of spacecraft intercalibration has been addressed by Diodato, et al. (ref. 19) who have intercalibrated in-situ plasma measurements for a number of Earth orbiters during the period 1965 to 1971. The process of intercalibrating spacecraft is in itself subject to error, as is discussed by M. Neugebauer (Ref. 20); however, the Diodato data are the best available and are expected to provide a reasonably valid picture. The Diodato data will be utilized to examine the variation of density and particle flux with the solar cycle. For solar wind velocity variations with solar cycle, the recent and significantly more encompassing work of Gosling, et al. (Ref. 21), will be utilized.[3]

The basic format of the data will be presentations in bar graph form of various parameter yearly averages, as compared to the observed sunspot number during the same time frame.

[3] Intercalibration of spacecraft solar wind velocity measurements is a considerably less severe problem than for density measurements (on a percentage basis).

A. Proton Density

Although electron density is the parameter of interest in regard to navigational data quality, the approximate equality between solar wind electrons and protons allows the usage of proton density for the same purpose. The slight difference between the two occurs because of the presence of a small amount of helium in the solar wind; Ogilvie, et al. (Ref. 22) shows the helium presence, although correlated with solar cycle, to be only about 4% ± 0.5% (of hydrogen) over the solar cycle, and hence not particularly significant to the overall density picture. The density parameters from Diodato, with the exception of Fig. 5 which is from M. Neugebauer (Ref. 23), are:

Figure 2. Proton density yearly average at 1 AU, 1965–1971

Figure 3. Proton fluctuation density yearly average at 1 AU, 1965–1971

Figure 4. Proton fluctuation to density ratio, yearly average from 1965–1971, at 1 AU

Figure 5. Long-term averages of fractional time density $> 10\ cm^{-3}$ at 1 AU, from 1962–1972

Examination of Fig. 2 clearly indicates a pronounced (anti) correlation of density with solar cycle. The data in Fig. 2 indicate a solar cycle ratio of approximately 0.65. Feldman, et al. (Ref. 24) give more recent density information from the Imp spacecraft as follows:

1972/1973 average (Imp 7): $N_p = 9.0\ cm^{-3}$

1973/1974 average (Imp 8): $N_p = 11.3\ cm^{-3}$

Even allowing for a possible 10 to 20% calibration difference, these numbers clearly continue the strong trend of Fig. 2.

Figure 3 shows the same solar cycle anticorrelation for the average yearly density fluctuation (standard deviation); the solar cycle ratio is again approximately 0.65. The Feldman, et al. Imp 7 and 8 density fluctuation numbers are:

1972/1973 average: $\sigma(N_p) = 4.3\ cm^{-3}$

1973/1974 average: $\sigma(N_p) = 5.4\ cm^{-3}$

continuing the same pronounced trend in the density fluctuation as in the (mean) density itself.

The ratio of density fluctuation to (mean) density as seen in Fig. 4 does not show a clear trend with solar cycle; the average value for this parameter over the seven year period 0.56. The corresponding Feldman et al. numbers are:

1972/1973 average $\epsilon = 0.48$

1973/1974 average $\epsilon = 0.48$

Finally, Fig. 5 (from Neugebauer, Ref. 23), which presents long-term averages of fractional time density $> 10\ cm^{-3}$, and encompasses a greater number of spacecraft and a longer time frame (than the Diodato data), corroborates and strengthens the density fluctuation data presented in Fig. 3. Figure 5 is a most dramatic view of the pronounced anticorrelation of density and density fluctuation with solar cycle at 1 AU, and indicates that the corruption of navigational data (at least in the general vicinity of 1 AU) will be highest at solar cycle minimum, and lowest at solar cycle maximum, both in regard to range errors (density) and doppler errors (density fluctuation).

B. Proton Flux

The proton (particle) flux data from Diodato is presented as follows:

Figure 6. Proton flux yearly average at 1 AU, 1965 to 1971

Figure 7. Proton fluctuation flux yearly average at 1 AU, 1965 to 1971

Figure 8. Proton flux fluctuation to flux ratio, yearly average from 1965 to 1971, at 1 AU

These proton flux data very much pattern the behavior of the equivalent proton density parameters, which is mostly a reflection that the solar wind velocity is far more stable (percentage wise) with the solar cycle than is density. The solar cycle ratio of proton flux is 0.7, while for flux fluctuation it is 0.65. The average ratio of flux fluctuation to flux is approximately 0.52, or slightly lower than the equivalent density ratio.

C. Solar Wind Radial Velocity

Solar wind radial velocity from Gosling, et al. is presented as follows:

Figure 9. Solar wind radial velocity yearly average at 1 AU, 1964 to 1974

Figure 10. Solar wind fluctuation radial velocity yearly average at 1 AU, 1964 to 1974

Figure 11. Solar wind velocity fluctuation to velocity ratio, yearly average from 1964 to 1974, at 1 AU

In sharp contrast to the density and flux at 1 AU, it is difficult to discern a clear variation of solar wind velocity with solar cycle; of the three years of significantly enhanced velocity (1968, 1973, 1974), one occurs at solar cycle maximum and

two occur during the declining portion of the cycle, near to solar cycle minimum. If one is forced to make a decision, one would have to decide in favor of anticorrelation with the solar cycle, albeit much less pronounced than that displayed by density and flux. Gosling et al. were much more firm in this conviction (i.e., of definite anticorrelation) based on their data.[4] At any rate, the solar cycle ratio for the radial velocity would seem to be at least 0.8. Somewhat strangely, the radial velocity fluctuation data seen in Fig. 10 demonstrate a much more pronounced anticorrelation with solar cycle; the solar cycle ratio for radial velocity fluctuation is 0.7. Finally, the ratio of velocity fluctuation to (mean) velocity averages about 0.17, or only about 30% of the equivalent density parameter.

III. Electron Density Variation With Solar Cycle at $r = 10r_\odot$

Even as solar cycle 20 was beginning in the mid-1960s, there was information available which suggested that the near corona density enhancement observed at solar cycle maximum did not necessarily apply to the extended corona. The eclipse photometry of Blackwell is summarized by Anderson (Ref. 29) as follows:

Solar cycle maximum:

$$N_e(r) = \frac{2.62 \times 10^8}{r^6} + \frac{2.07 \times 10^6}{r^{2.33}}, \text{cm}^{-3}$$

Solar cycle minimum:

$$N_e(r) = \frac{1.01 \times 10^8}{r^6} + \frac{2.01 \times 10^6}{r^{2.33}}, \text{cm}^{-3}$$

Although the near corona solar cycle ratio is approximately 2.6, the values of the Blackwell models at $r = 10r_\odot$ are:

Solar cycle maximum: $N_e(10r_\odot) = 9940\ \text{cm}^{-3}$

Solar cycle minimum: $N_e(10r_\odot) = 9500\ \text{cm}^{-3}$

or virtually no variation with solar cycle at $r = 10r_\odot$. Since the mid-1960s, a number of experiments have been conducted to (indirectly) measure and subsequently model electron density in the extended corona. These experiments have utilized either spacecraft signals or natural sources (primarily pulsars) as these signals passed through a wide variation of signal closest approach points. The measurements yield total columnar density, which is then mapped back to a radially dependent density model after making suitable assumptions. Table I presents these models as evaluated at $r = 10r_\odot$; the same data appear in Fig. 12. Examination of Fig. 12 indicates no significant correlation with solar cycle. Although the data appear sparse at first glance, it is important to bear in mind that in most cases each point represents the distillation of copious amounts of data taken over weeks or months; still, a better determination of the solar cycle variation of density at $r = 10r_\odot$ will have to await the expected high quality dual frequency range results of the Viking and Voyager spacecraft.

IV. Variation of the Columnar Fluctuation Spectral Index With the Solar Cycle

The columnar fluctuation spectral index is based on the commonly accepted assumption for a power law form of the columnar (two-dimensional) fluctuation spectrum:

$$P(\nu) = K_1 \nu^{-K_0}$$

where

P = columnar fluctuation spectrum

ν = fluctuation frequency

K_0 = spectral index

The significance of the spectral index is that, given the same level of low frequency (long time scale) fluctuation, a larger spectral index yields a smaller amount of high frequency (short time scale) fluctuation (i.e., the fluctuations "fall off" more rapidly with increasing frequency). Experiments have been performed to measure the in situ (one dimensional) density fluctuation spectrum as well as the columnar fluctuation spectrum; the two spectral indices are related (Cronyn, Ref. 34) via the relationship:

$$(K_0)_{\text{columnar}} = (K_0)_{\text{in situ}} + 1$$

Table 2 and Fig. 13 present the columnar fluctuation spectral indices as well as in situ "equivalents"; examination of Fig. 13 reveals no clear or significant variation with solar cycle. The data (points) are quite sparse, but again, each point represents a large amount of processed data, spanning time periods of several days to several months. If pressed, one would have to say that the spectral index looks to be slightly larger (steeper) at solar cycle maximum, indicating a more rapid falloff of

[4] An additional piece of data not shown in Fig. 9 is a (high) yearly average radial velocity of 489 km/s for 1962, which is a near solar cycle minimum year. With this additional data, the case for significant anticorrelation is strengthened.

high frequency fluctuations during cycle maximum, and thus in consonance with the low frequency fluctuation data of Figs. 3 and 5.

Berman has reported (Ref. 15) a new technique and DSN capability which allows spectral index information to be easily extracted from routine doppler noise. If proven out, this new technique should allow voluminous amounts of spectral index data to be acquired during solar cycle 21, and analyzed for solar cycle variation.

V. Summary and Conclusions

Table 3 summarizes the relationship to solar cycle of the various parameters described in this report. For navigational usage of radiometric data, the most important region is $r \gtrsim 30 r_{\odot}$, or a Sun-Earth-probe angle $\gtrsim 8$ degrees. For this region, the experience at $r = 1$ AU ($215 r_{\odot}$) should be the most applicable. The 1 AU experience during solar cycle *maximum* which is most important to navigational data is

Density	Strong minimum
Density fluctuation	Strong minimum
Fractional time	
Density $> 10\ cm^{-3}$	Strong minimum
Velocity fluctuation	Moderate minimum
Spectral index	No change or weak maximum

Based on the above, solar cycle *maximum* would appear to yield the lowest level of charged-particle corruption of navigational data, and hence the placement of the Pioneer 11 and Voyager Saturn encounters (near solar cycle 21 maximum) may in fact prove close to optimum, rather than decidedly inopportune, as is currently considered.

References

1. van de Hulst, H. C., "The Electron Density of the Solar Corona," *Bulletin of the Astronomical Institutes of the Netherlands*, Volume XI, Number 410, February 2, 1950.
2. van de Hulst, H. C., "The Chromosphere and the Corona," in *The Sun*, edited by G. P. Kuiper, The University of Chicago Press, Chicago, Illinois, 1953.
3. Billings, D. E., *A Guide to the Solar Corona*, Academic Press, New York, London, 1966.
4. Blackwell, D. E., Dewhirst, D. W., and Ingham, M. F., *Advances in Astronomy and Astrophysics* 5, Academic Press, New York, 1967.
5. Newkirk, G., "Structure of the Solar Corona," in *The Annual Review of Astronomy and Astrophysics*, Vol. 5, 1967.
6. Hansen, R. T., Garcia, C. J., Hansen, S. F., and Loomis, H. G., "Brightness Variations of the White Light Corona During the Years 1964-1967," in *Solar Physics* 7, 1969.
7. MacDoran, P. F., "A First Principles Derivation of the Differenced Range versus Integrated Doppler (DRVID) Charged Particle Calibration Method," in *The Deep Space Network, Space Programs Summary 37-62*, Volume II, Jet Propulsion Laboratory, Pasadena, California, March 31, 1970.
8. Berman, A. L., and Wackley, J. A., "Doppler Noise Considered as a Function of the Signal Path Integration of Electron Density," in *The Deep Space Network Progress Report 42-33*, Jet Propulsion Laboratory, Pasadena, California, 15 June 1976.
9. Berman, A. L., Wackley, J. A., Rockwell, S. T., and Yee, J. G., "The Pioneer 11 1976 Solar Conjunction: A Unique Opportunity to Explore the Heliographic Latitudinal Variations of the Solar Corona," in *The Deep Space Network Progress Report 42-35*, Jet Propulsion Laboratory, Pasadena, California, 15 October 1976.

10. Berman, A. L., Wackley, J. A., and Rockwell, S. T., "The 1976 Helios and Pioneer Solar Conjunctions — Continuing Corroboration of the Link Between Doppler Noise and Integrated Signal Path Electron Density," in *The Deep Space Network Progress Report 42-36*, Jet Propulsion Laboratory, Pasadena, California, 15 December 1976.

11. Berman, A. L., "A Comprehensive Two-Way Doppler Noise Model for Near-Real-Time Validation of Doppler Data," in *The Deep Space Network Progress Report 42-37*, Jet Propulsion Laboratory, Pasadena, California, February 15, 1977.

12. Berman, A. L., and Wackley, J. A., "Viking S-Band Doppler RMS Phase Fluctuations Used to Calibrate the Mean 1976 Equatorial Corona," in *The Deep Space Network Progress Report 42-38*, Jet Propulsion Laboratory, Pasadena, California, 15 April 1977.

13. Berman, A. L., Wackley, J. A., Rockwell, S. T., and Kwan, M., "Viking Doppler Noise used to Determine the Radial Dependence of Electron Density in the Extended Corona," in *The Deep Space Network Progress Report 42-38*, Jet Propulsion Laboratory, Pasadena, California, April 15, 1977.

14. Berman, A. L., "Proportionality Between Doppler Noise and Integrated Signal Path Electron Density Validated by Differenced S-X Range," in *The Deep Space Network Progress Report 42-38*, Jet Propulsion Laboratory, Pasadena, California, April 15, 1977.

15. Berman, A. L., "Phase Fluctuation Spectra: New Radio Science Information to Become Available in the DSN Tracking System Mark III-77," in *The Deep Space Network Progress Report 42-40*, Jet Propulsion Laboratory, Pasadena, California, August 15, 1977.

16. Berman, A. L., "Electron Density in the Extended Corona: Two Views," in *The Deep Space Network Progress Report 42-41*, Jet Propulsion Laboratory, Pasadena, California, October 15, 1977.

17. Berman, A. L., "An Empirical Model for the Solar Wind Velocity," in *The Deep Space Network Progress Report 42-42*, Jet Propulsion Laboratory, Pasadena, California, December 15, 1977.

18. Berman, A. L., "RMS Electron Density Fluctuation at 1 AU," in *The Deep Space Network Progress Report 42-42*, Jet Propulsion Laboratory, Pasadena, California, December 15, 1977.

19. Diodato, L., Moreno, G., Signorini, C., and Ogilvie, K. W., "Long Term Variations of the Solar Wind Proton Parameters," in *The Journal of Geophysical Research*, Volume 79, Number 34, Dec. 1, 1974.

20. Neugebauer, M., "The Quiet Solar Wind," in *The Journal of Geophysical Research*, Volume 81, Number 25, September 1, 1976.

21. Gosling, J. T., Asbridge, J. R., Bame, S. J., and Feldman, W. C., "Solar Wind Speed Variations: 1962–1974," *Journal of Geophysical Research*, Volume 81, Number 28, October 1, 1976.

22. Ogilvie, K. W., and Hirshberg, J., "The Solar Cycle Variation of the Solar Wind Helium Abundance," in *The Journal of Geophysical Research*, Volume 79, Number 31, November 1, 1974.

23. Neugebauer, M., "Large-Scale and Solar-Cycle Variations of the Solar Wind," in *Space Science Reviews* 17, 1975.

24. Feldman, W. C., Asbridge, J. R., Bame, S. J., Montgomery, M. D., and Gary, S. P., "Solar Wind Electrons," in *The Journal of Geophysical Research*, Volume 80, Number 31, November 1, 1975.

25. Edenhofer, P., Esposito, P. B., Hansen, R. T., Hansen, S. F., Luneburg, E., Martin, W. L., and Zygielbaum, A. I., "Time Delay Occultation Data of the Helios Spacecrafts and Preliminary Analysis for Probing the Solar Corona," in the *Journal of Geophysics* 42, 1977.

26. Weisberg, J. M., Rankin, J. M., Payne, R. R., and Counselman III, C. C., "Further Changes in the Distribution of Density and Radio Scattering in the Solar Corona," *The Astrophysical Journal*, Volume 209, October 1, 1976.

27. Anderson, J. D., Keesey, M. S. W., Lau, E. L., Standish, E. M., Jr., and Newhall, X. X., "Tests of General Relativity using Astrometric and Radiometric Observations of the Planets," Third International Space Relativity Symposium, International Astronautical Federation, XXVII Congress, Anaheim, October, 1976.

28. Counselman III, C. C., and Rankin, J. M., "Density of the Solar Corona from Occultations of NP0532," *The Astrophysical Journal*, Volume 175, August 1, 1972.

29. Anderson, J. D., Esposito, P. B., Martin, W. L., Thornton, C. L., and Muhleman, D. O., "Experimental Test of General Relativity Using Time Delay Data from Mariner 6 and Mariner 7," in *The Astrophysical Journal*, Volume 200, August 15, 1975.

30. Woo, R., Yang, F., Yip, W. K., and Kendall, W. B., "Measurements of Large Scale Density Fluctuations in the Solar Wind Using Dual Frequency Phase Scintillations," in *The Astrophysical Journal*, Volume 210, Number 2, Part 1, December 1, 1976.

31. Unti, T. W. J., Neugebauer, M., and Goldstein, B. E., "Direct Measurement of Solar Wind Fluctuations Between 0.0048 and 13.3 Hz," in *The Astrophysical Journal*, 180, March 1, 1973.

32. Goldstein, B., and Sisco, G. L., "Spectra and Cross Spectra of Solar Wind Parameters From Mariner 5," in *Solar Wind*, edited by Sonett, C. P., Coleman, P. J., Jr., and Wilcox, J. M., National Aeronautics and Space Administration, Washington, D.C., 1972.

33. Intriligator, D. S., and Wolfe, J. H., "Preliminary Power Spectra of the Interplanetary Plasma," in *The Astrophysical Journal, Letters*, 162, December 1970.

34. Cronyn, W. M., "Density Fluctuations in the Interplanetary Plasma: Agreement Between Space Probe and Radio Scattering Observations," *Astrophysical Journal*, Volume 171, February 1,1972.

Table 1. Electron Density Model Evaluations at $r = 10r_{\odot}$

Source	Reference	Time (center) of observations	Equatorial density, cm^{-3}	Type of experiment
Berman et al.	12	9–76	8610	VK doppler noise
Berman et al.	12	6–76	8190	PN, HE doppler noise
Edenhofer et al.	25	4–76	6340	HF, S-band range
Berman et al.	8,14	6–75	7080	PN, HE doppler noise
Weisberg et al.	26	6–73	8000[a]	Pulsar time delay
Anderson et al.	27	9–72	7500	MA9 S-band range
Counselman et al.	28	6–71	8400[b]	Pulsar time delay
Blackwell et al.	29	7–63	7440	Eclipse photometry

[a]One of several solutions. This solution in best agreement with average in situ density values at 1 AU.

[b]One of several solutions. This solution included heliographic latitude.

Table 2. Columnar (two-dimensional) fluctuation spectral index

Source	Reference	Time (center) of observations	Index	Type of experiment
Berman	11,15	10–76	2.41	VK doppler noise
Berman	11,15	5–76	2.43	HE doppler noise
Woo et al.	30	5–74	2.55	MVM S–X doppler
Unti et al.	31	3–68	2.55[a]	OGO 5 in situ density
Goldstein et al.	32	9–67	2.3[a]	MA 5 in situ density
Intriligator et al.	33	1–66	2.3[a]	PN 6 in situ density

[a]In situ "equivalent"; converted via the relationship columnar index ≡ in situ index + 1.

Table 3. Summary of parameter correlation with solar cycle

Parameter	Correlation appearance	Solar cycle ratio	Solar cycle phase
Density			
Near corona ($r \leq 5r_{\odot}$)	Strong	~2.0	Positive
$r = 10r_{\odot}$	None	–	–
$r = 1$ AU	Strong	~0.65	Negative
Density fluctuation 1 AU	Strong	~0.65	Negative
Fluctuation/density ratio 1 AU	Weak	–	–
Flux 1 AU	Strong	~0.70	Negative
Flux fluctuation 1 AU	Strong	~0.65	Negative
Fluctuation/flux ratio 1 AU	Moderate	~0.75	Negative
Radial velocity 1 AU	Weak	>0.8	Negative
Velocity fluctuation 1 AU	Moderate	~0.70	Negative
Fluctuation/velocity ratio 1 AU	Moderate	~0.75	Negative
Fluctuation spectral index	Weak/none	–	–

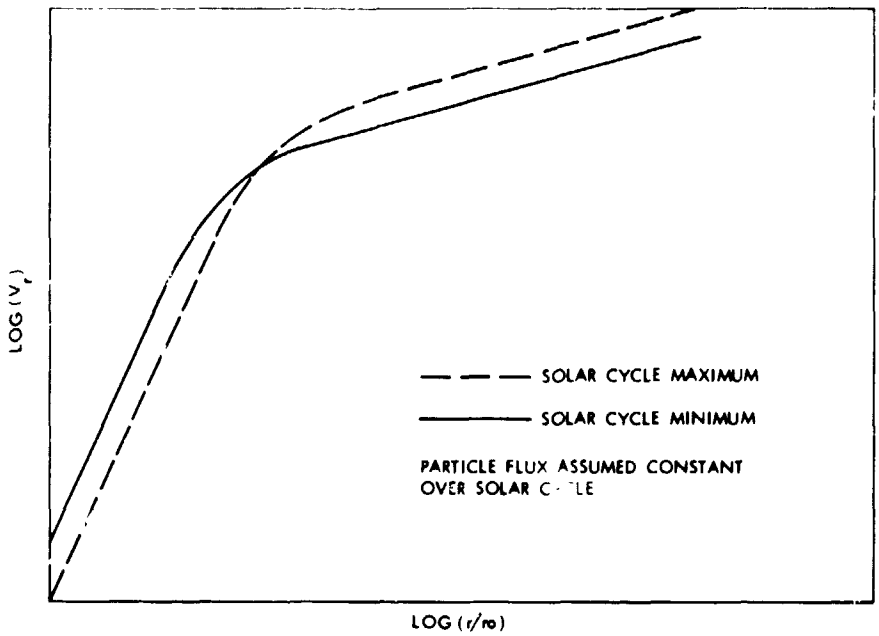

Fig. 1. Possible solar wind velocity signature with solar cycle

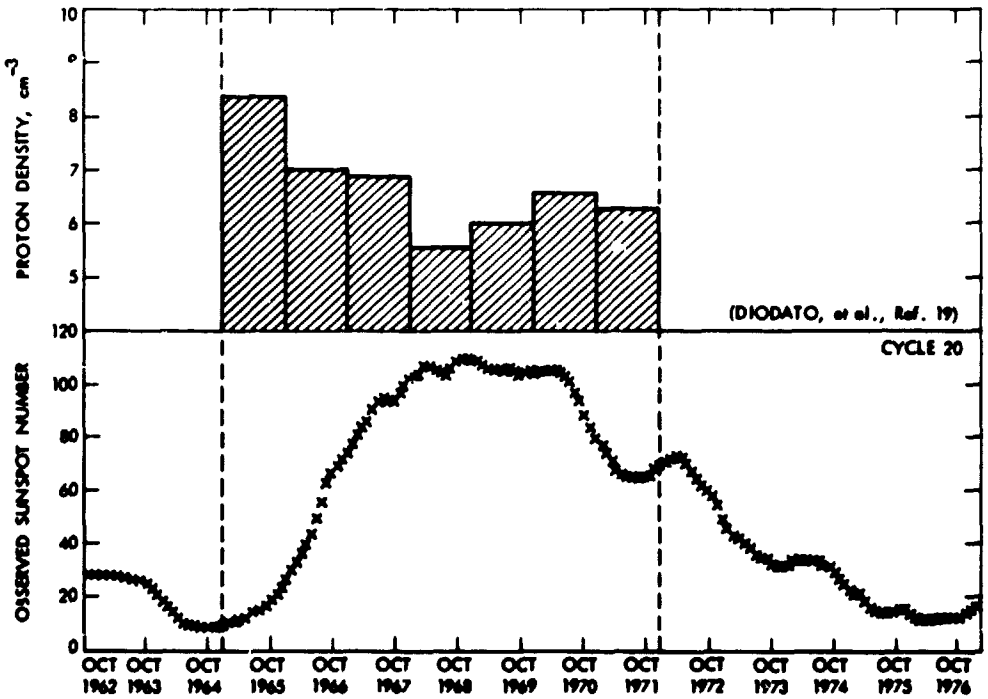

Fig. 2. Proton density yearly average at 1 a. u., 1965 to 1971

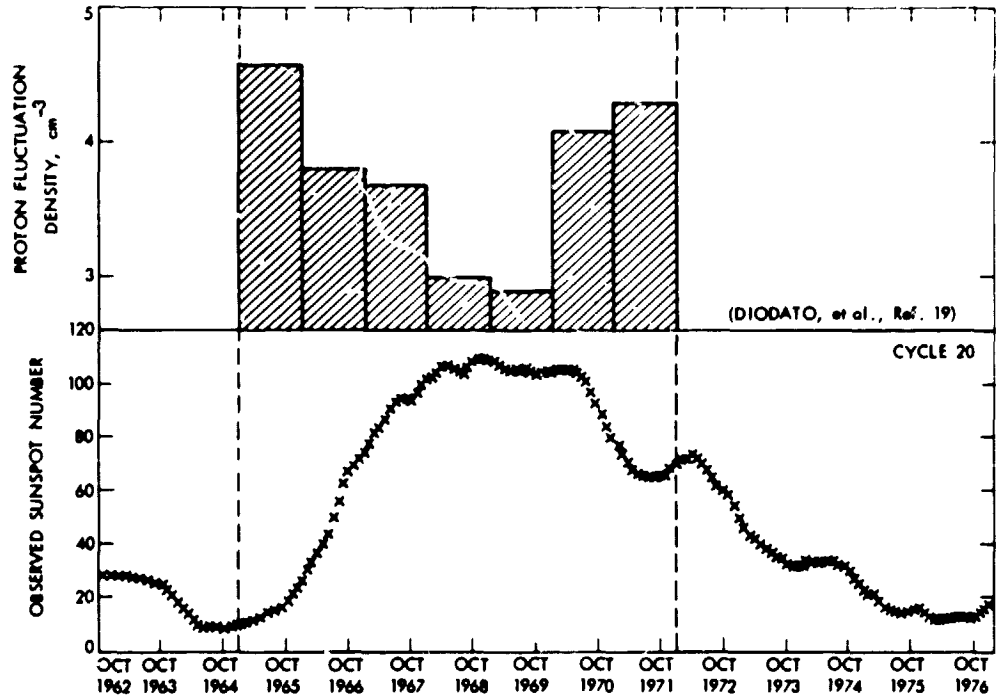

Fig. 3. Proton fluctuation density yearly average at 1 AU, 1965 to 1971

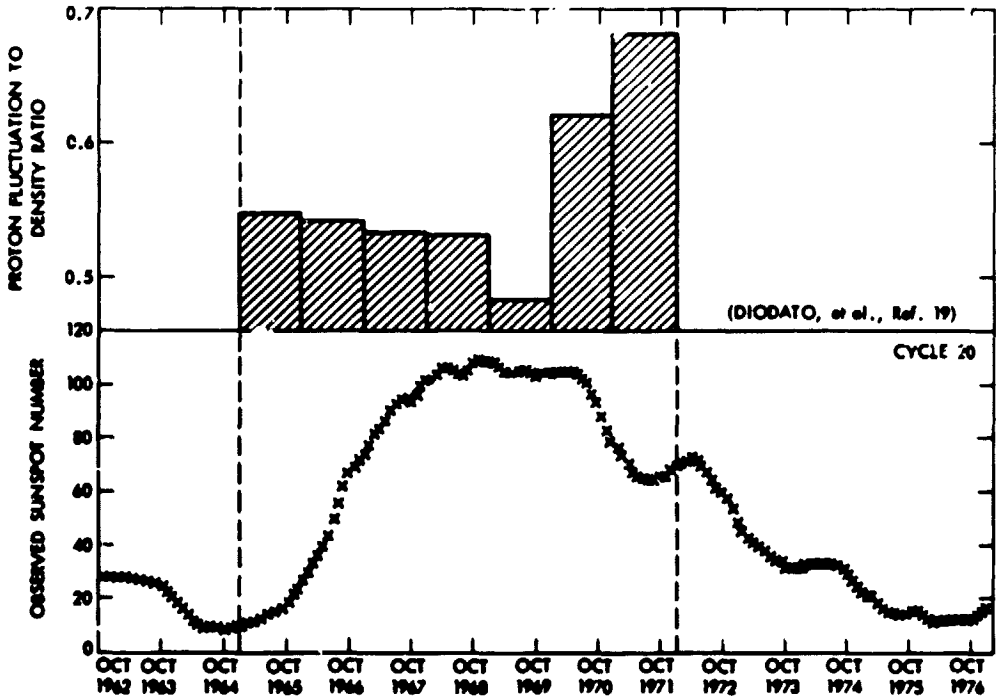

Fig. 4. Proton fluctuation to density ratio, yearly average from 1965 to 1971, at 1 AU

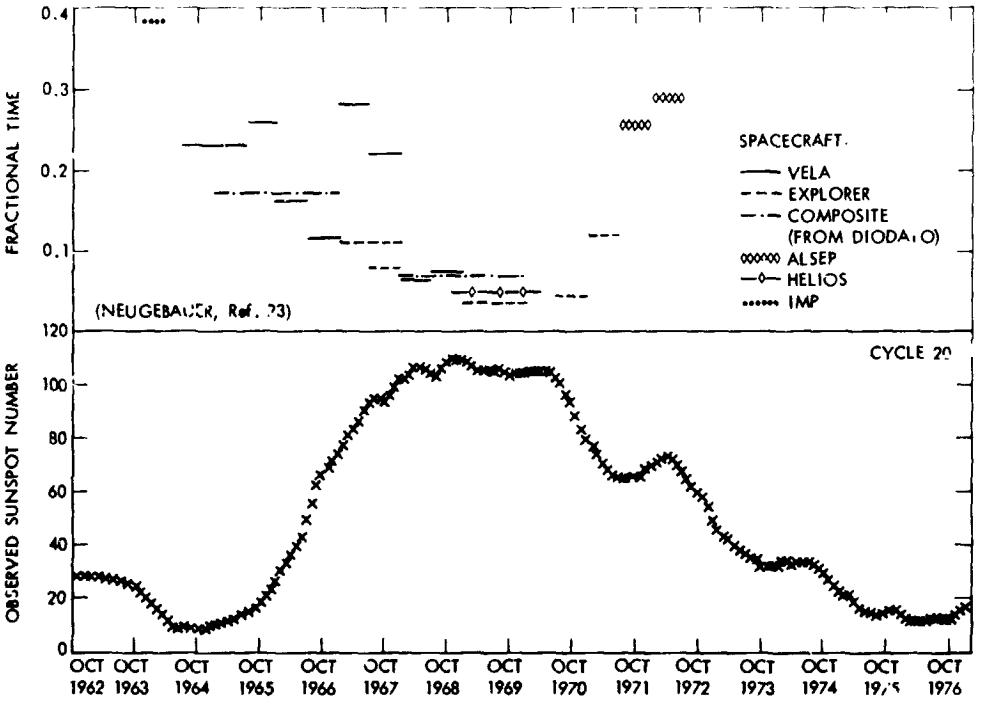

Fig. 5. Fractional time proton density observed greater than 10 cm^{-3}, at 1 AU

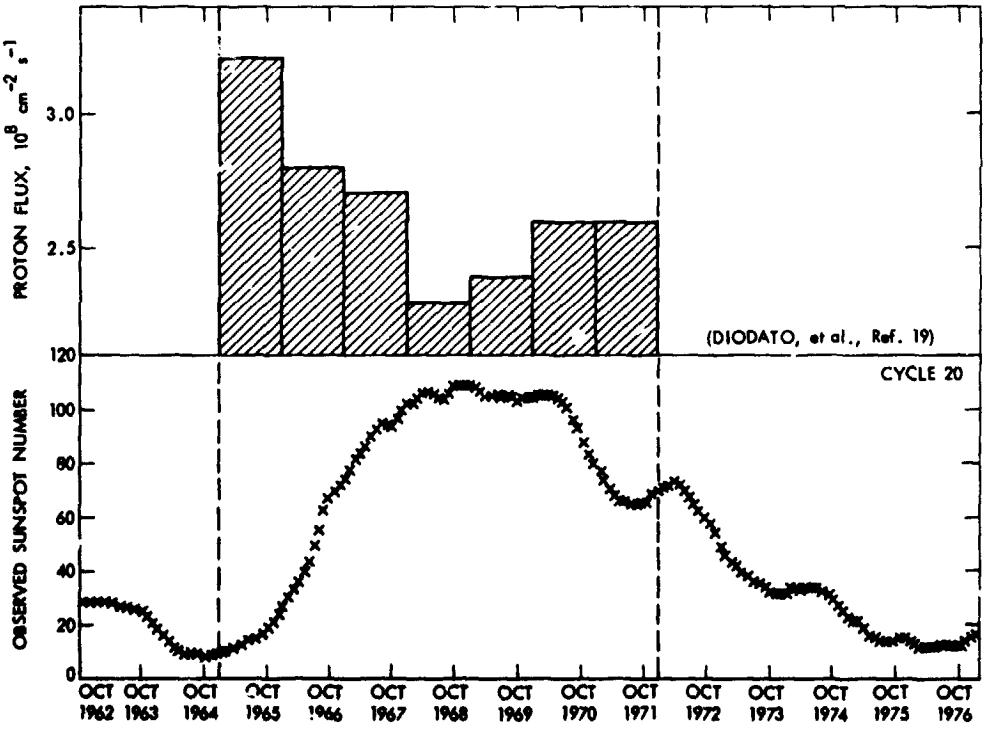

Fig. 6. Proton flux yearly average at 1 AU, 1965 to 1971

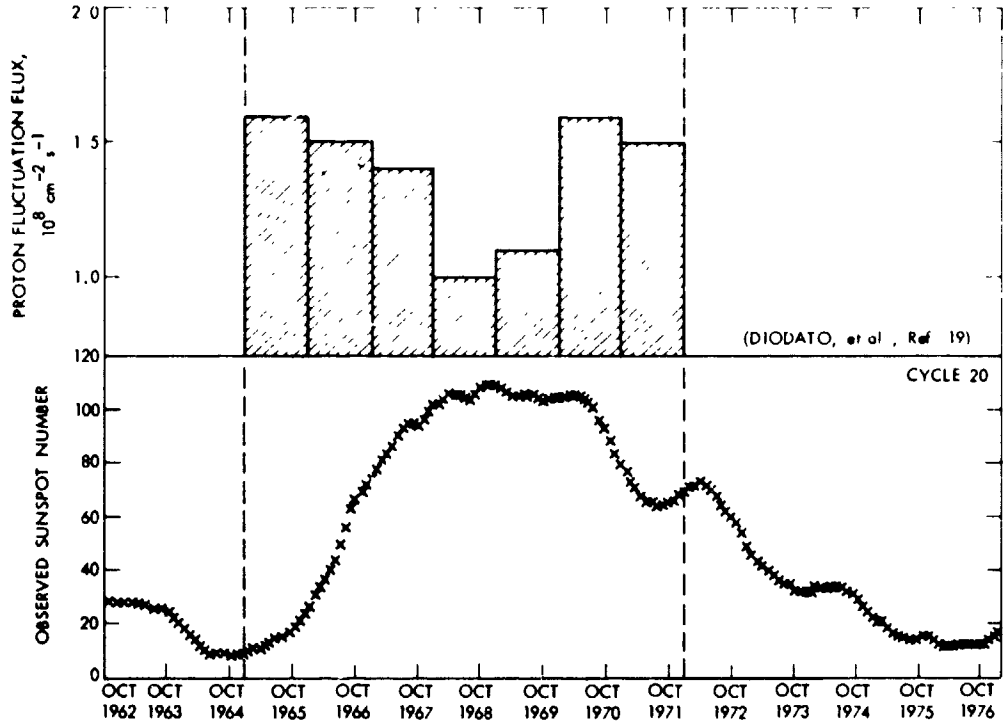

Fig. 7. Proton fluctuation flux yearly average at 1 AU, 1965 to 1971

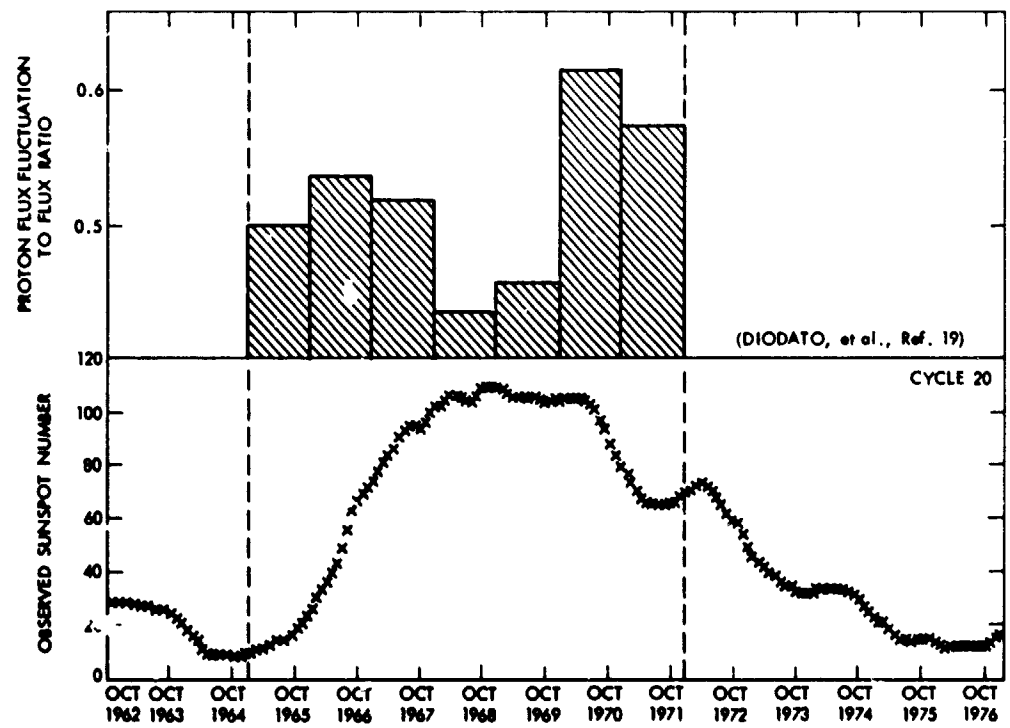

Fig. 8. Proton flux fluctuation to flux ratio, yearly average from 1965 to 1971 at 1 AU

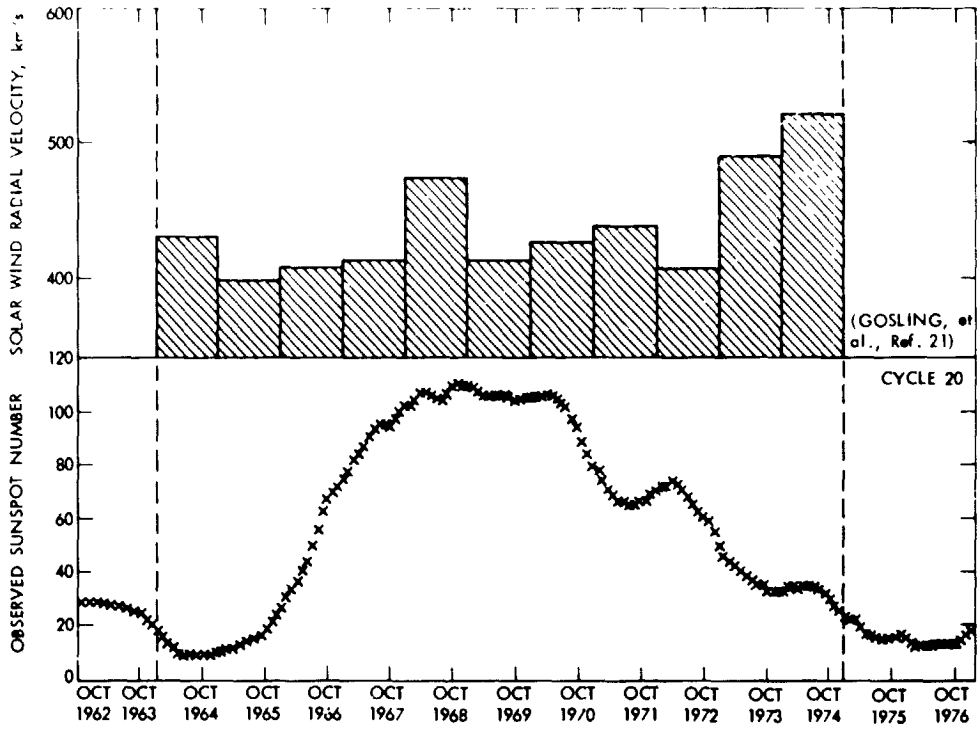

Fig. 9. Solar wind radial velocity yearly average at 1 AU, 1965 to 1974

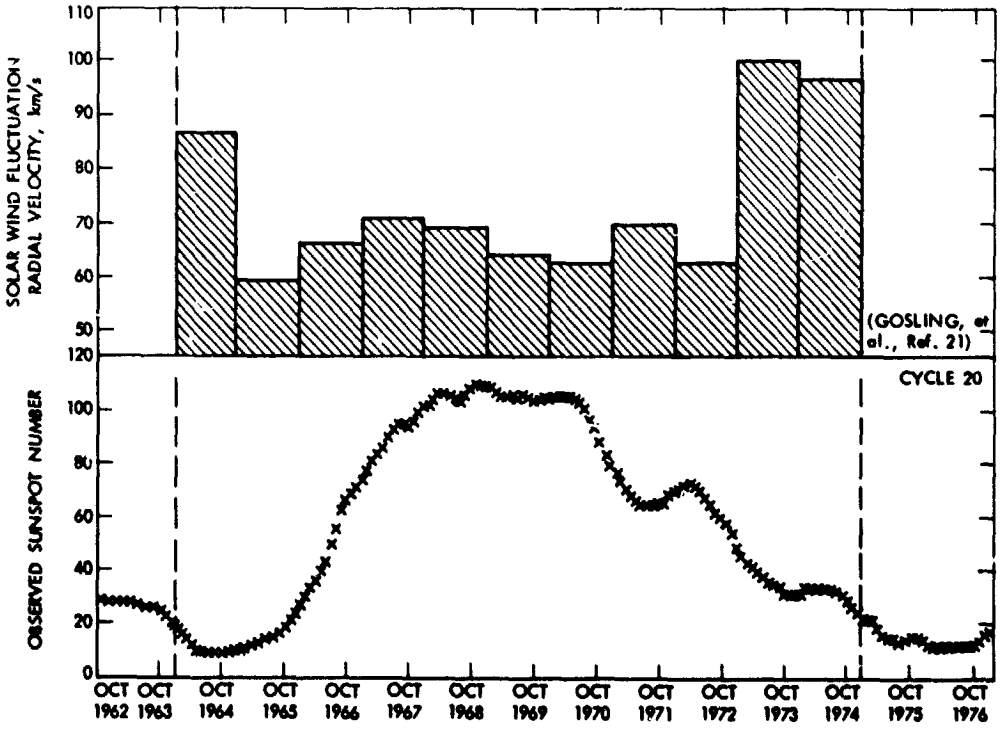

Fig. 10. Solar wind fluctuation radial velocity yearly average at 1 AU

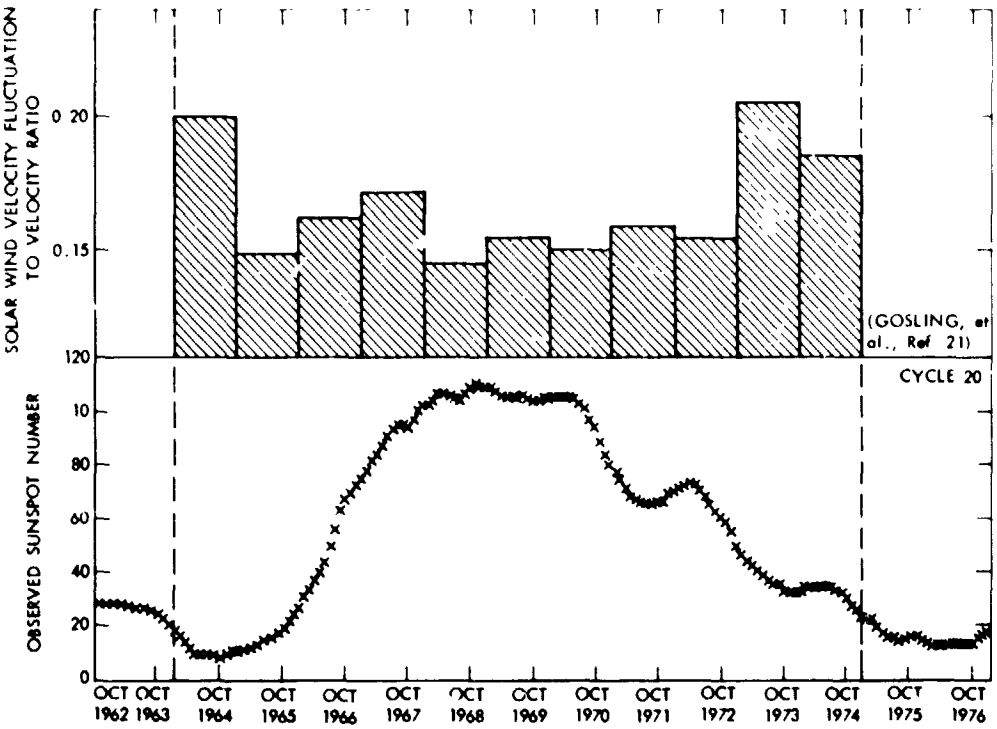

Fig. 11. Solar wind velocity fluctuation to velocity ratio, yearly average from 1964 to 1974 at 1 AU

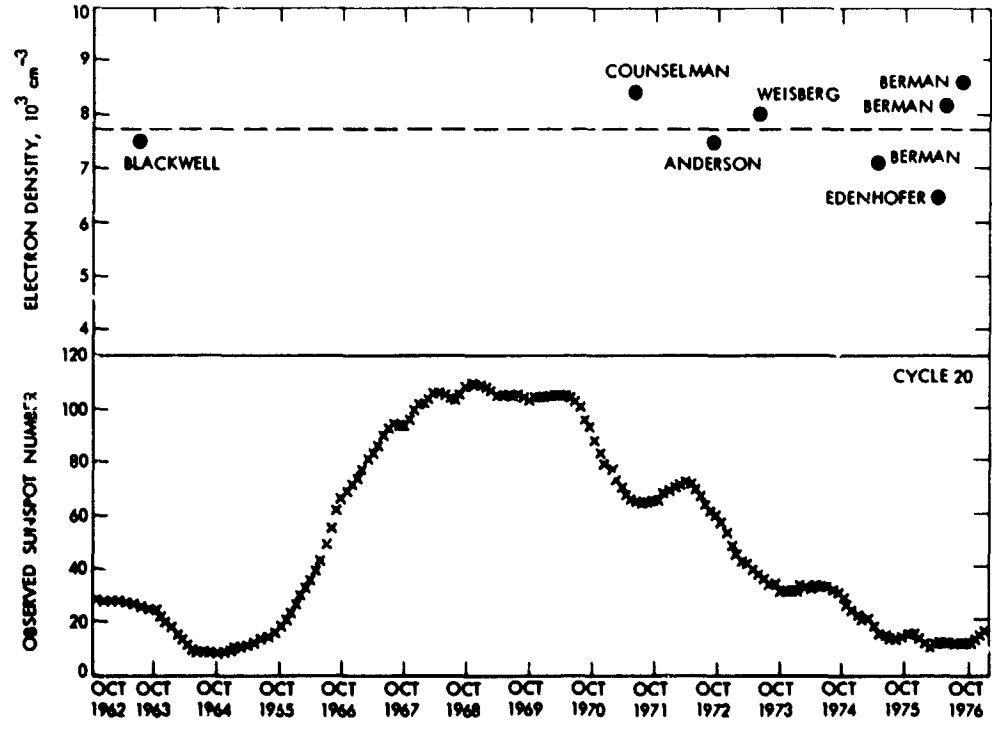

Fig. 12. Electron density model evaluations at $r = 10r_{\odot}$

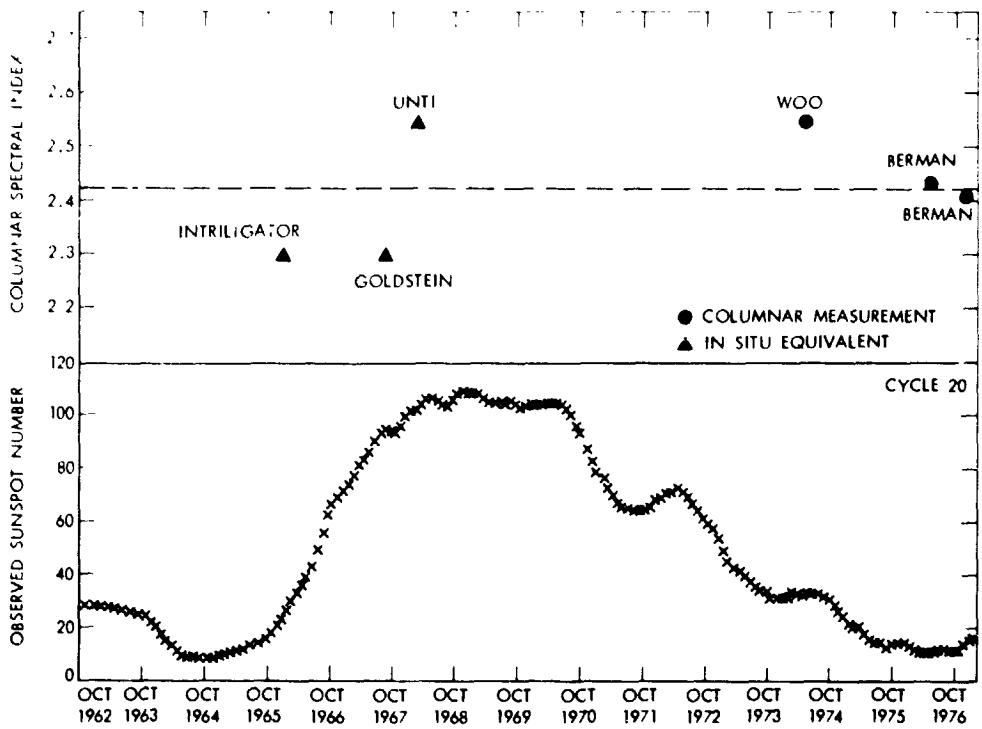

Fig. 13. Columnar (two-dimensional) density spectral ind

Ground Tracking System Phase Fluctuation Spectra

A. L. Berman
TDA Engineering Office

Spectral analysis of solar wind plasma fluctuation requires knowledge of the average ground tracking system phase fluctuation spectrum. This article presents typical ground tracking system phase fluctuation spectra as deduced from two-way S-band doppler noise measured at large Sun-Earth-Probe angles.

I. Introduction

An extremely important tool in solar wind investigations is the spectral analysis of either single-frequency (S) or dual-frequency (S-X) doppler phase fluctuations. As a part of this analysis, one needs to know something about the spectral characteristics of phase fluctuations induced in the ground tracking system, so that this effect may be separated out or at least known to be insignificant when compared to the particular solar-wind-induced phase fluctuations being analyzed. In Reference 1, test results are documented of measured two-way S-Band doppler (phase) noise for the Pioneer 10, Pioneer 11, Helios 1, and Helios 2 spacecraft when they were at large Sun-Earth-Probe (SEP) angles, so that the solar wind contribution (to the doppler noise) was minimized. The doppler noise was computed for sample intervals between 1 and 60 seconds, with the number of doppler samples fixed at 15 in all cases, hence resulting in an observational time scale proportional to sample interval. Reference 2 presents a method whereby sample interval dependent doppler noise is easily converted to the equivalent fluctuation spectrum; it will thus be the purpose of this article to translate the average doppler phase fluctuation (noise) data from Reference 1 into equivalent phase fluctuation spectra.

II. Measured Ground Tracking System Average Phase Fluctuation Spectra

In Reference 2 it was found that the relationship between doppler noise produced by the Network Operations Control Center (NOCC) tracking validation software doppler noise algorithm[1] and RMS phase (ϕ) was:

$$\phi(\tau) \cong \frac{5}{3}\tau \cdot \text{noise}(\tau)$$

τ = doppler sample interval, s

Reference 2 further assumed that the relationship between doppler sample interval and phase fluctuation frequency (ν) was:

$$\nu \approx (30\,\tau)^{-1}$$

[1] A "running" standard deviation computed from a least squares linear curve fit to 15 samples of actual minus predicted (average) doppler frequency.

so that the noise equivalent phase fluctuation spectrum ($P_g(\nu)$) was

$$P_g(\nu) \equiv \frac{d}{d\nu}\{[\phi(\nu)]^2\}$$

Using this technique, the doppler noise data from Reference 1 translates to the following (ground tracking system) spectra:

Pioneer 10 : $P_g(\nu) = 1.11 \times 10^{-1}\ \nu^{1.2}$ rad^2/Hz

Pioneer 11 : $P_g(\nu) = 1.98 \times 10^{-1}\ \nu^{1.2}$ rad^2/Hz

Helios 1 : $P_g(\nu) = 5.00 \times 10^{-2}\ \nu^{-1.4}$ rad^2/Hz

Helios 2 : $P_g(\nu) = (1.25 \times 10^{-2}\ \nu^{-1.4} + 4.70 \times 10^{-7}\ \nu^{-3})$ rad^2/Hz

Table 1 lists the decade spaced spectral density values for each spacecraft for the phase fluctuation frequency range:

$$10\ \text{Hz} \geq \nu \geq 10^{-5}\ \text{Hz}$$

while Figure 1 presents the results in graphical form.

Although the ground tracking system is believed to be the major contributor (in combination with the particular round-trip-light-time for each spacecraft) to these fluctuation spectra, there are also spacecraft and Solar Wind components. As an example, the Helios 2 spectra for the frequency region,

$$\nu \leq 10^{-3}\ \text{Hz}$$

would appear to be almost solely due to solar wind plasma fluctuation, and not the ground tracking system. The most important contributor to the tracking system stability is the Deep Space Station (DSS) frequency standard, which in these cases was a rubidium standard. For the DSS which have (or will have) a hydrogen maser frequency standard, the corresponding ground tracking system phase fluctuation spectra can be expected to be substantially decreased.

References

1. Berman, A. L., "A Comprehensive Two-Way Doppler Noise Model for Near-Real-Time Validation of Doppler Data," in *The Deep Space Network Progress Report* 42-37, Jet Propulsion Laboratory, Pasadena, California, February 15, 1977.

2. Berman, A. L., "Phase Fluctuation Spectra: New Radio Science Information to Become Available in the DSN Tracking System Mark III-77," in *The Deep Space Network Progress Report* 42-40, Jet Propulsion Laboratory, Pasadena, California, August 15, 1977.

Table 1. Average phase fluctuation spectral density versus fluctuation frequency

Fluctuation frequency, Hz	Average phase fluctuation spectra, rad^2/Hz			
	Pioneer 10	Pioneer 11	Helios 1	Helios 2
10^{1}	7.0×10^{-3}	1.2×10^{-2}	2.0×10^{-3}	5.0×10^{-4}
10^{0}	1.1×10^{-1}	2.0×10^{-1}	5.0×10^{-2}	1.3×10^{-2}
10^{-1}	1.8×10^{0}	3.1×10^{0}	1.3×10^{0}	3.1×10^{-1}
10^{-2}	2.8×10^{1}	5.0×10^{1}	3.2×10^{1}	7.9×10^{0}
10^{-3}	4.4×10^{2}	7.9×10^{2}	7.9×10^{2}	6.7×10^{2}
10^{-4}	7.0×10^{3}	1.2×10^{4}	2.0×10^{4}	4.8×10^{5}
10^{-5}	1.1×10^{5}	2.0×10^{5}	5.0×10^{5}	4.7×10^{8}

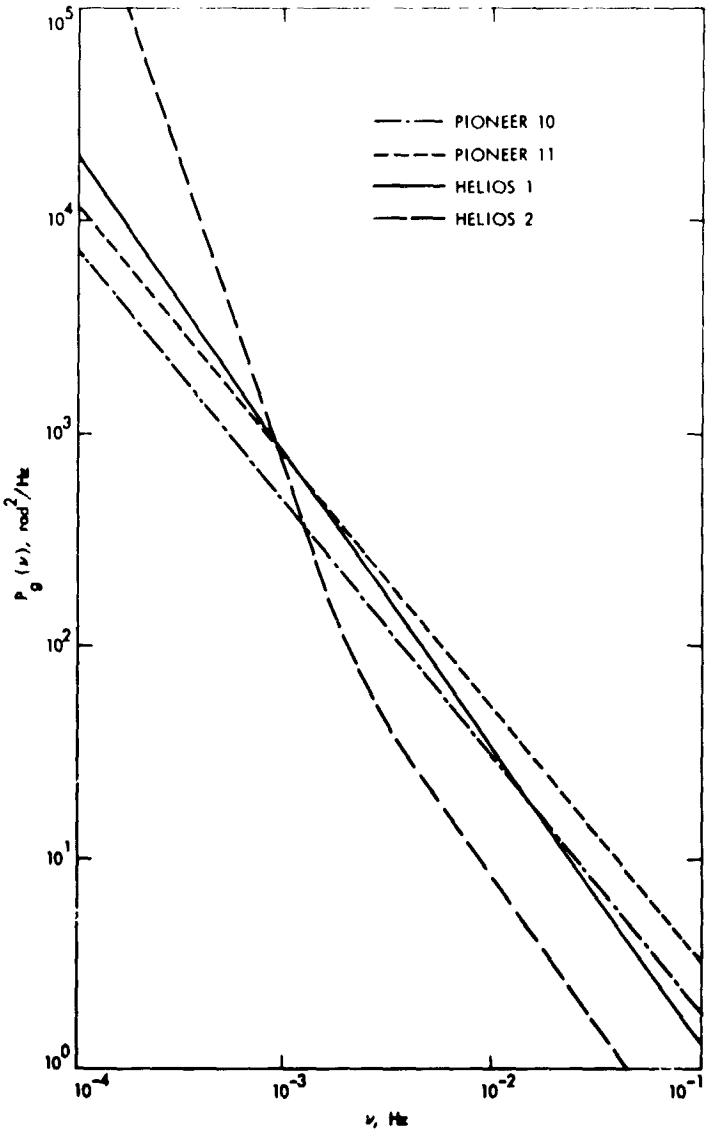

Fig. 1. Typical ground tracking system phase fluctuation spectra

System Performance Testing of the DSN Radio Science System, Mark III-78

A. L. Berman
TDA Engineering Office

J. S. Mehta
Deep Space Network Operations Section

System Performance Tests are required to evaluate system performance following initial system implementation and subsequent modification, and to validate system performance prior to actual operational usage. This article describes non-real-time end-to-end Radio Science system performance tests that are based on the comparison of open-loop radio science data to equivalent closed-loop radio metric data, as well as an abbreviated Radio Science real-time system performance test that validates critical Radio Science System elements at the Deep Space Station prior to actual operational usage.

I. Introduction

Radio Science data generated by the DSN Radio Science System are conveniently categorized as follows:

(1) Closed-loop radio metric data generated via the DSS Tracking Subsystem.

(2) Open-loop radio science data generated via the DSS Radio Science Subsystem (64-m subnet only).

System performance tests already exist for the closed-loop radio metric data generation system, so that the primary thrust of Radio Science system performance tests (SPTs) will be the verification and evaluation of the open-loop data generation paths. SPTs can be considered to have two primary functions, as follows:

(1) In-depth evaluation of system capabilities and performance following initial system implementation and significant system modification. Successful completion of SPTs allows system transfer to DSN operations for project usage.

(2) Routine validation of system performance prior to actual operational usage.

To satisfy the above functions, two conceptually distinct SPTs will be developed, as follows:

(1) An end-to-end Radio Science SPT which includes elements located within the Deep Space Stations (DSSs), the Ground Control Facility (GCF), and the Network Operations Control Center (NOCC). This test will be performed in non-real-time.

(2) An abbreviated Radio Science SPT which will include only the critical elements at the DSS, and will be performed in real-time prior to actual radio science operations.

These tests will be detailed in Sections II and III to follow.

II. End-to-End Radio Science System Performance Tests

Open-loop radio science data is generated via two independent paths identified as follows:

(1) Real-time bandwidth reduction.

(2) Wideband recording.

Although the two processes utilize very different equipment and techniques, both have similar inputs and outputs:

(1) Input – Spacecraft signal acquired by an open-loop receiver.

(2) Output – A digitized recording of a narrow frequency bandwidth which contains the actual spacecraft frequency mixed with the predicted spacecraft frequency, and a numerical representation of the predicted spacecraft frequency.

It is thus apparent that to thoroughly perform an end-to-end test of the Radio Science System, two separate tests will be required. The tests will be conceptually similar; however, the assemblies and subsystems that actually compose the two separate data acquisition paths will be quite dissimilar.

The basic approach utilized to implement a Radio Science System end-to-end SPT is rather novel – the final (open-loop) radio science deliverable to the project (bandwidth reduced frequency data) will be compared to the equivalent (closed-loop) radio metric deliverable to the project (doppler data). This test will be quite flexible in that it can be performed routinely when tracking any spacecraft, and further allows any desired downlink frequency signature to be approximated via the use of uplink ramping (one round-trip-light-time earlier).

The inputs to the system performance test software that will perform the radio science data-radio metric data comparison are the radio science data (real-time bandwidth reduction) Intermediate Data Record (IDR), the wideband radio science data (wideband recording) IDR, and the radio metric IDR. The DSN elements exercised in the generation of a radio science data IDR are:

(1) Narrowband Open-Loop Receiver (OLR)

(2) Programmed Oscillator Control Assembly (POCA)

(3) Programmed Oscillator (PO)

(4) Occultation Data Assembly (ODA)

(5) POEAS Software Program

(6) PREDIK Software Program

(7) High Speed Data transmission (HSD)

(8) Data Records Subsystem (GDR)

In generation of a wideband radio science IDR they are:

(1) Wideband Open-loop Receiver (OLR)

(2) Digital Recording Assembly (DRA)

(3) PREDIK Software Program

(4) CTA 21 Radio Science Subsystem (CRS)

(5) High Speed Data Transmission (HSD).

Figure 1 provides the functional block diagram for the real-time bandwidth reduction SPT, while Fig. 2 provides the functional block diagram for the wideband recording SPT.

Radio Science System performance evaluation and acceptance criteria in conjunction with these tests will be based on:

(1) Absolute differences in 1 second averaged frequencies.

(2) RMS differences over various time scales of 1 second averaged frequencies.

III. Abbreviated Radio Science System Performance Test

The critical elements which require checkout prior to actual operational usage of the real-time bandwidth reduction capability are:

(1) Open-loop receiver (OLR)

(2) Programmed Oscillator Control Assembly (POCA)

(3) Programmed Oscillator (PO)

(4) Spectral Signal Indicator (SSI)

(5) Occultation Data Assembly (ODA).

Figure 3 illustrates a very simple configuration that will adequately validate real-time bandwidth reduction capability (in concert with the available Occultation Data Assembly internal software tests). Essentially, the initial frequency of a given predict set provides the POCA-PO driver; at the same time, the corresponding S- and X-Band frequencies from the test translator are input to the narrowband OLR. The OLR output is recorded by the ODA and displayed on the SSI; acceptance criteria are simply that the ODA recorded signals be centered in the SSI (displayed) bandpass. Additionally, the ODA recorded signals will be included in the IDR delivered to the project and may find use as a system calibration.

A corresponding abbreviated SPT for wideband recording capability is not required, as the three critical elements:

(1) Open-loop receiver (OLR)

(2) Digital Recording Assembly (DRA)

(3) CTA 21 Radio Science Subsystem (CRS)

function independently of each other, and hence existing individual assembly and subsystem level tests should suffice

IV. System Performance Test Development Schedule

The planned schedule for availability of the various Radio Science SPTs is as follows:

(1) End-to-end wideband recording SPT — April 1, 1978.

(2) End-to-end real-time bandwidth reduction SPT — July 1, 1978.

(3) Abbreviated real-time bandwidth reduction SPT — July 1, 1978.

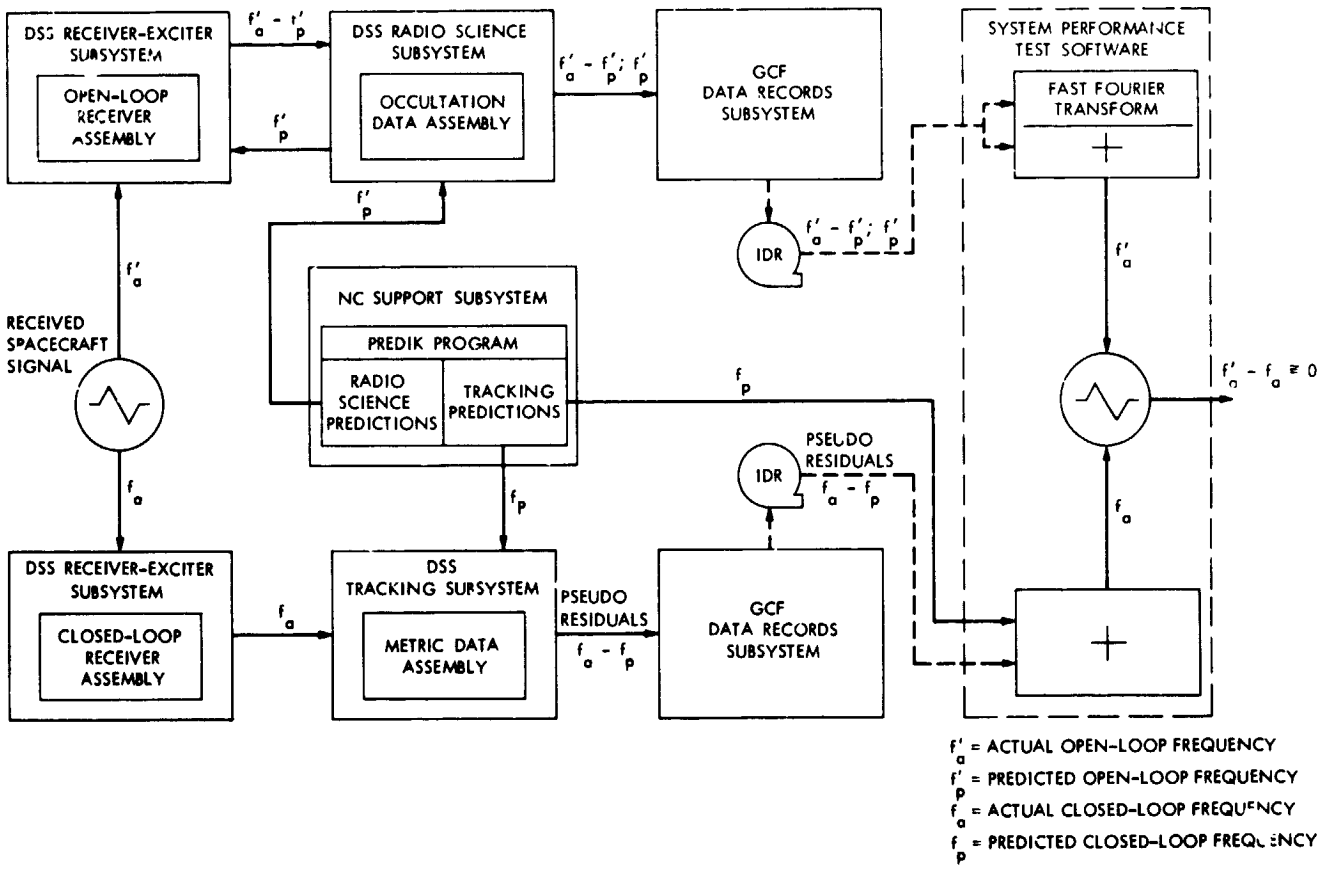

Fig. 1. DSN Radio Science system performance test of real-time bandwidth reduction capability

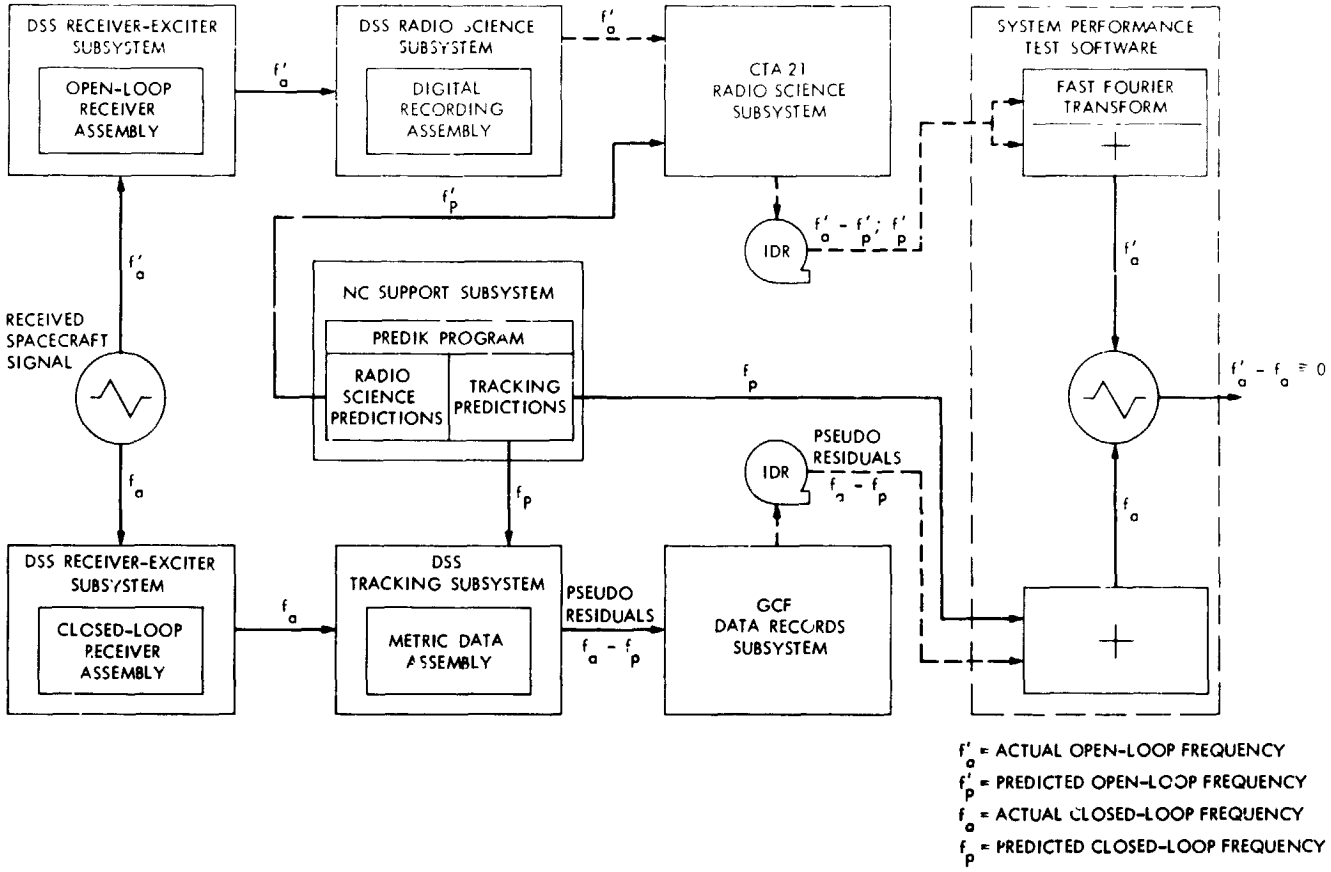

Fig. 2. DSN Radio Science system performance test of wide-band recording capability

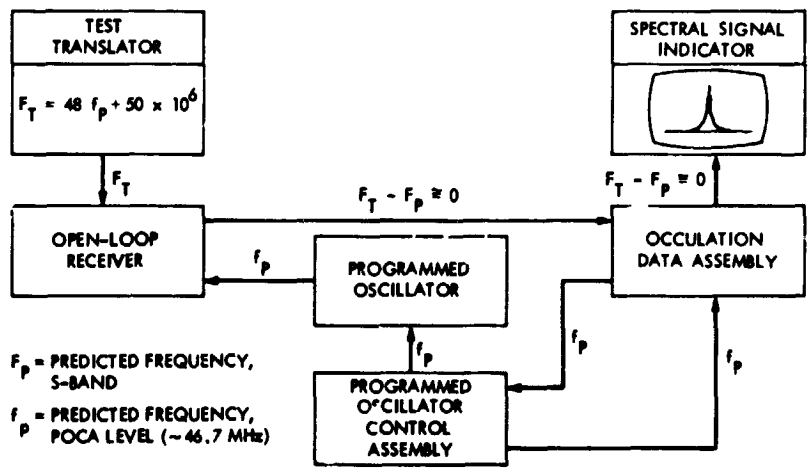

Fig. 3. DSN Radio Science system pre-pass performance test of real-time bandwidth reduction capability

A Fast DFT Algorithm Using Complex Integer Transforms[1]

I. S. Reed
University of Southern California
Department of Electrical Engineering

T. K. Truong
Tracking and Data Acquisition Engineering Section

In this article Winograd's algorithm for computing the discrete Fourier transform (DFT) is extended considerably for certain large transform lengths. This is accomplished by performing the cyclic convolution, required by Winograd's method, by a fast transform over certain complex integer fields developed previously by the authors. This new algorithm requires fewer multiplications than either the standard fast Fourier transform (FFT) or Winograd's more conventional algorithm.

I. Introduction

Several authors (Refs. 1-12) have shown that transforms over finite fields or rings can be used to compute circular convolutions without round-off error. Recently, Winograd (Ref. 13) developed a new class of algorithms that depend heavily on the computation of a cyclic convolution for computing the conventional discrete Fourier transform (DFT). This new algorithm, for a few hundred transform points, requires substantially fewer multiplications than the conventional fast Fourier transform (FFT) algorithm.

The authors (Ref. 5) defined a special class of finite Fourier-like transforms over $GF(q^2)$ where $q = 2^p - 1$ is a Mersene prime for $p = 2,3,5,7,13,17,19,31,61 \ldots$. These transforms have a transform length of d points, where $d|8p$. The advantage of this transform over others is that it can be accomplished simply by circular shifts instead of by multiplications (Ref. 11).

In this paper, it is shown that Winograd's algorithm can be combined with the above-mentioned Fourier-like transform over $GF(q^2)$ to yield a new hybrid algorithm for computing the discrete Fourier transform (DFT). By this means a fast method for accurately computing the DFT of a sequence of complex numbers of very long transform lengths is obtained.

II. Cyclic Convolution

The following algorithm for the cyclic convolution of two sequences is based on ideas due to Winograd (Ref. 13). Let the field of rationals be R. Also let $X(u) = x_0 + x_1u + x_2u^2 + \ldots + x_nu^{n-1}$, $Y(u) = y_0 + y_1u + y_2u^2 + \ldots + y_nu^{n-1}$ be two polynomials over R. The product $T(u) = X(u) \cdot Y(u)$ can be computed by

[1]This work was supported in part by the U.S. Air Force Office of Scientific Research.

$$T(u) = X(u) \cdot Y(u) \bmod \prod_{i=0}^{2n-2} (u - \alpha_i) \qquad (1)$$

where

$$\alpha_i \in R$$

It is shown in (Ref. 13) that a minimum of $2n - 1$ multiplications are needed to compute Eq. (1).

It is readily shown that the cyclic convolution of $X(u)$ and $Y(u)$ is the set of coefficients of the polynomial

$$T'(u) = X(u) \cdot Y(u) \bmod (u^n - 1)$$

Let the polynomial $u^n - 1$ be factored into irreducible relatively prime factors, i.e.,

$$u^n - 1 = \prod_{i=1}^{K} g_i(u)$$

where

$$(g_i(u), g_j(u)) = 1 \text{ for } i \neq j$$

Then $T'(u) \bmod g_i(u)$ for $i = 1,2,\ldots,k$ can be computed, using Eq. (1). Finally, the Chinese Remainder Theorem is used to evaluate $T(u)$ from these residues. The above summarizes Winograd's method for performing a cyclic convolution.

The following theorem is due to Winograd (Ref. 14).

Theorem 1. Let a and b be relatively prime positive integers and A be the cyclic $ab \times ab$ matrix, given by

$$A(x,y) = f(x + y \bmod a \cdot b), \qquad 0 \leq x,y < ab$$

If π is a permutation of the set of integers $\{0, 1, \ldots, ab-1\}$, let

$$B(x,y) = A(\pi(x), \pi(y))$$

Then there exists a permutation π such that, if B is partitioned into $b \times b$ submatrices, each submatrix is cyclic and the submatrices form an $a \times a$ cyclic matrices.

It was shown by Winograd (Ref. 14) that the number of multiplications needed to perform a circular convolution of 2,3,4,5 and 6 points is 2,4,5,10 and 8 multiplications, respectively. To compute the cyclic convolution of two longer sequences of complex integers, a d-point transform over $GF(q^2)$ where $d|8p$ is utilized here. Since the latter transform can be evaluted without multiplications (Ref. 11), it can be used with considerable advantage to compute a cyclic convolution without roundoff error of two d-point complex number sequences. Hence, for the transform over $GF(q^2)$, the number of integer complex multiplications needed to perform a circular convolution is precisely d.

III. The DFT When Transform Length Is a Prime $d = q'$

The DFT is defined by

$$A_j = \sum_{i=0}^{d-1} a_i w^{ij}$$

where w is a dth root of unity. Let

$$A_0 = \sum_{i=0}^{d-1} a_i \qquad (2a)$$

and

$$A_j = a_0 + B_j \quad \text{for} \quad j = 1,2,\ldots,d-1$$

where

$$B_j = \sum_{i=1}^{d-1} a_i w^{ij}$$

That is, let

$$\bar{B} = W\bar{a} \qquad (2b)$$

where W is the $(d-1) \times (d-1)$ matrix (w^{ij}) and $\bar{a}, \bar{B}$ are the column matrices (a_i) and (B_k), respectively. If $d = q'$ is a prime, then, by Ref. 12 one can find an element α in $GF(q')$ that generates its cyclic multiplicative subgroup of $q' - 1$ elements. Using the element α a cyclic permutation of the elements of $GF(q')$ can be defined by

$$\alpha = \begin{pmatrix} 1, & 2, \ldots, q'-2, & q'-1 \\ \alpha, \alpha^2, \ldots, & \alpha^{q'-2}, & \alpha^{q'-1} \end{pmatrix} \qquad (2c)$$

With this permutation, one can permute the indices of B, a, W defined in Eq. (2b) so that the matrix $W' = (w^{\sigma(i)\sigma(j)})_{i,j\neq 0}$ is cyclic. That is

$$B_{\sigma(j)} = \sum_{i=1}^{q'-1} a_{\sigma(i)} w^{\sigma(i)\sigma(j)}$$

$$= \sum_{i=1}^{q'-1} a_{\sigma(i)} w^{\sigma(i+j)}$$

for

$$j = 1,2,\ldots,q'-1 \tag{3}$$

Thus, $B_{\sigma(j)}$ is a cyclic convolution of $a_{\sigma(i)}$ and $w^{\sigma(i)}$ for $j = 1,2,\ldots,q'-1$.

Let $q'-1 = p_1 \cdot p_2 \cdots p_r$ be the factorization of $q'-1$ into prime integers. If one lets $a_1 = p_1 \cdot p_2 \cdots p_{r-1}$ and $b_1 = p_r$, by Theorem 1 the cyclic matrix can be partitioned into $b_1^2 = p_r^2$ matrices of size $a_1 \times a_1$. Next let $a_1 = a_2 \times b_2$, where $a_2 = p_1 \cdots p_{r-2}$ and $b_2 = p_{r-1}$. If a_2 is not a prime, then each $a_1 \times a_1$ cyclic matrix can be partitioned into b_2^2 matrices of size $a_2 \times a_2$. In general, $a_i = a_{i+1} \cdot b_{i+1}$, where b_{i+1} is a prime. If $a_{i+1} \neq 1$, then each $a_i \times a_i$ cyclic matrix can be partitioned into b_{i+1}^2 matrices of size $a_{i+1} \times a_{i+1}$. Otherwise, the procedure terminates. If the number of multiplications used to compute the cyclic convolution of p_i points is m_i for $i = 1,2,\ldots,r$, then the number of multiplications for computing a q'-point DFT is equal to $N = m_1 \cdot m_2 \cdots m_r$.

For most applications the two Mersenne primes $2^{31}-1$ and $2^{61}-1$ will provide enough bit accuracy and dynamic range for computing the DFT. For these primes, we choose the prime q' to have the form

$$q' = 1 + a \cdot 2^2 \cdot p$$

where $2^2 \cdot p | (2^p - 1)^2 - 1$ for $p = 31$ or 61 and $a = 3$ or 5. Such values for the prime q' are 373, 733, 1861, and 2441. If $d = q'$ is the transform length of the DFT, then, by Theorem 1, there exists a permutation of rows and columns so that the cyclic matrix $\bar{W}$ can be partitioned into blocks of $(2^2 \cdot p) \times (2^2 \cdot p)$ cyclic matrices, such that the blocks form an $a \times a$ cyclic matrix. A cyclic convolution of $a = 3$ or 5 complex number points can be accomplished by Winograd's algorithm. As it was mentioned in the last section, the transform of length $2^2 \cdot p$ over $GF(q^2)$ can be used to compute the cyclic convolution of $2^2 \cdot p$ complex number points. The number of multiplications needed to perform this convolution is $2^2 \cdot p$. Hence for a prime q' the total number of multiplications, needed to perform a DFT of $d = q'$ complex number points is shown in Table 1. To illustrate the above procedure consider the following example.

Example. Consider the DFT for $d = 7$ points. Let the input function be defined by

$$a_n = 1 + \hat{i}0 \qquad 0 \leq n \leq 1$$

$$= 0 + \hat{i}0 \qquad 2 \leq n \leq 6$$

By Eq. (2a), this transform is

$$A_0 = \sum_{i=0}^{6} a_i = 2 + \hat{i}0 \tag{3a}$$

and

$$A_j = a_0 + b_j \quad \text{for} \quad j = 1,2,\ldots,6 \tag{3b}$$

where

$$b_j = \sum_{i=1}^{6-1} a_i w^{ij}, \quad w = e^{\hat{i}2\pi/7}$$

For $d = 7$, the permutation σ is given by

$$\sigma = \begin{pmatrix} 1, 2, 3, 4, 5, 6 \\ 3, 2, 6, 4, 5, 1 \end{pmatrix}$$

Applying the above permutation to Eq. (3b), one obtains $\bar{B} = \bar{W}\bar{a}$ as

$$\begin{pmatrix} b_3 \\ b_2 \\ b_6 \\ b_4 \\ b_5 \\ b_1 \end{pmatrix} = \begin{pmatrix} w^2 & w^6 & w^4 & w^5 & w^1 & w^3 \\ w^6 & w^4 & w^5 & w^1 & w^3 & w^2 \\ w^4 & w^5 & w^1 & w^3 & w^2 & w^6 \\ w^5 & w^1 & w^3 & w^2 & w^6 & w^4 \\ w^1 & w^3 & w^2 & w^6 & w^4 & w^5 \\ w^3 & w^2 & w^6 & w^4 & w^5 & w^1 \end{pmatrix} \begin{pmatrix} a_3 \\ a_2 \\ a_6 \\ a_4 \\ a_5 \\ a_1 \end{pmatrix}$$

By Theorem 1, there exists a permutation π of rows and columns so that the above cyclic matrix can be partitioned into 2×2 block matrix of 3×3 cyclic blocks as follows

$$\begin{pmatrix} b_3 \\ b_5 \\ b_6 \\ b_4 \\ b_2 \\ b_1 \end{pmatrix} = \begin{pmatrix} w^2 & w^1 & w^4 & w^5 & w^6 & w^3 \\ w^1 & w^4 & w^2 & w^6 & w^3 & w^5 \\ w^4 & w^2 & w^1 & w^3 & w^5 & w^6 \\ w^5 & w^6 & w^3 & w^2 & w^1 & w^4 \\ w^6 & w^3 & w^5 & w^1 & w^4 & w^2 \\ w^3 & w^5 & w^6 & w^4 & w^2 & w^1 \end{pmatrix} \begin{pmatrix} 0 \\ 0 \\ 0 \\ 0 \\ 1 \\ 0 \end{pmatrix}$$

This matrix equation has the block forms,

$$\begin{pmatrix} B_1 \\ B_2 \end{pmatrix} = \begin{pmatrix} C & D \\ D & C \end{pmatrix} \begin{pmatrix} Z_1 \\ Z_2 \end{pmatrix}$$

$$= 2^{-1} \begin{pmatrix} (C+D)(Z_1+Z_2) + (C-D)(Z_1-Z_2) \\ (C+D)(Z_1+Z_2) - (C-D)(Z_1-Z_2) \end{pmatrix}$$

$$= 2^{-1} \begin{pmatrix} E+F \\ E \quad F \end{pmatrix} \tag{4}$$

Since C and D are 3×3 cyclic matrices, it is evident that the matrices $C+D$ and $C-D$ are also 3×3 cyclic matrices. In (4), E is

$$E = \begin{pmatrix} e_0 \\ e_1 \\ e_2 \end{pmatrix} = \begin{pmatrix} -0.445, & 1.247, & -1.802 \\ 1.247, & -1.802, & -0.445 \\ -1.802, & -0.445, & 1.247 \end{pmatrix} \begin{pmatrix} 0 \\ 1 \\ 0 \end{pmatrix} \tag{5}$$

where approximately $1/2Re(w^2 + w^5) = -0.445$, $1/2Re(w^1 + w^6) = 1.247$, etc. Let $a_0 = -1.802$, $a_1 = -0.445$, $a_2 = 1.247$ and $y_0 = 0$, $y_1 = 1$, $y_2 = 0$. Then the matrix defined in Eq. (4) can be obtained by computing the convolution of the two sequences a_n and b_n. To do this use a transform $GF(q^2)$ where $q = 2^3 - 1$.

By (Ref. 6), the sequence of a_n is converted first to a sequence of integers x_n in the dynamic range $4 - 2$. Since 2 is a 3rd root of unity the transform over $GF(7^2)$ of x_n is

$$X_k = \sum_{n=0}^{3-1} x_n \cdot 2^{nk} = -1 + 2^{2k} \qquad \text{for } k = 0,1,2$$

Thus $X_0 = 0$, $X_1 = 3$, $X_2 = 1$

Similarly, the DFT of sequence y_n is

$$Y_k = \sum_{n=0}^{3-1} y_n \cdot 2^{nk} = 1 \cdot 2^{2k}$$

for

$$k = 0,1,2$$

That is, $Y_0 = 1$, $Y_1 = 2$, $Y_2 = 4$. But $E_k = X_k \cdot Y_k$, i.e., $E_0 = 0$, $E_1 = 6$, $E_2 = 4$. These are the only integer multiplications needed to perform this DFT. The inverse transform of E_k is

$$e_k = 3^{-1} \sum_{i=0}^{3-1} E_k \cdot 2^{-nk} \quad \text{for} \quad k = 0,1,2$$

or $e_0 = 1$, $e_1 = -1$, $e_2 = 0$.

In a similar fashion matrix F, given in Eq. (4) can also be obtained as $f_0 = -\hat{i}$, $f_1 = \hat{i} \cdot 0$, $f_2 = -\hat{i}$. Thus, by Eq. (4), one obtains $b_1 = 1/2\hat{i}$, $b_2 = -1/2\hat{i}$, $b_3 = (1-\hat{i})/2$, $b_4 = (1+\hat{i})/2$, $b_5 = -1/2$, $b_6 = -\hat{i}/2$. Hence, finally $A_0 = 2 + \hat{i}0$, $A_1 = 1 + 1/2\hat{i}$, $A_2 = 1/2 + \hat{i}0$, $A_3 = 1/2(3 - \hat{i})$, $A_4 = 1/2(3 + \hat{i})$, $A_5 = 1/2 + \hat{i}0$, $A_6 = 1 - 1/2\hat{i}$. For this example, the dynamic range of $GF(7)$ is inadequate. There is a large truncation error due to the approximation of the roots of unity. Evidently, the DFT in this example has an accuracy of precisely 2 binary digits, including the sign bit. This example, though only illustrative, suggests that the large finite fields given above have more than adequate dynamic range to compute the DFT with small truncation error.

IV. Transforms of Very Long Sequences

In order to compute the DFT of much longer sequences than considered in the last section, let $d = d_1 \cdot d_2 \ldots d_r$, where $(d_i, d_j) = 1$ for $i \neq j$. By using the Chinese Remainder Theorem (Ref. 15), it is shown by Winograd in (Ref. 13) that the DFT matrix W can be transformed into the direct product

of $W_1, W_2, \ldots, W_r$, where W_i is the matrix of a d_i-point DFT. Assume the number of multiplications used to perform the d_i-point DFT for $i = 1, 2, \ldots, r$ is m_i. Then, the number of multiplications for computing a d-point DFT is $N = m_1 \cdot m_2 \cdots m_r$. To illustrate this, see the example for computing a 12-point DFT given in Ref. 14. By the same procedure used in the computation of this example, the number of integer multiplications needed to perform the transforms of longer sequences of complex numbers can be obtained by using Table 1 above and Table 1 in Ref. 13. These numbers are given in Table 2. The present algorithm, and conventional FFT algorithm (Ref. 16) are compared in Table 2 by giving the number of real multiplications needed to perform these algorithms. The number of real multiplications needed to perform a transform of a few thousand points is given in Table 2 of Ref. 13.

Acknowledgement

The authors wish to thank Dr. N. A. Renzetti, Manager of Tracking and Data Acquisition Engineering, and the members of the Advanced Engineering Group in that organization for their early support, suggestions, and encouragement of the research that led to this paper.

References

1. Pollar, J. M., "The Fast Fourier Transform in a Finite Field," *Math. Comput.*, 1971, 25, pp. 365-374.

2. Schonhage, A. and Strassen, V., "Schnelle Multiplication Grosser Zahlen," *Computing*, 1971, 7, pp. 281-292.

3. Rader, C. M., "Discrete Convolution via Mersenne Transforms," *IEEE Trans. Comp.*, 1972, C-21, pp. 1269-1273.

4. Agarwal, R. C. and Burrus, C. S., "Number Theoretic Transforms to Implement Fast Digital Convolution," *Proc. IEEE*, 1975, 63, pp. 550-560.

5. Reed, I. S. and Truong, T. K., "The Use of Finite Fields to Compute Convolution," *IEEE Trans.*, 1975, IT-21, pp. 208-213.

6. Reed, I. S. and Truong, T. K., "Complex Integer Convolution Over a Direct Sum of Galois Fields," *IEEE Trans.*, 1975, IT-21, pp. 657-661.

7. Vegh, E. and Leibowitz, L. M., "Fast Complex Convolution in Finite Rings," *IEEE Trans.*, 1976, ASSP-24, pp. 343-344.

8. Golomb, S. W., Reed, I. S., and Truong, T. K., "Integer Convolutions Over the Finite Field $GF(3 \cdot 2^n + 1)$," *SIAM J. on Applied Math.*, Vol. 32, No. 2, March 1977.

9. Pollar, J. M., "Implementation of Number-Theoretic Transforms," *Electro. Lett.*, 1976, 12, pp. 378-379.

10. Liu, K. Y., Reed, I. S., and Truong, T. K., "Fast Number-Theoretic Transforms for Digital Filtering," *Electron. Lett.*, 1976, 12, pp. 644-646.

11. Reed, I. S., Truong, T. K., and Liu, K. Y., "A New Fast Algorithm for Computing Complex Number-Theoretic Transforms," *Electron. Lett.*, 1977, pp. 278-280.

12. Reed, I. S. and Truong, T. K., "Fast Algorithms for Computing Mersenne-Prime Number-Theoretic Transforms," *The Deep Space Network Progress Report 42-41*, pp. 176-205, Jet Propulsion Laboratory, Pasadena, California, October 15, 1977.

13. Winograd, S., "On Computing the Discrete Fourier Transform," *Proc. Nat. Acad. Sci. USA*, 1976, 73, pp. 1005-1006.

14. Winograd, S., "On Computing the Discrete Fourier Transform," Research Report, Math. Science Dept., IBM Thomas J. Watson Research Center, Yorktown Heights, New York, 10592.

15. Niven, I. and Zuckerman, H. S., *An Introduction to the Theory of Numbers*, John Wiley and Sons, Inc., New York, 1966.

16. Cooley, J. W., and Tukey, J. W., "An Algorithm for the Machine Calculation of Complex Fourier Series," *Math. Comput.*, Vol. 19, pp. 297-301, April, 1965.

Table I. Complexity of complex number DFT of prime number length

$d = p$	$p - 1$	No. of Integer Complex Multiplications
373	$2^2 \cdot 3 \cdot 31$	496
733	$2^2 \cdot 3 \cdot 61$	976
1831	$2 \cdot 3 \cdot 5 \cdot 61$	4880
1861	$2^2 \cdot 3 \cdot 5 \cdot 31$	4960
2441	$2^3 \cdot 5 \cdot 61$	4880

Table 2. Complexity of new algorithm for DFT

d	Factors	New algorithm No integer multiplications complex data	Radix-2 FFT No. real multiplications $2d\log_2 d$
4096	2^{12}		98,304
4476	373 x 4 x 3	23,904	
8192	2^{13}		212,992
8796	733 x 4 x 3	46,944	
16384	2^{14}		458,752
20888	373 x 8 x 7	143,424	
32768	2^{15}		983,040
41048	733 x 8 x 7	281,664	
62664	373 x 8 x 7 x 3	430,272	
65536	2^{16}		2,09 ×2
123144	733 x 8 x 7 x 3	844,992	
131072	2^{17}		4,456,448
262144	2^{18}		9,437,184
268560	373 x 16 x 9 x 5	2,796,768	
524288	2^{19}		19,922,944
527760	733 x 16 x 9 x 5	5,492,448	

Transform Decoding of Reed-Solomon Codes Over GF(2^{2^n}) Using the Techniques of Winograd*

I. S. Reed
University of Southern California

T. K. Truong and B. Benjauthrit
TDA Engineering Office

A new algorithm for computing a Fourier-like transform over GF(2^{2^n}), where n = 1,2,3,4,5, is developed to encode and decode Reed-Solomon (RS) codes of length 2^{2^n}. Such an RS decoder is considerably faster than a decoder that uses the conventional fast transform over GF(2^{2^n}).

I. Introduction

Fast real-valued transforms over the group $(Z_2)^n$ were developed first by Green (Ref. 1) to decode the (32,6) Reed-Muller code (Ref. 2) used by JPL in the Mariner and Viking space probes. Recently Gore (Ref. 3) extended Mandelbaum's methods (Ref. 4) for decoding Reed-Solomon codes. He proposed to decode RS codes with a finite field transform over GF(2^n), where n is an integer. Michelson (Ref. 5) has implemented Mandelbaum's algorithm and showed that the decoder, using the transform over GF(2^n), requires substantially fewer multiplications than a more standard decoder (Refs. 6, 7). The disadvantage of his transform method over GF(2^n) is that the transform length is an odd number, so that the most efficient FFT algorithm cannot be used.

For a space communication link, it was shown in (Ref. 8) that the concatenated 16-error-correcting, 255-symbol RS code, each symbol with 8 bits, and a k = 7, rate = 1/2 or 1/3, Viterbi decoded convolutional code, can be used to reduce the value of E_b/N_o required to meet a specified bit-error rate P_b. Here E_b is the received energy for each bit, and N_o is the noise power spectral density at the receiver input. Such a concatenated RS – convolutional code is being considered currently by JPL for the Voyager missions.

*This work was supported in part by the U.S. Air Force Office of Scientific Research under Grant Number AFOSR 75-2798.

The Voyager RS code utilizes 255 symbols for information and error control out of a possible 256 symbols. Of the 255 RS symbols only 223 are actually used as information symbols. The remaining 32 symbols are parity check symbols. It is by this means that the 255-symbol RS code is concatenated with a k = 7, r = 1/2 or 1/3 convolutional code.

In this paper, a new algorithm based on the methods of Winograd (Refs. 9, 10) is developed to compute a transform over GF(2^8) or more generally over GF(2^{2^n}) for n = 1,2, . . . ,5. This transform algorithm over GF(2^{2^n}) for n = 1,2,3,4 requires fewer multiplications than the more conventional fast transform algorithm described by Gentleman (Ref. 11). The algorithm is presented in detail in this paper only for the cases n = 2,3. This algorithm for other values of n and for RS codes over GF(2^m) where $m \neq 2^n$ can be treated in a similar manner though perhaps not as simply.

II. A New Algorithm for Computing a Transform over GF(2^{2^n}) of $2^{2^n} - 1$ Points for n = 1, 2, . . . , 5

Let GF(2^{2^n}) be the finite field of 2^{2^n} elements. Also let N be an integer that divides $2^{2^n} - 1$. Next, let the element $\gamma \in GF(2^{2^n})$ generate the cyclic subgroup of N elements, $G_N = (\gamma, \gamma^2, \ldots, \gamma^N = 1)$, in the multiplicative group of GF(2^{2^n}). The transform over this subgroup G_N can be defined by

$$A_j = \sum_{i=0}^{N-1} a_i \gamma^{ij}$$

for

$$0 \leq j \leq N - 1$$

where

$$a_i \in GF(2^{2^n})$$

Rewrite this in matrix form as

$$\bar{A} = W'\bar{a} , \tag{1}$$

where

$$W' = (w'_{i,j})$$

and

$$w'_{i,j} = \gamma^{ij}$$

Also let

$$A_0 = \sum_{i=0}^{N-1} a_i$$

and

$$A_j = A_0 + B_j$$

for

$$j = 1,2,\ldots, N-i$$

where

$$B_j = \sum_{i=1}^{N-i} a_{i'}^{ij}$$

That is, let

$$\bar{B} = W\bar{a} \tag{2}$$

where W is the $(N-1) \times (N-1)$ matrix $(\gamma^{ij})_{i,j \neq 0}$ and $\bar{a}$, B are the column matrices (a_i) and (B_k), respectively.

For $n = 1,2,\ldots,5$, the order of a multiplicative group of $GF(2^{2^n})$ can be factored into Fermat prime factors, i.e.,

$$2^{2^n}-1 = \prod_{i=0}^{n-1} (2^{2^i} + 1)$$

If N is a Fermat prime p, one can find an element $\alpha \in GF(P)$ which generates the cyclic subgroup of p-1 elements. Hence a permutation or substitution σ can be defined by

$$\sigma = \begin{pmatrix} 1, & 2, & \ldots, & P-2, & P-1 \\ \alpha, & \alpha^2, & \ldots, & \alpha^{P-2}, & \alpha^{P-1} = 1 \end{pmatrix} \mod p$$

where all the elements of this substitution are taken modulo p.

Using the above permutation, by (Ref. 12), one can permute the indices of $\bar{B}$, $\bar{a}$, W defined in (2) so that the matrix $\bar{W} = (\gamma^{\sigma(i)\sigma(j)})_{i,j\neq 0}$ is cyclic. That is,

$$B_{(j)} = \sum_{i=1}^{p-1} a_{\sigma(i)} \gamma^{\sigma(i)\,\sigma(j)}$$

$$= \sum_{i=1}^{p-1} a_{\sigma(i)} \gamma^{\sigma(i+j)} \qquad (3a)$$

$$= \sum_{i=1}^{p-1} a_{\sigma(i)} \gamma^{\sigma(i+j)}$$

for

$$j = 1, 2, \ldots, p-1.$$

This is reexpressed in matrix form as

$$\tilde{B} = \tilde{W}\,\tilde{a} \qquad (3b)$$

where

$$\tilde{B} = (B_{\sigma(j)}), \quad \tilde{W} = \left(\gamma^{\sigma(i+j)}\right)_{i,j\neq 0}$$

and

$$\tilde{a} = (a_{\sigma(i)})$$

By (3a) $B_{\sigma(j)}$ is a cyclic convolution of $a_{\sigma(i)}$ and $\gamma^{\sigma(i)}$ for $j = 1,2,\cdots,p-1$. But also (3a) is the set of coefficients of

$$T(u) = \left(\sum_{i=1}^{p-1} a_{\sigma(p-i)}\, u^{i-1}\right) \times \left(\sum_{i=1}^{p-1} \gamma^{\sigma(i)}\, u^{i-1}\right) \bmod u^{p-1} - 1$$

Since p is a Fermat prime, $u^{p-1} - 1 \equiv (u+1)^{p-1} \bmod 2$ so that one cannot factor $u^{p-1} - 1$ over GF(2) into irreducible relatively prime factors. Hence, Winograd's method (Refs. 9, 10) for using the Chinese remainder theorem to evaluate T(u) with the residues

of these factors cannot be used directly. Thus, special techniques are developed in the following sections to calculate the p-point transform over $GF(2^{2^n})$, where p is a Fermat prime.

Let

$$N = 2^{2^n} - 1 = \prod_{i=0}^{n-1} \left(2^{2^i} + 1\right) = N_1 N_2 \ldots N_k ,$$

where

$$(N_i, N_j) = 1$$

for $i \neq j$. Using the Chinese remainder theorem (Ref. 13), it is shown by Winograd in (Refs 9, 10) that the transform matrix W' defined in (1) can be transformed into the direct product of $W'_1, W'_2, \ldots, W'_k$, where W'_i is the matrix of an N_i-point discrete Fourier-like transform. Assume the number of multiplications needed to perform an N_i-point transform over $GF(2^{2^n})$ for $i = 1,2, \ldots, k$ is m_i. Then, the number of multiplications for computing an N-point transform is $m_1 m_2 \ldots m_k$.

III. Transform Over $GF(2^4)$ of 15 Points

Consider the finite field $GF(2^4)$. Since $N = 2^4 - 1 = 3 \times 5$, the algorithm described in the previous section can be used to calculate the transform of 15 points over $GF(2^4)$. To do this the N_i-point transforms over $GF(2^{2^n})$ are first developed individually for $N_i = 3,5$. Let γ be a 3rd root of unity in $GF(2^{2^n})$ for $n = 1,2, \ldots, 5$.

For $N_i = 3$, the transform over $GF(2^{2^n})$ for $n = 1,2, \ldots, 5$ is expressible as

$$\begin{pmatrix} A_0 \\ A_1 \\ A_2 \end{pmatrix} = \begin{pmatrix} \gamma^0, & \gamma^0, & \gamma^0 \\ \gamma^0, & \gamma^1, & \gamma^2 \\ \gamma^0, & \gamma^2, & \gamma^1 \end{pmatrix} \begin{pmatrix} a_0 \\ a_1 \\ a_2 \end{pmatrix} \tag{4}$$

Let

$$\begin{aligned} m_0 &= \gamma^0 (a_o + a_1 + a_2) \\ m_1 &= (a_1 + a_2) \cdot \gamma^1 \\ m_2 &= (\gamma^2 - \gamma^1) \cdot a_1 = \gamma^0 a_1 \\ m_3 &= (\gamma^2 - \gamma^1) \cdot a_2 = \gamma^0 a_2 \end{aligned} \tag{5}$$

Thus,

$$\begin{aligned} A_0 &= m_0 \\ A_1 &= m_0 + m_1 + m_2 \\ A_2 &= m_0 + m_1 + m_3 \end{aligned} \tag{6}$$

In what follows, a multiplication by the element γ^0 will need to be considered sometimes as a multiplication. Hence by (5), if one includes multiplications by the unit $\gamma^0 = 1$, the total number of multiplications needed to perform the above transform is 4.

Next consider the case $N_1 = 5$. Let γ be a 5th root of unity in $GF(2^{2^n})$ for $n = 2,3, \ldots ,5$. The 5-point transform is equivalent to

$$\begin{pmatrix} A_0 \\ A_1 \\ A_2 \\ A_3 \\ A_4 \end{pmatrix} = \begin{pmatrix} \gamma^0 & \gamma^0 & \gamma^0 & \gamma^0 & \gamma^0 \\ \gamma^0 & \gamma^1 & \gamma^2 & \gamma^3 & \gamma^4 \\ \gamma^0 & \gamma^2 & \gamma^4 & \gamma^1 & \gamma^3 \\ \gamma^0 & \gamma^3 & \gamma^1 & \gamma^4 & \gamma^2 \\ \gamma^0 & \gamma^4 & \gamma^3 & \gamma^2 & \gamma^1 \end{pmatrix} \begin{pmatrix} a_0 \\ a_1 \\ a_2 \\ a_3 \\ a_4 \end{pmatrix} \tag{7}$$

Thus,

$$A_0 = \gamma^0 (a_o + a_1 + a_2 + a_3 + a_4 + a_5)$$

and

$$\bar{B} : (B_i) = \begin{pmatrix} B_1 \\ B_2 \\ B_3 \\ B_4 \end{pmatrix} = \begin{pmatrix} \gamma^1 & \gamma^2 & \gamma^3 & \gamma^4 \\ \gamma^2 & \gamma^4 & \gamma^1 & \gamma^3 \\ \gamma^3 & \gamma^1 & \gamma^4 & \gamma^2 \\ \gamma^4 & \gamma^3 & \gamma^2 & \gamma^1 \end{pmatrix} \begin{pmatrix} a_1 \\ a_2 \\ a_3 \\ a_4 \end{pmatrix}$$

$$= \bar{W}\bar{a} = (w_{ij})\ (a_i)$$

Let

$$\sigma = \begin{pmatrix} 1 & 2 & 3 & 4 \\ 2 & 2^2 & 2^3 & 2^4 \end{pmatrix} = \begin{pmatrix} 1 & 2 & 3 & 4 \\ 2 & 4 & 3 & 1 \end{pmatrix} \mod 5$$

Now

$$(B_{\sigma(i)}) = (w_{\sigma(i),\,\sigma(j)})\, a_{\sigma(i)}$$

or

$$\tilde{B} = \begin{pmatrix} B_2 \\ B_4 \\ B_3 \\ B_1 \end{pmatrix} = \begin{pmatrix} w_{2,2} & w_{2,4} & w_{2,3} & w_{2,1} \\ w_{4,2} & w_{4,4} & w_{4,3} & w_{4,1} \\ w_{3,2} & w_{3,4} & w_{3,3} & w_{3,1} \\ w_{1,2} & w_{1,4} & w_{1,3} & w_{1,1} \end{pmatrix} \begin{pmatrix} a_2 \\ a_4 \\ a_3 \\ a_1 \end{pmatrix} \quad (8)$$

$$= \begin{pmatrix} \gamma^4 & \gamma^3 & \gamma^1 & \gamma^2 \\ \gamma^3 & \gamma^1 & \gamma^2 & \gamma^4 \\ \gamma^1 & \gamma^2 & \gamma^4 & \gamma^3 \\ \gamma^2 & \gamma^4 & \gamma^3 & \gamma^1 \end{pmatrix} \begin{pmatrix} a_2 \\ a_4 \\ a_3 \\ a_1 \end{pmatrix} = \tilde{W}\tilde{a}$$

This is of form

$$\begin{pmatrix} Y_1 \\ Y_2 \end{pmatrix} = \begin{pmatrix} A & B \\ B & A \end{pmatrix} \begin{pmatrix} X_1 \\ X_2 \end{pmatrix}$$

where

$$Y_1 = \begin{pmatrix} B_2 \\ B_4 \end{pmatrix}, \quad Y_2 = \begin{pmatrix} B_3 \\ B_1 \end{pmatrix},$$

$$X_1 = \begin{pmatrix} a_2 \\ a_4 \end{pmatrix}, \quad X_2 = \begin{pmatrix} a_3 \\ a_2 \end{pmatrix},$$

$$A = \begin{pmatrix} \gamma^4 & \gamma^3 \\ \gamma^3 & \gamma^1 \end{pmatrix}, \quad B = \begin{pmatrix} \gamma^1 & \gamma^2 \\ \gamma^2 & \gamma^4 \end{pmatrix}$$

Thus

$$\begin{pmatrix} Y_1 \\ Y_2 \end{pmatrix} = \begin{pmatrix} A X_1 + B X_2 \\ B X_1 + A X_2 \end{pmatrix} = \begin{pmatrix} A (X_1 + X_2) + (B - A) X_2 \\ A (X_1 + X_2) + (B - A) X_1 \end{pmatrix}$$

$$= \begin{pmatrix} D + E \\ D + F \end{pmatrix}$$

where

$$D = A (X_1 + X_2), \quad E = (B - A) X_2,$$

$$F = (B - A) X_1$$

Now

$$D = \begin{pmatrix} d_1 \\ d_2 \end{pmatrix} = A (X_1 + X_2)$$

$$= \begin{pmatrix} \gamma^4 & \gamma^3 \\ \gamma^3 & \gamma^1 \end{pmatrix} \begin{pmatrix} a_2 + a_3 \\ a_4 + a_1 \end{pmatrix}$$

$$= \begin{pmatrix} \gamma^3 (a_1 + a_2 + a_3 + a_4) + (\gamma^4 + \gamma^3) (a_2 + a_3) \\ \gamma^3 (a_1 + a_2 + a_3 + a_4) + (\gamma^1 + \gamma^3) (a_4 + a_1) \end{pmatrix}$$

$$E = (B - A)\ (X_2) = \begin{pmatrix} \gamma^4 - \gamma^1, & \gamma^3 - \gamma^2 \\ \gamma^3 - \gamma^2, & \gamma^1 - \gamma^4 \end{pmatrix} \begin{pmatrix} a_3 \\ a_1 \end{pmatrix}$$

$$= \begin{pmatrix} (\gamma^1 + \gamma^4)\ (a_1 + a_3) + \gamma^0\ a_1 \\ (\gamma^1 + \gamma^4)\ (a_2 + a_4) + \gamma^0\ a_3 \end{pmatrix}$$

Similarly

$$F = \begin{pmatrix} (\gamma^1 + \gamma^4)\ (a_2 + a_4) + \gamma^0\ a_4 \\ (\gamma^1 + \gamma^4)\ (a_2 + a_4) + \gamma^0\ a_2 \end{pmatrix}$$

Thus

$$\begin{pmatrix} B_2 \\ B_4 \\ B_3 \\ B_1 \end{pmatrix} \begin{pmatrix} \gamma^3 (a_1 + a_2 + a_3 + a_4) + (\gamma^3 + \gamma^3) \cdot (a_2 + a_3) + (\gamma^1 + \gamma^3)\ (a_1 + a_3) + \gamma^0\ a_1 \\ \gamma^3 (a_1 + a_2 + a_3 + a_4) + (\gamma^1 + \gamma^3) \cdot (a_1 + a_4) + (\gamma^1 + \gamma^3)\ (a_1 + a_3) + \gamma^0\ a_3 \\ \gamma^3 (a_1 + a_2 + a_3 + a_4) + (\gamma^3 + \gamma^3)\ (a_2 + a_3) + (\gamma^1 + \gamma^3)\ (a_2 + a_4) + \gamma^0\ a_4 \\ \gamma^3 (a_1 + a_2 + a_3 + a_4) + (\gamma^1 + \gamma^3)\ (a_1 + a_4) + (\gamma + \gamma^4)\ (a_2 + a_4) + \gamma^0\ a_2 \end{pmatrix}$$

Hence

$$A_1 = \gamma^0\ a_0 + B_1 = \gamma^0\ a_0 + \gamma^3\ (a_1 + a_2 + a_3 + a_4) + (\gamma^1 + \gamma^3)\ (a_1 + a_4) + (\gamma + \gamma^4)\ (a_2 + a_4) + \gamma^0\ a_2$$

$$= \gamma^0\ (a_0 + a_1 + a_2 + a_3 + a_4) + (\gamma^0 + \gamma^3)\ (a_1 + a_2 + a_3 + a_4) + (\gamma^1 + \gamma^3)\ (a_1 + a_4) + (\gamma + \gamma^4)\ (a_2 + a_4) + \gamma^0\ a_2$$

$$A_2 = \gamma^0\ (a_0 + a_1 + a_2 + a_3 + a_4) + (\gamma^0 + \gamma^3)\ (a_2 + a_3 + a_4 + a_1) + (\gamma^3 + \gamma^4)\ (a_2 + a_3) + (\gamma + \gamma^4)\ (a_3 + a_1) + \gamma^0\ a_1$$

$$A_3 = \gamma^0 (a_0 + a_1 + a_2 + a_3 + a_4) + (\gamma^0 + \gamma^3) (a_2 + a_3 + a_4 + a_1) + (\gamma^3 + \gamma^4) (a_2 + a_3) + (\gamma + \gamma^4) (a_2 + a_4) + \gamma^0 a_4$$

$$A_4 = \gamma^0 (a_0 + a_1 + a_2 + a_3 + a_4) + (\gamma^0 + \gamma^3) (a_2 + a_3 + a_4 + a_1) + (\gamma^1 + \gamma^3) (a_1 + a_4) + (\gamma + \gamma^4) (a_1 + a_3) + \gamma^0 a_3$$

Now let

$$\begin{aligned}
m_0 &= \gamma^0 (a_0 + a_1 + a_2 + a_3 + a_4) \\
m_1 &= (\gamma^0 + \gamma^3) \cdot (a_1 + a_2 + a_3 + a_4) \\
m_2 &= (\gamma^3 + \gamma^4) \cdot (a_2 + a_3) \\
m_3 &= (\gamma^1 + \gamma^3) \cdot (a_1 + a_4) \\
m_4 &= (\gamma + \gamma^4) \cdot (a_1 + a_3) \\
m_5 &= (\gamma + \gamma^4) \cdot (a_2 + a_4) \\
m_6 &= \gamma^0 \cdot a_1 \\
m_7 &= \gamma^0 \cdot a_3 \\
m_8 &= \gamma^0 \cdot a_4 \\
m_9 &= \gamma^0 \cdot a_2 \\
S_1 &= m_0 + m_1 + m_2 \\
S_2 &= m_0 + m_1 + m_3
\end{aligned} \tag{9}$$

Then

$$\begin{aligned}
A_0 &= m_0 \\
A_1 &= S_2 + m_5 + m_9 \\
A_2 &= S_1 + m_4 + m_6 \\
A_3 &= S_1 + m_5 + m_8 \\
A_4 &= S_2 + m_4 + m_7
\end{aligned} \tag{10}$$

If again one includes multiplications by the unit γ^0, it follows from the algorithm in (9) that the number of integer multiplications needed to perform a 5-point transform is 10. If multiplications by γ^0 are excluded, evidently only 5 multiplies are actually needed.

Now consider the case $N = 15 = N_1 N_2 = 3 \cdot 5$. Let integer $0 \leq i < 15$ be represented by a pair $(i_1, i_2) = (i \bmod 3, i \bmod 5)$. Since $(3,5) = 1$, by the Chinese remainder theorem,

$$i \equiv (i_1 \cdot 10 + i_2 \cdot 6) \bmod 15 \tag{11}$$

Let γ_1 and γ_2 be 3rd and 5th roots of unity in $GF(2^4)$, respectively. The 15-point transform over $GF(2^4)$ in i_1 and i_2 is

$$A_j = \sum_{i=0}^{15} a_i \gamma^{ij}$$

or

$$\begin{aligned} A_{(j_1,j_2)} &= \sum_{i_1=0}^{3-1} \left[\sum_{i_2=0}^{5-1} a_{(i_1,i_2)} \gamma_2^{i_2 \cdot j_2} \right] \gamma_1^{i_1 \cdot j_1} \\ &= \sum_{i_1=0}^{2} a_{i_1}(j_2) \gamma_1^{i_1 \cdot j_1} \end{aligned} \tag{12}$$

where

$$a_{i_1}(j_2) = \sum_{i_2=0}^{5-1} a_{(i_1,i_2)} \gamma_2^{i_2 \cdot j_2},$$

$$j_1 = 0,1,2, \quad \text{and}$$

$$j_2 = 0,1,\ldots, 4$$

or in matrix notation,

$$\left(a_{i_1}(j_2)\right) = W_2' \bar{a}_{i_1}$$

where

$$W_2' = \begin{pmatrix} \gamma_2^0 & \gamma_2^0 & \gamma_2^0 & \gamma_2^0 & \gamma_2^0 \\ \gamma_2^0 & \gamma_2^1 & \gamma_2^2 & \gamma_2^3 & \gamma_2^4 \\ \gamma_2^0 & \gamma_2^2 & \gamma_2^4 & \gamma_2^1 & \gamma_2^3 \\ \gamma_2^0 & \gamma_2^3 & \gamma_2^1 & \gamma_2^4 & \gamma_2^2 \\ \gamma_2^0 & \gamma_2^4 & \gamma_2^3 & \gamma_2^2 & \gamma_2^1 \end{pmatrix}, \quad \bar{a}_{i_1} = \begin{pmatrix} a_{(i_1,0)} \\ a_{(i_1,1)} \\ a_{(i_1,2)} \\ a_{(i_1,3)} \\ a_{(i_1,4)} \end{pmatrix}$$

Thus (12) becomes

$$\bar{A}_{j_1} = \sum_{i_1=0}^{2} \gamma_1^{i_1 j_1} W_2' \bar{a}_{i_1} \tag{13}$$

for

$$j_1 = 0,1,2$$

or

$$\begin{pmatrix} \bar{A}_0 \\ \bar{A}_1 \\ \bar{A}_2 \end{pmatrix} = \begin{pmatrix} W_2' & W_2' & W_2' \\ W_2' & W_2'\gamma_1 & W_2'\gamma_1^2 \\ W_2' & W_2'\gamma_1^2 & W_2'\gamma_1 \end{pmatrix} \begin{pmatrix} \bar{a}_0 \\ \bar{a}_1 \\ \bar{a}_2 \end{pmatrix}$$

Now by (11), one obtains $\bar{A}_0$ in terms of A_k:

$$\bar{A}_0 = \begin{pmatrix} A_{(0,0)} \\ A_{(0,1)} \\ A_{(0,2)} \\ A_{(0,3)} \\ A_{(0,4)} \end{pmatrix} = \begin{pmatrix} A_0 \\ A_6 \\ A_{12} \\ A_3 \\ A_9 \end{pmatrix}$$

Similarly

$$\bar{A}_1 = \begin{pmatrix} A_{10} \\ A_1 \\ A_7 \\ A_{13} \\ A_4 \end{pmatrix}, \quad A_2 = \begin{pmatrix} A_5 \\ A_{11} \\ A_2 \\ A_8 \\ A_{14} \end{pmatrix}$$

and

$$\bar{a}_0 = \begin{pmatrix} a_0 \\ a_6 \\ a_{12} \\ a_3 \\ a_9 \end{pmatrix}, \quad \bar{a}_1 = \begin{pmatrix} a_{10} \\ a_1 \\ a_7 \\ a_{13} \\ a_4 \end{pmatrix}, \quad \bar{a}_2 = \begin{pmatrix} a_5 \\ a_{11} \\ a_2 \\ a_8 \\ a_{14} \end{pmatrix}$$

Using the 3-point transform in (4) and making the correspondances, $\gamma^0 \leftrightarrow W_2'$, $\gamma^1 \leftrightarrow W_2'\gamma_1$, $\gamma^2 \leftrightarrow W_2'\gamma_1^2$, one obtains

$$M_0 = W_2' \cdot (\bar{a}_0 + \bar{a}_1 + \bar{a}_2) = W_2' \begin{pmatrix} a_0 + a_{10} + a_5 \\ a_6 + a_1 + a_{11} \\ a_{12} + a_7 + a_2 \\ a_3 + a_{13} + a_8 \\ a_9 + a_4 + a_{14} \end{pmatrix}, \quad (14)$$

$$M_1 = W_2' \gamma_1 (\bar{a}_1 + \bar{a}_2) = W_2' \begin{pmatrix} \gamma_1 (a_{10} + a_5) \\ \gamma_1 (a_1 + a_{11}) \\ \gamma_1 (a_7 + a_2) \\ \gamma_1 (a_{13} + a_8) \\ \gamma_1 (a_4 + a_{14}) \end{pmatrix},$$

$$M_2 = W_2' \cdot \bar{a}_1 \quad ,$$

$$M_3 = W_2' \cdot \bar{a}_2$$

Equation (14) requires 4 matrix multiplies. Thus,

$$\begin{aligned} \bar{A}_0 &= M_0 \, , \\ \bar{A}_1 &= M_0 + M_1 + M_2 \quad , \end{aligned} \tag{15}$$

and

$$\bar{A}_3 = M_0 + M_1 + M_3$$

Observe that all four matrix multiplies in (14) are 5-point transforms of exactly the same form as (7). Thus one may compute M_j for j = 0,1,2,3 in (14) with a procedure similar to that used to compute the matrix defined in (7).

The number of multiplications for computing an M_j for j = 0,1,2,3 in (14) is 5 excluding multiplication by γ^0. Thus, the total number of multiplications needed is $4 \times 5 = 20$.

IV. Transform Over GF(2^8) of 255 Points

Since $N = 255 = 3 \cdot 5 \cdot 17 = N_1 \cdot N_2 \cdot N_3$, by Winograd's algorithm, one needs to compute an N_i-point transform over GF(2^8) for $N_i = 3,5,17$. An N_i-transform over GF(2^8) for $N_i = 3$ or 5 was computed in the last section. For $N_i = 17$, the permutation σ is given by

$$\sigma = \begin{pmatrix} 1, & 2, & 3, & 4, & 5, & 6, & 7, & 8, & 9, & 10, & 11, & 12, & 13, & 14, & 15, & 16 \\ 5, & 8, & 6, & 13, & 14, & 2, & 10, & 16, & 12, & 9, & 11, & 4, & 3, & 15, & 7, & 1 \end{pmatrix}$$

Applying the above permutation to (2), one obtains a 16 X 16 cyclic matrix. By theorem 1 in Appendix A, the cyclic matrix can be partitioned into blocks of 4 X 4 matrices so that the blocks form a 4 X 4 cyclic matrix. This has the form

$$\begin{pmatrix} T_2 \\ T_4 \\ T_3 \\ T_1 \end{pmatrix} = \begin{pmatrix} A & B & C & D \\ B & C & D & A \\ C & D & A & B \\ D & A & B & C \end{pmatrix} \begin{pmatrix} S_2 \\ S_4 \\ S_3 \\ S_1 \end{pmatrix} \tag{16}$$

where

$$T_2 = \begin{pmatrix} b_5 \\ b_8 \\ b_6 \\ b_{13} \end{pmatrix}, \quad T_4 = \begin{pmatrix} b_{14} \\ b_2 \\ b_{10} \\ b_{16} \end{pmatrix},$$

$$T_3 = \begin{pmatrix} b_{12} \\ b_9 \\ b_{11} \\ b_4 \end{pmatrix}, \quad T_1 = \begin{pmatrix} b_3 \\ b_5 \\ b_7 \\ b_1 \end{pmatrix},$$

$$A = \begin{pmatrix} \gamma^8 & \gamma^6 & \gamma^{13} & \gamma^{14} \\ \gamma^6 & \gamma^{13} & \gamma^{14} & \gamma^2 \\ \gamma^{13} & \gamma^{14} & \gamma^2 & \gamma^{10} \\ \gamma^{14} & \gamma^2 & \gamma^{10} & \gamma^{16} \end{pmatrix},$$

$$B = \begin{pmatrix} \gamma^2 & \gamma^{10} & \gamma^{16} & \gamma^{12} \\ \gamma^{10} & \gamma^{16} & \gamma^{12} & \gamma^9 \\ \gamma^{16} & \gamma^{12} & \gamma^9 & \gamma^{11} \\ \gamma^{12} & \gamma^9 & \gamma^{11} & \gamma^4 \end{pmatrix},$$

$$C = \begin{pmatrix} \gamma^9 & \gamma^{11} & \gamma^4 & \gamma^3 \\ \gamma^{11} & \gamma^4 & 3 & \gamma^{15} \\ \gamma^4 & \gamma^3 & \gamma^{15} & \gamma^7 \\ \gamma^3 & \gamma^{15} & \gamma^7 & \gamma^1 \end{pmatrix},$$

$$\gamma = \begin{pmatrix} 15 & 7 & 1 & 5 \\ 7 & 1 & 5 & 8 \\ 1 & 5 & 8 & 6 \\ 5 & 8 & 6 & 13 \end{pmatrix},$$

$$S_2 = \begin{pmatrix} a_5 \\ a_8 \\ a_6 \\ a_{13} \end{pmatrix}, \qquad S_4 = \begin{pmatrix} a_{14} \\ a_2 \\ a_{10} \\ a_{16} \end{pmatrix},$$

$$S_3 = \begin{pmatrix} a_{12} \\ a_9 \\ a_{11} \\ a_4 \end{pmatrix}, \qquad S_1 = \begin{pmatrix} a_3 \\ a_{15} \\ a_7 \\ a_1 \end{pmatrix}.$$

Now if one makes the correspondences, $A \leftrightarrow \gamma^4$, $B \leftrightarrow \gamma^3$, $C \leftrightarrow \gamma$, $D \leftrightarrow \gamma^2$, and $I_0 = A + B + C + D \leftrightarrow \gamma + \gamma^2 + \gamma^3 + \gamma^4 = 1$ in (8), then by a procedure similar to that used to compute the matrix defined in (8) one obtains

$$\begin{aligned} N_1 &= B \cdot (S_1 + S_2 + S_3 + S_4) \\ N_2 &= (A + B) \cdot (S_2 + S_3) \\ N_3 &= (C + B) \cdot (S_1 + S_4) \\ N_4 &= (C + A) \cdot (S_3 + S_1) \\ N_5 &= (C + A) \cdot (S_2 + S_4) \\ N_6 &= I_0 \cdot S_1 \\ N_7 &= I_0 \cdot S_3 \\ N_8 &= I_0 \cdot S_4 \\ N_9 &= I_0 \cdot S_2 \end{aligned} \tag{17}$$

and

$$V_1 = N_1 + N_2$$

$$V_2 = N_1 + N_3$$

Equation (17) requires 9 (4 × 4) matrix multiplies. Then

$$\begin{aligned} T_2 &= V_1 + N_4 + N_6 \\ T_4 &= V_2 + N_4 + N_7 \\ T_3 &= V_1 + N_5 + N_8 \\ T_1 &= V_2 + N_5 + N_9 \end{aligned} \tag{18}$$

To find $N_1, \ldots N_9$, one needs to multiply matrices of form (A + B), (C + B), etc., by vectors $(S_i + S_j)$, S_i, etc. For example, consider $N_2 = (A + B) \cdot (S_1 + S_3)$.

$$N_2 = \begin{pmatrix} t_0 \\ f_1 \\ f_2 \\ f_3 \end{pmatrix} = \begin{pmatrix} {}_f{}^8{}_f{}^2, {}_f{}^6{}_f{}^{10}, {}_f{}^{13}{}_f{}^{1}, {}_f{}^{14}{}_f{}^{12} \\ {}_f{}^6{}_f{}^{10}, {}_f{}^{13}{}_f{}^{16}, {}_f{}^{14}{}_f{}^{12}, {}_f{}^2{}_f{}^9 \\ {}_f{}^{13}{}_f{}^{16}, {}_f{}^{14}{}_f{}^{12}, {}_f{}^2{}_f{}^9, {}_f{}^{10}{}_f{}^{11} \\ {}_f{}^{14}{}_f{}^{12}, {}_f{}^2{}_f{}^9, {}_f{}^{10}{}_f{}^{11}, {}_f{}^{16}{}_f{}^4 \end{pmatrix} \begin{pmatrix} a_5 + a_{12} \\ a_8 + a_9 \\ a_6 + a_{11} \\ a_{13} + a_4 \end{pmatrix} \tag{19}$$

$$= \begin{pmatrix} J, & K \\ K, & L \end{pmatrix} \begin{pmatrix} E_0 \\ E_1 \end{pmatrix}$$

where J, K, L are 2 × 2 matrices. Hence

$$N_2 = \begin{pmatrix} F_0 \\ F_1 \end{pmatrix} = \begin{pmatrix} J & K \\ K & L \end{pmatrix} \begin{pmatrix} E_0 \\ E_1 \end{pmatrix} = \begin{pmatrix} (E_0+E_1)K + (J+K)E_0 \\ (E_0+E_1)K + (L+K)E_0 \end{pmatrix}$$

Let

$$\begin{aligned} U_1 &= (E_0+E_1) \cdot K \\ U_2 &= (J+K) \cdot E_0 \\ U_3 &= (L+K) \cdot E_0 \end{aligned} \tag{20}$$

Then $F_0 = U_1 + U_2$, $F_4 = U_1 + U_3$. Note that 3 (2 + 2) matrix multiplies are necessary to perform (20). The matrix U_1 in (20) is given by the relationship,

$$U_1 = \begin{pmatrix} u_1 \\ u_2 \end{pmatrix} = \begin{pmatrix} \cdot^{13}+\cdot^{16}, \cdot^{17}+\cdot^{12} \\ \cdot^{14}+\cdot^{12}, \cdot^{2}+\cdot^{9} \end{pmatrix} \begin{pmatrix} a_5+a_{12}+a_6+a_{11} \\ a_8+a_9+a_{13}+a_4 \end{pmatrix} \tag{21}$$

$$= \begin{pmatrix} a & b \\ b & c \end{pmatrix} \begin{pmatrix} k_1 \\ k_2 \end{pmatrix} = \begin{pmatrix} b \cdot (k_1+k_2) + (a+b) \cdot k_1 \\ b \cdot (k_1+k_2) + (b+c) \cdot k_1 \end{pmatrix}$$

Equation (21) requires 3 multiplies. In a similar manner, the matrices U_2 and U_3 in (20) can be obtained, using 3 multiplications. Thus the total number of multiplications needed to perform (19) is 9.

In a similar fashion, matrices N_1 and N_i for $i = 3, \ldots, 9$ given in (17) can also be obtained, each requiring 9 multiplications. Hence, the number of multiplications needed to perform a 17-point transform over $GF(2^{2^n})$ for $n = 3,4,5$ is $9 \times 5 = 45$, excluding multiplications by γ^0. To include multiplications by γ^0, it follows from (18) that the total number of multiplications needed is $9 \times 9 + 1 = 82$.

By the same procedure used to compute the 15-point transform over $GF(2^4)$ in the last section, the total number of multiplications needed to perform a 255-point transform over $GF(2^8)$ is $4 \times 10 \times 45 = 1800$ multiplies. If $N = 2^{2^n} - 1 = N_1 \cdot N_2 \cdot \cdots N_k$, where N_i is a prime number for $i = 1,2, \ldots, k$, then the total number of multiplications needed to perform a $(2^{2^n} - 1)$ - point transform is

$$M = \prod_{i=0}^{k-2} (3^{2^i} + 1) + 5 \times 3^{2^{n-1}-2}$$

By the principle of mathematical induction one can show that

$$\prod_{i=0}^{n} m^{2^i} + 1 = \frac{m^{2^{n+1}} - 1}{m-1}$$

for any integers $m > 1$ and $n \geq 0$. Thus

$$M = (3^{2^{k-1}} - 1)/2 + 5 \times 3^{2^{n-1}} - 2$$

By using a more conventional fast transform technique, Gentleman shows (Refs. 5, 11) that an N-point transform of such an N requires $N(N_1 + N_2 + \cdots + N_k - k + 1)$ multiplications, including multiplications by unity. The present algorithm for computing the $(2^{2^n} - 1)$ - point transform for $n = 1,2, \ldots, 5$ and Gentleman's algorithm are compared in Table 1. The number of multiplications needed to perform these algorithms

is given for both cases. From Table 1, one sees that for n = 1, 2, 3, 4, the new algorithm for computing the $(2^{2^n} - 1)$-point transform requires fewer multiplications than Gentleman's algorithm. This is not true for n = 5, however.

V. Transform Decoder for Reed-Solomon Codes

It is shown in (Ref. 14) that RS codes can be decoded with a fast transform algorithm over $GF(p^n)$ and continued fractions. There it was shown that the decoding of RS codes with a finite field transform over $GF(p^n)$ where p is a prime and n is an integer, was composed of the following 4 steps.

(a) Compute the transform over $GF(p^n)$ of the received N-tuple,

$$E_k = \sum_{i=0}^{N-1} \gamma_i (\alpha^i)^k = \sum_{i=1}^{t} Y_i X_i^k$$

for k = 1,2, . . . 2t

where t is the number of errors, Y_i is the i-th error amplitude and $X_i = \alpha^i$ is the i-th error position.

(b) Define the generating function of the sequence (E_k) as a formal power series. That is,

$$E(x) = E_1 x^{-1} + E_2 x^{-2} + \cdots + E_{2t} x^{-2t} + \cdots$$

$$= \frac{\sum_{i=0}^{t-1} P_i x^i}{x^t + \sum_{k=1}^{t} (-1)^k \sigma_k x^{t-k}} = \frac{P(x)}{\sigma(x)}$$

Use Berlekamp's algorithm implemented by continued fraction approximations to determine the error locator polynomial $\sigma(x)$ and error evaluator polynomial P(x) from the known E_j for j = 1,2, . . . ,2t.

(c) Use these polynomials to compute the remaining transform of the error vector e_0, $e_1, \ldots e_{N-1}$.

(d) Invert the transform to recover the error vector and then obtain the corrected code.

In order to compare the above transform decoder with the standard RS decoder, the steps used in the standard RS decoder are stated as follows:

(1) Syndrome calculation

(2) Berlekamp's algorithm or continued fractions to determine $\sigma(x)$

(3) Chien's algorithm for finding the error locations

(4) Compute error magnitudes.

One observes that step 3 in both approaches are equivalent. It is shown in (Ref. 5) that step 3 in the transform decoder requires approximately the same number of multiplications as step 3 in the standard decoder. Step 1 and step 4 in the standard decoder require more multiplications than those in the transform decoder over GF(2^{2^n}). To see this, let N be the block length of the RS code in GF(2^{2^n}). Also let $d = 2t + 1$ be the minimum distance of the code, where t is the number of allowable errors. It follows from (Refs. 5 and 15) that the number of multiplications required to perform the syndrome and error magnitude calculations for the standard decoder is approximately $(N - 1)(d - 1) + t^2$. (Note that the performance of the conventional decoder is dependent on the number of allowable errors.)

For a $(2^{2^n} - 1)$-symbol, 2^n symbol error - correcting, RS code for $n = 2,3$, the number of multiplications needed to compute the syndrome and the error magnitudes is given in Table 2. The new algorithm, Gentleman's algorithm, and the standard algorithm are compared in Table 2 in terms of the number of multiplications needed to compute the syndrome and the error magnitudes for decoding these RS codes.

Acknowledgment

The authors wish to thank Dr. N. A. Renzetti, Manager of Tracking and Data Acquisition Engineering, and the members of the Advanced Engineering Group in that organization at the Jet Propulsion Laboratory for their early support, suggestions, and encouragement of the research which led to this paper. We also thank Dr. C. A. Greenhall for his mathematical suggestions.

References

1. Green, R. R., "Analysis of a Serial Orthogonal Decoder," *Space Programs Summary 37-53*, Vol. III, 1968, pp. 185-187.

2. Reed, I. S., "A Class of Multiple-Error-Correcting Codes and the Decoding Scheme," *IRE Trans.*, PGIT-4, 1954, pp. 38-49.

3. Gore, W. C., "Transmitting Binary Symbols with Reed-Solomon Code," Johns Hopkins EE Report No. 73-5, April 1973.

4. Mandelbaum, D., "On Decoding Reed-Solomon Codes," *IEEE Trans. on Inform. Theory*, Vol. IT-17, No. 6, pp. 707-712, November 1971.

5. Michelson, A., "A New Decoder for the Reed-Solomon Codes Using a Fast Transform Technique," Systems Engineering Technical Memorandum, No. 52, Electronic Systems Group Eastern Division GTE Sylvania, August 1975.

6. Peterson, W. W., "Error-Correcting Codes," MIT Press, Cambridge, Mass., 1961, pp. 168-169.

7. Lin, S., *An Introduction to Error-Correcting Codes*, Englewood Cliffs, N.J., Prentice-Hall, 1970.

8. Odenwalder, J., et al., "Hybrid Coding Systems Study Final Report," Linkabit Corp., NASA CR 114,486, Sept. 1972.

9. Winograd, S., "On Computing the Discrete Fourier Transform," *Proc. Nat. Acad. Sci. USA*, 1976, 73, pp. 1005-1006.

10. Winograd, S., "On Computing the Discrete Fourier Transform," Research Report, Math. Science Dept., IBM Thomas J. Watson Research Center, Yorktown Heights, New York, 10592.

11. Gentleman, W. M., "Matrix Multiplication and Fast Fourier Transforms," *Bell System Technical Journal*, 1968, pp. 1099-1103.

12. Reed, S. I., and Truong, T. K., "Fast Mersenne Prime Transforms for Digital Filters," to be published in the Proceedings IEE.

13. Niven, I., and Zuckerman, H. S., *An Introduction to the Theory of Numbers*, John Wiley and Sons, Inc., New York, 1972, p. 49.

14. Reed, I. S., Scholtz, R. A., Truong, T. K., and Welch, L. R., "The Fast Decoding of Reed-Solomon Codes Using Fermat Theoretic Transforms and Continued Fractions," to be published in *IEEE Trans. on Inform. Theory*.

15. Forney, G. D., "On Decoding BCH Codes," *IEEE Transactions on Information Theory*, IT-11, October 1965.

Table 1. The complexity of transform over GF(2^{2^n}) for n = 1, 2, . . . , 5

$N = 2^{2^n} - 1$	Factors $N_1 \cdot N_2 \cdots N_k = \prod_{i=0}^{k} (2^2 + 1)$	No. mult. of new algorithm $(3^{2^{k-1}} - 1)/2 + 5 \times 3^{2^{n-1}-2}$ for n > 1	No. mult. of Gentleman's algorithm $N(N_1 + N_2 + \ldots + N_k - k + 1)$
$2^2 - 1$	3	1	9
$2^{2^2} - 1$	3 × 5	4 × 5 = 20	15(3 + 5 − 1) = 105
$2^{2^3} - 1$	3 × 5 × 17	4 × 10 × 45 = 1800	255(3 + 5 + 17 − 2) = 5865
$2^{2^4} - 1$	3 × 5 × 17 × 257	4 × 10 × 82 × 3645 = 11,955,600	65535(3 + 5 + 17 + 257 − 3) = 18,284,265
$2^{2^5} - 1$	3 × 5 × 17 × 257 × 65537	4 × 10 × 82 × 6562 × 23914845 = 514,727,818,279,200	$(2^{32} - 1)$(3 + 5 + 17 + 257 + 65537 − 4) = 282,673,272, 520,425

Table 2. The complexity of decoding RS of $2^{2^n} - 1$ points for n = 2, 3

N	Factors $N_1, N_2 \ldots N_k$	No. mult. of new algorithn	No. mult. of Gentleman's algorithm $2N(N_1 + N_2 + \cdots + N_k - k + 1)$	No. mult. of the standard algorithm $(N - 1)(d - 1) + t^2$
15	3 × 5	2 × 20 = 40	2 × 105 = 210	$(14)(?) + 4^2 = 128$
255	3 × 5 × 17	2 × 1800 = 3600	2 × 5862 = 11724	$(254)(32) + 16^2 = 8384$

Appendix A

Definition: A matrix A(i,j),i,j ϵ Z_n is cyclic if for some function f on Z_n,

$$A(i,j) = f\ ((i+j)\ \text{mod}\ n)$$

where

$$Z_n = \{1,2,..,n\}$$

Theorem 1: Let n = ab. If A(i,j) is a cyclic matrix, then A(i,j) is a matrix of b X b submatrices such that the submatrices form an a X a cyclic matrix.

Proof: Let $A_{ij}(k,\ell)$ be (k,ℓ) - th element of the (i,j) - th b X b submatrix of A, where $i,j \epsilon Z_a$, $k,\ell \epsilon Z_b$.

Then

$$A_{ij}(k,\ell) = A(bi+k,bj+\ell)$$

$$= f((b(i+j)+k+\ell)\ \text{mod}\ ab)$$

For $i \epsilon Z_a$, define the matrix $(G_i(k,\ell))$ by

$$G_i(k,\ell) = f((bi+k+\ell)\ \text{mod}\ ab)$$

for $k,\ell \epsilon Z_b$. Since b[(i + j) mod a] $\equiv$ b(i + j) mod ab, we have

$$A_{ij}(k,\ell) = G_{(i+j)\ \text{mod}\ a}\ (k,\ell)$$

Therefore, the a X a array of submatrices A_{ij} is cyclic.

CCIR Papers on Telecommunications for Deep Space Research

N. F. deGroot
Telecommunications Systems Section

Three JPL papers on telecommunications for deep space research have been adopted by Study Group 2 of the International Radio Consultative Committee (CCIR). In this article we present the paper that deals with the selection of preferred frequency bands in the 1-20 GHz range. Topics include propagation factors, equipment considerations, and communication link performance.

Study Group 2 of the International Radio Consultative Committee (CCIR) is concerned with the technical aspects of telecommunications for space research and radio astronomy. Three JPL papers on deep space research were submitted by the United States for consideration at a meeting held in Geneva during September, 1977. The papers were adopted and are:

Doc. 2/296 Telecommunication Requirements for Manned and Unmanned Deep Space Research

Doc. 2/269 Preferred Frequency Bands for Deep Space Research Using Manned and Unmanned Spacecraft

Doc. 2/279 Protection Criteria and Sharing Considerations Relating to Deep Space Research

The first of these papers was included in the September-October issue of the *Deep Space Network Progress Report* (PR 42-42). Also in that report was a description of the role of CCIR papers in the establishment of worldwide regulations that determine the use of the radio frequency spectrum.

In this article the second paper is presented. It considers the selection of frequencies most appropriate for meeting the telecommunication requirements of deep space research.

The third paper considers interference protection and band sharing with other users. This paper will appear in a future issue of the *DSN Progress Report*.

Documents
C.C.I.R. Study Groups
Period 1974-1978

Doc. 2/269-E
22 September 1977

Original: English

WORKING GROUP 2-B

Draft New REPORT*
PREFERRED FREQUENCY BANDS FOR DEEP SPACE RESEARCH USING MANNED AND UNMANNED SPACECRAFT
(Study Programme AQ/2)

1. Introduction

Mission requirements, equipment factors and link performance define the frequency bands that are preferred for deep space research using manned and unmanned spacecraft. This report presents the preferred bands and selection considerations. Doc. 2/296 contains a detailed discussion of the telecommunications requirements for deep space research that were used in determining the preferred frequency bands.

2. Mission requirements

2.1 Telecommand and maintenance telemetering

Mission safety and success require that telecommand and maintenance telemetering be accomplished regardless of weather conditions. These functions must be possible during planned and unplanned space station attitudes that preclude use of the space station high gain primary antenna. Where link performance permits, a low gain secondary antenna may be carried for use in such cases. This antenna is nearly isotropic and must be considered when selecting operating frequencies.

2.2 Science telemetering

Selection of the best frequency for mission science telemetering includes consideration of the risk of degraded link performance caused by weather conditions. For some missions, unique data must be sent at a particular time, and reliable telemetering during adverse weather conditions is a necessity. For missions where unique data can be stored for most effective playback to Earth, a frequency may be selected for maximum data rate during clear weather. The maximum data rate objective can also be satisfied for those missions where data timing is not important or when particular data may be repeatedly acquired, as in some planetary orbiter missions.

2.3 Doppler and range tracking

Doppler and range tracking must be accomplished with an exactitude that satisfies mission navigation and radio science requirements. These determine the needed ranging accuracy and the necessary precision in the measurement of the effects of charged particles.

Charged particle calibration can be done with paired Earth-to-space and space-to-Earth frequencies in a single band. Increasing tracking accuracy requirements will necessitate calibration using two or more frequency pairs in different bands.

2.4 RF carrier tracking

For missions where it is required to maintain communication as the ray path passes close to the Sun, frequency selection must consider the scintillation effects of transmission through the solar plasma. These cause broadening of the RF carrier and difficulty in maintaining coherence in a narrow band phase-locked loop. No telemetering, Doppler measurements, or ranging can be conducted unless the carrier can be phase-locked.

---

*Proposed replacement for Draft Report AN/2, SG 2 Interim Meeting, Geneva, March 1976.

2.5 Bandwidth

Telemetering and telecommand data rates tend to rise with improving technology. Increased rates require wider bandwidth, particularly for coded transmission.

The need for increased ranging accuracy will require greater ranging bandwidths. In some cases, the ranging signal will determine the total bandwidth requirement, and frequency selection for this function may be constrained by the width of the allocated band.

Where simultaneous communication is conducted with several spacecraft within a single antenna beam, the total needed bandwidth is increased proportionally. A detailed discussion of bandwidth requirements will be found in Doc. 2/296.

3. Equipment factors

Earth stations include large steerable parabolic antennae, high power transmitters and sensitive receivers. All of these are very expensive and infrequently constructed. For this reason, analysis of link performance versus frequency considers the earth station antennae to be of fixed diameter.

Earth station equipment has been built and is operating in the 2 and 8 GHz allocations. The selection of frequency bands must consider the realities of existing equipment. There is more freedom of choice in higher frequency bands, since operational capability has yet to be developed above 10 GHz.

The link analyses presented in the Annex are based upon a fixed diameter earth station antenna, and both fixed diameter and fixed beamwidth space station antennae. The fixed diameter space station case arises when the largest possible antenna may be used, free of pointing limitations. The fixed beamwidth case is in effect when antenna pointing accuracy determines the minimum beamwidth, or when the antenna must give wide coverage to permit communication without regard to space station attitude.

Because of the practical limits of diplexers, Earth-to-space and space-to-Earth pairs of frequency bands must be separated by at least 7% to allow simultaneous transmit-receive operations with a single antenna.

Standard transponder designs currently used at 2 and 8 GHz employ specific receive/transmit frequency ratios that must be considered in determining preferred frequency bands.

4. Link performance

Maximum data rate capability is obtained by using bands appropriate for weather conditions and space station antenna limitations. Tables I and II show optimum link frequencies selected on the basis of the analysis in the Annex.

Optimum frequencies for clear weather will tend to increase as technology improves. For rain, the optimum space-to-Earth frequency will tend to decrease slightly because the sky noise caused by rain will dominate system performance.

Table I. Optimum frequency bands for space-to-Earth links

Space Station Antenna Limitation	Weather Condition	Best Performance Frequency Band (GHz)
Fixed diameter	Clear	10-14
Fixed diameter	Rain	4-6
Fixed beamwidth	Clear	1-2
Fixed beamwidth	Rain	1-2

Table II. Optimum frequency bands for Earth-to-space links

Space Station Antenna Limitation	Weather Condition	Best Performance Frequency Band (GHz)
Fixed diameter	Clear	12-20
Fixed diameter	Rain	7-9
Fixed beamwidth	Clear	1-2
Fixed beamwidth	Rain	1-2

5. Preferred frequencies

For each telecommunication function, i.e., maintenance and science telemetering, telecommand, tracking and radio science, there is a frequency, band, or set of frequency bands that will provide best performance. Best performance refers to error rate, measurement accuracy, data rate, link reliability or some combination of these parameters. The best performance that is obtainable at a particular time with a particular system depends upon propagation conditions. The objective of identifying preferred frequencies is to provide the basis for allocations from which the designer can select operating frequencies best suited to mission requirements.

Table III lists the preferred frequency bands and associated characteristics that would provide the needed range of choices for the conduct of deep space research.

Table IV compares the preferred frequencies with current allocations for deep space research. Existing earth and space stations use current allocations, even though these are not always optimum. Allocations in the 10-20 GHz range are needed for future missions requiring optimum link performance for very high telemetering rates and wide-band ranging.

6. Conclusion

To meet the needs of the deep space research service, at least three pairs of Earth-to-space and space-to-Earth bands are required. The preferred frequencies for these pairs are shown in Tables III and IV.

The existing 2110-2120 MHz and 2290-2300 MHz allocated pair meet the requirement for weather independent links using either high or low gain spacecraft antenna. The 10 MHz allocation width imposes a limit on telemetering data rate and ranging precision, especially when communicating with two or more spacecraft within the earth-station antenna beam.

The existing 7145-7235 MHz and 8400-8500 MHz allocated pair provides increased link performance using the spacecraft high gain antenna. The 8 GHz allocation is not optimum, but provides acceptable performance. The 100 MHz allocation width allows telemetering and ranging that is adequate for current and near-future missions. These bands in combination with the 2 GHz allocations provide for multi-frequency charged particle calibration.

A new pair of bands between 10 and 20 GHz will be needed for clear weather use by future missions. These bands should be approximately 500 MHz wide to permit advanced radio science experiments that require ranging to centimetre accuracy, very high telemetering rates, and simultaneous operation with several spacecraft. These bands will also provide reduced charged particle delays and scintillation and thus permit operations with ray paths passing close to the Sun. In combination with the 2, 7 and 8 GHz allocations, they will allow very accurate measurement of charged particle effects.

Table III. Preferred frequencies and their uses

Region of Preferred Frequency	Use	Other Requirements
1-2 GHz	All weather Earth-to-space and space-to-Earth links using either the spacecraft high-gain, or the widebeam low-gain antennae. Used for telemetering, telecommand, tracking, and as part of multifrequency charged-particle calibration.	Earth-to-space and space-to-Earth bands separated by at least 7%.
4-6 GHz	All weather space-to-Earth link using the spacecraft high-gain antenna. Used for telemetering, tracking, and as part of multifrequency charged-particle calibration.	Requires Earth-to-space band of equal width to support two way tracking. (See 7-9 GHz preferred frequency.)
7-9 GHz	All weather Earth-to-space link using the spacecraft high gain antenna. Used for telecommand, tracking, and as part of multifrequency charged-particle calibration.	Requires space-to-Earth band of equal width to support two-way tracking. (See 4-6 GHz preferred frequency.)
10-14 GHz	Clear weather space-to-Earth link using the spacecraft high gain antenna. Used for telemetering, tracking, and as part of multifrequency charged-particle calibration.	Requires similar Earth-to-space band of equal width to support two-way tracking. (See 12-20 GHz preferred frequency.)
12-20 GHz	Clear weather Earth-to-space link using the spacecraft high gain antenna. Used for telecommand, tracking, and as part of multifrequency charged-particle calibration.	Requires similar space-to-Earth band of equal width to support two-way tracking. (See 10-14 GHz preferred frequency.)

Table IV. Preferred frequencies and current allocations

Region of Preferred Frequency (GHz)	Current Allocation (GHz)
1-2 Earth-to-space	2.110-2.120 Earth-to-space
1-2 Space-to-Earth	2.290-2.300 Space-to-Earth
7-9 Earth-to-space	7.145-7.235 Earth-to-space
4-6 Space-to-Earth	8.400-8.500 Space-to-Earth
12-20 Earth-to-space	None
10-14 Space-to-Earth	None

Frequencies near 30 GHz, and perhaps higher, will also be needed in the future for space-to-space communication.

ANNEX

FREQUENCY SELECTION CONSIDERATIONS FOR DEEP SPACE RESEARCH

1. Introduction

This Annex presents an analysis that provides the basis for the selection of frequencies for communication between deep space research earth and space stations.

The Annex considers link performance as a function of frequency by establishing an index of performance, using propagation factors derived from Reports 233-3, 205-2, 564 (Rev. 76), 234-3 (Rev. 76) and 263-3, and the principal elements of equipment technology which affect performance. Sets of curves are provided to illustrate the relative performance under various weather and antenna elevation angle conditions.

2. Calculation of link performance as a function of frequency

Telecommunication link performance includes frequency dependent parameters related to propagation and equipment factors. One index of performance is the ratio of received power-to-noise spectral density:

$$P_R - N_o = P_T + G_T - L_P - L_A - L_{Ra} + G_R - KT_T \quad \text{(dB)}$$

where

P_R	=	received power	(dBW)
N_o	=	noise spectral density	(dBW/Hz)
P_T	=	transmitter power	(dBW)
G_T	=	transmitting antenna gain	(dBi)
L_P	=	path loss between isotropic antennae	(dB)
L_A	=	transmission loss through the atmosphere including water vapour	(dB)
L_{Ra}	=	transmission loss through rain	(dB)
G_R	=	receiving antenna gain	(dBi)
K	=	1.38×10^{-23}	(Joule/K)
T_T	=	total noise temperature	(K)

$$T_T = T_A + T_{Ra} + T_G + T_R \quad \text{(K)}$$

where

T_A	=	noise temperature related to L_A	(K)
T_{Ra}	=	noise temperature related to L_{Ra}	(K)

T_G = galactic background noise temperature, after transmission losses through the propagation media (K)

T_R = noise temperature of receiver (K)

For an Earth-to-space link the noise power contribution of earth atmosphere and rain may be neglected and:

$$T_T = T_G + T_R .$$

The optimum frequency for a link with particular antenna and weather requirements may be determined by calculating the index of performance as a function of frequency.

3. Propagation considerations

Communication system performance depends on propagation characteristics, and these are frequency dependent.

3.1 Absorption attenuation by atmospheric gases and precipitation

Radio transmission through a clear atmosphere is subject to attenuation and reradiation by molecular oxygen and water vapour. The attenuation is a function of radio frequency and the oxygen and water vapour content along the transmission path. This is discussed in detail in Report 234-3 (Rev. 76).

Rain attenuation is a function of the radio frequency, rainfall rate, rain drop size, and drop distribution within the rain volume. This is discussed in detail in Report 233-3.

Figure 1 presents curves of attenuation between space and Earth as a function of frequency and elevation of the earth station antenna. The figure was derived from data in Reports 205-2, 233-3 (Rev. 76), 563 and 564 (Rev. 76). The curves labeled "clear weather" were calculated for one way attenuation through a moderately humid atmosphere (7.5 gm/m^3 at the surface). The curves for rain are for a rate (32 mm/hr) exceeded 0.01% of an average year in rain climate 4, and include the attenuation of the atmosphere.

3.2 Sky noise temperature

The following factors contribute to sky noise: atmospheric gases (principally oxygen and water vapour), precipitation, and galactic noise and cosmic background. Sky noise temperature caused by atmospheric gases and precipitation is a function of temperature and the attenuation along the transmission path, and is thus related to frequency and antenna elevation angle as discussed in Report 234-3 (Rev. 76). Report 205-2 contains curves of galactic and cosmic background noise. The contribution of these sources to total sky noise is modified by the attenuation along the path.

Figure 2 presents curves of total sky-noise temperature for the weather conditions of Figure 1, plus the contributions of galactic and cosmic background noise, calculated according to the preceding considerations.

3.3 Tropospheric scintillation and refraction

Reports 234-3 (Rev. 76) and 564 (Rev. 76) indicate that the propagation effects caused by tropospheric scintillation and refraction may be negligible, if transmission frequencies are below 20 GHz and antenna elevation angles are greater than 3°. These effects have not been included in the analysis of preferred frequencies.

3.4 Ionospheric scintillation

Electron-density irregularities in the ionosphere create refractive inhomogeneities that result in signal amplitude and phase variations. Fading of 3 to 4 dB at frequencies in the 4 and 8 GHz range has been observed. Current information is insufficient for including this factor in frequency selection. Scintillation effects in the ionosphere are discussed in Report 263-3 (Rev. 76).

3.5 Variations in propagation velocity caused by charged particles

In passing through an ionized medium the phase velocity of a radio signal is increased and the group velocity is decreased. The effect is proportional to the integrated electron density along the ray path, and inversely proportional to the square of the frequency. The group delay has been shown to be [Trask and Efron, 1966]:

$$\Delta t = \frac{40.3}{cf^2} \int N ds \text{ seconds}$$

where

Δt = group delay in seconds

f = the frequency of signal transmission in Hz

N = electron density in electrons/metre^3

s = ray path length in metres

c = speed of light in free space in metres/second

The effect is not a constant. Velocity scintillation phenomena are also observed. These cause phase modulation and spectrum broadening of the signal traversing the ionized medium.

An estimate of the upper limit on the propagation delay through the ionosphere ranges from 0.25 μs at 1 GHz to 62 nS at 20 GHz. Further discussion will be found in Report 263-3.

The solar plasma in interplanetary space modifies radio wave propagation velocity in the same way as the ionosphere. Deep space tracking measurements have yielded delay measurements from several locations in the solar system. The resulting electron density profile which those measurements provided is the basis for an approximation formula

$$N = 10^{12}\left(\frac{70}{r^6} + \frac{0.6}{r^2}\right)$$

where

N = electron density in electrons/metre^3

r = distance from Sun surface in Sun radii

Propagation delay can result in range measurement error. Consider the case of a spacecraft at a distance of 1 AU (1.5×10^8 km). The difference between indicated and actual range depends upon charged particle density along the path from Earth to the spacecraft, and is shown in Figure 3 for three different radio frequencies, as a function of the angle between the Earth-Sun (surface) line and Earth-spacecraft line. The figure was obtained by calculating propagation delay and then multiplying by the speed of light.

Spacecraft tracking depends on very accurate knowledge of propagation velocity to determine range for use in orbital calculations and charged particle effects are therefore important factors in frequency selection.

4. Equipment considerations

Equipment parameters considered in link performance analysis include transmitter power, antenna gain, and receiving system noise temperature. For additional discussion of these parameters see Doc. 2/296.

4.1 Transmitter power

Space station transmitter power is limited primarily by the available spacecraft primary power so that the obtainable RF output power is approximately independent of frequency in the 1-20 GHz range. Earth station transmitter power in the same frequency range is limited primarily by development cost.

For link performance analysis in this Annex, transmitter power is considered to be independent of frequency.

4.2 Antenna gain

Antenna gain is limited by size, surface precision and structural deformation. For space stations, antenna size is limited by space available in the launch vehicle, by the state of development of unfurlable structures, and by the pointing capability of the space station.

Link analysis in this Annex assumes that the gain of a space station fixed diameter antenna increases directly as the frequency squared, since the effect of imperfections is negligible in the frequency range being considered. For the fixed beamwidth case the gain is assumed to be independent of frequency.

The earth station antenna gain for 1977 implementation is considered to follow the curve in Figure 3 of Doc. 2/296.

4.3 Receiving equipment noise temperature

The space station receiving system noise temperature is dominated by the input preamplifier. Antenna feedline losses are relatively unimportant in their noise contribution.

At earth stations there is no important size, weight, or complexity limitation, and the most sensitive possible receiver is needed.

Link analysis in this Annex assumes that for 1977 implementation the noise temperatures are as shown in Figure 2, Doc. 2/296.

5. Link performance

The frequency dependence of link performance may be shown by the variation in the ratio of total received power to noise spectral density, P_R/N_o. Curves of P_R/N_o, shown in Figures 4 through 7, were calculated by using data in Figures 1 and 2, equipment characteristics described in Doc. 2/296, and the following assumptions:

Communication distance	8×10^8 km
Earth station antenna	64 m
Earth station transmitter	100 kW

Space station antenna	3.7 m
Space station transmitter	25 W

The important features of the performance curves are the location of maxima and the effects of elevation angle and weather. The numerical values of P_R/N_o depend upon the assumed link parameters. Different assumptions about communication distance, antennae characteristics and transmitter power would not significantly change the shape of the curves.

Figures 4 through 7 show curves for clear and rainy weather, and for earth station antenna elevation angles of 15^o (near horizon), 30^o and 75^o. Figures 4(a), 5(a), 6(a) and 7(a) reflect the implementation limitations typical of 1977 earth and deep space stations. Gravity induced structural distortions on large earth station antennae reduce gain to an extent dependent on elevation angle. This effect is included in the figures for 1977, and is the cause of the crossing of several curves.

Figures 4(b), 5(b), 6(b) and 7(b) assume the use of perfect antennae and noiseless receivers. These curves illustrate ultimate performance as limited by natural phenomena, and demonstrate the effect of advancing technology.

6. Discussion

The performance curves were developed for clear weather and heavy rainfall conditions. The rainfall rate used in the analysis is the amount that is exceeded 0.01% of the time in rain climate 4. This rate, 32 mm/hr, was chosen to allow frequency selection that will satisfy the requirement for reliable telecommunication under adverse conditions. In Annex II, Report 536 (Geneva, 1974), there are curves for the condition of clouds and 4 mm/hr rain. Comparison of shape and maxima of the curves shows that selection of preferred frequencies is not significantly altered by consideration of more moderate weather.

The curves for the future performance as limited only by natural phenomena, i.e weather and cosmic noise, show the link performance that may be approached as equipment and techniques become more fully developed.

References

Trask, D.W. and Efron, L. [1966]. DSIF Two-way Doppler Inherent Accuracy Limitations: III. Charged Particles. Space Programs Summary 37-41, Vol. III, Jet Propulsion Laboratory, 3-11.

Bibliography

Blackband, W. T. [1967]. Propagation Factors in Space Communication. McKay and Co. Ltd.

Key Words

Deep space research
Frequency selection
Performance
Telecommunications
Propagation effects

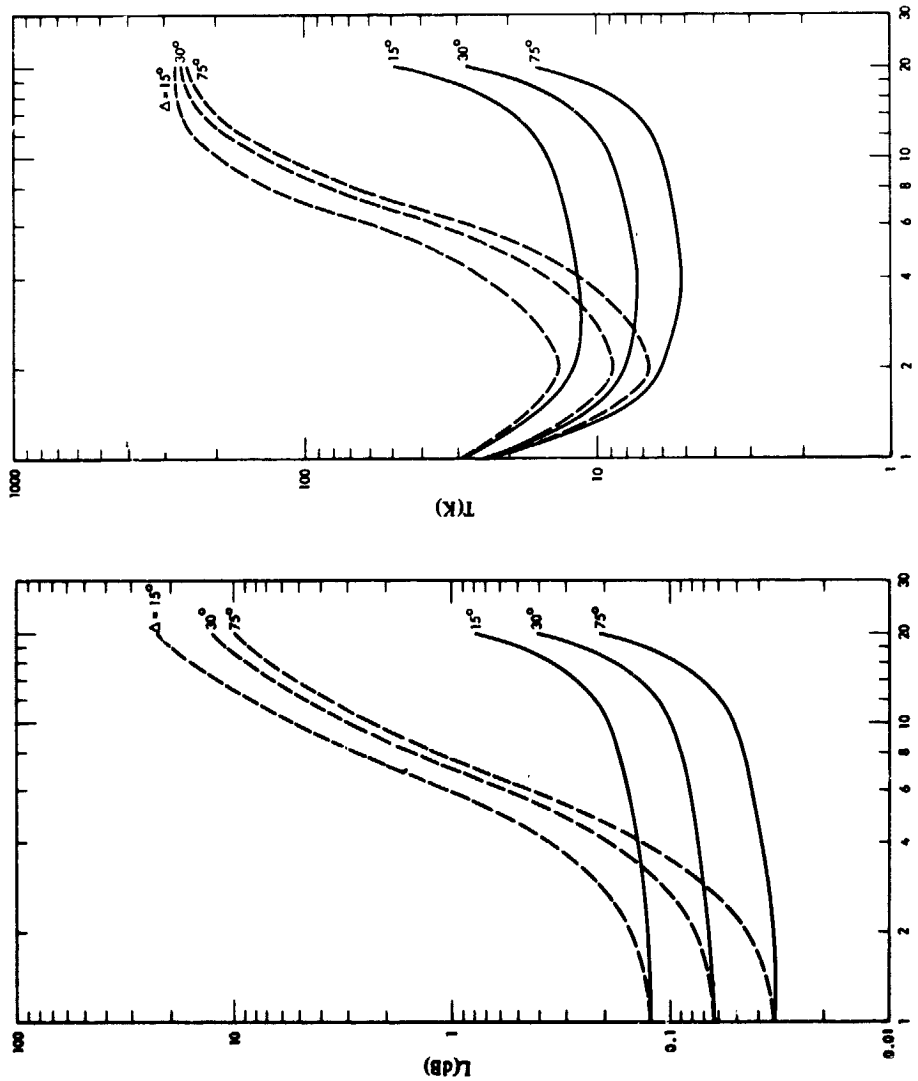

FIGURE 1

Attenuation (L) by atmosphere and rain

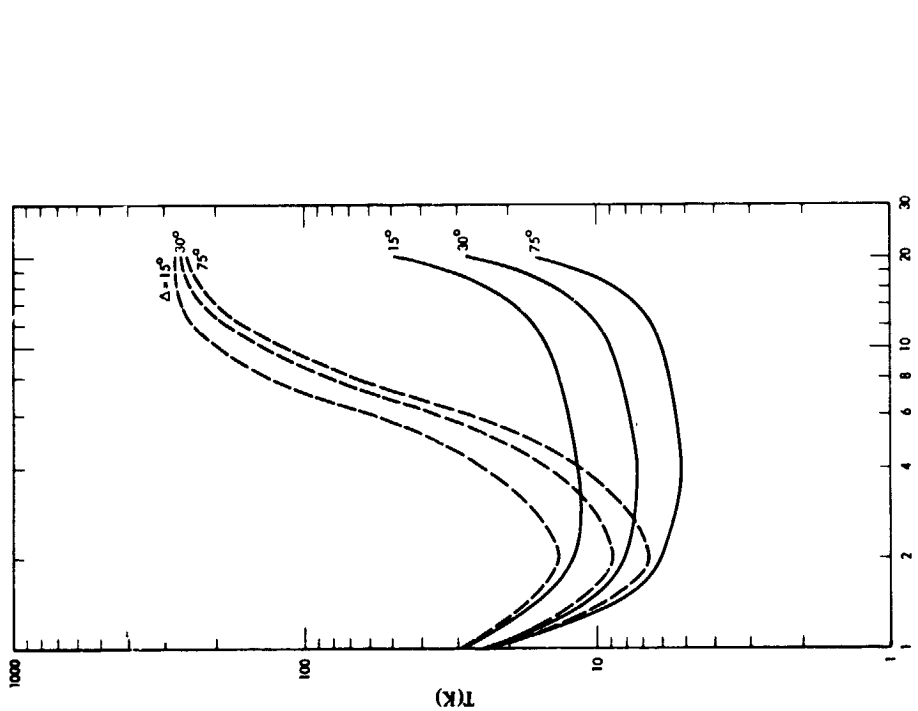

FIGURE 2

Sky noise temperature (T)

——— clear weather, atmosphere only

— — — rain and atmosphere

Δ, elevation of earth station antenna

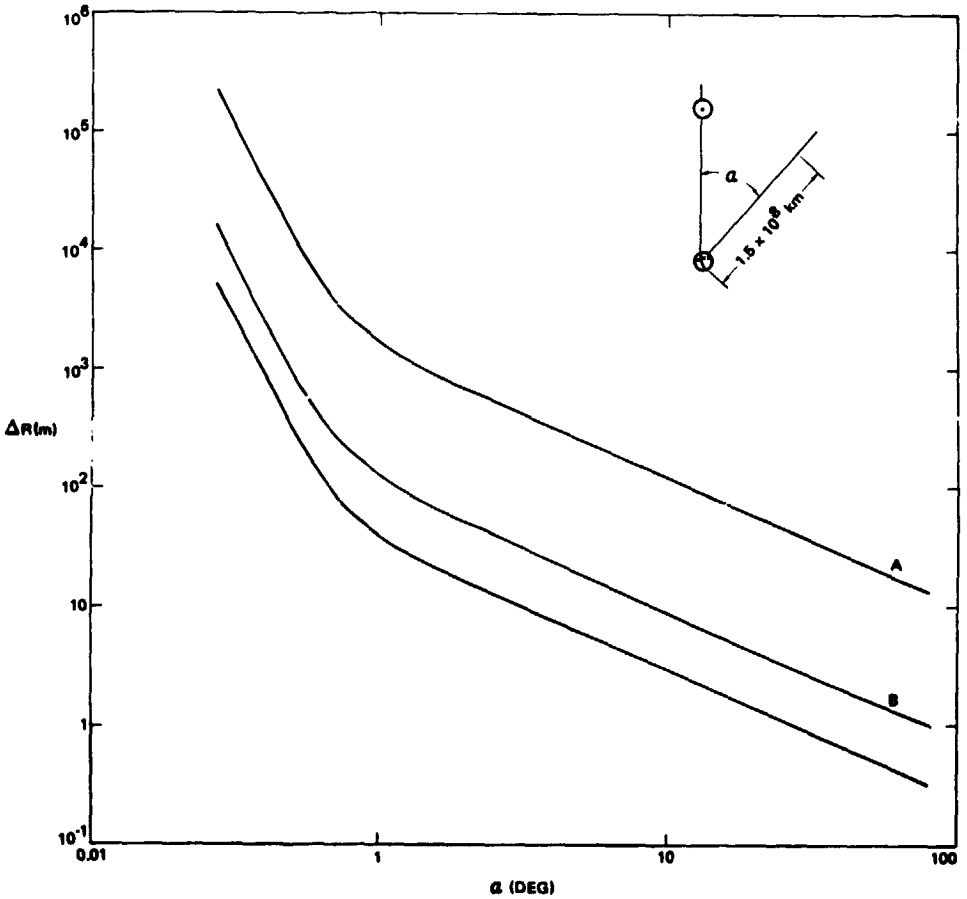

FIGURE 2.

Approximate error (ΔR) in measured spacecraft range caused by charged particles along a 1.5 X 10^8 km path, as a function of angle from center of sun (α)

A: 2.295 GHz
B: 8.450 GHz
C: 15.0 GHz

⊙ : *SUN*
⊕ : *EARTH*

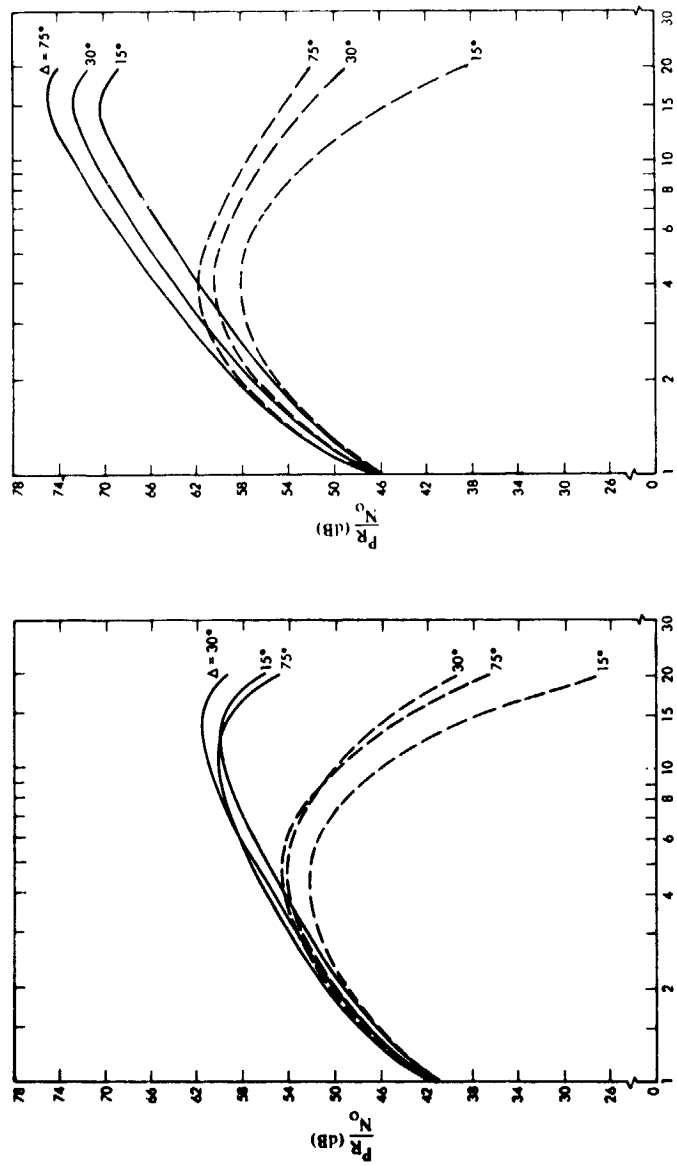

(a) 1977 implementation

(b) Future limits from natural phenomena only

FIGURE 4

Space-to-earth link performance $\left(\frac{P_R}{N_o}\right)$

Two fixed diameter antennae

——— clear weather, atmosphere only

– – – – rain and atmosphere

Δ elevation angle of earth station antenna

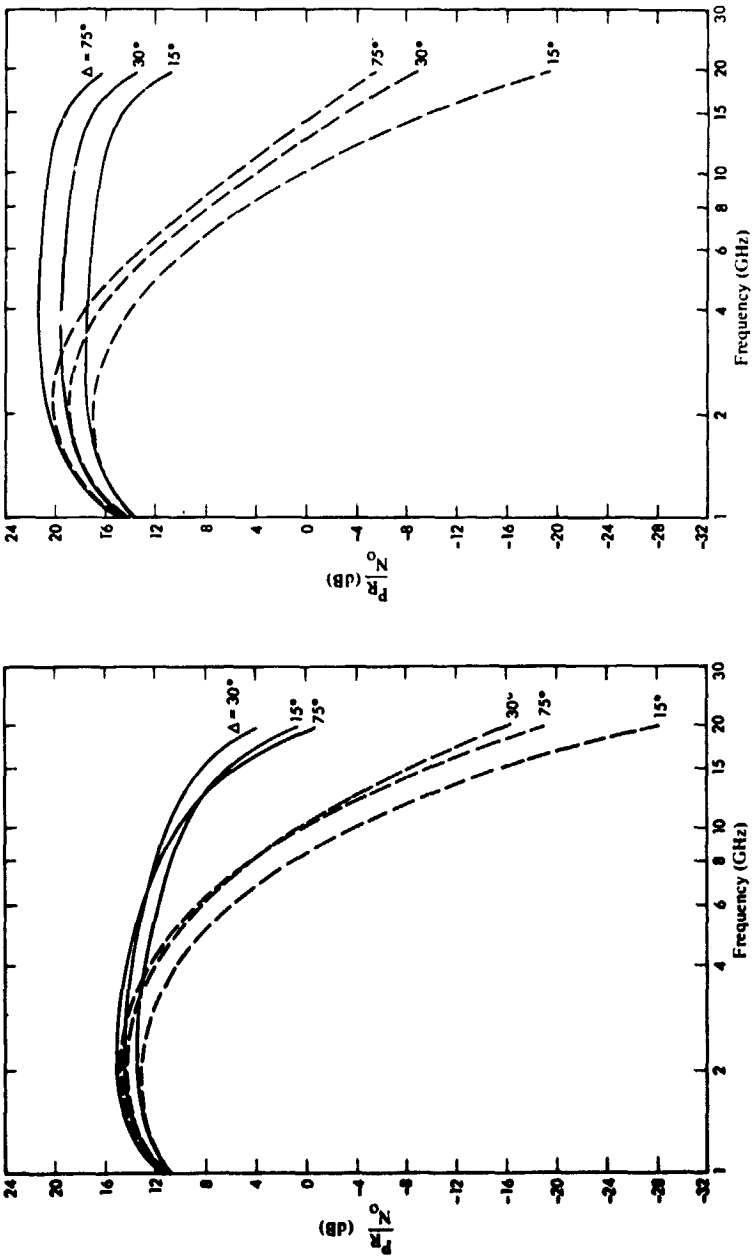

(b) Future / ·vis from natural phenomena only

(a) 1977 implementation

FIGURE 5

Space-to-earth link performance $\left(\frac{P_R}{N_o}\right)$

Fixed beamwidth space station antenna, fixed diameter earth station antenna

——— clear weather, atmosphere only
– – – – rain and atmosphere

Δ: elevation angle of earth station antenna

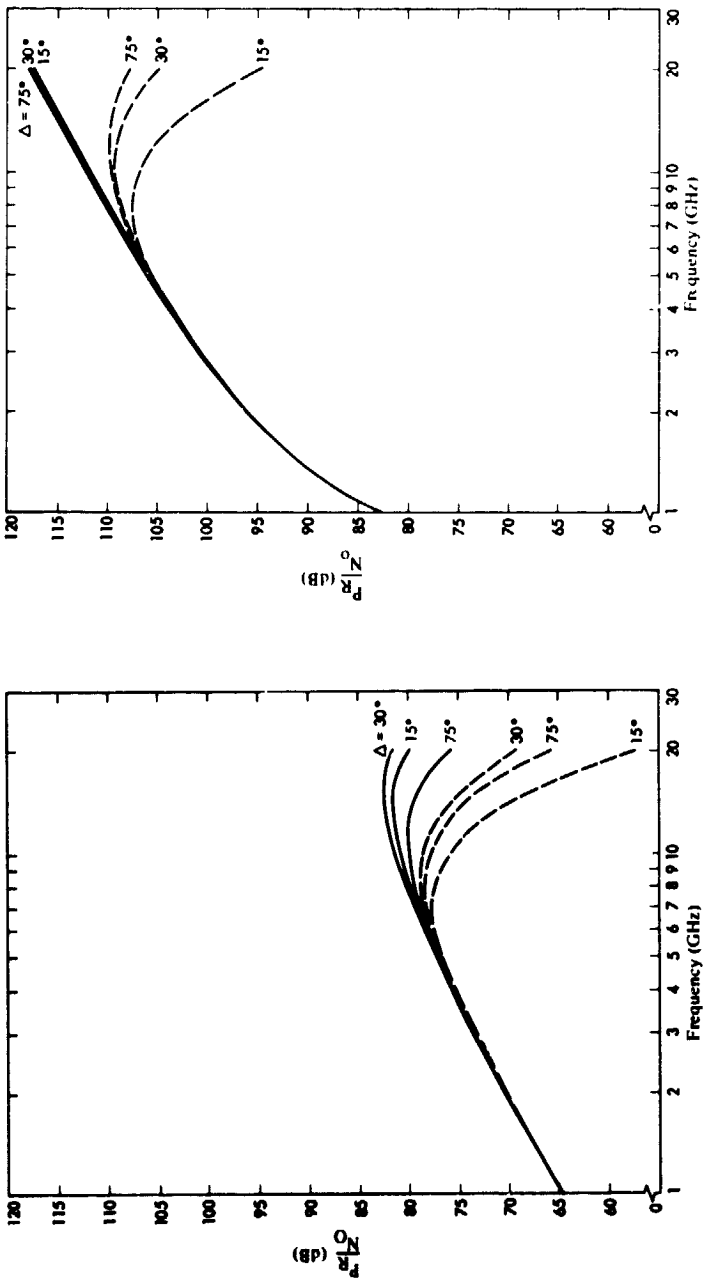

FIGURE 6

Earth-to-space link performance $\left(\frac{P_R}{N_o}\right)$
Two fixed diameter antennae

clear weather, atmosphere only
rain and atmosphere

Δ elevation angle of earth station antenna

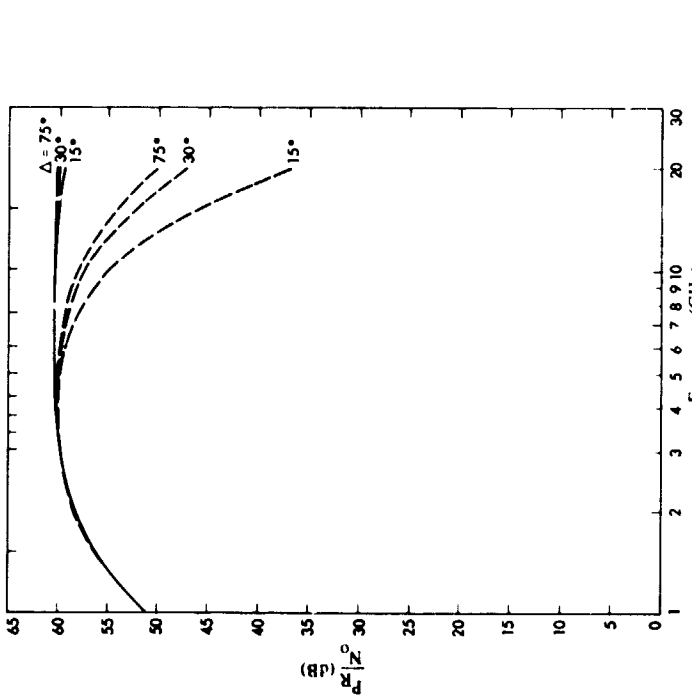

(b) Future limits from natural phenomena only

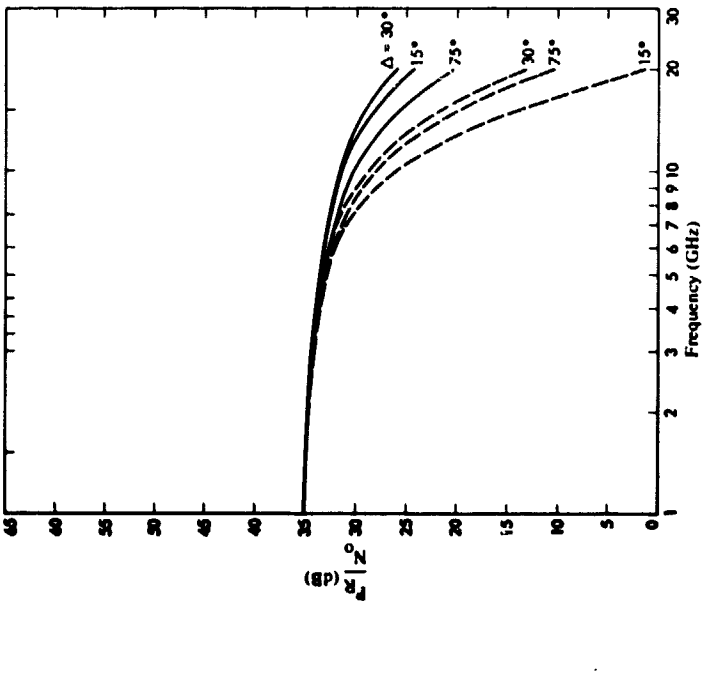

(a) 1977 implementation

FIGURE 1

Earth-to-space link performance $\left(\frac{P_R}{N_o}\right)$

Fixed diameter earth station antenna, fixed beamwidth space station antenna

clear weather, atmosphere only
rain and atmosphere

Δ elevation angle of earth station antenna

Radio Frequency Interference Between Spacecraft in Different Missions

N. F. deGroot
Telecommunication Systems Section

This article presents the results of a study to determine the possibility of separately receiving signals transmitted in a common frequency band from spacecraft in different missions. For the 18 mission pairs that were examined, co-channel operation without interference is generally possible. For some mission pairs, co-channel interference would occur during brief post-launch periods. Problems that may arise from simultaneous co-channel Earth-to-space transmissions from two stations at a single DSN complex were not considered.

I. Introduction

In a multimission environment, spacecraft in different missions may be simultaneously in view of a single deep space Earth station. The amount of radio frequency spectrum needed to allow separate reception of signals from these spacecraft is determined by the possibility of selecting each signal by means of the directivity of the Earth station antenna. When this can be done, the several spacecraft may transmit in a common frequency band. If the directivity of the Earth station is insufficient, the spacecraft must use different frequencies in order to avoid interference.

II. Method

Potential interference between signals from spacecraft in selected mission pairs was studied. The pairs were selected on the basis of a previous analysis whose purpose was to identify missions that would be simultaneously in view of DSN stations.

The interference calculation considered the relative signal strength from the nearer of the two spacecraft while the Earth station antenna was pointed at the more distant spacecraft. Equal radiated power from both spacecraft was assumed. The computation was:

$$I = (20 \log R_1 - 20 \log R_2) - (G_{max} - G_\theta)$$

where

I = interference level, dB

R_1 = range to most distant spacecraft, any length unit consistent with R_2

R_2 = range to nearer spacecraft, any length unit consistent with R_1

G_θ = antenna gain at θ degrees off the main beam axis

G_{max} = on-axis main beam gain

The value used for G_{max} was 67 dBi, assuming a 34-m antenna and 8400-MHz downlink frequency. The 8400-MHz frequency

was selected for analysis purposes since it is expected to be used by many future spacecraft. It is recognized that several of the missions included in the analysis do not employ spacecraft with the capability for communication in that band.

Trajectories were computed using geocentric conic elements. The resulting spacecraft ranges and angular separation as a function of time were determined. Earth station antenna directivity was modeled by the expressions.

$$G_\theta = G_{max} - (G_{max} - 32) \cdot \theta \text{ dB} \qquad 0 \leqslant \theta < 1 \text{ deg}$$

$$= 32 - 25 \log_{10} \theta \text{ dB} \qquad 1 \leqslant \theta < 48 \text{ deg}$$

$$= -10 \text{ dB} \qquad \theta \geqslant 48 \text{ deg}$$

In consideration of the interference calculation, it must be kept in mind that equal radiated power from the two spacecraft has been assumed. Where this is not true, a correction must be applied. Similarly, the allowable ratio of interference power to desired signal power must be established: the calculation reported here compares the relative strength of the desired and interfering signals and does not include an additional margin of protection.

III. Results

Table 1 lists the mission pairs that were studied. As an example, a plot of calculated interference for the JOP/Voyager mission pair is shown in Fig. 1. For this case, the interference is always below the level of the desired signal. The desired signal was taken to be the relatively weaker signal from the more distant spacecraft. During the first 50 days of the period following launch of Jupiter Orbiter/Probe 82, the interference rapidly drops from 10 dB below to 30 dB below the Voyager 2 signal. During a 10-day period in July 1982 the interference to signals from the more distance spacecraft rises to -27 dB, an insignificant amount.

Interference calculations for the other mission pairs yield the results shown in Table 2.

IV. Conclusions

For the mission pairs that have been examined with the method and assumptions of this study, significant radio frequency interference occurs only in some cases and only during the immediate post-launch period. For the greater part of time, either of the signals from co-channel spacecraft in the mission pair could be selected by the Earth station. This is not to say that there would not be other problems connected with simultaneous co-channel operation of two stations at a particular deep space complex. For example, simultaneous transmission of two different but co-channel Earth-to-space signals from two stations at a single complex might create interstation interference not considered in this study.

Co-channel operation of two or more spacecraft in a single mission is usually considered not possible. This is evident for the case of simultaneous orbiters around a target planet. During the analysis of selected missions pairs, a question was raised regarding the possibility of co-channel operation of the two Voyager spacecraft. Of particular interest in this case is the circumstance that the spacecraft trajectories are such that the Voyager that was launched last will overtake the other spacecraft and be the first to arrive at Jupiter. The perhaps surprising result of interference analysis for the two Voyagers is that either downlink signal could be individually selected and received, with the potentially interfering signal from the other spacecraft at least 30 dB weaker, throughout the mission. From the standpoint of downlink interference, co-channel operation of the two spacecraft would be possible.

The study reported in this article assumed the use of a 34-m Earth station antenna. The 64-m antenna would provide additional directivity and thus extend the possibility of selecting individual co-channel signals. The angular resolving power of the deep space Earth station antennas is truly impressive and is a consequence of their very narrow beam width.

Table 1. Mission pairs

Venus Orbiter Imaging Radar (VOIR)	and Pion . 11
Pioneer 11 (PIO 11)	Jupiter Orbiter/Probe 82
Pioneer Venus Orbiter (PVO)	Jupiter Orbiter/Probe 82
Pioneer Venus Orbiter	Out-of-Eclipti 83
Pioneer Venus Orbiter	Pioneer 10
Pioneer Venus Orbiter	Pioneer 11
Pioneer Venus Orbiter	Venus Orbiter Imaging Radar
Venus Orbiter Imaging Radar	Out-of-Ecliptic 83
Voyager 2 (JSX)	Pioneer Venus Orbiter
Pioneer 10 (PIO 10)	Pioneer 11
Voyager 2	Pioneer Venus Orbiter
Out-of-Ecliptic 83 (OOE)	Pioneer 11
Voyager 2	Venus Orbiter Imaging Radar
Jupiter Orbiter/Probe 82 (JOP 82)	Venus Orbiter Imaging Radar
Jupiter Orbiter/Probe 82	Out-of-Ecliptic 83
Voyager 2	Pioneer 10
Voyager 2	Out-of-Ecliptic 83
Voyager 2	Jupiter Orbiter/Probe 82

Table 2. Mission pairs with interference greater than -30dB

Pair	Time (month/ year)	Interference		Remarks
		Maximum (dB)	Duration Above -10 dB (days)	
JSX-JOP82	1/82-3, 32 7/82	-9	1	JOP82 launch
PIO 11-JOP82	1/82	-20		JOP82 launch
JSX-PIO 10	8/77	+3	5	JSX launch
JSX-VOIR	6/83	-19		
JSX-PVO	5/78 11/80 10/82	-7 -27 -22	4	PVO launch
JSX-OOE	1/82 8/82	+13 -24	10	OOE launch
JSX-PIO 11	8/77	-10	1	JSX launch
VOIR-PIO 11	6/83	-18		VOIR launch
VOIR-OOE	6/83	-27		VOIR launch
PVO-PIO 10	5/78-6/78 3/80 6/80 4/81	+6 -22 -28 -26	17	PVO launch
PVO-PIO 11	5/78	-1	9	PVO launch
OOE-PIO 11	2/82			OOE launch

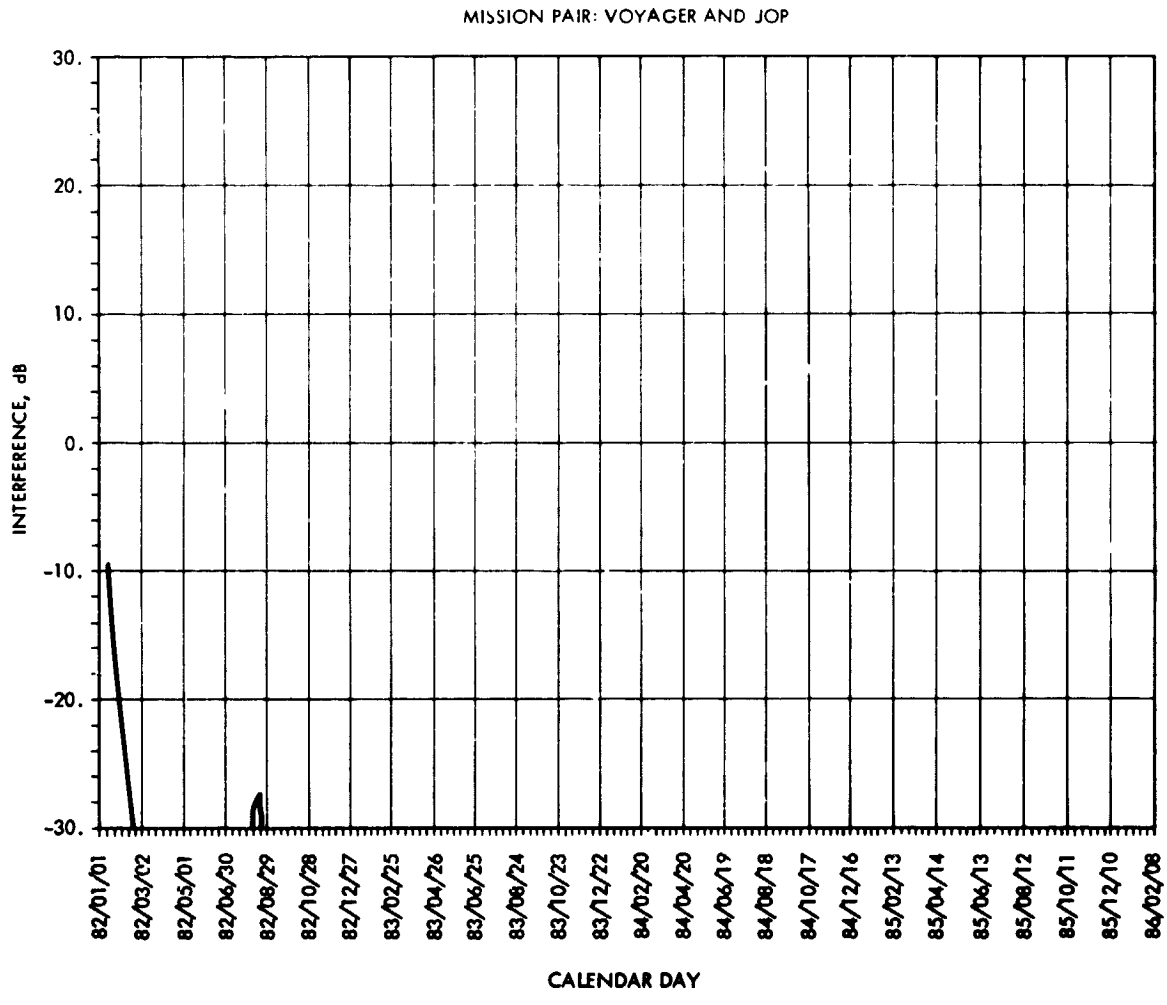

Fig. 1. Interference from nearest spacecraft while receiving signal from more distant spacecraft

Network Operations Control Center Block III Modifications

E. A. Garcia
DSN Data Systems Section

This article provides information regarding changes to the Block III Network Operations Control Center hardware and software implemented to support Voyager and Pioneer Venus Projects and the upgrading of the Deep Space Stations to the Mark III Data Subsystems Configuration.

I. Introduction

The Network Operations Control Center (NOCC) Block III configuration is in the process of being upgraded to provide the capabilities required to support Voyager and Pioneer Venus 1978 (PV78) Project commitments as well as to support Deep Space Station DSS changes arising from the Mark III DSN Data Subsystem (MDS) implementation. Figure 1 depicts the NOCC Configuration planned to become operational by June 1978. The dark-cornered blocks represent additions to the system configuration needed to support the following capabilities:

(1) Increased high speed data (HSD) rates from 4.8 kbits/sec to 7.2 kbits/sec for eight full duplex and eight simplex HSD lines. The eight full duplex HSD lines are for input-output communications with the Deep Space Stations, while the eight simplex HSD lines are for monitoring HSD data transmitted to the DSS by other operating centers, such as JPL's Mission Control and Computing Center (MCCC).

(2) Increased wideband data (WBD) rates from 27 and 50 kbits/sec to three full duplex lines at 56, 168 and 230 kbits/sec, respectively, scheduled to support Voyager and Viking extended missions.

(3) Modification of the HSD and WBD block formats and block sizes. Block formats required to be processed are the current 33-bit error polynomial type as well as the new 22 bit error polynomial type for three different data block sizes, 1200, 2400 and 4800 bits per block.

(4) Addition of an interface between the Network Log Processor (NLP) and the Ground Communications Facility (GCF) computerized High Speed Switch Assembly (HSW). The interface to the HSW will replace the direct high speed data input to the NLP as the GCF system converts to the new 22 bit error polynomial block format.

(5) Modification to the NOCC Real-Time Monitor (RTM) software packages to accommodate the above identified changes (Items 1 through 4) as well as changes required to handle the new MDS-equipped DSSs and their modes of operation (Command Store and Forward; Tracking Variable Data Format, DSS Monitor Status to MCCC).

(6) Modification to the NOCC Display Subsystem software to add (1) the new HSD and WBD block formats and sizes, (2) Operator Control Inputs (OCI) to

control the new data modes of operation for the Command (Store and Forward) and Tracking (Tracking Variable Data format) RTMs, (3) 13 new tracking variable data display formats, and (4) the third telemetry RTM display formats and OCIs.

(7) Modification to the Data Records Processor software to add the capability of recalling and merging HSD and WBD from MDS-implemented stations, as well as to add the capability to generate Intermediate Data Records (IDR) tapes from the NLP log tapes, the DSS Telemetry Processor Assembly (TPA), wideband Original Data Records tapes, and DSS Communications Formatter Assembly (CMFA), high speed data Original Data Record tapes. Included will be the capability to generate tracking data and radio science IDR's.

(8) Modification to the NOCC Network Support Controller (NSC) hardware and software to (1) add a second terminal to support Command Store and Forward operations, (2) accommodate HSD block format changes, (3) provide transmission of binary predicts to the DSS Metric Data Assembly (MDA), and Radio Science Predicts, and (4) accommodate changes to RTM interfaces with Subsystem Performance Records and Standard Limits files.

(9) Upgrade of NOCC test and training to allow remote control of the Simulation Conversion Assembly (SCA) and new Voyager and PV'78 telemetry simulation data types.

(10) Upgrade of the Video Assembly Processor software to provide three channels of digital television displays containing high-resolution graphical presentations of radio science tracking data parameters.

II. Hardware Configuration Changes

The following hardware changes to the NOCC Block III configuration have been made to support Voyager, PV'78, and MSD-configured Deep Space Stations:

(1) Addition of a third NLP processor to handle the added high speed wideband and GCF high speed switch processor interface data traffic.

(2) Addition of a third NCE processor to interface with the added third NLP.

(3) Addition of four magnetic tape transports to handle the added logging of high speed, wideband, high speed switch data.

(4) The addition of a second remote computer terminal between the Network Support Controller (Sigma 5) and Command Operations work station in the DSN Network Analysis Team (NAT) area.

(5) The addition of two NOCC Digital Television (DTV) channels with drives and synchronization modules to support the Voyager Project through an interface with the MCCC video distribution system.

(6) The addition of peripheral equipment, such as wideband communications buffer assemblies and 230-kbit modems required to support the above identified major installations.

(7) The addition of core memory (to 80k words) and disc storage (to 50 megabytes) to the Network Support Sigma 5 computers required to support expanded tracking predict generation, as well as providing capability to handle the increased volume of data required to support Voyager, PV'78 and DSS MDS subsystems.

(8) The addition of core memory to the Video Assembly Processor and three DTV channels required to support radio science high-resolution graphical displays.

III. Software Configuration Changes

Figures 2 through 9 depict in block diagram form each of the major NOCC subsystem software programs. As noted in the software block diagrams, the dark-cornered modules indicate where the software underwent modifications to comply with the added set of requirements identified in Section I herein.

The following paragraphs provide a short description of the program module modifications:

A. Network Log Processor (NLP)

A new Star Switch Controller (SSC) handler is being implemented to allow interfacing of the NLP to the GCF HSW. This handler is required to process the 22-bit polynomial-type high speed data blocks transmitted on 1264-bit block message format that includes an intracomputer control subheader and a message checksum word.

The routing and buffer pool control modules were modified to accommodate new 4800-bit block size (Voyager wideband) and packing of four 1200-bit or two 2400-bit blocks into a 4800-bit block transmission to and from the NCE. In addition, these two program modules were modified to allow packing eight 1200-bit, four 2400-bit or two 4800-bit magnetic tape log records for logging as well as directly transferring data to the DRP during ODR recalls from the TPA, CMF and Radio Science Occultation Data Assembly.

B. Network Data Processing Area Communications Equipment (NCE) Software (Fig. 3)

The NCE's routing buffer pool and control program modules were modified to allow transmission and reception of 4800-bit blocks from the NLP, as well as to allow operation using two active NCE's at the NOCC's NDPA area in Building 202.

C. Data Display Processor (DDP) Software, (Fig. 4)

The display software was updated to include the many display parameter mnemonic name-changes brought about by the MDS system implementation of the Deep Space Stations, as well as modifications to the buffer management program modules to allow processing of Voyager 4800-bit block raw data destined for the line printer in the DSN NAT area.

D. Real-Time Monitor Program Changes (Fig. 5)

Figure 5 depicts the typical NOCC Real-Time Monitor (RTM) software block diagram. All of the RTM processors have been modified to include the processing of data transmitted by the MDS-equipped DSSs, as well as the processing capability to support Voyager and Pioneer Venus 1978 (PV'78) as follows:

(1) Monitor RTM. Addition of new DSS monitor data block processing and transmission of selected DSS monitor data to the Voyager Project (820 – 13 module MON 5 – 8).

(2) Telemetry RTM. Addition of Voyager and PV'78 high speed and wideband telemetry processing, as well as the addition of a third telemetry stream (TLM-C). Telemetry C software is expected to operate in the NDPA's spare RTM whenever the scheduled telemetry stream loading is greater than the 18 streams currently handled by TLM-A and TLM-B.

(3) Tracking RTM. The tracking RTM software has been updated to include the processing of data transmitted by the DSS Metric Data Assembly (MDA) and the handling of the new variable tracking data high speed block format (820-13 module TRK 2-14), which provides for an additional 13 new display formats available to operations via the DTV displays in NOCC.

(4) Command RTM. The command RTM software has been modified to include the processing of data transmitted to and from DSS Command Processor Assembly (CPA) and the handling of Command Store and Forward capability in accordance with 820-13 module COM-4-4.

E. Network Support Subsystem (NSC) Software (Fig. 6)

The Sigma 5 operating system software was updated to include the added core and disc storage hardware expansions. In addition, smaller updates were made to the high speed I/O handlers due to the new block formats as well as the changes brought about by the DSS MDS upgrade, Voyager/PV'78 support requirements and new Tracking and Radio Science binary predict generation.

F. Data Records Processor (DRP) Software (Fig. 7)

The Data Records Processor software has been updated to include the capability to handle 4800-bit Voyager wideband data blocks, automatic ODR recall from the DSSs TPAs and CMFs, and the generation of Intermediate Data Records (IDR) tapes for Tracking and Radio Science support. The IDR tapes can be produced from previously generated IDRs, via merging DSS-logged TPA and CMF ODRs and merging NDL log tapes and fill tapes generated via an automatic recall of missing data blocks.

G. Test and Training (NTT) Subsystem (Fig. 8)

Test and training software was updated to include 4800-bit block size data handling, the addition of DSS Simulation Conversion Assembly (SCA) Control and Text Data, high speed data block processing, and Real-Time Monitor software test block generation which simulates a Deep Space Station interface to the RTMs.

H. Video Assembly Processor (VAP) Software (Fig. 9)

The Video Assembly processor software is being updated to include the capability to display up to 12 high-resolution graphical plot presentations of Radio Science data derived from the DSS tracking data stream. New OCIs for the control and selection of the graphical data are being added, as well as the handlers to interface the new DTV channels and tracking data from the tracking RTM.

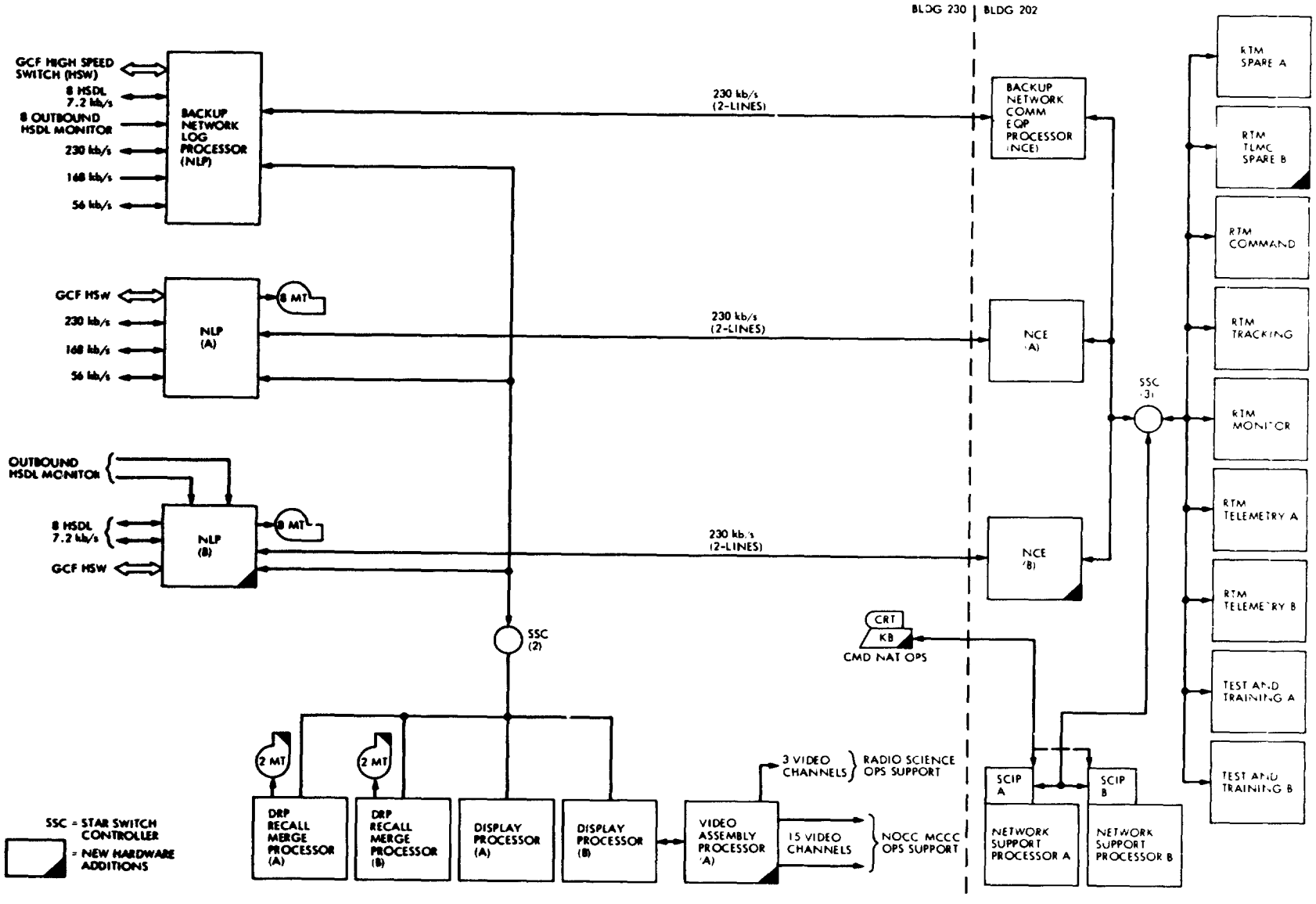

Fig. 1. Network Control System Block III Configuration (June 1978)

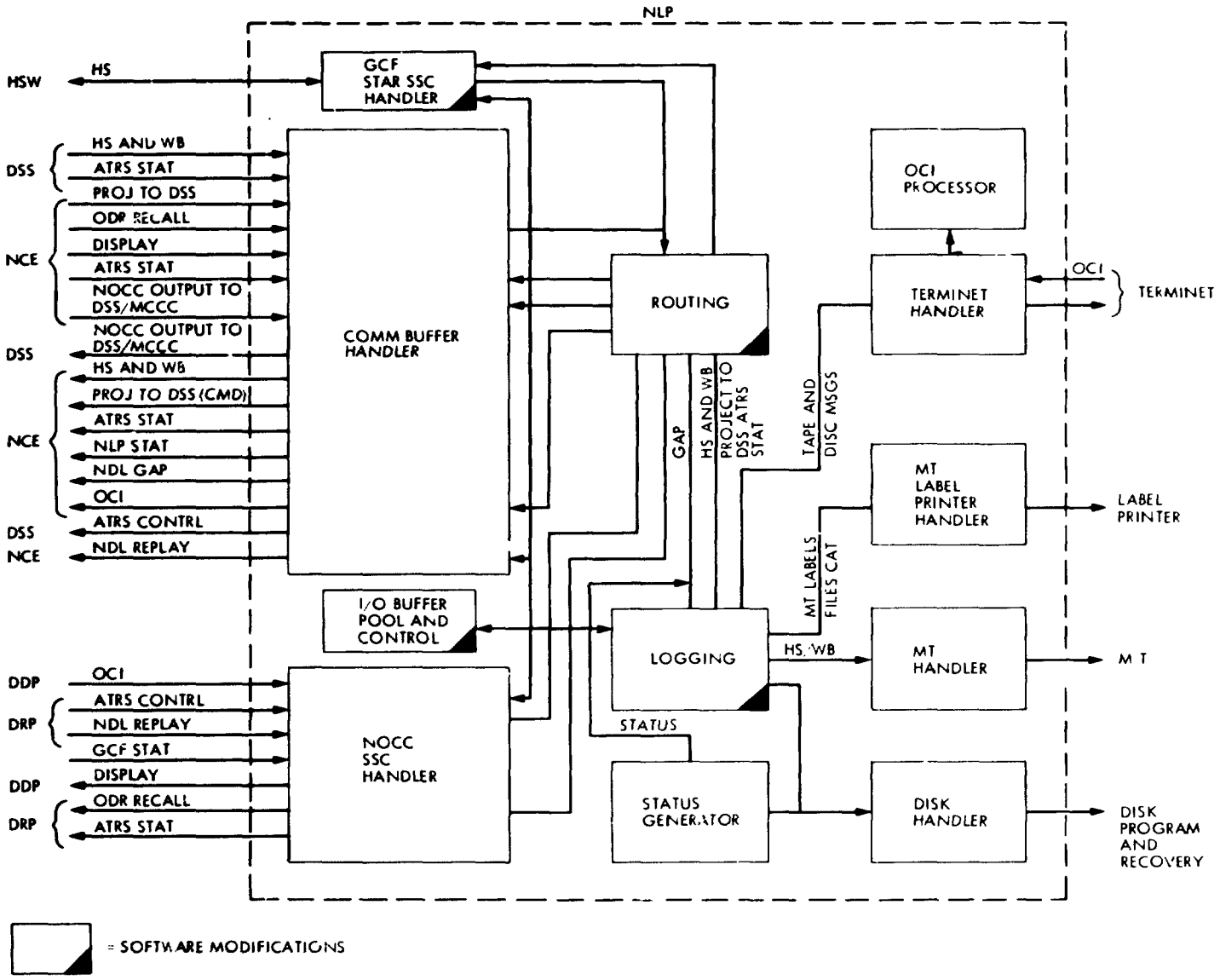

Fig. 2. Network Log Processor Software Module Diagram

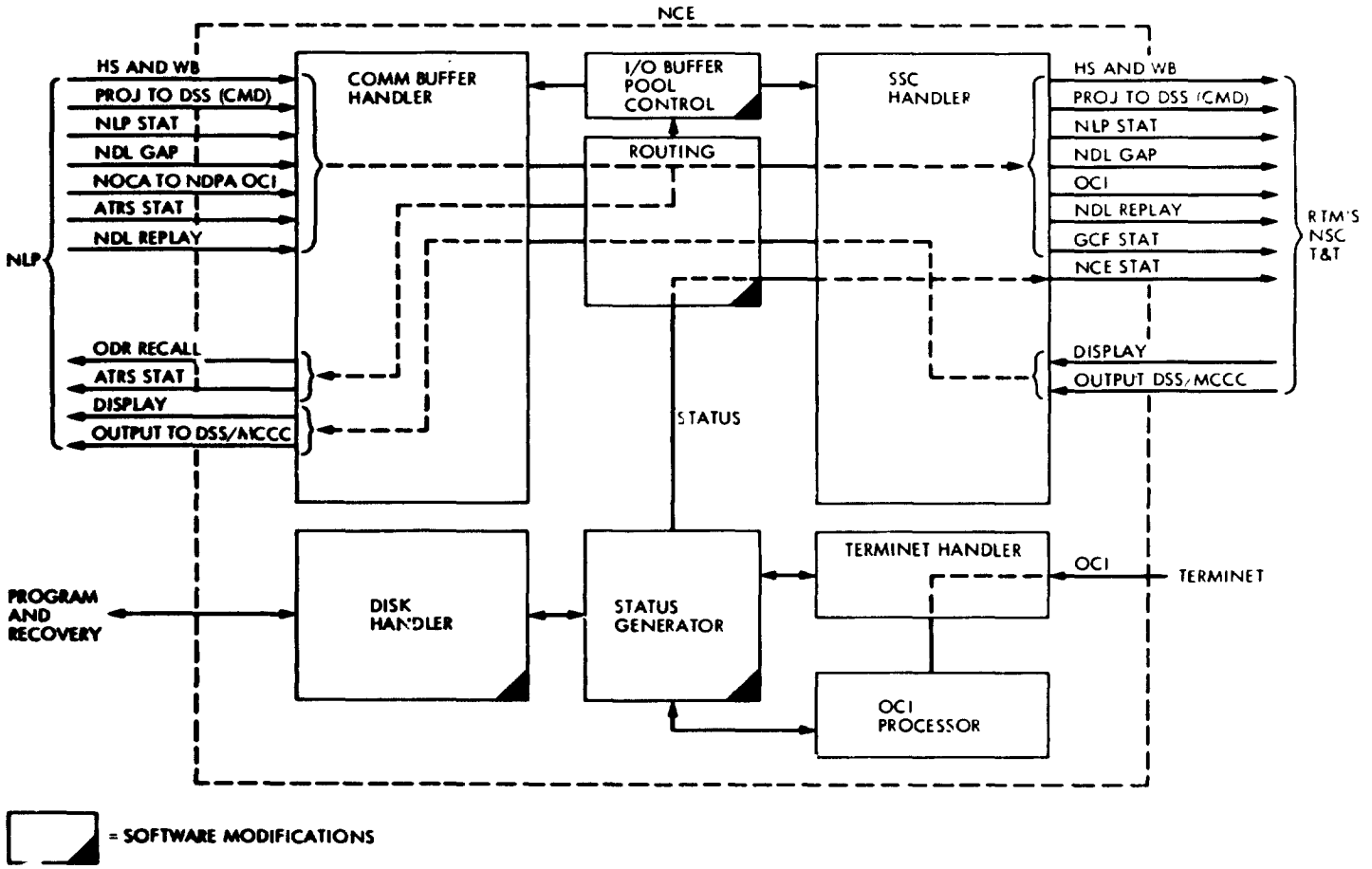

Fig. 3. Network Data Processing Area Communications Equipment Software Diagram

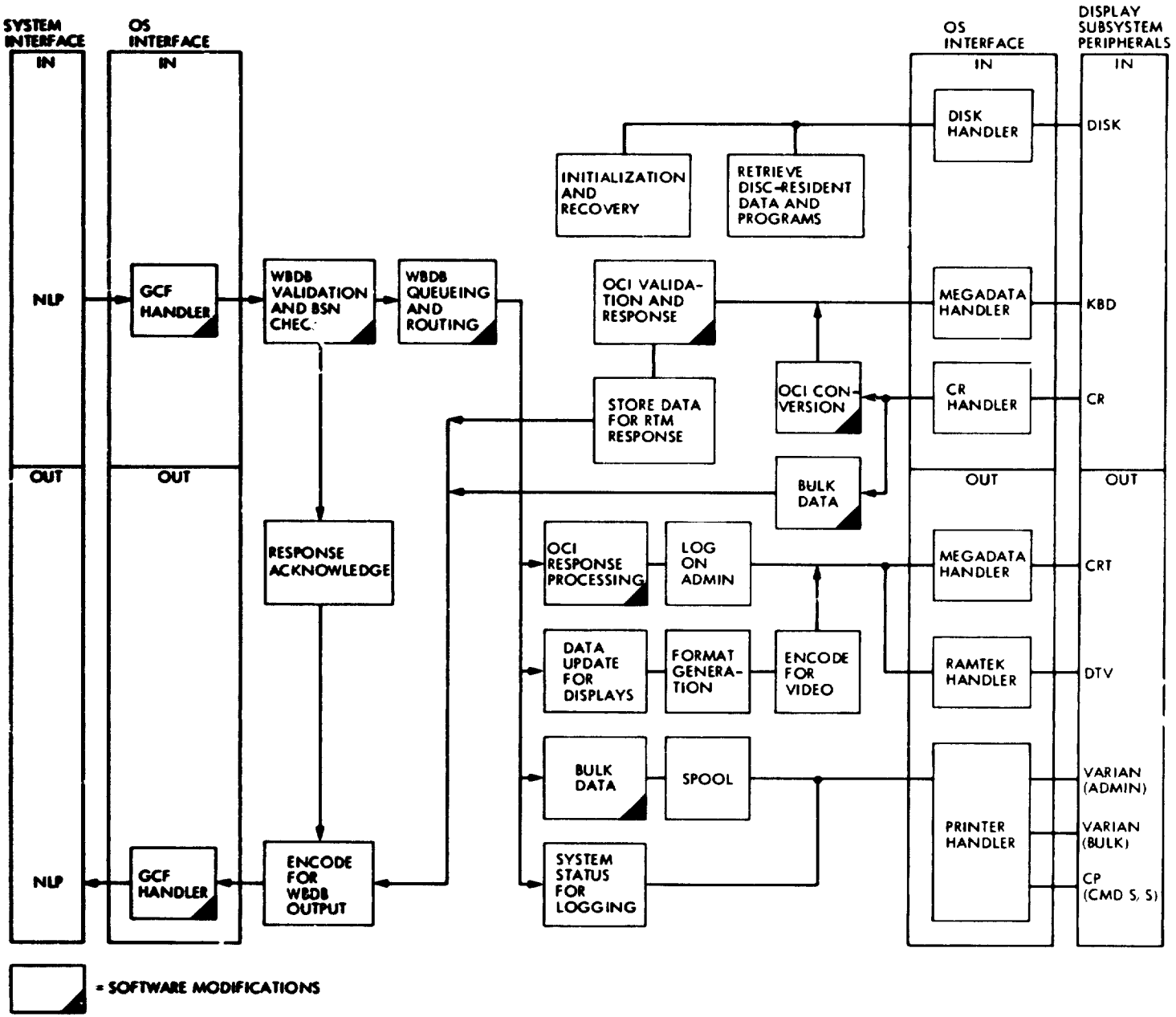

Fig. 4. Data Display Processor Software Module Diagram

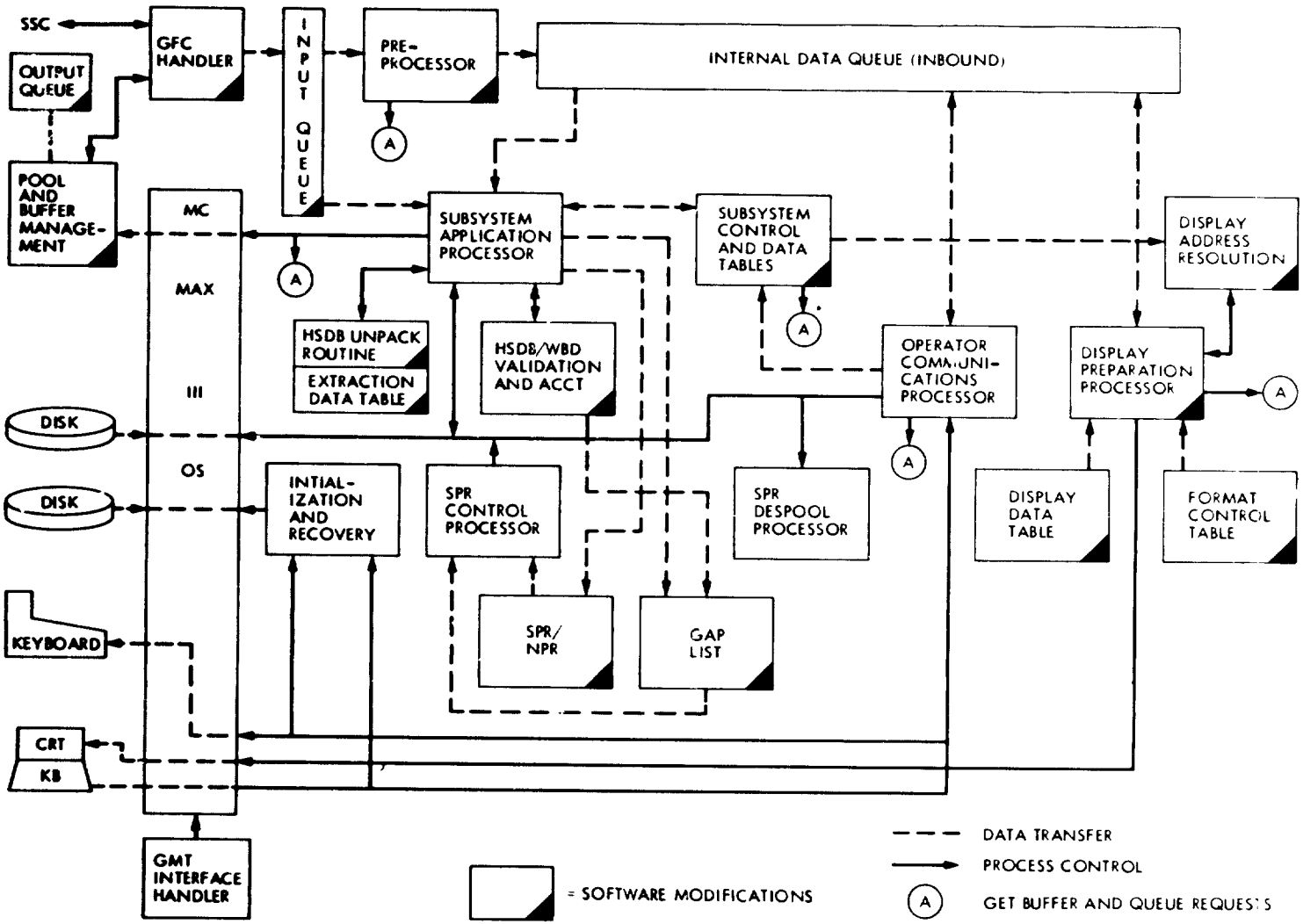

Fig. 5. Typical Real-Time Monitor Software Module Diagram

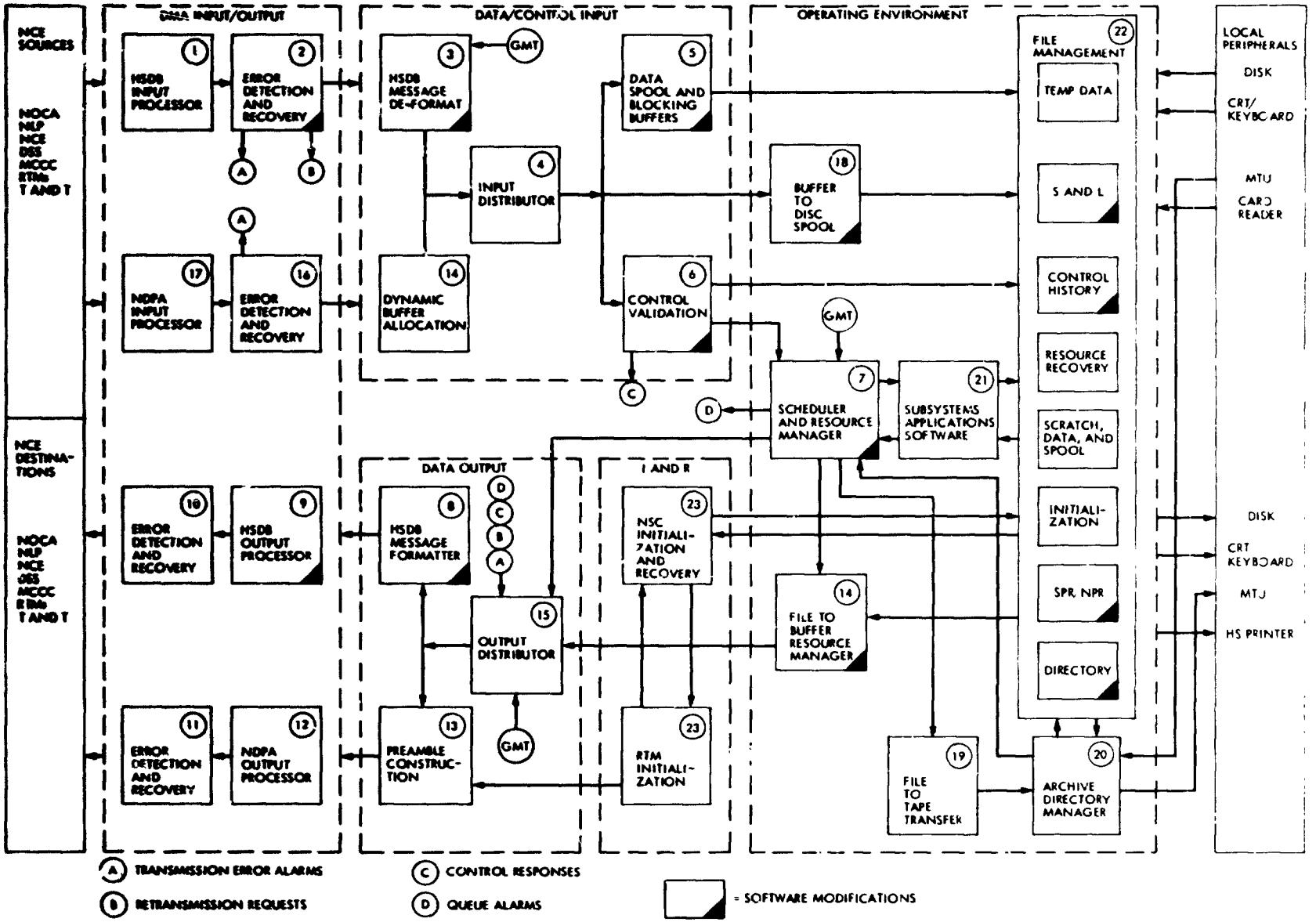

Fig. 6. Network Support Subsystem Software Module Diagram

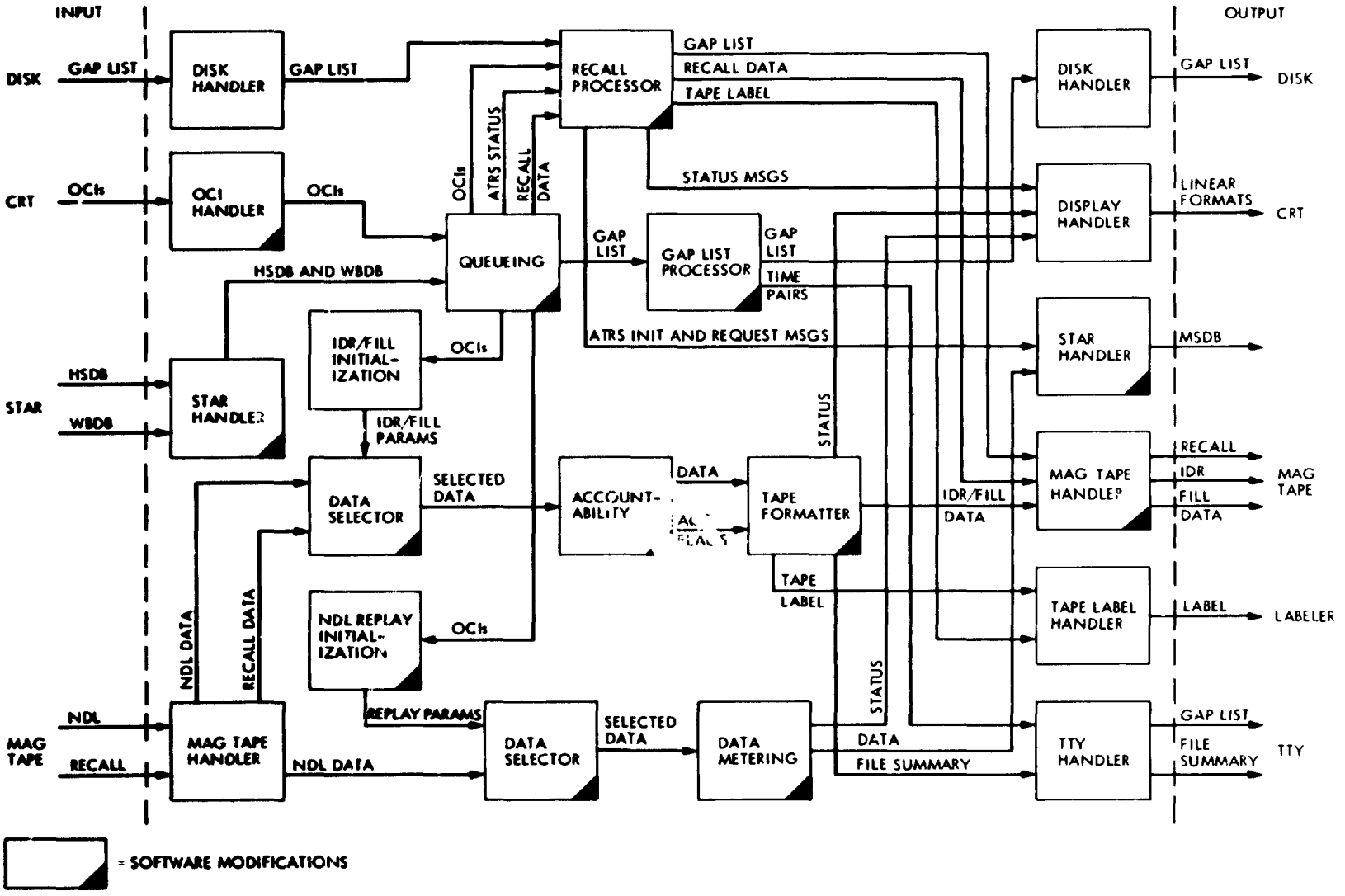

Fig. 7. Data Records Processor Software Module Diagram

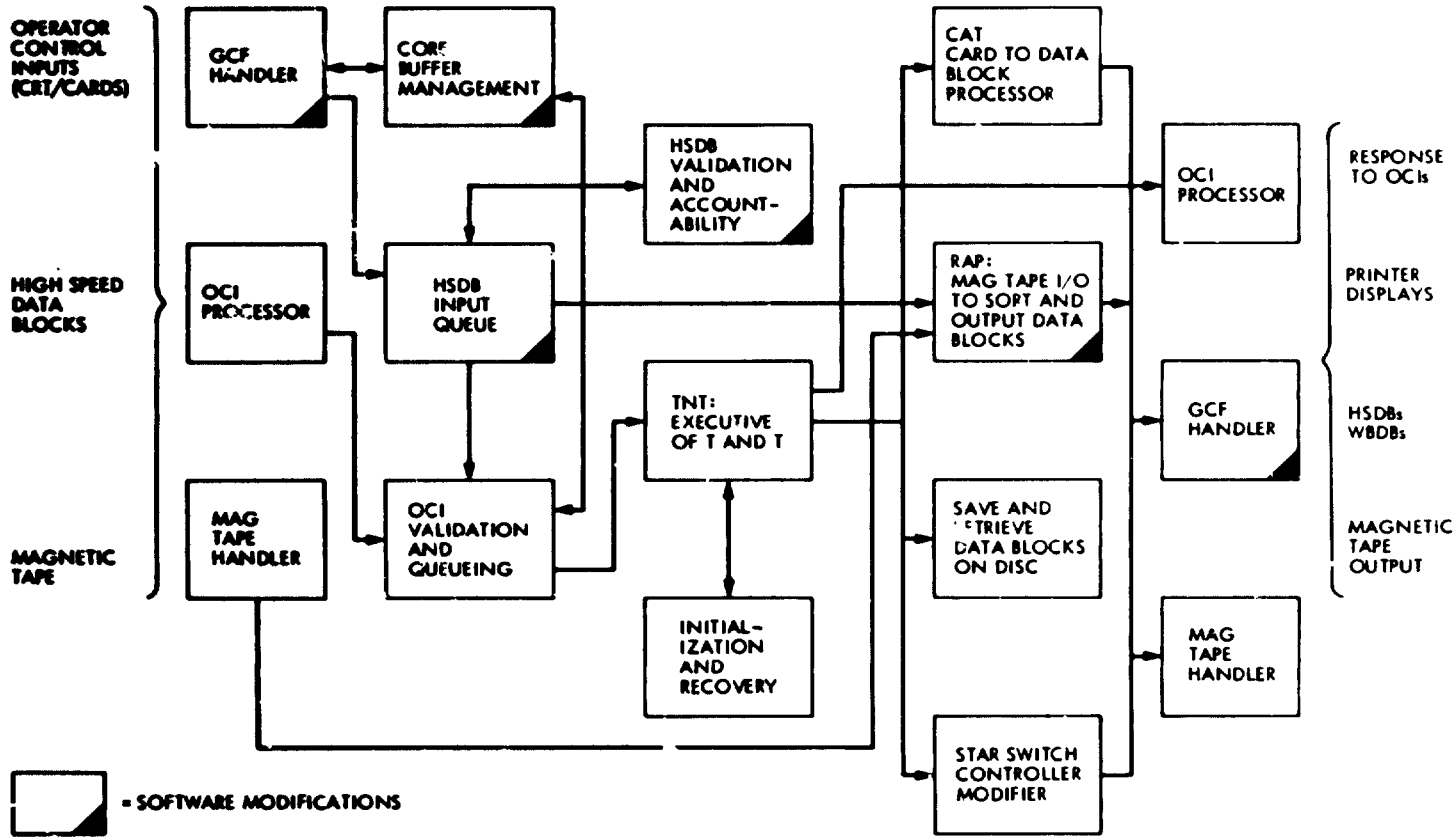

Fig. 8. Test and Training Subsystem Software Module Diagram

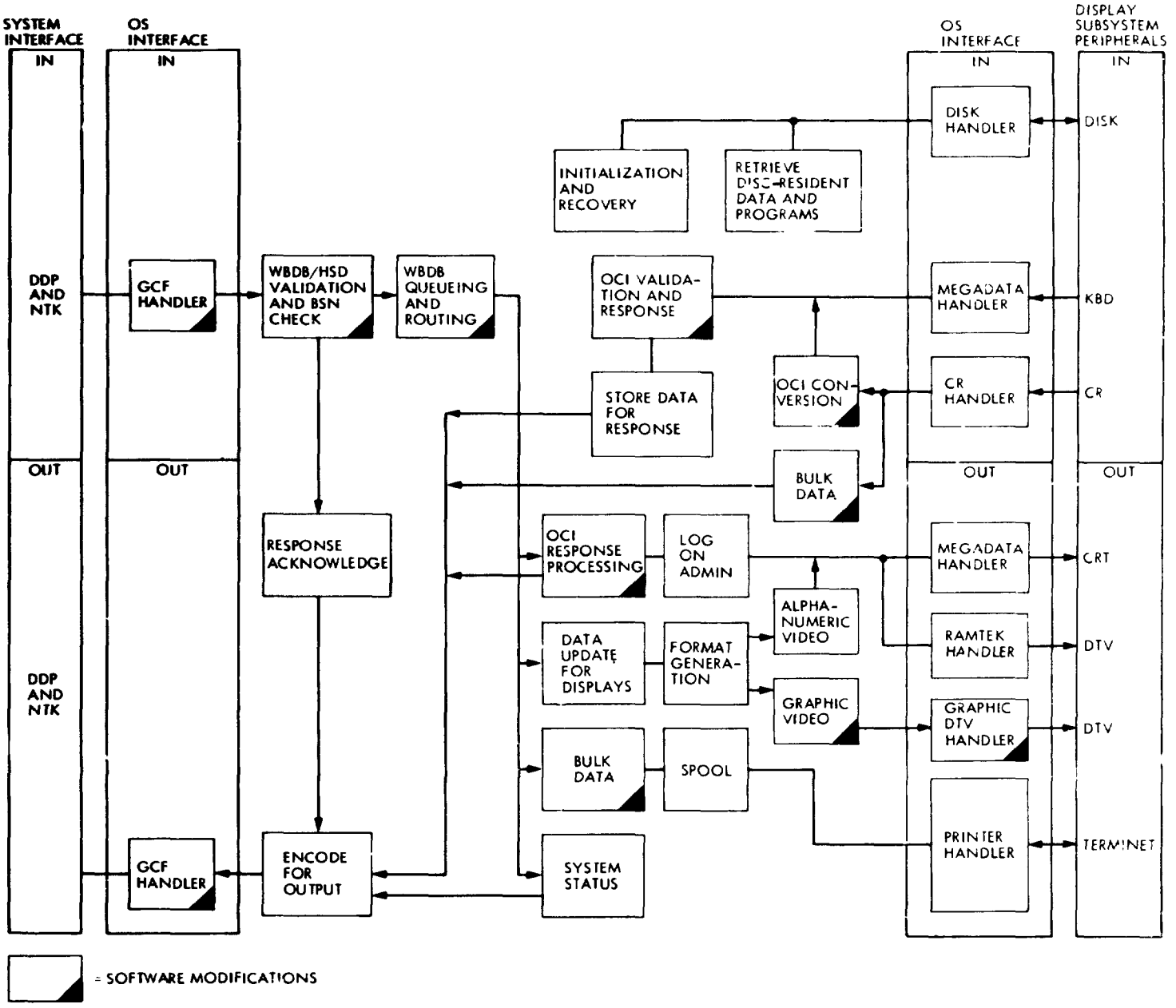

Fig. 9. Video Assembly Processor Software Module Diagram

Predetection Telemetry Analog Recording and Playback for Pioneer Venus 1978

S. S. Kent
Radio Frequency and Microwave Subsystems Section

Equipment and techniques have been developed to assure the DSN will meet the 1.5-dB degradation commitment to the mission for data recovery during the mission probes encounter.

I. Introduction

The Pioneer-Venus 1978 (PV-78) Mission has a requirement for predetection telemetry analog recordings of the received signals from each of the four probes during the active probe mission phase (Ref. 1). The DSN has committed to record and play back these data with no more than 1.5-dB signal-to-noise ratio (SNR) degradation due to the recording and playback processes. The recordings are to be made at DSS 14 and 43 and the playback is to be done at Compatibility Test Area (CTA) 21.

In order to insure meeting the DSN commitment, new equipment had to be incorporated into the stations and new techniques and procedures had to be developed. This article discusses the considerations involved for assurance that the commitment would be met.

II. Basic Concept

The basic concept of predetection recording and playback is shown in the simplified diagram of Fig. 1. The incoming S-band telemetry signal is heterodyned to a frequency low enough to permit recording on the analog recorder (for PV-78, less than 300 kHz). On playback, this signal is upconverted to an S-band frequency and injected into a standard DSN closed-loop receiver (CLR), and the data is then processed in the conventional manner.

Each probe has its own dedicated receiver and each receiver output has a dedicated track on the recorder. Playback can be accomplished on only one probe at a time due to upconverter limitations.

III. SNR Degradation Causes

There are three primary causes for SNR degradation in this basic concept:

(1) Phase nonlinearities.

(2) Additive noise.

(3) Analog recorder perturbations.

A secondary cause is signal suppression due to amplitude limiting (saturation) occurring in any of the amplifiers. This cause is eliminated simply by controlling the total gain and the gain distribution.

IV. Phase Nonlinearities

The degradation of SNR due to a reduction in signal power caused by phase nonlinearities can be determined from the following equations (Eqs. 9 and 11 of Ref. 2):

$$S = \frac{1}{4} \sum_{n=1}^{N} \left(a_n^2 \cos \theta_n^u + a_n^2 \cos \theta_n^L \right) \quad (1)$$

$$p = 10 \log_{10} S \quad (2)$$

where

S = signal power relative to unity

$a_n = \frac{4}{\pi n}$

n = subcarrier harmonic number (for square wave modulation, n = odd numbers)

θ^u, θ^L = deviation of upper and lower sidebands from a linear phase relationship

p = reduction of signal power in dB

If $\theta^u = \theta^L = \theta$ for all n, Eq. (1) becomes

$$S = \frac{8 \cos \theta}{\pi^2} \sum_{n=1}^{N} \frac{1}{n^2}$$

from which

$$P = 10 \log_{10} \left(\frac{8}{\pi^2} \sum_{n=1}^{N} \frac{1}{n^2} \right) + 10 \log_{10} (\cos \theta) \quad (3)$$

Thus the additional signal power reduction due to fixed deviation from a linear phase relationship is

$$P_a = 10 \log_{10} (\cos \theta), \text{ dB} \quad (4)$$

which of course translates directly into SNR degradation. To minimize this degradation, the open-loop receiver phase response is linear to within 2 deg over the 300-kHz passband of the receiver, for a negligible SNR degradation of 0.003 dB.

At a tape recorder speed of 76.20 cm/sec (30 in./sec), the recorder 3-dB amplitude response is from 400 Hz to 500 kHz and its linear phase response is from approximately 1.0 to 300 kHz. The group delay variation of the analog recorder is specified at 1.0 μsec peak over a 40-kHz passband, which is equivalent to a deviation from a linear phase response of 2 deg in 5 kHz (assuming a constant slope to the group delay variation). This also results in a SNR degradation of 0.003 dB. Since the total required bandwidth for any of the probes never exceeds 240 kHz (Ref. 1), bandwidth limitations and phase nonlinearities problems are negligible.

V. Additive Noise

Additive noise (for purposes of this discussion) is simply noise that is added as a result of the signal processing employed specifically for recording and playback purposes. The open-loop receiver (to be described in a later DSN Progress Report) consists of front-end and first intermediate frequency (IF) amplifier designs similar to those of the existing closed-loop receivers, thus resulting in no difference in signal processing to this point. The second IF covers the frequency range of 15 to 300 kHz and presents the first additive noise problem due to "image noise rejection" difficulties. This problem is solved through the use of a single-sideband mixer in which the image noise is rejected by a factor of 1000 (30 dB). Thus, the additive noise power due to image noise is 0.1% relative to the desired passband noise for an SNR degradation of 0.004 dB.

The second additive noise source is the analog tape recorder. The H-96 recorder performance specification is such that for a 300-kHz bandwidth, the output SNR is ≥22 dB for an input signal level of +10 dBm (50 ohms). This additive noise (≤0.62%) results in an SNR degradation of ≤0.027 dB.

The upconverter is the third additive noise source. It is specified to operate at a signal input level of +10 dBm (50 ohms). With an effective noise temperature of 30,000 kelvins, the additive noise power is -99 dBm, resulting in negligible degradation.

The final additive noise source is the closed-loop receiver. For PV-78 the tape playbacks will be done at CTA 21 where the system operating temperature is approximately 1000 kelvins. In a bandwidth of 300 kHz at 1000 kelvins, the input noise level of the closed-loop receiver is -114 dBm. To limit the SNR degradation to ≤0.04 dB (1%), the upconverted noise level should be ≥94 dBm.

The total noise then at the CLR input becomes

$$P_{NT} = (1.001)(1.006)(1.01) N_1 = 1.017 P_{N1}$$

where P_{N1} = OLR effective noise input power level from which the additive noise is 0.017 N_1 for a degradation of 0.07 dB.

VI. Analog Recorder Perturbation

Velocity perturbations of the analog recorder can result in SNR degradations. These perturbations are generally referred to as *flutter, jitter,* and *time base error* and are defined as follows:

Flutter: The instantaneous "short term" speed deviation from the "long term" average speed of the recorder. It is usually expressed in peak-to-peak percentage of velocity deviation.

Jitter: The maximum peak-to-peak spacing change in time of a series of pulses of a given nominal spacing. Varying frequencies of flutter result in varying amounts of jitter.

Time Base Error (TBE): The error in the spacing in time of any two points on the tape as compared with the actual spacing that existed during the recording. Time-base-error is related to flutter and can be expressed mathematically as

$$TBE = \int_0^t A \cos \omega t \, dt$$

$$= \frac{1}{2\pi} \frac{A}{f} \sin \omega t$$

where A = peak flutter and f = flutter frequency in cycles per second. The impact of the perturbations on SNR can only be measured indirectly by comparing real-time SNR with that SNR achieved during tape playback.

With the advent of the newer generation analog recorders (i.e., Honeywell H-96, Ampex FR-2000, Ampex FR-3010) employing low inertia capstans and speed-lock servo loops, analog recorder perturbations cause about 0.5 dB SNR degradation (for PV-78 data rates) when operated at tape speeds of 38.10 cm/sec (15 in./sec) or faster. For PV-78, the Honeywell H-96 recorders are being installed at DSS 14 and 43 for recording and CTA 21 for playback. Tape speed will be 76.20 cm/sec (30 in./sec).

A field demonstration (Ref. 3) conducted on Pioneer 11 in June of 1975 demonstrated that degradation due to analog recorder perturbations should be well below 1.0 dB for the PV-78 mission. In fact, if 0.1 dB degradation is assumed for additive noise (which is reasonable, based on above), the field demonstration indicates that recorder perturbations contributions are about 0.5 dB. Recent PV-78 compatibility testing (Nov. 1977) conducted at CTA 21 showed total SNR degradation to average about 0.5 dB, indicating recorder perturbations contribution to be about 0.4 dB. Other testing conducted at CTA 21 in the past confirms the above findings (these tests will be the subject of a later DSN Progress Report).

VII. Gain Requirements

Using the relationships

$$P_S = P_C + P_D \ll P_{N1}$$

where

P_S = total received signal power

P_C = carrier power

P_D = data power

P_{N1} = OLR input noise level, (KT_1B_1)

K = Boltzmann's constant, -198.6 dBm

T_1 = OLR system temperature

B_1 = OLR noise bandwidth

the gain requirements can be determined once an acceptable level of degradation due to additive noise is established. Selecting the additive noise degradation at ≤0.07 dB, the following equations can be written:

$$P_{NT} = GP_{N1} + P_{NA} \leq 1.017\, GP_{N1} \qquad (5)$$

$$\frac{P_{NA}}{GP_{N1}} \leq 0.017$$

where

G = total gain from OLR in to CLR in

P_{NA} = total additive noise power

From Figure 1

$$G = G_1 G_2 G_3$$

$$P_{NA} = G_2 G_3 P_{N2} + G_3 P_{N3} + P_{N4}$$

from which

$$\frac{P_{NA}}{GP_{N1}} \leqslant \frac{P_{N2}}{G_1 P_{N1}} + \frac{P_{N3}}{G_1 G_2 P_{N1}} + \frac{P_{N4}}{G_1 G_2 G_3 PN_1}$$

From the additive noise discussion

$$P_{N3} \ll G_1 G_2 P_{N1}$$

$$G_2 = 1.0$$

$$\frac{P_{N2}}{G_1 P_{N1}} = 0.0062$$

Now,

$$P_{N1} = KT_1 B_1$$

$$P_{N4} = KT_4 B_4$$

where

$$B_1 = B_4 \text{ (our case)}$$

$$0.017 \geqslant .0062 + \frac{T_4}{GT_1}$$

$$\frac{GT_1}{T_4} \geqslant 92.6$$

or

$$G \geqslant 19.7 + 10 \log T_4 - 10 \log T_1, \text{ dB} \qquad (6)$$

The minimum required gain is when Eq (6) is equal The maximum gain allowable is a function of amplitude limiting and is determined as follows:

$$P_{N\,MAX} = G_{MAX} P_{N1} + P_{NA}$$

$$G_{MAX} = \frac{P_{N\,MAX} - P_{NA}}{P_{N1}} \approx \frac{P_{N\,MAX}}{P_{N1}} = \frac{P_{N\,MAX}}{KT_1 B_1}$$

Thus

$$G_{MAX} = P_{N\,MAX}(\text{dBm}) + 198.6 - 10 \log T_1 - 10 \log B_1, \text{ dB} \qquad (7)$$

and

$$G_{MIN} = 19.7 + 10 \log T_4 - 10 \log T_1 \text{ db} \qquad (8)$$

For recording at a 64-meter station and playing back at CTA 21:

$$P_{N\,MAX} = -80 \text{ dBm}$$

$$T_1 = 25 \text{ kelvins}$$

$$B_1 = 300 \text{ kHz}$$

$$T_4 = 1000 \text{ kelvins}$$

from which

$$G_{MAX} = 50 \text{ dB}$$

$$G_{MIN} = 36 \text{ dB}$$

Table 1 tabulates the gain limits for various recording and playback station combinations. Examination of the table shows that playback at the 64-m stations at a system temperature of 300 kelvins is not feasible due to noise limiting under minimum gain requirements.

VIII. Gain Settings

The method of establishing the correct playback gain setting is to "lock" the CLR to the S-band carrier signal and

adjust the input level until the automatic gain control voltage indicates the correct gain has been achieved. This method is based on knowing what the original incoming signal carrier level was during the recording period. This information is available from the mission predicts or from the CLR that was tracking in real-time.

IX. Summary

Predetection telemetry recording and playback capability is being implemented in the DSN to meet PV-78 mission requirements. Test data, along with theoretical considerations, gives assurance that the data degradation commitment of 1.5 dB will be met, and it is anticipated that in actual performance the design goal of 1.0 dB will be met.

Operation of the equipments is straightforward and can be summarized as follows:

Recording

1. Adjust OLR output level to +10 dBm
2. Adjust OLR frequency to predicts
3. Record OLR output at 76.2 cm/sec

Playback

1. Set UC output level to maximum
2. Lock the CLR to the carrier signal
3. Adjust the UC output level to within the gain limits of Table 1.
4. Lock the SDA, SSA and TPA per conventional procedures and process data.

The major technical problems requiring solving were the elimination of "image noise" in the OLR and the reduction of analog recorder instabilities. These were solved through the use of single-sideband mixing techniques and the use of newer generation analog recorders.

Acknowledgment

The author credits M. Brockman for the basic concept of the recording and playback design; J. Molinder for his invaluable assistance in understanding the theory and its applications; and C. Johns for providing the breadboard equipments that made it possible to do the initial testing of the concept.

References

1. Miller, R. B., "Pioneer Venus 1978 Mission Support," in *The Deep Space Network Progress Report 42-27*, pp. 28-35, Jet Propulsion Laboratory, Pasadena, Calif., June 15, 1975.
2. Molinder, J. I., "Effect of Phase Distortion on Effective Signal Power – a Simple Mathematical Model," in *The Deep Space Network Progress Report 42-29*, pp. 136-140, Jet Propulsion Laboratory, Pasadena, Calif., Oct. 15, 1975.
3. Kent, S. S., "Open-Loop Receiver Recording for Telemetry Data Recovery: a Field Demonstration," in *The Deep Space Network Progress Report 42-30*, pp. 208-213, Jet Propulsion Laboratory, Pasadena, Calif., Dec. 15, 1975.

Table 1. Gain limits

Record station	Playback station	T_1, K	T_4, K	G_{MIN}, dB	G_{MAX}[a], dB
64-m	64-m	25	25	20	25
64-m	64-m	25	300[b]	31	25
64-m	64-m	300	25	9	14
64-m	64-m	300	300[b]	20	14
CTA 21	CTA 21	1000	1000	20	34
64-m	CTA 21	25	1000	36	50

[a]At 64-m stations $P_{T\,MAX} = -105$ dBm.
[b]Unacceptable combination.

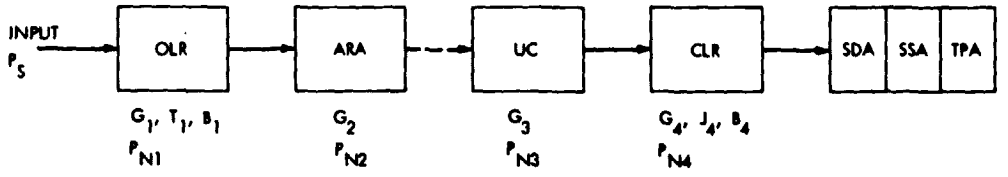

OLR = OPEN LOOP RECEIVER
ARA = ANALOG RECORDING ASSEMBLY
UC = UPCONVERTER
CLR = CLOSED LOOP RECEIVER
SDA = SYMBOL DEMODULATOR ASSEMBLY
SSA = SYMBOL SYNCHRONIZER ASSEMBLY
TPA = TELEMETRY PROCESSOR ASSEMBLY

Fig. 1. Simplified diagram of telemetry recording and playback

NASTRAN Analysis of a Wheel-Rail Loading on its Foundation

M. S. Katow
DSN Engineering Section

One type of azimuth bearing for a large ground antenna (100 m) will consist of steel wheels, mounted at four corners of the alidade, rolling on a circular flat rail which provides the vertical restraints; a radial constraining bearing at the center of the alidade provides the horizontal restraints. One important design feature is the compressive stresses in the grout or concrete foundation under the wheel-rail load.

This report describes a finite element analysis check of a particular design by H. McGinness that consists of a steel rail resting on a concrete foundation. Symmetry is assumed as much as possible in order to minimize the models, but meaningful element sizes are used. Recently developed isoparametric hexahedron elements available in the NASTRAN computing program, which minimizes the number of elements required while maintaining the accuracy of the computed stresses, are used with two versions of NASTRAN. Test cases to check with the analytical solutions are made. A side loading is also applied to calculate the increase in the concrete stresses.

I. Introduction

One design of an azimuth bearing of a ground antenna restrains the vertical component (mostly the weight) by mounting wheels at the four corners of the alidade, which rolls on a flat surfaced circular rail. The rail, in turn, is supported by a concrete foundation. Figure 1 shows a cross-sectional view of this particular rail-foundation design. The wheel rolls around an approximate 35-m-radius circle on a hardened wear strip fastened to a mild steel rail. This rail is supported by the concrete foundation with a grout material between the two. A one-piece circular rail with welded joints will be required.

II. Model Description

The wear strip and the grout were deleted from the model because of their minimal effects on the design questions at hand.

The first model generated was a two-dimensional type in order to simplify and reduce the model size as much as possible. First, we assumed an infinite number of wheel loads with a 1.02-m separation instead of the actual case of four wheels approximately 1.02 m apart. This enables the use of a model 1/2 of 1.02 m length by using symmetric boundary conditions. If the wheel width is assumed to be infinitely wide along with the concrete foundation, the model is reduced to one element width (0.02 m) of the cubic hexahedron elements.

Thus the computer model shown in Fig. 2 has uniform stresses across the width of the rail/foundation. The smallest element size of 0.02 m cube occurs for the concrete just under the wheel loads on the steel rail where the stress is the highest. The long aspect ratio elements are farthest from the concentrated loading.

The steel rail in Fig. 2 is modeled by the linear isoparametric hexahedron cubes with six layers in depth. Connections are made between the bottom modes of the rail and the top modes of the concrete foundation with MPC (multipoint constraint) sets, which transfer only vertical or Z forces. This simulates the two surfaces in sliding connection, transferring vertical forces only.

In Fig. 3, the steel rail is modeled by NASTRAN's CBAR beam elements, which requires inputs of the cross-sectional area, moment of inertia, Young's and shear moduli, and the shear area factors. Two rows of CBARS are required to replace the one layer of hexahedron modeled beam.

In order to first test the accuracy of the steel rail models, they were modeled separately and NASTRAN-analyzed. Figure 4 shows the modeling techniques. In effect, the continuous concrete reaction points were replaced by one reaction at the center, thus reducing the model to a center-loaded beam with fixed ends. In other words, the model is equivalent to four cantilever beams of length 0.255 m, each connected at the inflection points M.

The cantilever beam with a built-in cross section (Fig. 4-III) that is completely prevented from warping has an analytical solution (Ref. 3). The $-Z/2$ deflection δ equals

$$\delta = \frac{Pl^3}{3EI}\left(1 + 0.74\frac{h^2}{l^2} - 0.01\frac{h}{l}\right)$$

The terms in the parenthesis cover the shear deflection for a rectangular cross section beam where

l = length (0.255 m)

P = load

h = depth of cross section

E = Young's modulus

I = moment of inertia

$$E' = E\left(\frac{1}{1-\mu^2}\right)$$

μ = Poisson's ratio = 0.3 for steel

The initial models (sequence number 3 to 5 in Table 2) used the meshes shown in Figs. 2 and 7 where the finer divisions are in the left end. Because this mesh can be improved for concentrated loadings at both ends, Fig. 5 shows the symmetric divisions used for models of sequence numbers 7 and 8 of Table 1.

The loading applied to the beam-rail and the two-dimensional models was computed by assuming that the wheel width was equal to the rail width of 0.61 m. Then the loading at the corners of the 0.02-m-wide models equals

$$2{,}624{,}550\ N(590{,}000\ \text{lb}) \times \frac{0.02}{0.61} \times \frac{1}{4} = 21{,}526\ N$$

Figure 6 shows how the loading for the three-dimensional model (Fig. 7) was derived.

Finally, a three-dimensional model was generated as shown in Fig. 5. The 0.04-m smallest cube was used for this model since computing costs were a factor for models of this large size. A sup time of one hour was required on the 1108 computer.

III. Analysis Discussion

The isoparametric solid hexahedron element appeared in level 16 of NASA NASTRAN (Ref. 1). MSC NASTRAN (Ref. 2) had an earlier version of this element which was recently modified to improve the deflection computation due to shear stresses. The stresses and deflections can vary through each element so its use allows a more accurately defined structure with fewer elements. These elements take into account pressure loads, which are of primary interest in the problem under discussion.

With no previous experiences in the use of these elements, a decision was made to utilize both versions of NASTRAN, since it appeared that the finally developed elements were independently generated. This analysis method should provide some checks on the veracity of our inputs and computed outputs.

To minimize the input data errors, a 1108 program was written to generate the complete input data for the three-dimensional problem shown in Fig. 7. It was only necessary to define the number of elements in the three directions and the progressive element lengths. The two-dimensional models were generated by editing out extraneous data and adding constraints where necessary. By progressively increasing the GRID numbers for the foundation portion through each cross-section to the next cross-section and adding a large number to the connecting GRID nodes to the top steel beam and repeating the numbering operation for the beam itself, the NASTRAN runs were made with minimum spillage and acceptable run times.

The cantilever beam deflection equation (Eq. 1) was derived (Ref. 3) for application to the usual finite cross-sectional beams. By replacing E with the flexural rigidity quantity E' or $E(1/1-\mu^2)$, the equation is applicable to the segment of an infinitely wide beam, as used in Table 1 (Ref. 4).

The important compressive stress to be resolved is in the concrete foundation directly under the wheel loading point. The concentrated loadings on the rail must be dispersed as the effect of the loading progresses through the thickness of the rail to the bottom contact to the concrete. The thickness as well as the width should be important to the degree that the vertical loads are dispersed, while the width will be a factor for the side loading from the wheel.

The accuracy of this computed compressive stress will be highly dependent on accurate modeling of the steel beam-rail. For this determination, the beam alone was modeled as shown in Fig. 4. Since the hexahedron model accepts pressure loads and localized deflections occur, the total deflection number is also given for this model (Fig. 4-I) as well as the deflection of the neutral or center axis of the beam.

The localized deflections from these pressure loads on the bottom of the steel beam seem to have a large effect on the generated compressive stresses in the concrete. Figure 8 delineates the pressure forces in the MPC connections between the beam and the concrete nodes for the two-dimensional models as output by the GRID-point-force balance table.

IV. Results

Comparison of the $-Z$ deflections between the analytical cantilever beam (Fig. 4-III) and the CBAR beam (Fig. 4-II) shows a close match. The observation can be made that the CBAR element of NASTRAN accurately computes the shear deflections. The shear deflection is almost half of the bending in this model.

If the center axis (neutral axis) $-Z$ deflections of the NASA hexahedron beam is compared to the cantilever beam deflection, it is stiffer by about 15 percent. If the localized deformations from the concentrated loading are accounted for by comparing the $-Z'$ deflections, the standard beam is slightly stiffer (Table 1).

The two-dimensional beam and concrete models described in Table 2 show much higher node 2001 (Figs. 2 and 3) compressive stresses for the CBAR beam model: higher than explainable by the almost equal bending stiffnesses shown in Table 1 data. The slightly higher bending stiffness of the hexahedron may account for part of the decrease in compressive stresses. However, the localized deflections from the pressure loads must be responsible for a large portion of the differences of the compressive stresses. In Fig. 8, the pressure forces between the beam-rail and the concrete show large differences between the models.

From the foregoing data, it is recommended that the results from the hexahedron models using the 0.02 m smallest cubic elements should be increased 10 percent to account for their stiffer bending/localized deformation characteristics. The tolerance on this percentage is approximately plus 5 and minus 10. More analysis checks on the accuracy of the hexahedron models should be done.

Also, another 5 percent should be added for the increase in the smallest element size from 0.02 m to 0.04 m. Here again, more use experiences would be helpful in optimizing computer run time against accuracies in the computed results.

Bibliography

1. "The NASTRAN User's Manual," Level 16.1, National Aeronautics and Space Administration.
2. "The NASTRAN User's Manual," MSC-41, McNeal-Schwindler Corp., Los Angeles, Calif.
3. Timoshenko, S., "Strength of Materials," Part I, *Advanced Theory and Problems*, D. Van Nostrand Co., Inc., 1930, p. 191.
4. Timoshenko, S., "Strength of Materials," Part II, *Advanced Theory and Problems*, D. Van Nostrand Co., Inc., 1930, p. 475.

Table 1. Steel beam-rail only, vertical deflections

Seq	Beam type	NASTRAN level	-Z deflection x 10^4[a] m with E	with E'	-Z' x 10^4[b] m with E	Remarks	Program
1	Cantilever (Eq. 1)	–	-2.47	-2.28[c]	--	Fig. 4-III	--
2	CBAR	NASA-16.1	-2.45	-2.23	--	Fig. 4-II	F1CTNAST
3	Hexahedron	NASA-16.1	-1.98	--	-2.35	0.02 mesh, Fig. 5-I	F1CUNAST
4	Hexahedron	MSC-41	-2.11	--	-2.51	0.02 mesh, Fig. 5-I	FGANAST
5	Hexahedron	NASA-16.1	-1.69	--	-1.98	0.04 mesh, Fig. 5-II	F7BNAST
6	Hexahedron	MSC-41	-1.96	--	-2.24	0.04 mesh, Fig. 5-II	F7ANAST
7	Hexahedron	NASA-16.1	-2.10	--	-2.68	0.02 mesh, Fig. 5-III symmetric	F1ONAST
8	Hexahedron	NASA-16.1	-2.02	--	-2.47	0.04 mesh, Fig. 5-IV symmetric	F9NAST

[a]–Z Deflections are the neutral axis –Z differentials. E = Young's modulus, 2.1×10^{11} n/m^2, E' = E $(1/1 - \mu^2)$ μ = Poisson's ratio, 0.3.

[b]–Z' deflections measured per Fig. 4-I (includes compressive deformations from concentrated loads).

[c]E' used for the bending deflection portion.

Table 2. Concrete compressive stresses (node 2001), two-dimensional models (Figs. 2 and 3)

Seq	Steel rail-beam	NASTRAN level	Concrete stresses, x 10^{-6} N/m^2 (x 10^{-3} psi) Node 2001 compressive	Element mean pressure	Element octahedral shear	Remarks	Run no.
1	CBAR	NASA-16.1	-11.55 (-1.68)	7.03	3.88	Used E', Fig. 3	F1BNAST
2	CBAR	MSC-41	-11.44 (-1.70)	6.97	3.60	Used E' Fig. 3	F1BNAST
3	Hexahedron	NASA-16.1	-7.08 (-1.03)	4.63	2.47	Mesh = Fig. 5-I	F1CNAST
4	Hexahedron	MSC-41	-7.86 (-1.14)	4.66	2.48	Mesh = Fig. 5-I	F1CNAST
5	Hexahedron	NASA-16.1	-7.53 (-1.09)	4.39	2.43	Mesh = Fig. 5-II	F7ANAST

Table 3. Concrete compressive stresses/three-dimensional model (Fig. 7)

Seq	NASTRAN level	Loading	Top of concrete – compressive stress, × 10^{-6} N/m^2 (× 10^{-3} psi)[a]						
			*A	B	C	D	E	F	G
1	NASA 16.1	Top 2,624,450 N	10.22	– 9.94	–9.00	–8.08	–6 88	–5.54	–5.17
2	NASA 16.1	Side 868,000 N	0.0	± 0.70	±0.77	±0.91	±1.04	±1.27	±2.39
3	NASA 16.1	Total (max)	–10.22 (1.48)	–10.14	–9.77	–9.00	–7.92	–6.81	–7.56
4	MSC-41	Top 2,624,450 N	–10.39	–10.11	–9.35	–8.27	–7.10	–5.77	–5.61

[a]A – G = locations designated on Fig. 7

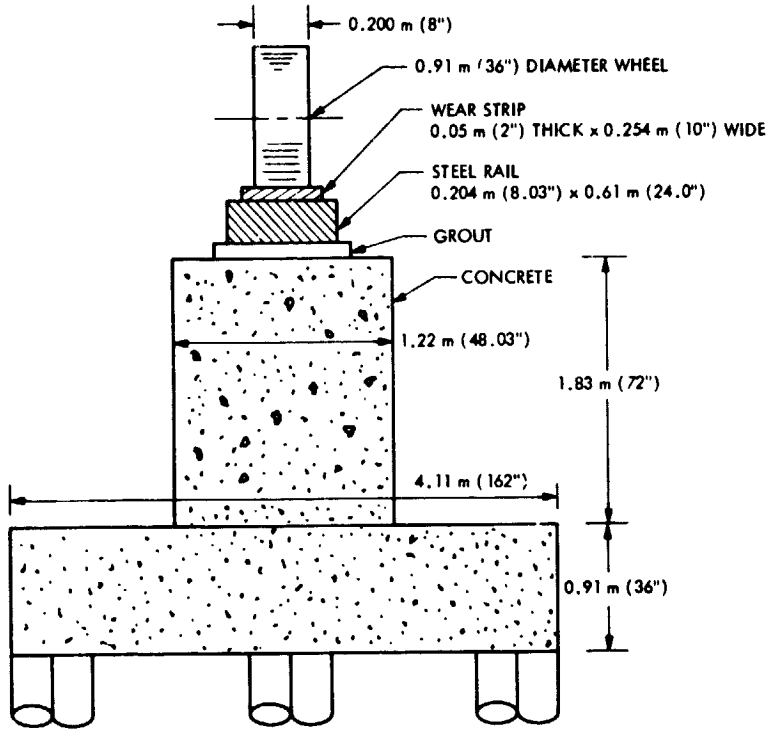

Fig. 1. Cross-sectional view, rail-foundation

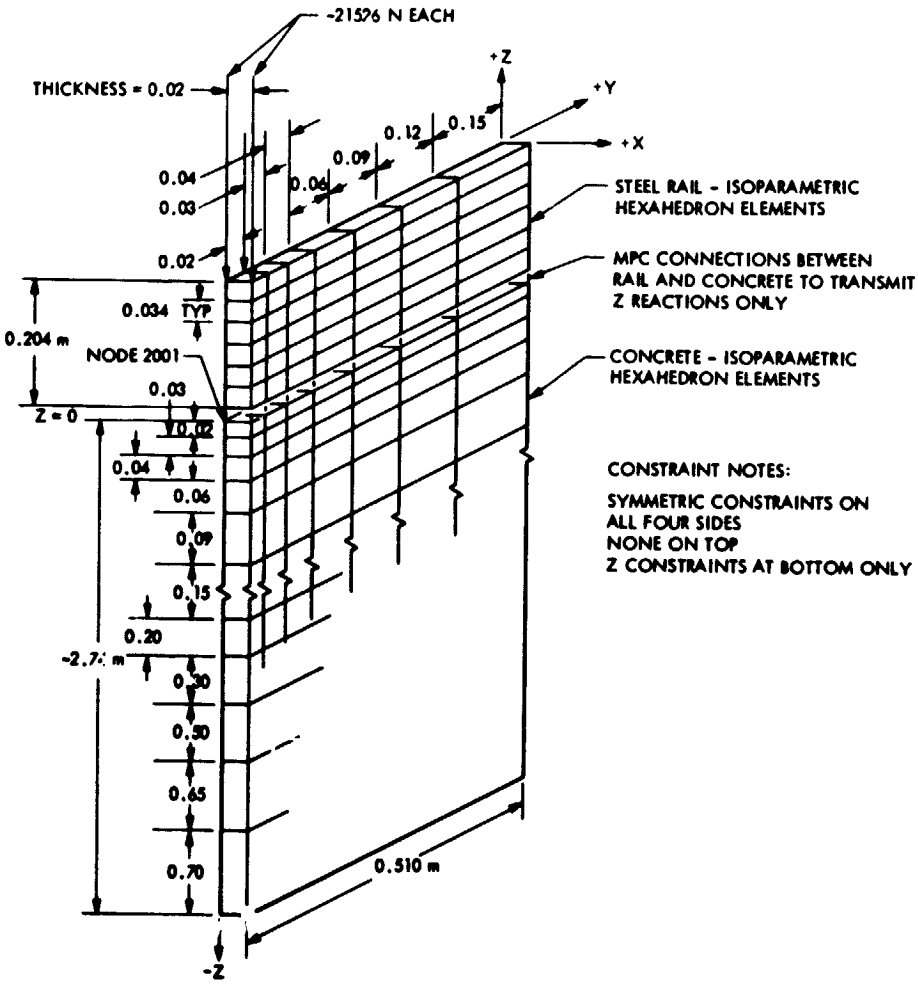

Fig. 2. Two-dimensional hexahedron model

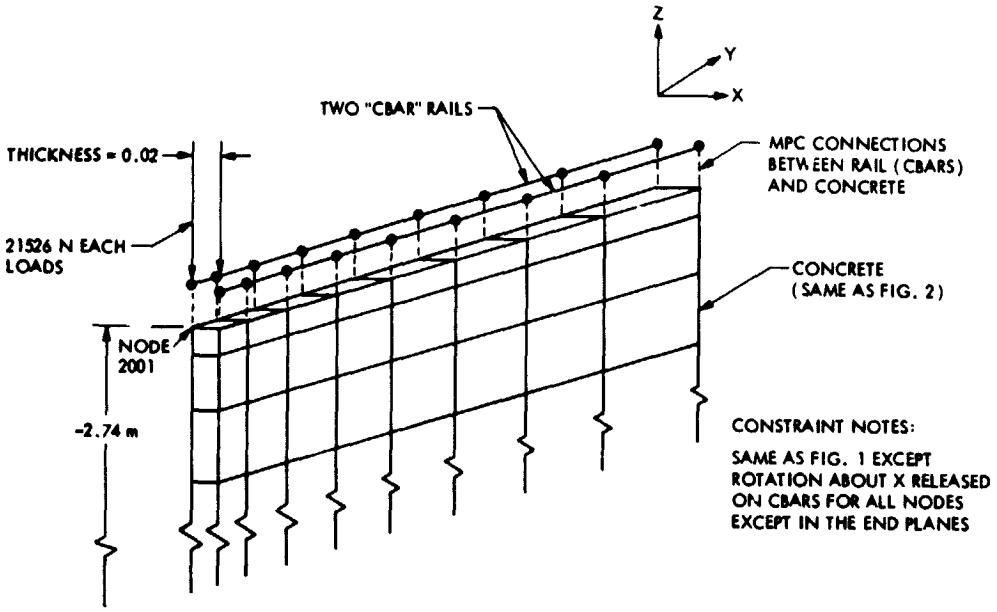

Fig. 3. Two-dimensional CBAR-hexahedron model

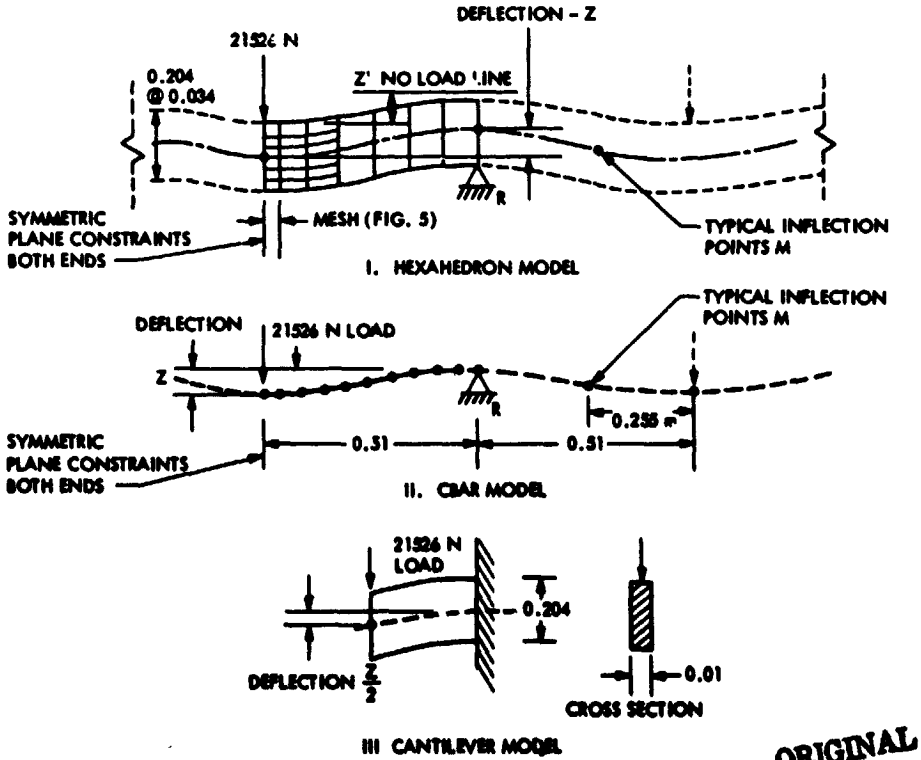

Fig. 4. Steel beam-rail only models

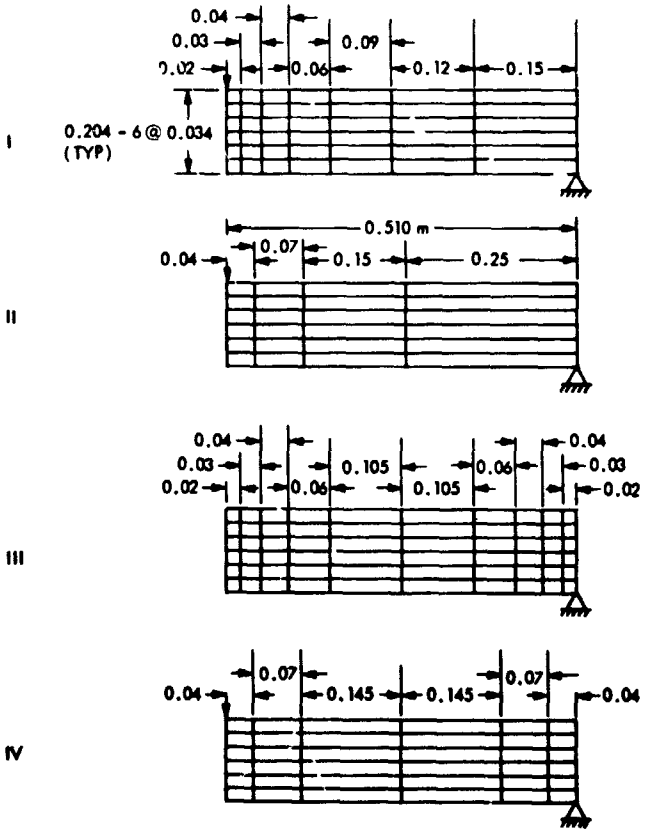

Fig. 5. Two-dimensional model, meshes

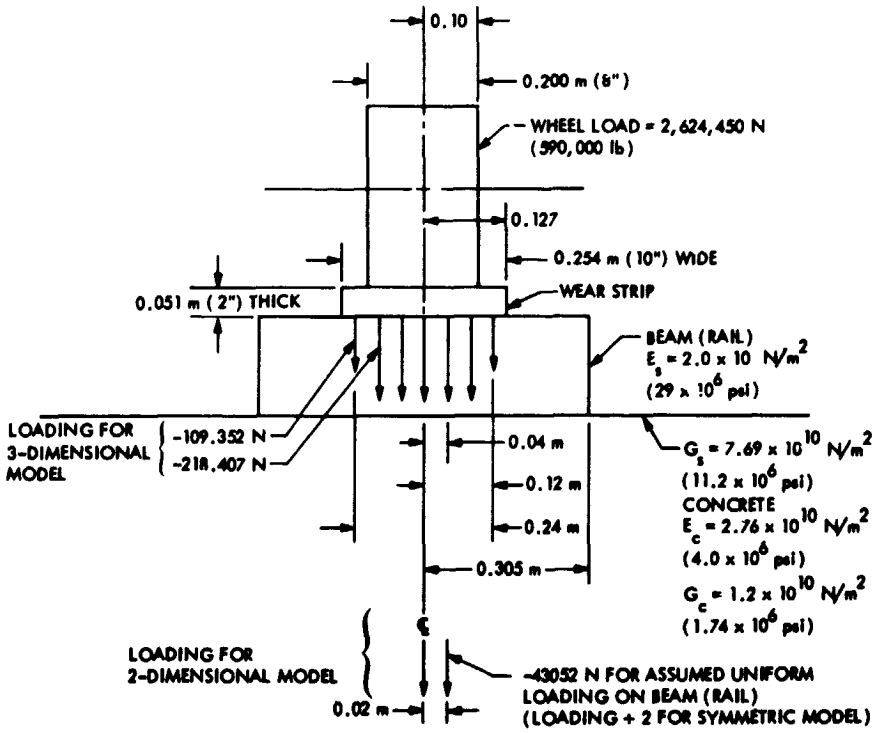

Fig. 6. Wheel loading data

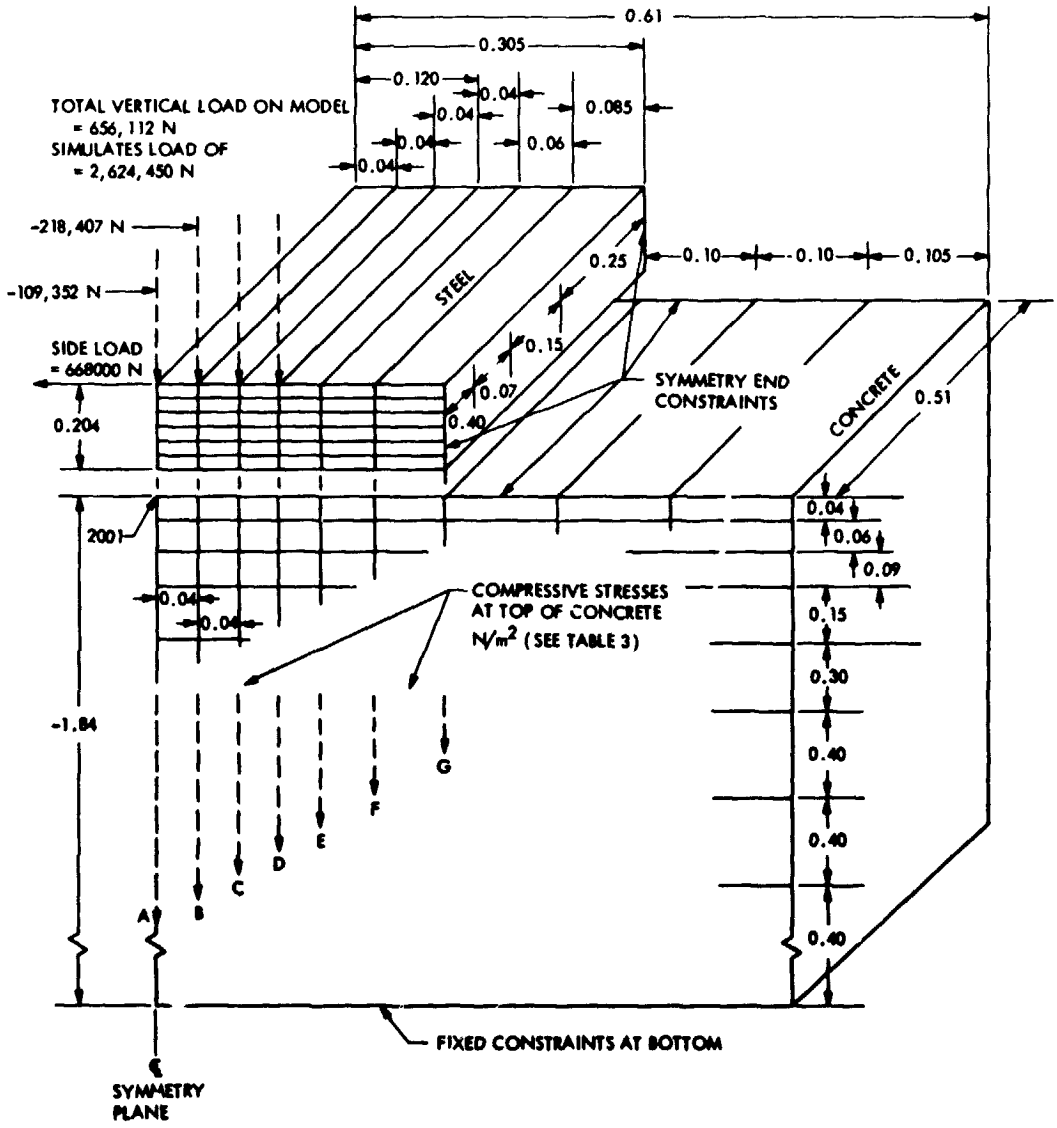

Fig. 7. Three-dimensional model

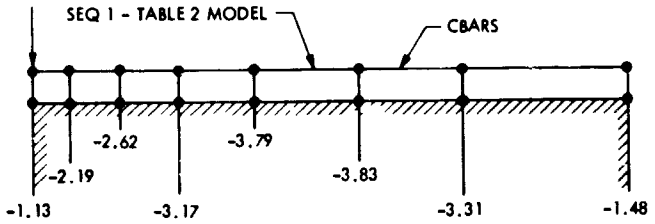

I. CBAR MODEL, FIG. 3

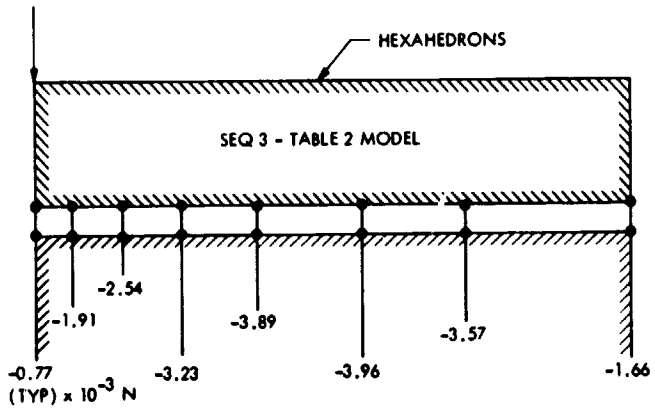

II. HEXAHEDRON MODEL, FIG. 2

Fig. 8. Pressure forces between beam-rail and concrete

An Empirical Spectral Bandwidth Model for Superior Conjunction

R. S. Rockwell
Deep Space Network Operations Section

The downlink signal from spacecraft in superior solar conjunction phases suffers a great reduction in signal-to-noise ratio. Responsible in large part for this effect is the line broadening of the signal spectrum. This article presents an analytic empirical expression for spectral bandwidth as a function of heliocentric distance from 1 to 20 solar radii. The study is based on spectral broadening data obtained from the superior conjunctions of Helios 1 (1975), Helios 2 (1976) and Pioneer 6 (1968). The empirical fit is based in part on a function describing the electron content in the solar corona.

I. Introduction

During superior conjunctions the signal from a spacecraft undergoes considerable distortion as a result of passing through the solar corona. One of the prime factors responsible for this distortion is the effect of spectral broadening and is graphically seen in the degradation of the signal-to-noise ratio (SNR).

In an effort to model SNR degradation during superior conjunction it is necessary to know how spectral lines broaden as a function of distance from the Sun. This information must be obtained either from actual measurement or a theoretical model.

For the purpose of this study, Richard Woo has supplied his theoretical work on spectral broadening (Ref. 1) and a graphical display of spectral broadening data-spectral bandwidth versus heliocentric distance.

II. The Data

The data to be used in this study are a composite collection of bandwidth measurements[1] from the superior conjunctions of Helios 1 (1975), Helios 2 (1976) and Pioneer 6 (1968). The data span the region from 1 solar radius (R_0) to 20 solar radii ($20R_0$).

The Woo paper defines the bandwidth BW, as:

$$\int_0^{BW/2} P(f)df = 1/2 \int_0^{\infty} P(f)df$$

where $P(f)$ is the power spectrum of the broadened spectral line.

[1] In Hz as a function of heliocentric distance.

To utilize the bandwidth data it was decided to curve fit the raw data points in the least square sense. The immediate problem was to determine a reasonable function to be used in the fitting process.

Initially, Woo's spectral broadening paper was consulted in an effort to find a suitable "fitting" function. However, no convenient closed-form expression could be found in his work. A straightforward polynomial was considered but was considered to be too cumbersome a function and not very elegant. Next, the ISED function (integrated solar electron density) from the A. Berman/J. Wackley doppler noise formulation (Ref. 2) was investigated. There were several good reasons for considering this function.

Spectral broadening is undoubtedly in some way related to the free electron content in the solar corona. Since the ISED function is simply a measure of the electron content along the signal raypath, it seems reasonable to hypothesize that spectral broadening, which is expressed in terms of the spectral bandwidth, might be proportional to this parameter. Furthermore, the ISED parameter successfully models one solar induced effect - doppler noise. Perhaps it can another - spectral broadening.

III. The Fitting of ISED

In its original form the ISED function is given by

$$\text{ISED} = \int_0^R N_e \, dr$$

where

$$N(r) = \frac{A}{r^6} + \frac{B}{r^{2.3}} \quad \frac{\text{el}}{\text{cm}^3}$$

and r is the heliocentric distance in solar radii.

The integration is along the signal path and when expressed in Sun-Earth-probe angle geometry yields:

$$\text{ISED}(\alpha,\beta) = A_0 \left[\frac{\beta}{(\sin\alpha)^{1.3}}\right] F(\alpha,\beta) + A_1 \left[\frac{1}{(\sin\alpha)^5}\right]$$

with

$$F(\alpha,\beta) = 1 - 0.05 \left[\frac{(\beta - \pi/2 + \alpha)^3 - (\alpha - \pi/2)^3}{\beta}\right] - 0.00275 \left[\frac{(\beta - \pi/2 + \alpha)^5 - (\alpha - \pi/2)^5}{\beta}\right]$$

where

α = Sun-Earth-probe angle (SEP), rad

β = Earth-Sun-probe angle (ESP), rad

When modeling doppler noise, Berman sets ISED proportional to the actual noise data and simultaneously solves for A_0, A_1 and a proportionality constant K.

In fitting the ISED function to the bandwidth data it was decided to first try using the doppler noise coefficients:

$$A_0 = 1.182 \times 10^{-3}$$

$$A_1 = 4.75 \times 10^{-10}$$

The function under consideration was of the form:

$$BW'_{H_z}(\alpha) = K\,(ISED_{DN})$$

where $ISED_{DN}$ represents ISED with the doppler noise coefficients. The form of ISED was simplified slightly by setting $\beta = \pi - \alpha$. This is a reasonable approximation considering the fact that the data spans the region $1R_0$ to $20R_0$ or 0.3 to 5 deg SEP.

In performing the curve fit, the sum of the squares of the logarithmic residuals were formed

$$\sigma = \sum_{i=1}^{n} \left\{\left[\log_{10} \frac{BW_{act}(\alpha_i)}{BW_{prd}(\alpha_i)}\right]\right\}^2$$

and then minimized with respect to K:

$$\frac{\partial \sigma}{\partial K} = 0$$

This yields $K = 7.657$ with a standard deviation $\sigma = 1.6513$ dB.

The results of this fit appear to be fairly good as the statistics and a glance at the graphical data (Fig. 1) show. To improve upon this fit the next logical step was to determine a new set of coefficients, A_0 and A_1, in addition to determining K. It was also decided to look more closely at the electron density function, N_e.

Most forms of the density function found in the literature can be expressed as:

$$N_e(r) = \frac{A}{r^6} + \frac{B}{r^{2+\epsilon}}$$

where ϵ has taken on a multitude of values ranging from approximately 0.0 - 0.5. In his study, Berman chose to use an a priori value of $\epsilon = 0.3$. Berman independently derived this same value $\epsilon = 0.30$ from his curve fitting of ISED to doppler noise.

Using the same basic idea, it was decided to reevaluate ϵ in addition to A_0 for the bandwidth data. Determining the values of K, A_0, and ϵ had the same effect as determining A_1, A_0 and ϵ.

IV. Evaluation of ϵ

To evaluate the parameters A_0 and ϵ, the ISED function was written in the form:

$$\text{ISED}(\alpha, \epsilon) = A_0 \left[\frac{\pi - \alpha}{(\sin\alpha)^{1+\epsilon}}\right] F(\alpha, \epsilon) + A_1 \left[\frac{1}{(\sin\alpha)^5}\right]$$

with

$$F(\alpha, \epsilon) = 1 - \left(\frac{\epsilon}{6}\right)\left[\frac{(\pi/2)^3 - (\alpha - \pi/2)^3}{\pi - \alpha}\right] + \frac{\epsilon}{120}(3\epsilon - 2)\left[\frac{(\pi/2)^5 - (\alpha - \pi/2)^5}{\pi - \alpha}\right]$$

where the substitution $\beta = \pi - \alpha$ has been included. This is the procedure followed by Berman (Ref. 3).

Again, the least-squares method was applied and the solutions of the conditions:

$$\frac{\partial \sigma}{\partial A_0} = 0$$

$$\frac{\partial \sigma}{\partial \epsilon} = 0$$

yielded the best fit values of A_0 and ϵ. One final application of least squares determined the constant of proportionality K between the bandwidth and ISED.

The values of the ISED parameters that provide the best fit, in the least squares sense, to the bandwidth data are

$$\epsilon = 0.77$$

$$A_0 = 0.22 \times 10^{-3}$$

$$K = 8.8521$$

The corresponding statistics are

$$\sigma(\text{dB}) = 1.4347$$

This fit is plotted over the Woo data in Figs. 2 and 3 and shows the scatter between the two.

It is interesting to note the value of ϵ just determined. The Berman value of $\epsilon = 0.30$ is about the average of most values determined by other investigators (Ref. 3). Although the value $\epsilon = 0.77$ is somewhat higher, it should be noted that:

(1) ϵ tends to take on higher values when evaluated over regions close to the Sun ($\sim 10R_0$)

(2) Spectral broadening is probably proportional to more than just the signal path electron content

Saito, for instance, obtains a value of $\epsilon = 0.5$ for the region 1 to 5 solar radii (Ref. 4).

In his paper, Woo states that the bandwidth is proportional to the solar wind flux. Assuming a spherically symmetric corona would imply that the bandwidth falls off as an inverse-square law. For completeness, a simple inverse-square function was fit in the least-squares sense to the bandwidth data. This fit yielded the statistics

$$\sigma\,(\text{dB}) = 2.0024$$

A plot of this function is seen in Fig. 4.

V. Conclusion

In its final form, the empirical model for the spectral bandwidth during superior conjunction is given by

$$BW(\alpha) = K(\mathrm{ISED})$$

$$= (1.95 \times 10^{-1}) \left[\frac{\pi - \alpha}{(\sin \alpha)^{1.77}}\right] F(\alpha)$$

$$+ (4.2 \times 10^{-9}) \left[\frac{1}{(\sin \alpha)^5}\right], \mathrm{Hz}$$

with

$$F(\alpha) = 1.0 - 0.13 \left[\frac{(\pi/2)^3 - (\alpha - \pi/2)^3}{\pi - \alpha}\right]$$

$$+ 0.002 \left[\frac{(\pi/2^5) - (\alpha - \pi/2)^5}{\pi - \alpha}\right]$$

α = SEP angle, rad

This expression is valid for the region $1R_0$ - $20R_0$

This bandwidth can be expressed in different units using the following conversion factors

$$5600 \ \frac{\text{meters}}{\text{Hz}}$$

$$1.95 \times 10^{20} \ \text{el/m}^2/\text{Hz}$$

The model presented gives the user a best-fit expression for the spectral bandwidth as a function of heliocentric distance during superior conjunction. The ISED function appears to reflect the basic signature of spectral broadening effects in the region $1R_0$ - $20R_0$.

Although spectral broadening is undoubtedly a result of more complicated processes than just the presence of electrons in the signal path (or even the fluctuations in the density of these electrons), ISED, with $\epsilon = 0.77$, describes the radial behavior of this effect to a good first order. Perhaps this model will be a good starting place for a more detailed description of solar corona spectral broadening effects.

References

1. Woo, R., Yang, F., and Ishimaru, A., "Structure of Density Fluctuations Near The Sun Deduced From Pioneer-6 Spectral Broadening Measurements," in *The Astrophysical Journal*, Vol. 210, No. 2, Part 1, December 1, 1976.

2. Berman, A. L., and Wackley, J. A., "Doppler Noise Considered as a Function of the Signal Path Integration of Electron Density," in *The Deep Space Network Progress Report 42-30*, Jet Propulsion Laboratory, Pasadena, California, June 15, 1976.

3. Berman, A. L., Wackley, J. A., Rockwell, S. T., and Kwan, M., "Viking Doppler Noise Used to Determine the Radial Dependence of Electron Density in the Extended Corona," in *The Deep Space Network Progress Report 42-38*, Jet Propulsion Laboratory, Pasadena, California, January 1977.

4. Saito, K., "A Non-Spherical Axisymmetric Model of the Solar K Corona of the Minimum Type," *Annals of the Tokyo Astronomical Observatory*, University of Tokyo, Second Series, Vol. XII, No. 2, Mitaka, Tokyo 1970.

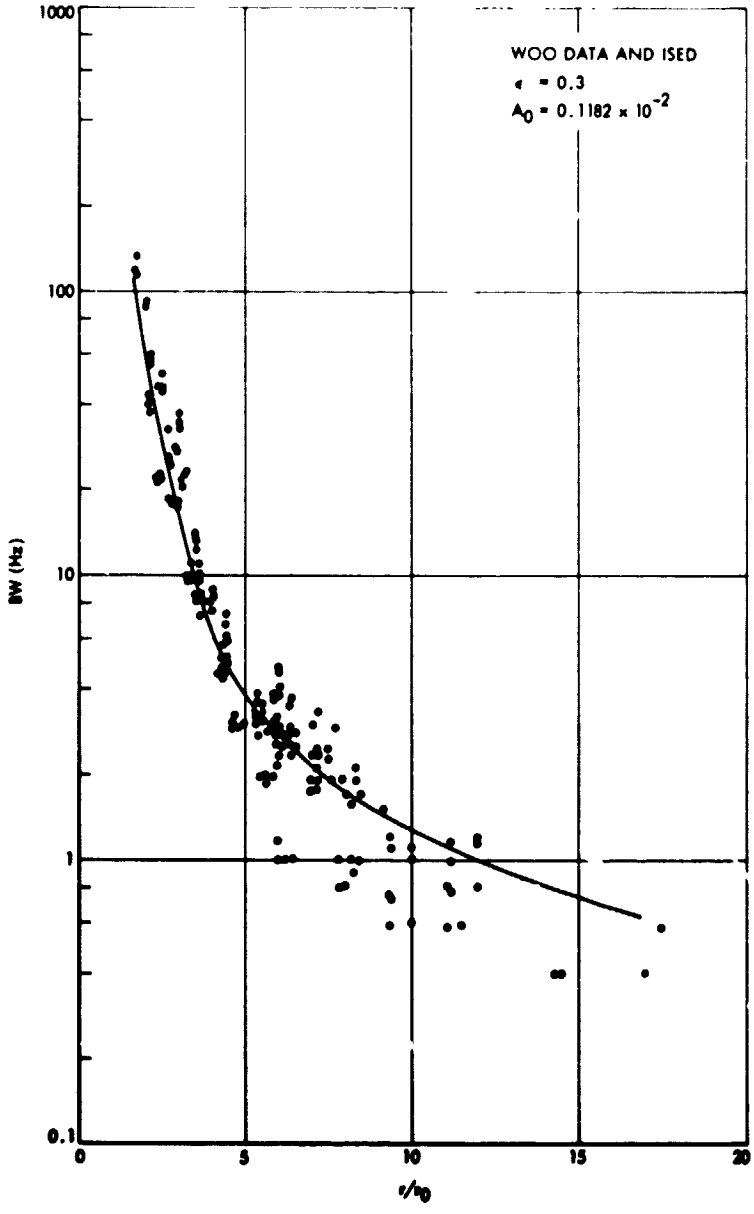

Fig. 1. Woo data and ISED, $\epsilon = 0.3$ and $A_0 = 0.1182 \times 10^{-2}$

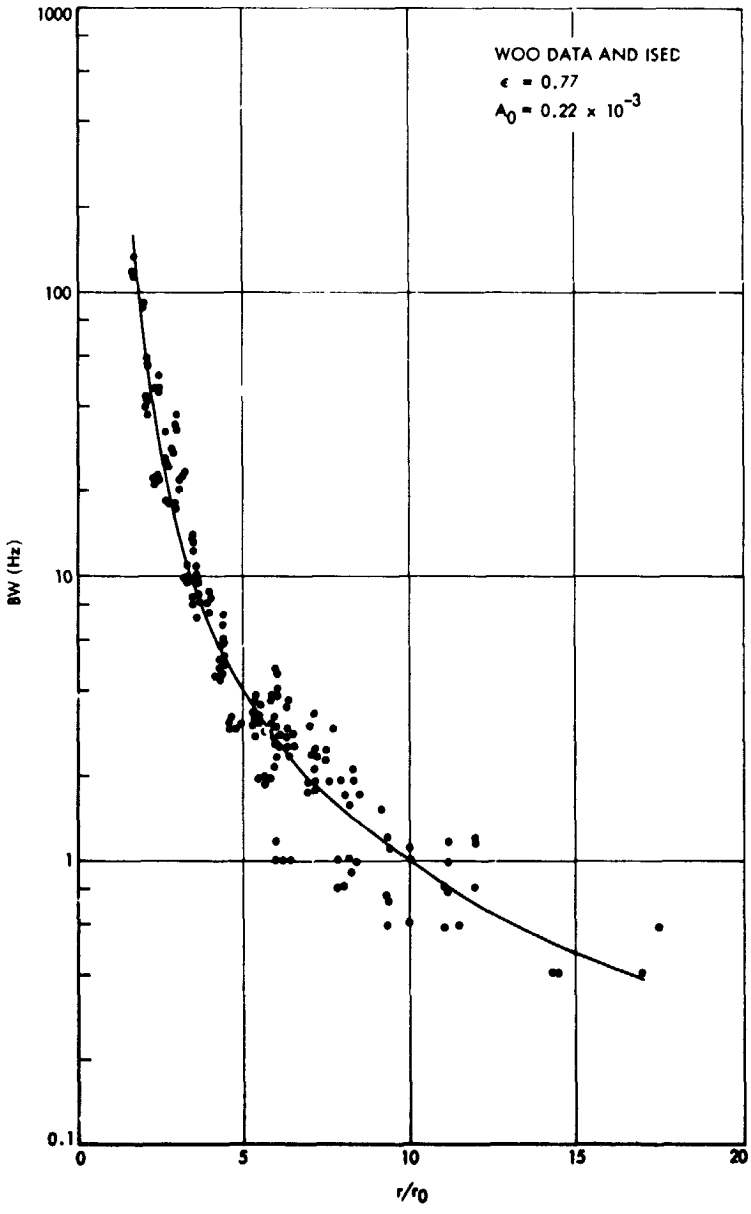

Fig. 2. Woo data and ISED, $\epsilon = 0.77$ and $A_0 = 0.22 \times 10^{-3}$

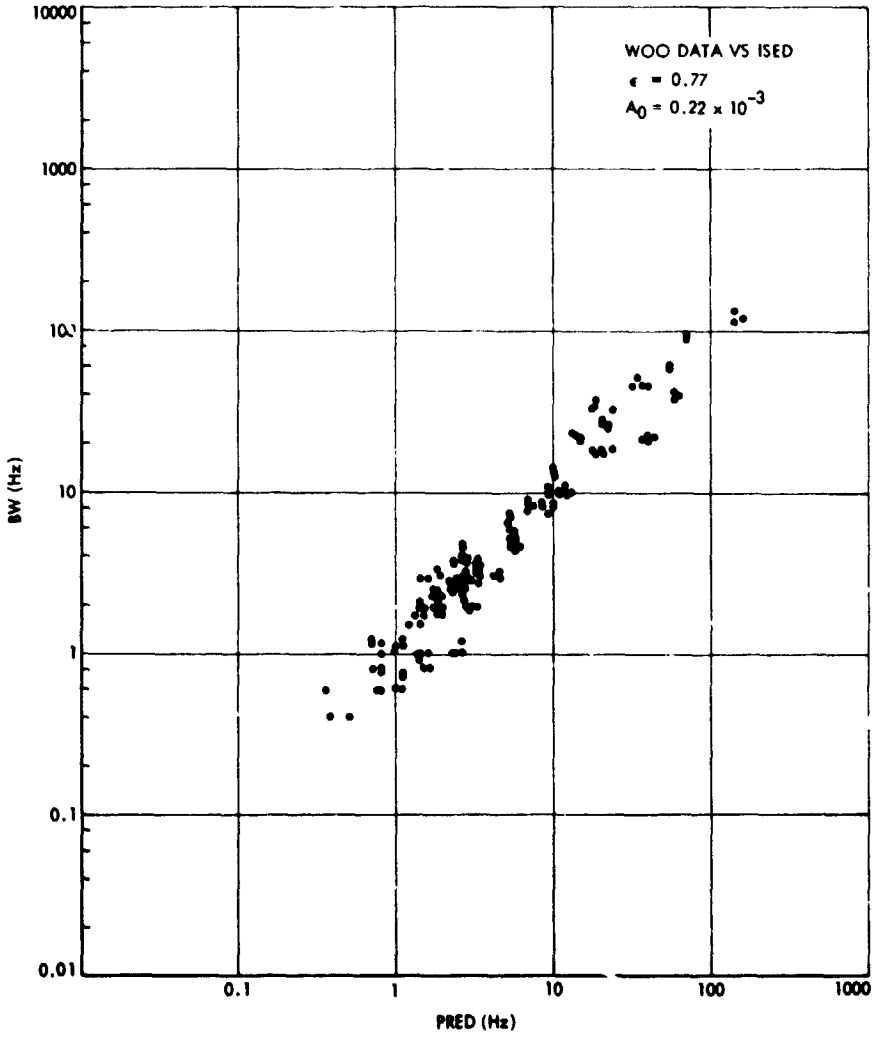

Fig. 3. Woo data vs ISED, $\epsilon = 0.77$ and $A_0 = 0.22 \times 10^{-3}$

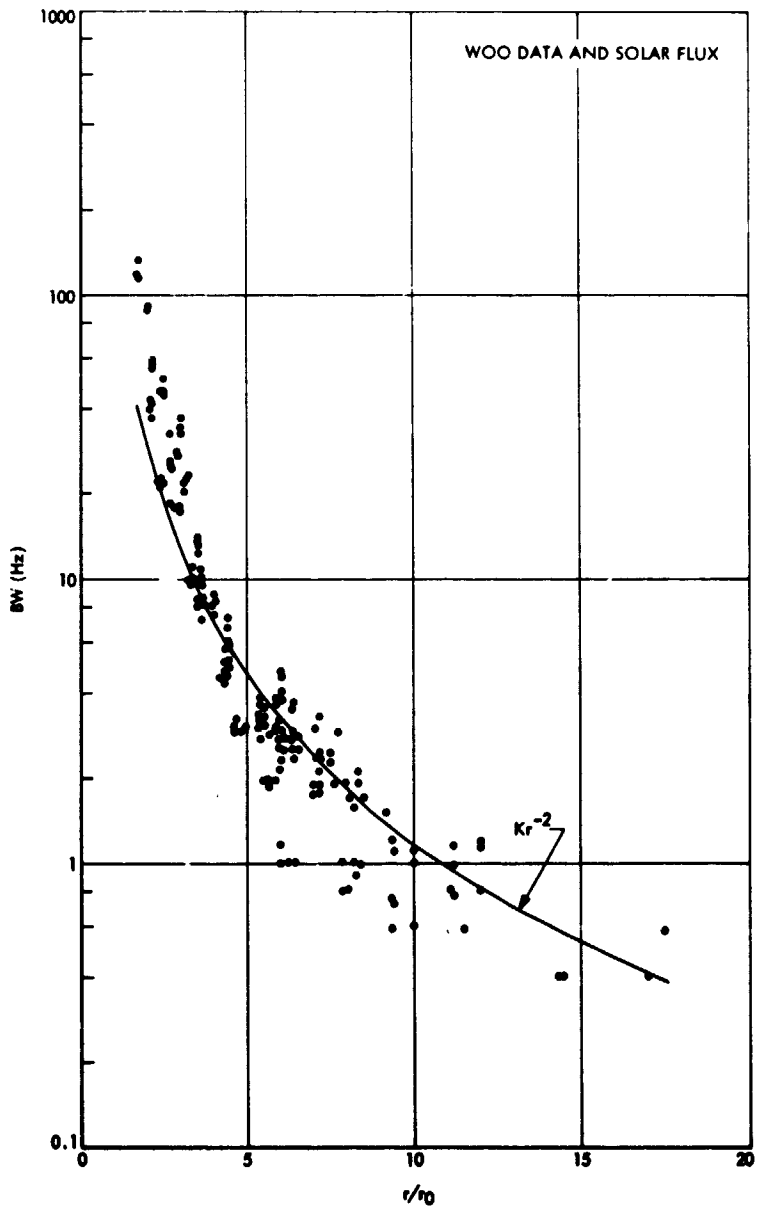

Fig. 4. Woo data and solar flux

DSN System Performance Test Software

M. Martin
Deep Space Network Operations Section

The Deep Space Network Operations Software Support Group has developed an entirely new, fully automated means of testing the performance of the Deep Space Station Data Subsystems. The DSN System Performance Test Software was developed for the new DSN Mark-III '77 Data System (MDS).

I. Introduction

In April of 1975 the Deep Space Network Software Support Group was given the assignment of developing System Performance Test Software to run in the DSN Mark-III Data System Modcomp-II computers at the Deep Space Stations. The original idea was to basically recode existing software for the Modcomp. During the first few months of the software definition and design phase, new requirements were pointed out, structured programming concepts were stressed, and the capabilities of the Modcomp computer were becoming more obvious. It was then decided that it would be better to develop a totally new MDS software package. DSN management concurred, and the Software Support Group was given the go-ahead to start software implementation.

By January of 1976 the Software Support Group produced a new, totally automated DSN System Performance Test Software design for DSN management review and approval.

II. Description

The DSN System Performance Test (SPT) Software package is comprised of a Test Executive and several individual test programs. The Test Executive is the main program. It controls the input and output of the individual test programs by routing data blocks and operator directives to those programs. It also processes data block dump requests from the operator.

The operation of the Test Executive is governed by the SPT Standard Operating System (SPTSOS), which contains the handlers and common software required by the Test Executive and the test programs. The SPT software package (Fig. 1) may be expanded vertically as well as horizontally as new requirements are defined and implemented. The expansion is limited only by the size of the disc. As new programs are developed, the disc configuration may be modified, if necessary, by the generation of a new Operating System (SYSGEN). A SYSGEN tailors an Operating System to the requirements of the project and allocates disc space as required.

III. System Performance Test Executive

The Test Executive routes all input directives, standard subsystem blocks (SSB's), and high-speed data (HSD) and wideband data (WBD) blocks to the proper test programs. It performs preliminary checks and error dumping on incoming data blocks. It routes HSD-WBD and SSB blocks as requested by the test programs and transmits acknowledge responses as required by the operational programs.

The Test Executive processes all directives routed to itself and activates such programs or routines as required. It also

handles operator messages and test log and test report output functions.

Probably the most important feature is the ability to read test procedures from disc. This capability allows the operator to perform semiautomatic testing. The procedure will output specific operator instructions to tell the operator how to configure the hardware, etc. In this manner, a test may be designed and tested prior to its required use. The operator does not have to sit at the console typewriter entering directives; the test may be performed at computer speed rather than at operator speed. Operator input errors are virtually eliminated and the computer and computer software are used in a very efficient manner.

IV. Monitor System Performance Test Software

The Monitor System Performance Test Software tests the DSS Monitor Subsystem by generating and transmitting simulated high-speed data blocks and standard subsystem blocks to the Monitor Operational Software which resides in the Digital Instrumentation Subsystem (DIS). It also has the ability to insert errors into the blocks and to generate text and backfeed blocks. The Monitor SPT Software also processes monitor blocks received from the DIS by performing header checks, verifying block timing, checking block serial number sequencing, testing for changes in selected block data fields, and by comparing received data to expected data.

V. Telemetry System Performance Test Software

The Telemetry System Performance Test Software is a table-driven multimission program capable of processing six telemetry channels simultaneously. In addition, it is capable of remotely controlling the Simulation Conversion Assembly (SCA) by generating text and control HSD blocks and transmitting them to the SCA. The outputs of the Telemetry Processor Assembly (TPA) are patched and become inputs to the Telemetry SPT Program, which accepts the inputs and performs header checks, time interval tests, and bit-word error rate tests and periodically reports errors and error summaries to the operator. An additional capability is also available which calculates Y-factor values given system parameters and calibration data.

VI. Tracking System Performance Test Program

The Tracking System Performance Test Software tests and evaluates the performance of the DSS doppler system by verifying doppler data formats, calculating long-term drift and phase jitter, computing theoretical jitter, and reporting S-band Programmed Oscillator Control Assembly (POCA) ramp delay and noise characteristics. It also tests and evaluates the DSS Planetary Ranging Assembly (PRA) by verifying range data formats and by determining range and differenced range versus integrated doppler (DRVID) characteristics. It tests the antenna subsystem by creating and transmitting angle predicts.

The Tracking SPT Software consists of a primary program and transient test report generators. The primary program accepts directives (from the Test Executive) for configuration and control, validates received data formats from tracking high-speed data blocks, and records doppler and ranging data on disc. At the conclusion of an SPT, a test report generator is activated to evaluate system performance from the data recorded and produces a test report showing test configuration, test data, and test results. Criteria for noise characteristics based on DSN system requirements provide a pass-fail judgment which is included in the test results.

VII. Command System Performance Test Program

The Command System Performance Test Program tests the operational integrity of the DSS Command Subsystem by simulating the functions of the Mission Control and Computing Center (MCCC) or other control center. The program receives operator directives and simulates high-speed data blocks, which are routed by the Test Executive to the Command Processor Assembly (CPA). The CPA returns standard subsystem blocks or high-speed data blocks in response to the blocks received from the test program. The test program then processes the incoming blocks by performing header checks and verifying that the received block contains the appropriate response. The test program expects the CPA to transmit blocks within certain time tolerances. If a block is not received on time an appropriate error message is output to the operator.

VIII. Mission-Independent Original Data Record (ODR) Validation Program

The Mission-Independent ODR Validation Program provides a means for validating an Original Data Record (ODR) tape generated by the Communications Monitor and Formatter Assembly (CMFA) during a System Performance Test. It also has the ability to validate the Referenced Original Data Record (RODR) tape generated by the System Performance Test Executive. Validation consists of performing simple header checks on the recorded blocks or by comparing two tapes for consistency. The ODR program can also be used to dump the ODR tapes.

IX. Conclusion

The System Performance Test Software is currently being modified to include additional capabilities and enhancements. Additional software programs are currently being developed for the Command Store and Forward System and the Automatic Total Recall System (ATRS). Additional projects which will be supported by future capabilities are the Network System Performance Tests, Mission Configuration Tests (MCT's) and the 26-Meter S-X Band Conversion Project.

The software is currently being used for Mission Prepass Readiness Tests (PRT's or countdowns), but future plans include modifying the software so that the command, tracking and telemetry programs may run simultaneously, thereby reducing required test time considerably.

Acknowledgments

Many individuals contributed to the success of the System Performance Test Software effort. Without their expertise and knowledge the SPT Software would still be a goal rather than a reality. Special thanks go to the following software engineers: J. E. Dewar (Test Executive), R. P. Leichnitz (Command), G. L. Mock (Telemetry), M. A. Pancino (Monitor), K. J. Seene (Tracking), and E. P. Straubel (ODR Validation). Appreciation is extended to the Network Operations System Support Group and to the following programmers who contributed to the effort: R. Billings, T. Gandet, D. Loar, L. Luegering, T. Thorman, and A. Murphy.

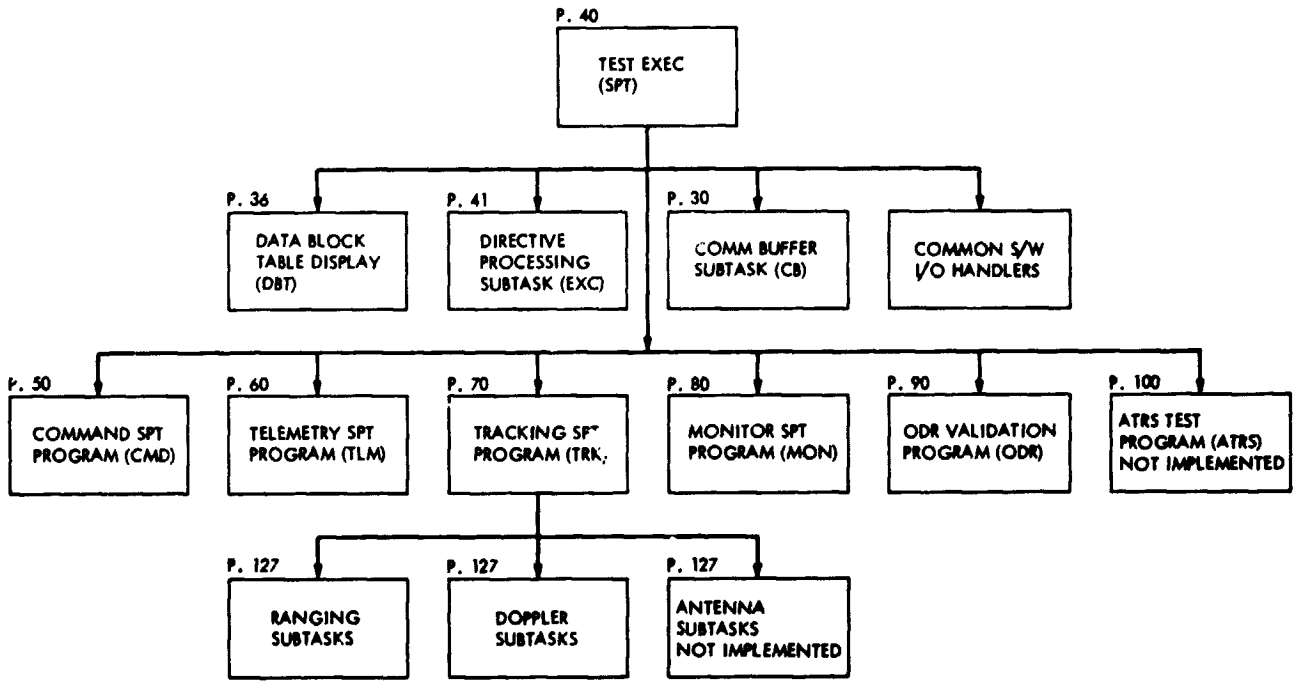

Fig. 1. SPT Software block diagram

Bibliography

Ananda, M. P., "Lunar Gravity: A Mass Point Model," *J. Geophys. Res.*, Vol. 82, No. 20, pp. 3049–3064, July 10, 1977.

Anderson, J. D., Null, G. W., and Thornton, C. T., *The Evaluation of Certain Astronomical Constants from the Radio Tracking of Mariner II*, Technical Report 32-476, Jet Propulsion Laboratory, Pasadena, Calif., reprinted from *Progr. Astronaut. Aeronaut.*, Vol. 14, 1964.

Anderson, J. D., *Determination of the Masses of the Moon and Venus and the Astronomical Unit from Radio Tracking Data of the Mariner II Spacecraft*, Technical Report 32-816, Jet Propulsion Laboratory, Pasadena, Calif., July 1, 1967.

Anderson, J. D., et al., "The Radius of Venus as Determined by Planetary Radar and Mariner V Radio Tracking Data," *J. Atmos. Sci.*, pp. 1171–1174, Sept. 25, 1968.

Anderson, J. D., and Hilt, D. E., "Improvement of Astronomical Constants and Ephemerides from Pioneer Radio Tracking Data," *AIAA J.*, Vol. 7, No. 6, pp. 1048–1054, June 1969.

Anderson, J. D., "Determination of Astrodynamic Constants and a Test of the General Relativistic Time Delay With S-Band Range and Doppler Data From Mariners 6 and 7," *Space Research*, Vol. XI, pp. 105–112, Akademie-Verlag, Berlin, 1971.

Anderson, J. D., et al., "Experimental Test of General Relativity Using Time-Delay Data From Mariner 6 and Mariner 7," *Astrophys. J.*, Vol. 200, No. 1, pp. 221–233, Aug. 15, 1975.

Barnum, P. W., et al., *Tracking and Data System Support for the Mariner Mars 1971 Mission: Orbit Insertion Through End of Primary Mission*, Technical Memorandum 33-523, Vol. III, Jet Propulsion Laboratory, Pasadena, Calif., May 15, 1973.

Barnum, P. W., and Renzetti, N. A., *Tracking and Data System Support for the Mariner Mars 1971 Mission: Extended Mission Operations*, Technical Memorandum 33-523, Vol. IV, Jet Propulsion Laboratory, Pasadena, Calif., Dec. 15, 1973.

Barton, W. R., and Miller, R. B., *Tracking and Data System Support for the Pioneer Project: Pioneer 11—Prelaunch Planning Through Second Trajectory Correction: to May 1, 1973*, Technical Memorandum 33-584, Vol. II, Jet Propulsion Laboratory, Pasadena, Calif., Mar. 15, 1975.

Bartos, K. P., et al., *Implementation of the 64-Meter-Diameter Antennas at the Deep Space Stations in Australia and Spain*, Technical Memorandum 33-692, Jet Propulsion Laboratory, Pasadena, Calif., Jan. 15, 1975.

Bathker, D. A., *Radio-Frequency Performance of an 85-ft Ground Antenna: X-Band*, Technical Report 32-1300, Jet Propulsion Laboratory, Pasadena, Calif., July 1, 1968.

Bathker, D. A., *Radio Frequency Performance of a 210-ft Ground Antenna: X-Band*, Technical Report 32-1417, Jet Propulsion Laboratory, Pasadena, Calif., Dec. 15, 1969.

Bathker, D. A., *Predicted and Measured Power Density Description of a Large Ground Microwave System*, Technical Memorandum 33-433, Jet Propulsion Laboratory, Pasadena, Calif., Apr. 15, 1971.

Bathker, D. A., Brown, D. W., and Petty, S. M., *Single- and Dual-Carrier Microwave Noise Abatement in the Deep Space Network*, Technical Memorandum 33-733, Jet Propulsion Laboratory, Pasadena, Calif., Aug. 1, 1975.

Bathker, D. A., *Microwave Performance Characterization of Large Space Antennas*, JPL Publication 77-21, Jet Propulsion Laboratory, Pasadena, Calif., May 15, 1977.

Baumert, L., et al., *Coding Theory and Its Applications to Communications Systems*, Technical Report 32-67, Jet Propulsion Laboratory, Pasadena, Calif., Mar. 31, 1961.

Baumgartner, W. S., *High-Power CW Radar Transmitter*, Technical Report 32-656, Jet Propulsion Laboratory, Pasadena, Calif., Sept. 1, 1964.

Beatty, R. W., and Otoshi, T. Y., "Effect of Discontinuities on the Group Delay of a Microwave Transmission Line," *IEEE Trans. Microwave Theor. Techniq.*, Vol. MTT-23, No. 11, pp. 919–923, Nov. 1975.

Berman, A. L., *Tracking System Data Analysis Report, Ranger VII Final Report*, Technical Report 32-719, Jet Propulsion Laboratory, Pasadena, Calif., June 1, 1965.

Berman, A. L., and Rockwell, S. T., *New Optical and Radio Frequency Angular Tropospheric Refraction Models for Deep Space Applications*, Technical Report 32-1601, Jet Propulsion Laboratory, Pasadena, Calif., Nov. 1, 1975.

Berman, A. L., *The Prediction of Zenith Range Refraction From Surface Measurements of Meteorological Parameters*, Technical Report 32-1602, Jet Propulsion Laboratory, Pasadena, Calif., July 15, 1976.

Biber, K. W., and Whittlesey, A. C., *Description and Analysis of 890-MHz Noise-Measuring Equipment*, Technical Report 32-898, Jet Propulsion Laboratory, Pasadena, Calif., Mar. 31, 1966.

Born, G. H., et al., "The Determination of the Satellite Orbit of Mariner 9," *Celest. Mech.*, Vol. 9, No. 3, pp. 395–414, May 1974.

Born, G. H., and Mohan, S. N., "Orbit Determination for Mariner 9 Using Radio and Optical Data," *J. Spacecraft Rockets*, Vol. 12, No. 7, pp. 4392–441, July 1975.

Brockman, M. H., et al., *Extraterrestrial Radio Tracking and Communication*, External Publication 808, Jet Propulsion Laboratory, Pasadena, Calif., Nov. 12, 1959. Also available in *Proc. IRE*, Vol. 48, 1960.

Brockman, M. H., and Posner, E. C., *Power Requirements for Deep-Space Telecommunication Links*, Technical Report 32-1395, Jet Propulsion Laboratory, Pasadena, Calif., reprinted from *IEEE Spectrum*, Vol. 6, No. 3, pp. 95–99, Mar. 1969.

Bunce, R. C., *Unified S-Band Receiver-Exciter Subsystem*, Technical Report 32-809, Jet Propulsion Laboratory, Pasadena, Calif., Sept. 15, 1966.

Butman, S., "A General Formulation of Linear Feedback Communication Systems with Solutions," *IEEE Trans. Inform. Theor.*, Vol. IT-15, No. 3, pp. 392–400, May 1969.

Butman, S., "Rate Distortion Over Band-Limited Feedback Channels," *IEEE Trans. Inform. Theor.*, Vol. IT-17, No. 1, pp. 110–112, Jan. 1971.

Butman, S., and Timor, U., "Interplex—An Efficient Multichannel PSK/PM Telemetry System", *IEEE Trans. Commun.*, Vol. COM-20, No. 3, pp. 415–419, June 1972.

Butman, S. A., "Linear Feedback Rate Bounds for Regressive Channels," *IEEE Trans. Inform. Theor.*, Vol. IT-22, No. 3, pp. 363–366, May 1976.

Butman, S. A., et al., "Design Criteria for Noncoherent Gaussian Channels With MFSK Signaling and Coding," *IEEE Trans. Commun.*, Vol. COM-24, No. 10, pp. 1078–1088, Oct. 1976.

Butman, S. A., and Lesh, J. R., "The Effects of Bandpass Limiters on *n*-Phase Tracking Systems," *IEEE Trans. Commun.*, Vol. COM-25, No. 6, pp. 569–576, June 1977.

Cain, D. L., and Hamilton, T. W., *Determination of Tracking Station Locations by Doppler and Range Measurements to an Earth Satellite*, Technical Report 32-534, Jet Propulsion Laboratory, Pasadena, Calif., Feb. 1, 1964.

Carey, C. N., and Sjogren, W. L., *Gravitational Inconsistency in the Lunar Theory: Confirmation by Radio Tracking*, Technical Report 32-1290, Pt. II, Jet Propulsion Laboratory, Pasadena, Calif., reprinted from *Science*, Vol. 160, No. 3830, pp. 875–876, May 24, 1968.

Carpenter, R. L., *Study of Venus by CW Radar—1964 Results*, Technical Report 32-963, Jet Propulsion Laboratory, Pasadena, Calif., reprinted from *Astron. J.*, Vol. 71, No. 2, pp. 142–152, Mar. 1966.

Carr, R. E., *The Jet Propulsion Laboratory Method of Tracking Lunar Probes*, External Publication 793, Jet Propulsion Laboratory, Pasadena, Calif., June 4, 1959.

Chadwick, H. D., and Springett, J. C., "The Design of a Low Data Rate MSFK Communication System," *IEEE Trans. Commun. Technol.*, Vol. COM-18, No. 6, pp. 740–750, Dec. 1970.

Chaney, W. D., *Final Mariner II Tracking System Data Analysis Report*, Technical Report 32-727, Jet Propulsion Laboratory, Pasadena, Calif., Sept. 1, 1965.

Charles, F. J., and Lindsey, W. C., *Some Analytical and Experimental Phase-Locked Loop Results for Low Signal-to-Noise Ratios*, Technical Report 32-1027, Jet Propulsion Laboratory, Pasadena, Calif., reprinted from *Proc. IEEE*, Vol. 54, No. 9, pp. 1152–1166, Sept. 1966.

Christensen, C. S., and Reinold, S. J., "Navigation of the Mariner 10 Spacecraft to Venus and Mercury," *J. Spacecraft Rockets*, Vol. 12, No. 5, pp. 280–286, May 1975.

Christensen, C. S., et al., "On Achieving Sufficient Dual Station Range Accuracy for Deep Space Navigation at Zero Declination," paper presented at AAS/AIAA Astrodynamics Specialist Conference, Jackson Hole, Wyo., Sept. 7–9, 1977.

Clark, B. G., et al., "High Resolution Observations of Compact Radio Sources at 13 cm," *Astrophys. J.*, Vol. 161, pp. 803–809, Sept. 1970.

Clauss, R. C., et al., *Total System Noise Temperature: 15°K*, Technical Report 32-691, Jet Propulsion Laboratory, Pasadena, Calif., Nov. 1964.

Clauss, R. C., *A 2388-Mc Two-Cavity Maser for Planetary Radar*, Technical Report 32-583, Jet Propulsion Laboratory, Pasadena, Calif., reprinted from *Microwave J.*, Vol. 8, pp. 74–77, May 1965.

Clauss, R. C., *A Traveling Wave Maser for Deep Space Communication at 2295 and 2388 MHz*, Technical Report 32-1072, Jet Propulsion Laboratory, Pasadena, Calif., Feb. 15, 1967.

Clauss, R., Flesner, L. D., and Schultz, S., "Simple Waveguide Refle ion Maser with Broad Tunability," *Rev. Sci. Instrum.*, Vol. 48, No. 8, pp. 1104–1105, Aug. 1977.

Cohen, M. H., et al., "Compact Radio Source in the Nucleus of M87," *Astrophys. J.*, Vol. 158, No. 2, Pt. 2, pp. L83–L85, Nov. 1969.

A Collection of Articles on S/X-Band Experiment Zero Delay Ranging Tests, Technical Memorandum 33-747, Vol. I, Jet Propulsion Laboratory, Pasadena, Calif., Nov. 1, 1975.

Coyner, J. V., Jr., *Radial Rib Antenna Surface Deviation Analysis Program*, Technical Memorandum 33-518, Jet Propulsion Laboratory, Pasadena, Calif., Dec. 15, 1971.

Curkendall, D. W., and McReynolds, S. R., "A Simplified Approach for Determining the Information Content of Radio Tracking Data," *J. Spacecraft Rockets*, Vol. 6, No. 5, pp. 520–525, May 1969.

Curkendall, D. W., and Stephenson, R. R., "Earthbased Tracking and Orbit Determination—Backbone of the Planetary Navigation System," *Astronaut. Aeronaut.*, Vol. 7, No. 5, pp. 30–36, May 1970.

Curkendall, D. W., "Planetary Navigation: The New Challenges," *Astronaut. Aeronaut.*, Vol. 7, No. 5, pp. 26–29, May 1970.

"The Deep Space Network—An Instrument for Radio Navigation for the Mariner Mission to Mars—1969," *Proceedings of the Second International Conference of STM and AERA*, Reidel Publishing Company, Holland, May 1969.

Description of the Deep Space Network Operational Capabilities as of January 1, 1966, Technical Memorandum 33-255, Jet Propulsion Laboratory, Pasadena, Calif., July 1, 1966.

Description of World Network for Radio Tracking of Space Vehicles, Publication 135, Jet Propulsion Laboratory, Pasadena, Calif., July 1, 1958.

Didday, R. L., and Lindsey, W. C., *Subcarrier Tracking Methods and Communication System Design*, Technical Report 32-1317, Jet Propulsion Laboratory, Pasadena, Calif., reprinted from *IEEE Trans. Commun. Technol.*, Vol. COM-16, No. 4, pp. 541–550, Aug. 1968.

Downs, G. S., and Reichley, P. E., "Observations of Interstellar Scintillations of Pulsar Signals at 2388 MHz," *Astrophys. J.*, Vol. 163, No. 1, Pt. 2, pp. L11–L16, Jan. 1971.

Downs, G. S., et al., "Mars Radar Observation, A Preliminary Report," *Science*, Vol. 174, No. 4016, pp. 1324–1327, Dec. 24, 1971.

Downs, G. S., et al., "Martian Topography and Surface Properties as Seen by Radar: The 1971 Opposition," *Icarus*, Vol. 18, No. 1, pp. 8–21, Jan. 1973.

Downs, G. S., Reichley, P. E., and Morris, G. A., "Pulsar Detections at Frequencies of 8.4 and 15.1 GHz," *Astrophys. J.*, Vol. 181, No. 3, Part 2, pp. L143–L146, May 1, 1973.

Duxbury, T. C., Johnson, T. V., and Matson, D. L., "Galilean Satellite Mutual Occultation Data Processing," *Icarus*, Vol. 25, No. 4, pp. 569–584, Aug. 1975.

Easterling, M., *A Long-Range Precision Ranging System*, Technical Report 32-80, Jet Propulsion Laboratory, Pasadena, Calif., July 10, 1961.

Easterling, M., *Methods for Obtaining Velocity and Range Information from CW Radars*, Technical Report 32-657, Jet Propulsion Laboratory, Pasadena, Calif., Sept. 1, 1964.

Easterling, M., and Goldstein, R., *The Effect of the Interplanetary Medium on S-Band Telecommunications*, Technical Report 32-825, Jet Propulsion Laboratory, Pasadena, Calif., Sept. 1, 1965.

Edelson, R. E. (ed.), *Telecommunications Systems Design Techniques Handbook*, Technical Memorandum 33-571, Jet Propulsion Laboratory, Pasadena, Calif., July 15, 1972.

Edelson, R. E., "An Observational Program to Search for Radio Signals From Extraterrestrial Intelligence Through the Use of Existing Facilities," Preprint IAF-A-76-033, Int. Astronaut. Fed. XXVII Congress, Anaheim, Calif., Oct. 10–16, 1976.

Edelson, R. E., and Levy, G. S., "The Search for Extraterrestrial Intelligence: Telecommunications Technology," *Proceedings of the 1976 National Telecommunications Conference*, Vol. I, Dallas, Tex., Nov. 29–Dec. 1, 1976.

Edelson, R. E., "An Experimental Protocol for a Search for Radio Signals of Extraterrestrial Intelligent Origin in the Presence of Man-Made Radio Frequency Sources," paper presented at the XXVIIIth International Astronautical Congress, Prague, Czechoslovakia, Sept. 25–Oct. 1, 1977.

Efron, L., and Solloway, C. B., *Proceedings of the Conference on Scientific Applications of Radio and Radar Tracking in the Space Program*, Technical Report 32-1475, Jet Propulsion Laboratory, Pasadena, Calif., July 1, 1970.

Eimer, M., and Stevens, R., *Tracking and Data Handling for the Pioneer III and Pioneer IV Firings*, External Publication 701, Jet Propulsion Laboratory, Pasadena, Calif., Aug. 14, 1959.

Esposito, P. B., and Wong, S. K., "Geocentric Gravitational Constant Determined from Mariner 9 Radio Tracking Data," paper presented at the International Symposium on Earth Gravity Models (American Geophysical Union, NASA), St. Louis, Aug. 1972.

Estabrook, F. B., and Wahlquist, H. D., "Response of Doppler Spacecraft Tracking to Gravitational Radiation," *Gen. Relat. Grav.*, Vol. 6, No. 5, pp. 439–447, Oct. 1975.

Estacion Espacial de Madrid: Madrid Space Station, Special Publication 43-26, Jet Propulsion Laboratory, Pasadena, Calif., Aug. 31, 1975.

Fearey, J. P., and Renzetti, N. A., "Navigation Results on the Mariner Mars Mission to Mars 1969," International Navigation Conference, Hamburg, Oct. 1969.

Ferrari, A. J., and Ananda, M. P., "Lunar Gravity: A Long-Term Keplerian Rate Method," *J. Geophys. Res.*, Vol. 82, No. 20, pp. 3085–3097, July 10, 1977.

Fjeldbo, G., Kliore, A. J., and Seidel, B. L., "Bistatic Radar Measurements of the Surface of Mars with Mariner 1969," *Icarus*, Vol. 16, No. 3, pp. 502–508, June 1972

Fjeldbo, G., and Eshleman, V. R., "Radio Occultation Measurements and Interpretations," in *The Atmospheres of Venus and Mars*, p. 225, Gordon and Breach, Science Publishers, Inc., New York, N.Y., 1968.

Fjeldbo, G., "Radio Occultation Experiments Planned for Pioneer and Mariner Missions to the Outer Planets," *Planet. Space Sci.*, Vol. 21, No. 9, pp. 1533–1547, Sept. 1973.

Flanagan, F. M., et al., *Deep Space Network Support of the Manned Space Flight Network for Apollo: 1962–1968*, Technical Memorandum 33-452, Vol. I, Jet Propulsion Laboratory, Pasadena, Calif., July 1970.

Flanagan, F. M., et al., *Deep Space Network Support of the Manned Space Flight Network for Apollo: 1969–1970*, Technical Memorandum 33-452, Vol. II, Jet Propulsion Laboratory, Pasadena, Calif., May 1, 1971.

Fortenberry, J. W., Freeland, R. E., and Moore, D. M., *Five-Meter-Diameter Conical Furlable Antenna*, Technical Report 32-1600, Jet Propulsion Laboratory, Pasadena, Calif., July 15, 1976.

Fredricksen, H., *Error Correction for Deep Space Network Teletype Circuits*, Technical Report 32-1275, Jet Propulsion Laboratory, Pasadena, Calif., June 1, 1968.

Gary, B., Olsen, E. T., and Rosenkranz, P. W., "Radio Observations of Cygnus X-3 and the Surrounding Region," *Nature Phys. Sci.*, Vol. 239, No. 95, pp. 128–130, Oct. 23, 1972.

Gates, C. R., and Johnson, M. S., *A Study of On-Site Computing and Data Processing for a World Tracking Network*, Publication 154, Jet Propulsion Laboratory, Pasadena, Calif., Feb. 9, 1959.

Georgevic, R. M., *Mathematical Model of the Solar Radiation Force and Torques Acting on the Components of a Spacecraft*, Technical Memorandum 33-494, Jet Propulsion Laboratory, Pasadena, Calif., Oct. 1, 1971.

Goldstein, R., Stevens, R., and Victor, W. K., *Radar Exploration of Venus: Goldstone Observatory Report for October–December 1962*, Technical Report 32-398, Jet Propulsion Laboratory, Pasadena, Calif., Mar. 1, 1965.

Goldstein, R. M., *The Analysis of Uncooperative Radar Targets*, Technical Report 32-858, Jet Propulsion Laboratory, Pasadena, Calif., Sept. 1, 1964.

Goldstein, R. M., et al., *The Superior Conjunction of Mariner IV*, Technical Report 32-1092, Jet Propulsion Laboratory, Pasadena, Calif., Apr. 1, 1967.

Goldstein, R. M., "Radar Time-of-Flight Measurements to Venus," *Astron. J.*, Vol. 73, No. 9, Aug. 1968.

Goldstein, R. M., et al., "Preliminary Radar Results of Mars," *Radio Sci.*, Vol. 5, No. 2, pp. 475–478, Feb. 1970.

Goldstein, R. M., and Rumsey, H., "A Radar Snapshot of Venus," *Science*, Vol. 169, Sept. 1970.

Goldstein, R. M., "Radar Observations of Mercury," *Astron. J.*, Vol. 76, No. 10, pp. 1152–1154, Dec. 1971.

Goldstein, R. M., Holdridge, D. B., and Lieske, J. H., "Minor Planets and Related Objects: XII. Radar Observations of (1685) Toro," *Astron. J.*, Vol. 78, No. 6, pp. 508–509, Aug. 1973

Goldstein, R. M., and Morris, G. ..., "Ganymede: Observations by Radar," *Science*, Vol. 188, No. 4194, pp. 1211–1212, June 20, 1975.

Goldstein, R. M., Green, R. R., and Rumsey, H., Jr., "Venus Radar Images," *J. Geophys. Res.*, Vol. 81, No. 26, pp. 4807–4817, Sept. 10, 1976.

Golomb, S. W., "New Problems of Space Communications: Part I. Beware of the Tigers," *Astronautics*, Vol. 7, No. 6, p. 19, June 1962.

Golomb, S. W., "New Problems in Space Communications: Part 3," *Astronautics*, Vol. 7, No. 8, p. 26, Aug. 1962.

Golomb, S. W., "Ferreting Signals Out of Noise," *Int. Sci. Technol.*, No. 22, pp. 72–82 and 120, Oct. 1963.

Goodwin, P. S., et al., *Tracking and Data Systems Support for the Helios Project: Project Development Through End of Mission Phase II*, Technical Memorandum 33-752, Vol. I, Jet Propulsion Laboratory, Pasadena, Calif., July 1, 1976.

Gordon, H. J., et al., *The Mariner 6 and 7 Flight Paths and Their Determination From Tracking Data*, Technical Memorandum 33-469, Jet Propulsion Laboratory, Pasadena, Calif., Dec. 1, 1970.

Gottlieb, P., et al., "Lunar Gravity over Large Craters from Apollo 12 Tracking Data," *Science*, Vol. 168, No. 3930, pp. 477–479, Apr. 1970.

Gray, R. M., and Tausworthe, R. C., "Frequency-Counted Measurements, and Phase Locking to Noise Oscillators," *IEEE Trans. Commun. Technol.*, Vol. COM-19, No. 1, pp. 21–30, Feb. 1971.

Gubbay, J., et al., "Variations of Small Quasar Components at 2,300 MHz," *Nature*, Vol. 224, No. 5224, pp. 1094–1095, Dec. 1969.

Gulkis, S., and Gary, B., "Circular Polarization and Total-Flux Measurements of Jupiter at 13.1 cm Wavelength," *Astron. J.*, Vol. 76, No. 1, pp. 12–16, Feb. 1971.

Gulkis, S., et al., "Observations of Jupiter at 13-cm Wavelength During 1969 and 1971," *Icarus*, Vol. 18, No. 2, pp. 181–191, Feb. 1973.

Gulkis, S., et al., "An All-Sky Search for Narrow-Band Radiation in the Frequency Range 1–25 GHz," paper presented at the 1976 U.S. National Commission, International Union of Radio Science, Amherst, Mass., Oct. 10–15, 1976.

Hachenberg, O., et al., "The 100-meter Radio Telescope at Effelsberg, "*Proc. IEEE*, Vol. 61, No. 9, pp. 1288–1295, Sept. 1973.

Hall, J. R., and Easterling, M., "The Technology of Ground Stations in the Deep Space Network from 1958 to 1968," *IEEE Conf. Rec.*, Vol. 4, pp. 576–585, 1968.

Hall, J. R., et al., "The General Problem of Data Return from Deep Space," *Space Sci. Rev.*, Vol. 8, pp. 595–664, 1968.

Hall, J. R., *Tracking and Data System Support for Lunar Orbiter*, Technical Memorandum 33-450, Jet Propulsion Laboratory, Pasadena, Calif., Apr. 1970.

Hamilton, T. W., et al., *The Ranger IV Flight Path and Its Determination From Tracking Data*, Technical Report 32-345, Jet Propulsion Laboratory, Pasadena, Calif., Sept. 15, 1962.

Harris, A. W., et al., "2290-MHz Flux Densities of 52 High-Declination Radio Sources," *Astron. J.*, Vol. 81, No. 4, pp. 222–224, Apr. 1976.

Hartop, R. W., *Power Loss Between Arbitrarily Polarized Antennas*, Technical Report 32-457, Jet Propulsion Laboratory, Pasadena, Calif., Sept. 1, 1964.

Havens, W. F., et al., *Scan Pointing Calibration for the Mariner Mars 1971 Spacecraft*, Technical Memorandum 33-556, Jet Propulsion Laboratory, Pasadena, Calif., Aug. 1, 1972.

Heftman, K., and Renzetti, N. A., "Data Return Capabilities of the Deep Space Network in the 1970's," AIAA Paper 67-648, *Proceedings of the AIAA Space Program Issues of the 70's Meeting*, Aug. 1967.

Higa, W. H., *Low-Level Microwave Mixing in Ruby*, Technical Report 32-1016, Jet Propulsion Laboratory, Pasadena, Calif., reprinted from *Proc. IEEE*, Vol. 54, No. 10, p. 1453, Oct. 1966.

Higa, W. H., "Time Synchronization via Lunar Radar," *Proc. IEEE*, Vol. 60, No. 5, pp. 552–557, May 1972.

Higa, W. H., "Spurious Signals Generated by Electron Tunneling on Large Reflector Antennas," *Proc. IEEE*, Vol. 63, No. 2, pp. 306–313, Feb. 1975.

Higa, W. H., *The Superconducting Cavity-Stabilized Maser Oscillator*, Technical Memorandum 33-805, Jet Propulsion Laboratory, Pasadena Calif., Dec. 15, 1976.

Holmes, J. K., "On a Solution to the Second-Order Phase-Locked Loop," *IEEE Trans. Commun. Technol.*, Vol. COM-18, No. 2, pp. 119–126, Apr. 1970.

Holmes, J. K., "First Slip Times Versus Static Phase Error Offset for the First and Passive Second-Order Phase-Locked Loop," *IEEE Trans. Commun. Technol.*, Vol. COM-19, No. 2, pp. 234–235, Apr. 1971.

Holmes, J. K., and Tegnelia, C. R., *Digital Command System Second-Order Subcarrier Tracking Performance*, Technical Report 32-1540, Jet Propulsion Laboratory, Pasadena, Calif., Oct. 1, 1971.

Holmes, J. K., "Performance of a First Order Transition Sampling Digital Phase-Locked Loop Using Random-Walk Models," *IEEE Trans. Commun.*, Vol. COM-20, No. 2, pp. 119–131, Apr. 1972.

Hurd, W. J., and Anderson, T. O., *Digital Transition Tracking Symbol Synchronizer for Low SNR Coded Systems*, Technical Report 32-1488, Jet Propulsion Laboratory, Pasadena, Calif., reprinted from *IEEE Trans. Commun. Technol.*, Vol. COM-18, No. 2, pp. 141–147, Apr. 1970.

Hurd, W. J., "An Analysis and Demonstration of Clock Synchronization by VLBI," *IEEE Trans. Instr. Meas.*, Vol. IM-23, No. 1, pp. 80–89, March 1974.

Jacobson, R. A., McDanell, J. P., and Rinker, G. C., "Use of Ballistic Arcs in Low Thrust Navigation," *J. Spacecraft Rockets*, Vol. 12, No. 3, pp. 138–145, Mar. 1975.

Jaffe, R., and Rechtin, E., *Design and Performance of Phase-Lock Loops Capable of Near-Optimum Performance over a Wide Range of Input Signal and Noise Levels*, Progress Report 20-243, Jet Propulsion Laboratory, Pasadena, Calif., Dec. 1, 1954; also available in *IRE Trans. Inform. Theory*, No. 1, pp. 66–67, Mar. 1955.

Jordan, J. F., "Orbit Determination for Powered Flight Space Vehicles on Deep Space Missions," *J. Spacecraft Rockets*, Vol. 6, No. 5, pp. 545–550, May 1969.

Jordan, J. F., Melbourne, W. G., and Anderson, J. D., "Testing Relativistic Gravity Theories Using Radio Tracking Data From Planetary Orbiting Spacecraft," *Space Research XIII*, pp. 83–92, Akademie-Verlag, Berlin, 1973.

Jurgens, R. F., and Goldstein, R. M., "Radar Observations at 3.5 and 12.6 cm Wavelength of Asteroid 433 Eros," *Icarus*, Vol. 28, No. 1, pp. 1–15, May 1976.

Jurgens, R. F., and Bender, D. F., "Radar Detectability of Asteroids," *Icarus*, Vol. 31, No. 4, pp. 483–497, Aug. 1977.

Kellerman, K. I., et al., "High Resolution Observations of Compact Radio Sources at 13 Centimeters," *Astrophys. J.*, Vol. 161, No. 3, pp. 803–809, Sept. 1970.

Kelly, A. J., *Microwave Probe for Plasma Plumes*, Technical Report 32-625, Jet Propulsion Laboratory, Pasadena, Calif., Feb. 1965.

Kliore, A., Cain, D. L., and Hamilton, T. W., *Determination of Some Physical Properties of the Atmosphere of Mars from Changes in the Doppler Signal of a Spacecraft on an Earth-Occultation Trajectory*, Technical Report 32-674, Jet Propulsion Laboratory, Pasadena, Calif., Oct. 15, 1964.

Kliore, A., and Tito, D. A., *Radio Occultation Investigations of the Atmosphere of Mars*, Technical Report 32-1157, Jet Propulsion Laboratory, Pasadena, Calif., reprinted from *J. Spacecraft Rockets*, Vol. 4, No. 5, pp. 578–582, May 1967.

Kliore, A., "Radio Occultation Measurements of the Atmospheres of Mars and Venus," in *The Atmospheres of Venus and Mars*, edited by J. C. Brandt and M. B. McElrow, p. 205, Gordon and Breach Science Publishers, Inc., New York, N.Y., 1968.

Kliore, A. J., et al., "Summary of Mariner 6 and 7 Radio Occultation Results on the Atmosphere of Mars," *Space Research*, Vol. XI, pp. 165–175, Akademie-Verlag, Berlin, 1971.

Kliore, A. J., et al., "Mariner 9 S-Band Martian Occultation Experiment: Initial Results on the Atmosphere and Topography of Mars," *Science*, Vol. 175, No. 4019, pp. 313–317, Jan. 1972.

Kliore, A. J., et al., "The Atmosphere of Mars From Mariner 9 Radio Occultation Measurements," *Icarus*, Vol. 17, No. 2, pp. 484–516, Oct. 1972.

Kliore, A. J., et al., "S Band Radio Occultation Measurements of the Atmosphere and Topography of Mars with Mariner 9: Extended Mission Coverage of Polar and Intermediate Latitudes," *J. Geophys. Res.*, Vol. 78, No. 20, pp. 4331–4351, July 10, 1973.

Kliore, A. J., "Radio Occultation Exploration of Mars," *Exploration of the Planetary System* (IAU Symposium, No. 65), pp. 295–316, D. Reidel Publishing Co., Dordrecht, Holland, 1974.

Labrum, R. G., et al., *The Surveyor V, VI, and VII Flight Paths and Their Determination from Tracking Data*, Technical Report 32-1302, Jet Propulsion Laboratory, Pasadena, Calif., Dec. 1, 1968.

Laeser, R. P., et al., *Tracking and Data System Support for the Mariner Mars 1971 Mission: Prelaunch Phase Through First Trajectory Correction Maneuver*, Technical Memorandum 33-523, Vol. I, Jet Propulsion Laboratory, Pasadena, Calif., Mar. 15, 1972.

Layland, J. W., "On Optimal Signals for Phase-Locked Loops," *IEEE Trans. Commun. Technol.*, Vol. COM-17, No. 5, pp. 526–531, Oct. 1969.

Layland, J. W., and Lushbaugh, W. A., "A Flexible High-Speed Sequential Decoder for Deep Space Channels," *IEEE Trans. Commun. Technol.*, Vol COM-19 No. 5, pp. 813–820, Oct. 1971.

Layland, J. W., "Buffer Management for Sequential Decoding," *IEEE Trans. Commun.*, Vol. COM-22, No. 10, pp. 1685–1690, Oct. 1974.

Leavitt, R. K., *The Least-Squares Process of MEDIA for Computing DRVID Calibration Polynomials*, Technical Memorandum 33-542, Jet Propulsion Laboratory, Pasadena, Calif., May 15, 1972.

Lesh, J. R., *Signal-to-Noise Ratios in Coherent Soft Limiters*, Technical Report 32-1589, Jet Propulsion Laboratory, Pasadena, Calif., Sept. 15, 1973.

Lesh, J. R., "Signal-to-Noise Ratios in Coherent Soft Limiters," *IEEE Trans. Commun.*, Vol. COM-22, No. 6, pp. 803–811, June 1974.

Lesh, J. R., "Sequential Decoding in the Presence of a Noisy Carrier Reference," *IEEE Trans. Commun.*, Vol. COM-23, No. 11, pp. 1292–1297, Nov. 1975.

Levitt, B. K., "Optimum Frame Synchronization for Biorthogonally Coded Data," *IEEE Trans. Commun.*, Vol. COM-22, No. 8, pp. 1130–1134, Aug. 1974.

Levitt, B. K., "Long Frame Sync Words for Binary PSK Telemetry," *IEEE Trans. Commun.*, COM-23, No. 11, pp. 1365–1367, Nov. 1975.

Levy, G. S., Otoshi, T. Y., and Seidel, B. L., *Ground Instrumentation for Mariner IV Occultation Experiment*, Technical Report 32-984, Jet Propulsion Laboratory, Pasadena, Calif., Sept. 15, 1966.

Levy, G. S., et al., *Lunar Range Radiation Patterns of a 210-Foot Antenna at S-Band*, Technical Report 32-1079, Jet Propulsion Laboratory, Pasadena, Calif., reprinted from *IEEE Trans. Antennas Propagation*, Vol. AP-15, No. 2, pp. 311–313, Mar. 1967.

Levy, G. S., et al., *The Ultra Cone: An Ultra-Low-Noise Space Communication Ground Radio-Frequency System*, Technical Report 32-1340, Jet Propulsion Laboratory, Pasadena, Calif., reprinted from *IEEE Trans. Microwave Theor. Tech.*, Vol. MTT-16, No. 9, pp. 596–602, Sept. 1968.

Levy, G. S., et al., "Pioneer 6: Measurement of Transient Faraday Rotation Phenomena Observed During Solar Occultation," *Science*, Vol. 166, No. 3905, pp. 596–598, Oct. 1969.

Levy, G. S., et al., "Helios-1 Faraday Rotation Experiment: R[illegible] and Interpretations of the Solar Occultations in 1975," *J. Geophys.*, Vol. 42, No. 6, pp. 659–672, 1977.

Levy, R., "Computer-Aided Design of Antenna Structures and Components," *Comput. Struc.*, Vol. 6, Nos. 4/5, pp. 419–428, Aug./Oct. 1976.

Levy, R., and McGinness, H., *Wind Power Prediction Models*, Technical Memorandum 33-802, Jet Propulsion Laboratory, Pasadena, Calif., Nov. 15, 1976.

Lieske, J. H., and Null, G. W., "Icarus and the Determination of Astronomical Constants," *Astron. J.*, Vol. 74, No. 2, Mar. 1969.

Lieske, J. H., et al., "Simultaneous Solution for the Masses of the Principal Planets from Analysis of Optical Radar and Radio Tracking Data," *Celest. Mech.*, Vol. 4, No. 2, pp. 233–245, Oct. 1971.

Lindsey, W. C., *Optimum and Suboptimum Frequency Demodulation*, Technical Report 32-637, Jet Propulsion Laboratory, Pasadena, Calif., June 15, 1964.

Lindsey, W. C., *Improvements to be Realized Through the Use of Block-Coded Communication Systems*, Technical Report 32-947, Jet Propulsion Laboratory, Pasadena, Calif., reprinted from *IEEE Trans. Aerosp. Electron. Syst.*, Vol. AES-2, No. 3, pp. 364–366, May 1966.

Lindsey, W. C., *Phase-Shift-Keyed Signal Detection with Noisy Reference Signals*, Technical Report 32-968, Jet Propulsion Laboratory, Pasadena, Calif., reprinted from *IEEE Trans. Aerosp. Electron. Syst.*, Vol. AES-2, No. 4, pp. 393–401, July 1966.

Lindsey, W. C., *A Theory for the Design of One-Way and Two-Way Phase-Coherent Communication Systems: Phase-Coherent Tracking Systems*, Technical Report 32-986, Jet Propulsion Laboratory, Pasadena, Calif., July 15, 1969.

Lindsey, W. C., *Optimal Design of One-Way and Two-Way Coherent Communication Links*, Technical Report 32-988, Jet Propulsion Laboratory, Pasadena, Calif., reprinted from *IEEE Trans. Commun. Technol.*, Vol. COM-14, No. 4, pp. 418–131, Aug. 1966.

Lindsey, W. C., and Charles, F. J., *A Model Distribution for the Phase Error in Second-Order Phase-Locked Loops*, Technical Report 32-1017, Jet Propulsion Laboratory, Pasadena, Calif., reprinted from *IEEE Trans. Commun. Technol.*, Vol. COM-14, No. 10, pp. 662–664, Oct. 1966.

Lindsey, W. C., *Performance of Phase-Coherent Receivers Preceded by Bandpass Limiters*, Technical Report 32-1162, Jet Propulsion Laboratory, Pasadena, Calif., Sept. 15, 1967.

Lindsey, W. C., "Block Coding for Space Communications," *IEEE Trans. Commun. Technol.*, Vol. COM-17, No. 2, pp. 217–225, Apr. 1969.

Lindsey, W. C., *Block-Coded Communications*, Technical Report 32-1380, Jet Propulsion Laboratory, Pasadena, Calif., Aug. 15, 1969.

Lindsey, W. C., *Nonlinear Analysis of Generalized Tracking Systems*, Technical Report 32-1453, Jet Propulsion Laboratory, Pasadena, Calif., reprinted from *Proc. IEEE*, Vol. 57, No. 10, pp. 1705–1722, Oct. 1969.

Lindsey, W. C., and Simon, M. K., "The Effect of Loop Stress on the Performance of Phase-Coherent Communication Systems", *IEEE Trans. Commun. Technol.*, Vol. COM-18, No. 5, pp. 569–588, Oct. 1970.

Lindsey, W. C., and Simon, M. K., "Carrier Synchronization and Detection of Polyphase Signals," *IEEE Trans. Commun.*, Vol. COM-20, No. 3, pp. 441–454, June 1972.

Lindsey, W. C., and Simon, M. K., "L-Orthogonal Signal Transmission and Detection," *IEEE Trans. Commun.*, Vol. COM-20, No. 5, pp. 953–960, Oct. 1972.

Lindsey, W. C., and Simon, M. K., "On the Detection of Differentially Encoded Polyphase Signals, " *IEEE Trans. Commun.*, Vol. COM-20, No. 6, pp. 1121–1128, Dec. 1972.

Lindsey, W. C., *Synchronization Systems in Communication and Control*, Prentice-Hall, Inc., Englewood Cliffs, N. J., 1972.

Lindsey, W. C., and Tausworthe, R. C., *A Bibliography of the Theory and Application of the Phase-Lock Principle*, Technical Report 32-1581, Jet Propulsion Laboratory, Pasadena, Calif., Apr. 1, 1973.

Lindsey, W. C., and Simon, M. K., *Telecommunication Systems Engineering*, Prentice-Hall, Inc., Englewood Cliffs, N. J., 1973.

Liu, A. S., and Pease, G. E., "Spacecraft Ranging From a Ground Digitally Controlled Oscillator," *J. Spacecraft Rockets*, Vol. 12, No. 9, pp. 528–532, Sept. 1975.

Lorell, J., Anderson, J. D., and Sjogren, W. L., *Characteristics and Format of the Tracking Data to Be Obtained by the NASA Deep Space Instrumentation Facility for Lunar Orbiter*, Technical Memorandum 33-230, Jet Propulsion Laboratory, Pasadena, Calif., June 15, 1965.

Lorell, J., Sjogren, W. L., and Boggs, D., *Compressed Tracking Data Used for First Iteration in Selenodesy Experiment, Lunar Orbiters I and II*, Technical Memorandum 33-343, Jet Propulsion Laboratory, Pasadena, Calif., May 1, 1967.

Lorell, J., and Sjogren, W. L., *Lunar Orbiter Data Analysis*, Technical Report 32-1220, Jet Propulsion Laboratory, Pasadena, Calif., Nov. 15, 1967.

Lorell, J., *Lunar Orbiter Gravity Analysis*, Technical Report 32-1387, Jet Propulsion Laboratory, Pasadena, Calif., June 15, 1969.

Lorell, J., et al., "Icarus: Celestial Mechanics Experiment for Mariner," *Int. J. Sol. Sys.*, Vol. 12, Jan. 1970.

Lorell, J., and Laing, P. A., *Compilation of Lunar Orbiter Tracking Data Used for Long-Term Selenodesy*, Technical Memorandum 33-419, Jet Propulsion Laboratory, Pasadena, Calif., Feb. 1, 1970.

Lorell, J., "Estimation of Gravity Field Harmonics in the Presence of Spin-Axis Direction Error Using Radio Tracking Data," *J. Astronaut. Sci.*, Vol. XX, No. 1, pp. 44–54, Aug. 1972.

Ludwig, A. C., et al., *Gain Calibration of a Horn Antenna Using Pattern Integration*, Technical Report 32-1572, Jet Propulsion Laboratory, Pasadena, Calif., Oct. 1, 1972.

Madrid, G. A., et al., *Tracking System Analytic Calibration Activities for the Mariner Mars 1971 Mission*, Technical Report 32-1587, Jet Propulsion Laboratory, Pasadena, Calif., Mar. 1, 1974.

Martin, D. P., *A Combined Radar-Radiometer With Variable Polarization*, Technical Memorandum 33-570, Jet Propulsion Laboratory, Pasadena. Calif., Oct. 15, 1972., May 15, 1977.

Martin, W. L., and Zygielbaum, A. I., *Mu-II Ranging*, Technical Memorandum 33-768, Jet Propulsion Laboratory, Pasadena, Calif., May 15, 1977.

Mathison, R. P., *Tracking Techniques for Interplanetary Spacecraft*, Technical Report 32-284, Jet Propulsion Laboratory, Pasadena, Calif., Aug. 1, 1962.

McEliece, R. J., *Optimal Communications Nets*, Technical Report 32-697, Jet Propulsion Laboratory, Pasadena, Calif., Apr. 15, 1965.

McNeal, C. E., *Ranger V Tracking Systems Data Analysis Final Report*, Technical Report 32-702, Jet Propulsion Laboratory, Pasadena, Calif., Apr. 15, 1965.

Melbourne, W. G., et al., *Constants and Related Information for Astrodynamical Calculations*, Technical Report 32-1306, Jet Propulsion Laboratory, Pasadena, Calif., July 15, 1968.

Melbourne, W. G., "Planetary Ephemerides," *Astronaut. Aeronaut.*, Vol. 7, No. 5, pp. 38–43, May 1970.

Melbourne, W. G., "Navigation between the Planets," *Sci. Amer.*, Vol. 234, No. 6, pp. 58–74, June 1976.

Merrick, W. D., et al., *Deep Space Communications*, Technical Release 34-10, Jet Propulsion Laboratory, Pasadena, Calif., Jan. 29, 1960; also available in *IRE Trans. Mil. Electron.*, Vol. MIL-4, No. 2-3, pp. 158–163, April–June 1960.

Miller, L., et al., *The Atlas-Centaur VI Flight Path and Its Determination from Tracking Data*, Technical Report 32-911, Jet Propulsion Laboratory, Pasadena, Calif., Apr. 15, 1966.

Miller, R. B., *Tracking and Data System Support for the Pioneer Project: Pioneers 6–9. Extended Missions: July 1, 1972–July 1, 1973*, Technical Memorandum 33-426, Vol. XII. Jet Propulsion Laboratory, Pasadena, Calif., March 1, 1974.

Miller, R. B., *Tracking and Data System Support for the Pioneer Project: Pioneer 10—From April 1, 1972, Through the Jupiter Encounter Period, January 1974*, Technical Memorandum 33-584, Vol. III, Jet Propulsion Laboratory, Pasadena, Calif., June 15, 1975.

Miller, R. B., et al., *Tracking and Data System Support for the Pioneer Project: Pioneer 10—From January 1974 to January 1975; Pioneer 11—From May 1, 1973 Through Jupiter Encounter Period, January 1975*, Technical Memorandum 33-584, Vol. IV, Jet Propulsion Laboratory, Pasadena, Calif., Dec. 1, 1975.

Moyer, T. D., *Mathematical Formulation of the Double-Precision Orbit Determination Program (DPODP)*, Technical Report 32-1527, Jet Propulsion Laboratory, Pasadena, Calif., May 17, 1971.

Muhleman, D. O., *Relationship Between the System of Astronomical Constants and the Radar Determinations of the Astronomical Unit*, Technical Report 32-477, Jet Propulsion Laboratory, Pasadena, Calif., Jan. 15, 1964.

Muhleman, D. O., Goldstein, R., and Carpenter, R., *A Review of Radar Astronomy—Parts I, II*, Technical Report 32-824, Jet Propulsion Laboratory, Pasadena, Calif., Jan. 30, 1966, reprinted from *IEEE Spectrum*, Oct. and Nov. 1965.

Muhleman, D. O., et al., *JPL Radar Range and Doppler Observations of Venus, 1961–1966*, Technical Report 32-1123, Jet Propulsion Laboratory, Pasadena, Calif., July 1, 1968.

Muhleman, D. O., et al., "Radio Propagation Measurements of the Solar Corona and Gravitational Field: Applications to Mariner 6 and 7," in *Proceedings of the Conference on Experimental Tests of Gravitational Theories*, California Institute of Technology, Pasadena, Calif., Nov. 1970.

Muhleman, D. O., Esposito, P. B., and Anderson, J. D., "The Electron Density Profile of the Outer Corona and the Interplanetary Medium From Mariner-6 and Mariner-7 Time-Delay Measurements," *Astrophys. J.*, No. 211, No. 3, Part 1, pp. 943–957, Feb. 1, 1977.

Mulhall, B. D., et al., *Tracking System Analytic Calibration Activities for the Mariner Mars 1969 Mission*, Technical Report 32-1499, Jet Propulsion Laboratory, Pasadena, Calif., Nov. 15, 1970.

Mulholland, J. D., and Sjogren, W. L., *Lunar Orbiter Ranging Data*, Technical Report 32-1087, Jet Propulsion Laboratory, Pasadena, Calif., reprinted from *Science*, Vol. 155, No. 3758, pp. 74–76, Jan. 6, 1967.

Mulholland, J. D., *Proceedings of the Symposium on Observation, Analysis and Space Research Applications of the Lunar Motion*, Technical Report 32-1386, Jet Propulsion Laboratory, Pasadena, Calif., Apr. 1969.

Muller, P. M., and Sjogren, W. L., *Consistency of Lunar Orbiter Residuals With Trajectory and Local Gravity Effects*, Technical Report 32-1307, Jet Propulsion Laboratory, Pasadena, Calif., Sept. 1, 1968.

Muller, P. M., and Sjogren, W. L., *Mascons: Lunar Mass Concentrations*, Technical Report 32-1339, Jet Propulsion Laboratory, Pasadena, Calif., reprinted from *Science*, Vol. 161, No. 3842, pp. 680–684, Aug. 16, 1968.

Muller, P. M., Sjogren, W. L., and Wollenhaupt, W. R., "Lunar Gravity: Apollo 15 Doppler Radio Tracking," *The Moon*, Vol. 10, No. 2, pp. 195–205, June 1974.

The NASA/JPL 64-Meter-Diameter Antenna at Goldstone, California: Project Report, Technical Memorandum 33-671, Jet Propulsion Laboratory, Pasadena, Calif., July 15, 1974.

Newburn, R. L., Jr., et al., *Earth-Based Research on the Outer Planets During the Period 1970–1985*, Technical Report 32-1456, Jet Propulsion Laboratory, Pasadena, Calif., M. r. 15, 1970.

Null, G. W., et al., *Mariner IV Flight Path and Its Determination From Tracking Data*, Technical Report 32-1108, Jet Propulsion Laboratory, Pasadena, Calif., Aug. 1, 1967.

Ohlson, J. E., "Polarization Tracking of a Partially Coherent Signal Using a Double Loop," *IEEE Trans. Commun.*, Vol. COM-23, No. 9, pp. 859 -866, Sept. 1975.

Ohlson, J. E., and Reid, M. S., *Conical-Scan Tracking With the 64-m-diameter Antenna at Goldstone*, Technical Report 32-1605, Jet Propulsion Laboratory, Pasadena, Calif., Oct. 1, 1976.

O'Neil, W. J., et al., *The Surveyor III and Surveyor IV Flight Paths and Their Determination From Tracking Data*, Technical Report 32-1292, Jet Propulsion Laboratory, Pasadena, Calif., Aug. 15, 1968.

O'Neil, W. J., et al., *Mariner 9 Navigation*, Technical Report 32-1586, Jet Propulsion Laboratory, Pasadena, Calif., Nov. 13, 1973.

Ong., K. M., et al., "A Demonstration of a Transportable Radio Interferometric Surveying System With 3-cm Accuracy on a 307-m Base Line" *J. Geophys. Res.*, Vol. 81, No. 20, pp. 3587–3593, July 10, 1976.

Otoshi, T. Y., *The Effect of Mismatched Components on Microwave Noise-Temperature Calibrations*, Technical Report 32-1345, Jet Propulsion Laboratory, Pasadena, Calif., reprinted from *IEEE Trans. Microwave Theor. Tech.*, Vol. MTT-16, No. 9, pp. 675–686, Sept. 1968.

Otoshi, T. Y., Stelzried, C. T., and Yates, B. C., "Comparisons of Waveguide Losses Calibrated by the DC Potentiometer, AC Ratio Transformer, and Reflectometer

Techniques," *IEEE Trans. Microwave Theor. Tech.*, Vol. MTT-18, No. 7, pp. 406–409, July 1970.

Otoshi, T. Y., and Stelzried, C. T., "A Precision Compact Rotary Vane Attenuator," *IEEE Trans. Micro. Theor. Technique*, Vol. MTT-19, No. 11, pp. 843–854, Nov. 1971.

Otoshi, T. Y., "Precision Reflectivity Loss Measurements of Perforated-Plate Mesh Materials by a Waveguide Technique," *IEEE Trans. Instr. Meas.*, Vol. IM-21, No. 4, pp. 451–457, Nov. 1972.

Otoshi, T. Y., and Stelzried, C. T., "Cosmic Background Noise Temperature Measurement at 13-cm Wavelength," *IEEE Trans. Instr. Meas.*, Vol. IM-24, No. 2, pp. 174–179, June 1975.

Pease, G. E., et al., *The Mariner V Flight Path and Its Determination From Tracking Data*, Technical Report 32-1363, Jet Propulsion Laboratory, Pasadena, Calif., July 1, 1969.

Posner, E. C., *Properties of Error-Correcting Codes at Low Signal-to-Noise Ratios* Technical Report 32-602, Jet Propulsion Laboratory, Pasadena, Calif., June 15, 1964.

Posner, E. C., "Random Coding Strategies for Minimum Entropy," *IEEE Trans. Inform. Theor.*, Vol. IT-21, No. 4, pp. 388–391, July 1975.

Potter, P. D., *The Design of a Very High Power, Very Low Noise Cassegrain Feed System for a Planetary Radar*, Technical Report 32-653, Jet Propulsion Laboratory, Pasadena, Calif., Aug. 24, 1964.

Potter, P. D., Merrick, W. D., and Ludwig, A. C., *Large Antenna Apertures and Arrays for Deep Space Communications*, Technical Report 32-848, Jet Propulsion Laboratory, Pasadena, Calif., Nov. 1, 1965.

Potter, P. D., *A Computer Program for Machine Design of Cassegrain Feed Systems*, Technical Report 32-1202, Jet Propulsion Laboratory, Pasadena, Calif., Dec. 15, 1967.

Potter, P. D., et al., *A Study of Weather-Dependent Data Links for Deep Space Applications*, Technical Report 32-1392, Jet Propulsion Laboratory, Pasadena, Calif., Oct. 15, 1969.

Preston, R. A., "Dual-Spacecraft Radio Metric Tracking," *The Deep Space Network: May and June 1974*, DSN Progress Report, pp. 51–65. Jet Propulsion Laboratory, Pasadena, Calif., Aug. 15, 1974.

Rechtin, E., "Communication Techniques for Space Exploration," *IRE Trans. Space Electron. Telem.*, Vol. SET-5, No. 3, pp. 95–98, Sept. 1959.

Rechtin, E., Stevens, R., and Victor, W. K., *Data Transmission and Communications*, Technical Release 34-55, Jet Propulsion Laboratory, Pasadena, Calif., Apr. 30, 1960.

Rechtin, E., *Space Communications*, Technical Release 34-68, Jet Propulsion Laboratory, Pasadena, Calif., May 1, 1960.

Rechtin, E., et al., *JPL Range and Doppler System*, Technical Memorandum 33-13, Jet Propulsion Laboratory, Pasadena, Calif., Sept. 22, 1961.

Rechtin, E., Rule, B., and Stevens, R., *Large Ground Antennas*, Technical Report 32-213, Jet Propulsion Laboratory, Pasadena, Calif., Mar. 20, 1962.

Rechtin, E., *Lunar Communications*, Technical Memorandum 33-133, Jet Propulsion Laboratory, Pasadena, Calif., June 28, 1963.

Rechtin, E., "Surprises on Venus," *Int. Sci. Technol.*, No. 20, pp. 13–14, Aug. 1963.

Rechtin, E., "Long Range Planning for the Deep Space Network," *Astronaut. Aeronaut.*, Vol. 6, No. 1, pp. 28–35, Jan. 1968.

Reid, M. S., et al., "Low-Noise Microwave Receiving Systems in a Worldwide Network of Large Antennas," *Proc. IEEE*, Vol. 61, No. 9, pp. 1330–1335, Sept. 1973.

Renzetti, N. A., et al., "Radio Tracking Techniques and Performance of the U.S. Deep Space Instrumentation Facility," *Space Research II, Proceedings of the Second International Space Science Symposium*, Florence, Italy, April 1961, North Holland Publishing Company, Amsterdam.

Renzetti, N. A., and Ostermier, B. J., *Communications with Lunar Probes*, Technical Report 32-143, Jet Propulsion Laboratory, Pasadena, Calif., Aug. 23, 1961.

Renzetti, N. A., "DSIF in the Ranger Project," *Astronautics*, Vol. 6, No. 1, pp. 34–37, 70, Sept. 1961.

Renzetti, N. A., *Tracking and Data Acquisition for Ranger Missions V*, Technical Memorandum 33-174, Jet Propulsion Laboratory, Pasadena, Calif., July 1, 1964.

Renzetti, N. A., *Tracking and Data Acquisition for Ranger Missions VI–IX*, Technical Memorandum 33-275, Jet Propulsion Laboratory, Pasadena, Calif., Sept. 15, 1966.

Renzetti, N. A., *Tracking and Data Acquisition Support for the Mariner Venus 1962 Mission*, Technical Memorandum 33-212, Jet Propulsion Laboratory, Pasadena, Calif., July 1, 1965.

Renzetti, N. A., *Tracking and Data Acquisition Report, Mariner Mars 1964 Mission: Near-Earth Trajectory Phase*, Technical Memorandum 33-239, Vol. I, Jet Propulsion Laboratory, Pasadena, Calif., Jan. 1, 1965.

Renzetti, N. A., *Tracking and Data Acquisition Report, Mariner Mars 1964 Mission: Cruise to Post-Encounter Phase*, Technical Memorandum 33-239, Vol. II, Jet Propulsion Laboratory, Pasadena, Calif., Oct. 1, 1967.

Renzetti, N. A., *Deep Space Network Support, Atlas/Centaur Missions 1–9*, Technical Memorandum 33-347, Jet Propulsion Laboratory, Pasadena, Calif., Sept. 15, 1967.

Renzetti, N. A., "Tracking and Data Acquisition System for Mariner Missions," *Proceedings of the Seventh International Symposium on Space Technology and Science*, Tokyo, 1967.

Renzetti, N. A., *Tracking and Data Acquisition Report, Mariner Mars 1964 Mission: Extended Mission*, Technical Memorandum 33-239, Vol. III, Jet Propulsion Laboratory, Pasadena, Calif., Dec. 1, 1968.

Renzetti, N. A., and Fearey, J. P., "The Deep Space Network: An Instrument for the Radio Navigation for the Mariner Mission to Mars 1969," IInd International Conference on Space Engineering, Venice, Italy, D. Reidel Publishing Co., Dordrecht, Holland, May 1969.

Renzetti, N. A., *Tracking and Data System Support for Surveyor: Missions I and II*, Technical Memorandum 33-301, Vol. I, Jet Propulsion Laboratory, Pasadena, Calif., July 15, 1969.

Renzetti, N. A., *Tracking and Data System Support for Surveyor: Missions III and IV*, Technical Memorandum 33-301, Vol. II, Jet Propulsion Laboratory, Pasadena, Calif., Sept. 1, 1969.

Renzetti, N. A., *Tracking and Data System Support for Surveyor: Mission V*, Technical Memorandum 33-301, Vol. III, Jet Propulsion Laboratory, Pasadena, Calif., Dec. 1, 1969.

Renzetti, N. A., *Tracking and Data System Support for Surveyor: Mission VI*, Technical Memorandum 33-301, Vol. IV, Jet Propulsion Laboratory, Pasadena, Calif., Dec. 1, 1969.

Renzetti, N. A., *Tracking and Data System Support for Surveyor: Mission VII*, Technical Memorandum 33-301, Vol. V, Jet Propulsion Laboratory, Pasadena, Calif., Dec. 1, 1969.

Renzetti, N. A., *Tracking and Data System Support for the Mariner Venus 67 Mission: Planning Phase Through Midcourse Maneuver*, Technical Memorandum 33-385, Vol. I, Jet Propulsion Laboratory, Pasadena, Calif., Sept. 1, 1969.

Renzetti, N. A., *Tracking and Data System Support for the Mariner Venus 67 Mission: Midcourse Maneuver Through End of Mission*, Technical Memorandum 33-385, Vol. II, Jet Propulsion Laboratory, Pasadena, Calif., Sept. 1, 1969.

Renzetti, N. A., *Tracking and Data System Support for the Pioneer Project: Pioneer VI. Prelaunch to End of Nominal Mission*, Technical Memorandum 33-426, Vol. I, Jet Propulsion Laboratory, Pasadena, Calif., Feb. 1, 1970.

Renzetti, N. A., *Tracking and Data System Support for the Pioneer Project: Pioneer VII. Prelaunch to End of Nominal Mission*, Technical Memorandum 33-426, Vol. II, Jet Propulsion Laboratory, Pasadena, Calif., Apr. 15, 1970.

Renzetti, N. A., *Tracking and Data System Support for the Pioneer Project: Pioneer VIII. Prelaunch Through May 1968*, Technical Memorandum 33-426, Vol. III, Jet Propulsion Laboratory, Pasadena, Calif., July 15, 1970.

Renzetti, N. A., *Tracking and Data System Support for the Pioneer Project: Pioneer IX. Prelaunch Through June 1969*, Technical Memorandum 33-426, Vol. IV, Jet Propulsion Laboratory, Pasadena, Calif., Nov. 15, 1970.

Renzetti, N. A., *Tracking and Data System Support for the Pioneer Project: Pioneer VI. Extended Mission: July 1, 1966–July 1, 1969*, Technical Memorandum 33-426, Vol. V, Jet Propulsion Laboratory, Pasadena, Calif., Feb. 1, 1971.

Renzetti, N. A., *Tracking and Data System Support for the Pioneer Project: Pioneer VII. Extended Mission: February 24, 1967–July 1, 1968*, Technical Memorandum 33-426, Vol. VI, Jet Propulsion Laboratory, Pasadena, Calif., Apr. 15, 1971.

Renzetti, N. A., *Tracking and Data System Support for the Pioneer Project: Pioneer VII. Extended Mission: July 1, 1968–July 1, 1969*, Technical Memorandum 33-426, Vol. VII, Jet Propulsion Laboratory, Pasadena, Calif., Apr. 15, 1971.

Renzetti, N. A., *Tracking and Data System Support for the Pioneer Project: Pioneer VIII. Extended Mission: June 1, 1968–July 1, 1969*, Technical

Memorandum 33-426, Vol. VIII, Jet Propulsion Laboratory, Pasadena, Calif., May 1, 1971.

Renzetti, N. A., *Tracking and Data System Support for the Pioneer Project: Pioneers VI–IX. Extended Missions: July 1, 1969–July 1, 1970*, Technical Memorandum 33-426, Vol. IX, Jet Propulsion Laboratory, Pasadena, Calif., Aug. 15, 1971.

Renzetti, N. A., and Siegmeth, A. J., *Tracking and Data System Support for the Pioneer Project: Pioneers 6–9. Extended Missions: July 1, 1971–July 1, 1972*, Technical Memorandum 33-426, Vol. XI, Jet Propulsion Laboratory, Pasadena, Calif., May 1, 1973.

Renzetti, N. A., et al., *Tracking and Data System Support for the Mariner Mars 1969 Mission: Planning Phase Through Midcourse Maneuver*, Technical Memorandum 33-474, Vol. I, Jet Propulsion Laboratory, Pasadena, Calif., May 15, 1971.

Renzetti, N. A., et al., *Tracking and Data System Support for the Mariner Mars 1969 Mission: Midcourse Maneuver Through End of Nominal Mission*, Technical Memorandum 33-474, Vol. II, Jet Propulsion Laboratory, Pasadena, Calif., Sept. 1, 1971.

Renzetti, N. A., Linnes, K. W., and Taylor, T. M., *Tracking and Data System Support for the Mariner Mars 1969 Mission: Extended Operations Mission*, Technical Memorandum 33-474, Vol. III, Jet Propulsion Laboratory, Pasadena, Calif., Sept. 15, 1971.

Renzetti, N. A., *A History of the Deep Space Network: From Inception to January 1, 1969*, Technical Report 32-1533, Vol. I, Jet Propulsion Laboratory, Pasadena, Calif., Sept. 1, 1971.

Renzetti, N. A., "Radio Communications at Planetary Distances," paper presented at the International Convention on Radio Communication, Rome and Bologna, Italy, Mar. 1974.

Richter, H. L., Rechtin, E., and Walter, W. K., *National Ground-Based Surveillance Complex (U)*, Publication 146, Jet Propulsion Laboratory, Pasadena, Calif., Feb. 16, 1959 (Confidential).

Rocci, S. A., "The 210-ft Parabolic Fully Steerable Tracking Antennas for a Deep Space Instrumentation Facility," in *Deep Space and Missile Tracking Antennas*, pp. 50–70, ASME, New York, 1966.

Rusch, W. V. T., *Phase Error and Associated Cross-Polarization Effects in Cassegrainian-Fed Microwave Antennas*, Technical Report 32-610, Jet Propulsion Laboratory, Pasadena, Calif., May 30, 1965.

Rusch, W. V. T., and Stelzried, C. T., *Observations of the Lunar Eclipse of December 19, 1964, at a Wavelength of 3.3 MM*, Technical Report 32-1097, Jet Propulsion Laboratory, Pasadena, Calif., reprinted from *Astrophys. J.*, Vol. 1[illegible], No. 1, pp. 255–259, Apr. 1967.

Rusch, W. V. T., *Applications of Two-Dimensional Integral-Equation Theory to Reflector-Antenna Analysis*, Technical Memorandum 33-478, Jet Propulsion Laboratory, Pasadena, Calif., May 1, 1971.

Rusch, W. V. T., "Double Aperture Blocking by Two Wavelength-Sized Feed-Support Struts," *Electron. Lett.*, Vol. 10, No. 15, pp. 296–297, July 25, 1974.

Sanger, D. K., *Digital Demodulation with Data Subcarrier Tracking*, Technical Report 32-1314, Jet Propulsion Laboratory, Pasadena, Calif., Aug. 1, 1968.

Siegmeth, A. J., Purdue, R. E., and Ryan, R. E., *Tracking and Data System Support for the Pioneer Project: Pioneers 6–9. Extended Missions: July 1, 1970–July 1, 1971*, Technical Memorandum 33-426, Vol. X, Jet Propulsion Laboratory, Pasadena, Calif., Aug. 15, 1972.

Siegmeth, A. J., et al., *Tracking and Data System Support for the Pioneer Project: Pioneer 10—Prelaunch Planning Through Second Trajectory Correction December 4, 1969 to April 1, 1972*, Technical Memorandum 33-584, Vol. I, Jet Propulsion Laboratory, Pasadena, Calif., Apr. 1, 1973.

Simon, M. K., "Nonlinear Analysis of an Absolute Value Type of an Early-Late Gate Bit Synchronizer," *IEEE Trans. Commun. Technol.*, Vol. COM-18, No. 5, pp. 589–596, Oct. 1970.

Simon, M. K., "Optimization of the Performance of a Digital-Data-Transition Tracking Loop," *IEEE Trans. Commun. Technol.*, Vol. COM-18, No. 5, pp. 686–689, Oct. 1970.

Simon, M. K., and Lindsey, W. C., "Data-Aided Carrier Tracking Loops," *IEEE Trans. Commun. Technol.*, Vol. COM-19, No. 2, pp. 157–168, Apr. 1971.

Simon, M. K., "On the Selection of an Optimum Design Point for Phase-Coherent Receivers Employing Bandpass Limiters," *IEEE Trans. Commun.*, Vol. COM-20, No. 2, pp. 210–214, Apr. 1972.

Simon, M. K., "On the Selection of a Sampling Filter Bandwidth for a Digital Data Detector," *IEEE Trans. Commun.*, Vol. COM-20, No. 3, pp. 438–441, June 1972.

Simon, M. K., and Springett, J. C., "The Performance of a Noncoherent FSK Receiver Preceded by a Bandpass Limiter," *IEEE Trans. Commun.*, Vol. COM-20, No. 6, pp. 1128–1136, Dec. 1972.

Simon, M. K., and Springett, J. C., *The Theory, Design, and Operation of the Suppressed Carrier Data-Aided Tracking Receiver*, Technical Report 32-1583, Jet Propulsion Laboratory, Pasadena, Calif., June 15, 1973.

Simon, M. K., and Smith, J. G., "Hexagonal Multiple Phase-and-Amplitude-Shift-Keyed Signal Sets," *IEEE Trans. Commun.*, Vol. COM-21, No. 10, pp. 1108–1115, Oct. 1973.

Simon, M. K., and Smith, J. G., "Carrier Synchronization and Detection of QASK Signal Sets," *IEEE Trans. Commun.*, Vol. COM-22, No. 2, pp. 98–106, Feb. 1974.

Simon, M. K., *Data-Derived Symbol Synchronization of MASK and QASK Signals*, Technical Memorandum 33-720, Jet Propulsion Laboratory, Pasadena, Calif., Dec. 15, 1974.

Simon, M. K., "A Generalization of Minimum-Shift-Keying (MSK) Type Signaling Based Upon Input Data Symbol Pulse Shaping," *IEEE Trans. Commun.*, Vol. COM-24, No. 8, pp. 845–856, Aug. 1976.

Simon, M. K., "An MSK Approach to Offset QASK," *IEEE Trans. Commun.*, Vol. COM-24, No. 8, pp. 921–923, Aug. 1976.

Sjogren, W. L., et al., *The Ranger V Flight Path and Its Determination From Tracking Data*, Technical Report 32-562, Jet Propulsion Laboratory, Pasadena, Calif., Dec. 6, 1963.

Sjogren, W. L., et al., *The Ranger VI Flight Path and Its Determination From Tracking Data*, Technical Report 32-605, Jet Propulsion Laboratory, Pasadena, Calif., Dec. 15, 1964.

Sjogren, W. L., *The Ranger III Flight Path and Its Determination From Tracking Data*, Technical Report 32-563, Jet Propulsion Laboratory, Pasadena, Calif., Sept. 15, 1965.

Sjogren, W. L., et al., *Physical Constants as Determined From Radio Tracking of the Ranger Lunar Probes*, Technical Report 32-1057, Jet Propulsion Laboratory, Pasadena, Calif., Dec. 30, 1966.

Sjogren, W. L., *Proceedings of the JPL Seminar on Uncertainties in the Lunar Ephemeris*, Technical Report 32-1247, Jet Propulsion Laboratory, Pasadena, Calif., May 1, 1968.

Sjogren, W. L., "Lunar Gravity Estimate: Independent Confirmation," *J. Geophys. Res.*, Vol. 76, No. 29, Oct. 10, 1971.

Sjogren, W. L., et al., "Lunar Gravity via Apollo 14 Doppler Radio Tracking," *Science*, Vol. 175, No. 4018, pp. 165–168, Jan. 14, 1972.

Sjogren, W. L., et al., "Gravity Fields," *IEEE Trans. Geosci. Electron.*, Vol. GE-14, No. 3, pp. 172–183, July 1976.

Slobin, S. D., "Beam Switching Cassegrain Feed System and Its Applications to Microwave and Millimeterwave Radioastronomical Observations," *Rev. Sci. Instr.*, Vol. 41, No. 3, pp. 439–443, Mar. 1970.

Spier, G. W., *Design and Implementation of Models for the Double Precision Trajectory Program (DPTRAJ)*, Technical Memorandum 33-451, Jet Propulsion Laboratory, Pasadena, Calif., Apr. 15, 1971.

Springett, J. C., *Telemetry and Command Techniques for Planetary Spacecraft*, Technical Report 32-495, Jet Propulsion Laboratory, Pasadena, Calif., Jan. 15, 1965.

Springett, J. C., and Simon, M. K., "An Analysis of the Phase Coherent-Incoherent Output of the Bandpass Limiter," *IEEE Trans. Commun. Technol.*, Vol. COM-19, No. 1, pp. 42–49, Feb. 1971.

Stelzried, C. T., *Post-Amplifier Noise Temperature Contribution in a Low-Noise Receiving System*, Technical Report 32-446, Jet Propulsion Laboratory, Pasadena, Calif., Jan. 1964.

Stelzried, C. T., Reid, M. S., and Petty, S. M., *A Precision DC-Potentiometer Microwave Insertion-Loss Test Set*, Technical Report 32-887, Jet Propulsion Laboratory, Pasadena, Calif., Mar. 15, 1966.

Stelzried, C. T., Reid, M. S., and Nixon, D., *Precision Power Measurements of Spacecraft CW Signal With Microwave Noise Standards*, Technical Report 32-1066, Jet Propulsion Laboratory, Pasadena, Calif., Feb. 15, 1968.

Stelzried, C. T and Reid, M. S., *Precision Power Measurements of Spacecraft CW Signal Level With Microwave Noise Standards*, Technical Report 32-1070, Jet Propulsion Laboratory, Pasadena, Calif., reprinted from *IEEE Trans. Instrum. Measurement*, Vol. IM-15, No. 4, pp. 318–324, Dec. 1966.

Stelzried, C. T., and Rusch, W. V. T., *Improved Determination of Atmospheric Opacity From Radio Astronomy Measurements*, Technical Report 32-1115, Jet

Propulsion Laboratory, Pasadena, Calif., reprinted from *J. Geophys. Res.*, Vol. 72, No. 9, pp. 2445–2447, May 1, 1967.

Stelzried, C. T., and Otoshi, T. Y., "Radiometric Evaluation of Antenna-Feed Component Losses," *IEEE Trans. Instrumen. Measurement*, Vol. IM-18, No. 3, pp. 172–183, Sept. 1969.

Stelzried, C. T., "Precision Microwave Waveguide Loss Calibrations," *IEEE Trans. Instrum. Measurement*, Vol. IM-19, No. 1, pp. 23–25, Feb. 1970.

Stelzried, C. T., *A Faraday Rotation Measurement of a 13-cm Signal in the Solar Corona*, Technical Report 32-1401, Jet Propulsion Laboratory, Pasadena, Calif., July 15, 1970.

Stelzried, C. T., et al., "The Quasi-Stationary Coronal Magnetic Field and Electron Density as Determined From a Faraday Rotation Experiment," *Sol. Phys.*, Vol. 14, No. 2, pp. 440–456, Oct. 1970.

Stelzried, C. T., "Operating Noise-Temperature Calibrations of Low-Noise Receiving Systems," *Microwave J.*, Vol. 14, No. 6, pp. 41–46, 48, June 1971.

Stelzried, C. T., et al., "Transformation of Received Signal Polarization Angle to the Plane of the Ecliptic," *J. Space. Rock.*, Vol. 9, No. 2, pp. 69–70, Feb. 1972.

Stevens, R., and Victor, W. K., *The Goldstone Station Communications and Tracking System for Project Echo*, Technical Report 32-59, Jet Propulsion Laboratory, Pasadena, Calif., Dec. 1, 1960.

System Capabilities and Development Schedule of the Deep Space Instrumentation Facility 1963–1967, Technical Memorandum 33-83, Jet Propulsion Laboratory, Pasadena, Calif., Mar. 2, 1962.

Tardani, P. A., *Madrid Site Selection Report*, Technical Memorandum 33-149, Jet Propulsion Laboratory, Pasadena, Calif., July 17, 1963.

Tausworthe, R. C., *A Precision Planetary Range-Tracking Radar*, Technical Report 32-779, Jet Propulsion Laboratory, Pasadena, Calif., reprinted from *IEEE Trans. Space Electron. Telem.*, Vol. SET-11, No. 2, pp. 78–85, June 1965.

Tausworthe, R. C., *Theory and Practical Design of Phase-Locked Receivers*, Technical Report 32-819, Vol. I, Jet Propulsion Laboratory, Pasadena, Calif., Feb. 15, 1966.

Tausworthe, R., *Cycle Slipping in Phase-Locked Loops*, Technical Report 32-1127, Jet Propulsion Laboratory, Pasadena, Calif., reprinted from *IEEE Trans. Commun. Technol.*, Vol. COM-15, No. 3, pp. 417–421, June 1967.

Tausworthe, R. C., Easterling, M. F., and Spear, A. J., *A High-Rate Telemetry System for the Mariner Mars 1969 Mission*, Technical Report 32-1354, Jet Propulsion Laboratory, Pasadena, Calif., Apr. 1, 1969.

Tausworthe, R. C., *DSS Subsystem Implementation by Time-Shared Computer*, Technical Memorandum 33-420, Jet Propulsion Laboratory, Pasadena, Calif., Oct. 1, 1969.

Tausworthe, R. C., "Convergence of Oscillator Spectral Estimators for Counted-Frequency Measurements," *IEEE Trans. Commun.*, Vol. COM-20 No. 2, pp. 213–217, Apr. 1972.

Tausworthe, R. C., "Simplified Formula for Mean-Slip Time of Phase-Locked Loops With Steady-State Phase Error," *IEEE Trans. Commun.*, Vol. COM-20, No. 3, pp. 331–337, June 1972.

Tausworthe, R. C., and Crow, R. B., "Improvements in Deep-Space Tracking by Use of Third-Order Loops," *Proceedings of the 1972 International Telemetering Conference, Los Angeles, California, October 10–12, 1972*, pp. 577–583.

Tausworthe, R. C., *Standard Classifications of Software Documentation*, Technical Memorandum 33-756, Jet Propulsion Laboratory, Pasadena, Calif., Jan. 15, 1976.

Telecommunications Systems Design Techniques Handbook, Technical Memorandum 33-571, edited by R. E. Edelson, Jet Propulsion Laboratory, Pasadena, Calif., July 15, 1972.

Textor, G. P., Kelly, I. B., and Kelly, M., *Tracking and Data System Support for the Mariner Mars 1971 Mission: First Trajectory Correction Maneuver Through Orbit Insertion*, Technical Memorandum 33-523, Vol. II, Jet Propulsion Laboratory, Pasadena, Calif., June 15, 1972.

Thomas, J. B., et al., "A Demonstration of an Independent-Station Radio Interferometry System With 4-cm Precision on a 16-km Base Line" *J. Geophys. Res.*, Vol. 81, No. 5, pp. 995–1005, Feb. 10, 1976.

Thornton, J. H., Jr., *The Surveyor I and Surveyor II Flight Paths and Their Determination From Tracking Data*, Technical Report 32-1285 Jet Propulsion Laboratory, Pasadena, Calif., Aug. 1, 1968.

Timor, U., "Equivalence of Time-Multiplexed and Frequency-Multiplexed Signals in Digital Communications," *IEEE Trans. Commun.*, Vol. COM-20, No. 3, pp. 435–438, June 1972.

Titsworth, R. C., and Welch, L. R., *Power Spectra of Signals Modulated by Random and Pseudorandom Sequences*, Technical Report 32-140, Jet Propulsion Laboratory, Pasadena, Calif., Oct. 10, 1961.

Titsworth, R. C., *The Algebra of Periodic Sequences*, Technical Report 32-381, Jet Propulsion Laboratory, Pasadena, Calif., Jan. 7, 1963.

Titsworth, R. C., *Correlation Properties of Cyclic Sequences*, Technical Report 32-388, Jet Propulsion Laboratory, Pasadena, Calif., July 1, 1963.

Titsworth, R. C., *Optimal Ranging Codes*, Technical Report 32-411, Jet Propulsion Laboratory, Pasadena, Calif., Apr. 15, 1963.

Titsworth, R. C., *Equivalence Classes of Periodic Sequences*, Technical Report 32-568, Jet Propulsion Laboratory, Pasadena, Calif., June 15, 1964, reprinted from *Ill. J. Math.*, Vol. 8. No. 2, June 1964.

Tausworth, R. C., *The Role of Pseudorandom Codes in Communications*, Technical Memorandum 33-185, Jet Propulsion Laboratory, Pasadena, Calif., Aug. 3, 1964.

Toukdarian, R. Z., *Final Engineering Report for Goldstone Operations Support Radar*, Technical Memorandum 33-800, Jet Propulsion Laboratory, Pasadena, Calif., Nov. 1, 1976.

"Tracking and Data Acquisition System for Mariner Missions," *Proceedings of the Seventh International Symposium on Space Technology and Science*, Tokyo, May 1967.

Truong, T. K., and Reed, I. S., "Convolutions Over Residue Classes of Quadratic Integers," *IEEE Trans. Inform. Theor.*, Vol. IT-22, No. 4, pp. 468–475, July 1976.

Truong, T. K., and Reed, I. S., "Convolutions over Quartic Integer Residue Classes," *Proceedings of the International Conference on Information Sciences and Systems*, Patras, Greece, Aug. 19–24, 1976.

Truong, T. K., Liu, K. Y., and Reed, I. S., "Fast Number-Theoretic Transforms for Digital Filtering," *Electron. Lett.*, Vol. 12, No. 24, Nov. 1976.

Truong, T. K., et al., "X-Ray Reconstruction by Finite Field Transforms," *IEEE Trans. Nucl. Sci.*, Vol. NS-24, No. 1, pp. 843–849, Feb. 1977.

Truong, T. K., Golomb, S. W., and Reed, I. S., "Integer Convolutions Over the Finite Field $GF(3 \cdot 2^n + 1)$," *SIAM J. Appl. Math.*, Vol. 32, No. 2, pp. 356–365, Mar. 1977.

Truong, T. K., Reed, I. S., and Liu, K. Y., "Fast Algorithm for Computing Complex Number-Theoretic Transforms," *Electron. Lett.*, Vol. 13, No. 10, pp. 278–280, May 12, 1977.

Vegos, C. J., et al., *The Ranger IX Flight Path and Its Determination From Tracking Data*, Technical Report 32-767, Jet Propulsion Laboratory, Pasadena, Calif., Nov. 1, 1968.

Victor, W. K., *Precision Frequency Control—A Communications Requirement of the Space Age*, External Publication 627, Jet Propulsion Laboratory, May 13, 1959.

Victor, W. K., and Stevens, R., "The Role of the Jet Propulsion Laboratory in Project Echo," *IRE Trans.*, Vol. SET-7, pp. 20–29, Mar. 1961.

Victor, W. K., Stevens, R., and Golomb, S. W., *Radar Exploration of Venus: Goldstone Observatory Report for March-May 1961*, Technical Report 32-132, Jet Propulsion Laboratory, Pasadena, Calif., Aug. 1, 1961.

Victor, W. K., Titsworth, R. C., and Rechtin, E., *Telecommunication Aspects of a Manned Mars Mission*, Technical Report 32-501, Jet Propulsion Laboratory, Pasadena, Calif., Aug. 20, 1963.

Viterbi, A. J., *Acquisition Range and Tracking Behavior of Phase-Locked Loops*, External Publication 673, Jet Propulsion Laboratory, Pasadena, Calif., July 14, 1959.

Viterbi, A. J., *On Coded Phase-Coherent Communications*, Technical Report 32-25, Jet Propulsion Laboratory, Pasadena, Calif., Aug. 15, 1960.

Viterbi, A. J., *Classification and Evaluation of Coherent Synchronous Sampled-Data Telemetry Systems*, Technical Report 32-123, Jet Propulsion Laboratory, Pasadena, Calif., June 15, 1961.

Viterbi, A. J., *Phase-Locked Loop Dynamics in the Presence of Noise by Fokker-Planck Techniques*, Technical Report 32-427, Jet Propulsion Laboratory, Pasadena, Calif., Mar. 28, 1963; also reprinted in *IEEE Proc.*, Vol. 51, No. 12, pp. 1737–1753, Dec. 1963.

Viterbi, A. J., *Orthogonal Tree Codes for Communication in the Presence of White Gaussian Noise*, Technical Report 32-1120, Jet Propulsion Laboratory, Pasadena, Calif., reprinted from *IEEE Trans. Commun. Technol.*, Vol. COM-15, No. 2, pp. 238–242, Apr. 1967.

von Roos, O. H., Yip, K. B. W., and Escobal, P. R., "A Global Model of the Earth's Ionosphere for Use in Space Applications," *Astronautica Acta*, Vol. 18 (Supplement), No. 3, pp. 215–232, Aug. 1974.

Weber, W. J., III, "Performance of Phase-Locked Loops in the Presence of Fading Communication Channels," *IEEE Trans. Commun.*, Vol. COM-24, No. 5, pp. 487–499, May 1976.

Weber, W. J., III, Ackerknecht, W. E., and Kollar, F. J., *Viking X-Band Telemetry Experiment Final Report*, Technical Memorandum 33-794, Jet Propulsion Laboratory, Pasadena, California, Sept. 1, 1976.

Winn, F. B., "Selenographic Location of Surveyor VI," in *Surveyor VI Mission Report. Part II. Science Results*, Technical Report 32-1262, Jet Propulsion Laboratory, Pasadena, Calif., Jan. 10, 1968.

Winn, F. B., "Post Landing Tracking Data Analysis," in *Surveyor VII Mission Report: Part II. Science Results*, Technical Report 32-1264, Jet Propulsion Laboratory, Pasadena, Calif., Mar. 15, 1968.

Winn, F. B., "Surveyor Post-Touchdown Analysis of Tracking Data," in *Surveyor Project Final Report: Part II. Science Results*, Technical Report 32-1265, Jet Propulsion Laboratory, Pasadena, Calif., June 15, 1968.

Winn, F. B., *Surveyor Posttouchdown Analyses of Tracking Data*, NASA SP-184, National Aeronautics and Space Administration, Washington, D.C., p. 369.

Wollenhaupt, W. R., *Tracking System Data Analysis Report, Ranger 4 Final Report*, Technical Report 32-523, Jet Propulsion Laboratory, Pasadena, Calif., Mar. 1, 1964.

Wollenhaupt, W. R., et al., *The Ranger VII Flight Path and Its Determination From Tracking Data*, Technical Report 32-694, Jet Propulsion Laboratory, Pasadena, Calif., Dec. 15, 1964.

Wong, S. K., and Reinbold, S. J., "Earth–Moon Mass Ratio From Mariner 9 Radio Tracking Data," *Nature*, Vol. 241, No. 5385, pp. 111–112, Jan. 12, 1973.

Woo, R., and Ishimaru, A., "Remote Sensing of the Turbulence Characteristics of a Planetary Atmosphere by Radio Occultation of a Space Probe," *Radio Sci.*, Vol. 8, No. 2, pp. 103–108, Feb. 1973.

Woo, R., et al., *Effects of Turbulence in the Atmosphere of Venus on Pioneer Venus Radio—Phase I*, Technical Memorandum 33-644, Jet Propulsion Laboratory, Pasadena, Calif., June 30, 1973.

Woo, R. T., "Observations of Turbulence in the Atmosphere of Venus Using Mariner 10 Radio Occultation Measurements," *J. Atmos. Sci.*, Vol. 32, No. 6, pp. 1084–1090, June 1975.

Yuen, J. H., "A Double-Loop Tracking System," *IEEE Trans. Commun.*, Vol. COM-20, No. 6, pp. 1142–1150, Dec. 1972.

Yuen, J. H., *A Practical Statistical Model for Telecommunications Performance Uncertainty*, Technical Memorandum 33-732, Jet Propulsion Laboratory, Pasadena, Calif., June 15, 1975.